

ISTANBUL TECHNICAL UNIVERSITY ★ EURASIA INSTITUTE OF EARTH SCIENCES

**ACTIVE FAULTING AND EARTHQUAKE SCARPS
ALONG THE NORTH ANATOLIAN FAULT IN THE SEA OF MARMARA**

**Ph.D. Thesis by
Glсен UÇARKUŞ**

Department : Solid Earth Sciences

Programme : Earth System Science

JUNE 2010

**ACTIVE FAULTING AND EARTHQUAKE SCARPS
ALONG THE NORTH ANATOLIAN FAULT IN THE SEA OF MARMARA**

**Ph.D. Thesis by
Glsen UÇARKUŞ
(602022013)**

**Date of submission : 01 June 2010
Date of defence examination: 18 June 2010**

**Supervisor (Chairman) : Doç. Dr. Ziyadin ÇAKIR (ITU)
Members of the Examining Committee : Prof. Dr. A.M. Celal ŐENGÖR (ITU)
Prof. Dr. Namık ÇAĖATAY (ITU)
Prof. Dr. Mustapha MEGHRAOUI (IPGS)
Doç. Dr. Semih ERĖINTAV (TUBITAK)**

JUNE 2010

İSTANBUL TEKNİK ÜNİVERSİTESİ ★ AVRASYA YER BİLİMLERİ ENSTİTÜSÜ

**MARMARA DENİZİ'NDE KUZEY ANADOLU FAYI BOYUNCA AKTİF
FAYLANMA VE DEPREM SARPLIKLARI**

**DOKTORA TEZİ
Gölsen UÇARKUŞ
(602022013)**

Tezin Enstitüye Verildiği Tarih : 1 Haziran 2010

Tezin Savunulduğu Tarih : 18 Haziran 2010

**Tez Danışmanı : Prof. Dr. Ziyadin ÇAKIR (İTÜ)
Diğer Jüri Üyeleri : Prof. Dr. A.M. Celal ŞENGÖR (İTÜ)
Prof. Dr. Namık ÇAĞATAY (İTÜ)
Prof. Dr. Mustapha MEGHRAOUI (IPGS)
Doç. Dr. Semih ERGİNTAV (TÜBİTAK)**

HAZİRAN 2010

FOREWORD

PhD is a long journey for the person who experiences it. Along this road, many people walk with you, inspire and support you. Foreword is the exact place to tell all these people that you are really sincerely grateful. There are so many people to thank and mention here for their help, guidance, support and friendship throughout the course of my entire Ph.D

First of all, I would like to thank late Aykut Barka for changing my life in many ways; for opening doors that I would never expect, for giving me chances to be myself and to take responsibility, for showing me that any difficulty can be beaten with good passion, for teaching us the only important criteria we should care is to do good science with quality work and with good people. It is with Aykut Barka's will that I started studying this PhD subject on the Sea of Marmara. Therefore, I want to dedicate my work to his beloved memory. He'll always be my driving force to do good science.

I'd like to thank most sincerely to my advisor Dr. Ziyadin Çakır who has been extremely supportive during my entire PhD. It was his encouragement that proved me there was the light at the end of the tunnel and so I was able to complete my thesis. His strong scientific vision and patience to teach new things put me in a place that I'll always be grateful to him and I can't express enough my gratitude. He has been a good mentor and a sincere brother through the entire period.

I would like to thank Prof. Rolando Armijo, my co-advisor from IPG Paris, for giving me the opportunity to work on this very exciting and important project. It was a great honour for me to work with such a dedicated scientist and to learn from him. Thanks to all our scientific discussions that improved my vision in science.

During this study I had many constructive discussions with Prof. Namık Çağatay to improve my thesis. I'm also grateful to his support in helping me to better understand the marine geological problems. I would like to thank Prof. A.M. Celal Şengör for forwarding me to exquisite problems of the NAF in the Sea of Marmara; encouraging me to discover more. I also want to present my gratitude to him for providing me the chance to dive with the Nautil (submersible) during the MARNAUT cruise which turned out to be the most amazing experience in my life.

My special thanks to Prof. Mustapha Maghraoui who has been very supportive through the entire time. He gave me opportunities to gain experience in other European projects and he has been a constant mentor to improve myself. I'd like to thank Dr. Daniela Pantosti who always encouraged me to finish my PhD. She has been a very special friend and supporter.

I'm grateful to Dr. Semih Ergintav from TUBITAK MAM for providing additional data to enrich my results and sparing his time for constructive discussions. I owe special thanks to Dr. Onur Tan who provided new seismologic data to this work. Prof. Serdar Akyüz also contributed with helpful discussions.

We worked together with Dr. Sabine Schmidt (Bordeaux University) to analyze the short cores for ^{210}Pb geochronology. I'd like to thank her for her efforts and our fruitful discussions. Dr. Christian Beck and Dr. Bernard Mercier de Lepinay are also thanked for their collaboration.

My very good friend and colleague Dr. Murat Ersen Aksoy has to be mentioned here specially. His unique friendship and constant support was the ultimate driving force behind my PhD life. Many scientific discussions we made together during our PhD education improved my vision. My dear friend Dr. Şafak Altunkaynak was an enormous supporter and encourager. She became an academic coach during this period. I'm grateful to her. I'm so thankful to Dr. Tayfun Kındap for his precious friendship. He constantly encouraged and supported me to get over the problems of my thesis.

My very special thanks go to dearest Kezban Saki Yaltrık and Dr. Cenk Yaltrık for their invaluable support and friendship. My dear friends and colleagues, Umut Barış Ülgen, Sena Akçer, Cengiz Zabcı, Dr. Doğa Düşünür, Dr. Dilek Şatır and Dr. Ufuk Tarı were always there for me for discussions and encouragement. They are sincerely and deeply thanked.

The French Embassy in Ankara supported me financially under the cotutelle program during my stays in Paris. I would like to thank for their contribution.

A very close circle of friends supported me during this period. I'm so grateful to all of them. Some of them was directly involved into my struggles. I'd like to mention their names here and thank sincerely to Dr. Fulya Özgün, Oya Kılar Topaç, Didem Alacahanlı and Nuray Salman for their precious friendship.

And finally but most precious, I would like to express my deep gratitude to my beloved family members, my father Nurettin, my mother Seniye, my sister Nursen, my brother-in-law Aydın and my nephew Eray, who patiently tolerated and supported me during the entire process. I'm so lucky to be a part of this beautiful family.

June, 2010

Gülsen Uçarkuş

TABLE OF CONTENTS

	<u>Page</u>
FOREWORD	v
TABLE OF CONTENTS	vii
ABBREVIATIONS	ix
LIST OF TABLES	xi
LIST OF FIGURES	xiii
SUMMARY	xxv
ÖZET	xxix
1. INTRODUCTION	1
1.1 Scope of the study	1
2. GEOLOGICAL AND TECTONIC OVERVIEW OF THE SEA OF MARMARA REGION: STATE OF THE ART	5
2.1 Introduction	5
2.2 Geology of the Marmara Region.....	5
2.3 Tectonic Background	8
2.3.1 Paleo-tectonic setting of Turkey: A link to the present-day tectonics	8
2.3.2 The North Anatolian Fault	11
2.3.3 North Anatolian Fault in the Sea of Marmara.....	21
3. CHARACTERISTICS OF ACTIVE FAULTING ALONG THE NORTH ANATOLIAN FAULT IN THE SEA OF MARMARA	33
3.1 Introduction	33
3.2 The Northern Marmara Fault System and associated active basins.....	35
3.2.1 Tectonic and morphologic structure of the Çınarcık Basin	36
3.2.2 Tectonic and morphologic structure of the Central Basin	55
3.2.3 Tectonic and morphologic structure of the Tekirdağ Basin.....	65
3.3 Late Pleistocene-Holocene subsidence and faulting rates in the Sea of Marmara	68
3.3.1 Relation between stratigraphy, climate change, and sedimentation rates in the Sea of Marmara	70
3.3.2 The 3.5 kHz chirp data and the correlation of ¹⁴ C dated cores	72
3.3.3 Tectonic and stratigraphic implications on Late Pleistocene-Holocene subsidence and faulting rates	75
3.4 Discussion	86
4. EARTHQUAKE SCARPS IN THE SEA OF MARMARA	89
4.1 General introduction.....	89
4.2 Method: Seafloor Observations in the Sea of Marmara and the new dataset... 91	91
4.3 Western Termination of the Mw 7.4, 1999 İzmit Earthquake Rupture: Implications for the Expected Large Earthquake in the Sea of Marmara	93
4.3.1 Seismotectonic background	93
4.3.2 The Mw 7.4, 17 August 1999 İzmit earthquake	95

4.3.3 Submarine fault scarps west of Hersek: evidence for the 1999 İzmit earthquake rupture.....	98
4.3.4 Coulomb stress modeling of the 1999 İzmit earthquake.....	106
4.3.5 Discussion and conclusions.....	107
4.4 1912 Ganos earthquake rupture in the Sea of Marmara: rupture geometry and morphology of the scarps.....	109
4.4.1 Introduction.....	109
4.4.2 Field observations of the 1912 Ganos earthquake rupture on land.....	110
4.4.3 Morphology of submarine fault scarps in Tekirdağ and Central basins .	112
4.4.4 Conclusions.....	122
4.5 Re-constructing the the history of earthquakes in the the Sea of Marmara over the last century based on ^{210}Pb geochronology.....	124
4.5.1 Strategy and methods.....	125
4.5.2 Use of ^{210}Pb geochronology in sediment dating.....	128
4.5.3 Results and Discussion.....	131
4.6 Discussion: earthquake ruptures in the Sea of Marmara and implications for the seismic hazard for the region.....	145
5. THE AGE AND THE OFFSET OF THE NORTH ANATOLIAN FAULT IN MARMARA REGION.....	147
5.1 Introduction.....	147
5.2 The age of the NAF.....	147
5.3 The offset of the NAF.....	148
5.4 Discussion.....	156
6. CONCLUSIONS.....	157
REFERENCES.....	161
CURRICULUM VITAE.....	177

ABBREVIATIONS

AIC	: Akaike Information Criteria
ANN	: Artificial Neural Network
App	: Appendix
3D	: 3 Dimensional
AD	: Anno Domini
An	: Anatolia
Ar	: Arabia
B.C.	: Before Christ
CMT	: Centroid Moment Tensor
DEM	: Digital Elevation Model
DGPS	: Differential GPS
DSF	: Dead Sea Fault
E	: East
EAF	: East Anatolian Fault
EGF	: Empirical Green Function
Eu	: Eurasia
exg.	: Exaggeration
GMT	: Generic Mapping Tools
GPS	: Global Positioning System
Kyr	: Kilo years
Ka	: Kilo years
LPH	: Late Pleistocene Horizon
LT	: Local Time
MAM	: Marmara Research Center
Ma	: Million years
MCS	: Multi Channel Seismic
m.s.	: Milisecond
MSK	: Medvedev-Sponheuer-Karnik intensity
MTA	: Maden Tetkik ve Arama
N	: North
NAF	: North Anatolian Fault
NAT	: North Aegean Through
NAFZ	: North Anatolian Fault Zone
NCF	: Northern Çınarcık Fault
NE	: Northeast
NMT	: Northern Marmara Trough
NNAF	: Northern North Anatolian Fault
NNW	: North-Northwest
NW	: Northwest
InSAR	: Interferometric Synthetic Aperture Radar
PIF	: Princes Islands Fault (Northern Çınarcık Fault)
ROV	: Remotely operated vehicle
R/V	: Research vessel
S	: South

SCF	: Southern Çınarcık fault
SE	: Southeast
SHOD	: Seyir Hidrografi ve Oşinografi
SRTM	: Shuttle Radar Topography Mission
SW	: Southwest
TMM	: MTA TAMAM profiles
TUBITAK	: The Scientific and Technological Research Council of Turkey
Twtt	: Two way travel time
USGS	: United State Geological Survey
W	: West
WWSSN	: World Wide Standardized Seismograph Network

LIST OF TABLES

	<u>Page</u>
Table 1 : All the sedimentation rates determined from the $^{210}\text{Pb}_{\text{xs}}$ Profiles of selected MARMARASCARPS short cores in the Sea of Marmara	145

LIST OF FIGURES

	<u>Page</u>
Figure 1.1 : Tectonic map of Turkey and its vicinity where four plates, i.e., the Arabian, African, Eurasian and Anatolian plates meet. Blue arrows with white fill are GPS vector that shows the anticlockwise rotation of Anatolia and Arabia relative to fixed Eurasia driven by the opening and seafloor spreading of the Red Sea (McClusky et al., 2000). The increase in GPS velocity towards the west demonstrates that the westward extrusion of Anatolia cannot be attributed to the collision between Arabia and Eurasia along the Bitlis-Assyrian suture in Eastern Turkey alone, and that the trench suction has an important contribution to anticlockwise rotation of Anatolia in the Aegean. Black block arrows show areas of local extension and compression. Red lines are active faults (from Şaroğlu et al., 1992). Yellow strips are showing schematically the Aegean extensional region.....	2
Figure 1.2 : Splays of the North Anatolian fault in the Marmara region. The northern splays runs through İzmit, the Sea of Marmara, Ganos and Saros bay while the southern branch runs through the İznik Lake, Bursa and Gulf of Edremit. Faults (black lines) with thick color shadows indicate earthquake ruptures in the 20th century. Fault map modified from Armijo et al. (2002).	3
Figure 2.1 : Tectonic map of Turkey and its surroundings showing the major sutures and continental blocks (from Okay and Tüysüz, 1999).....	6
Figure 2.2 : Representative paleotectonic maps showing the tectonic processes that Turkey went through from Permian to Early Eocene (Yılmaz et al., 1997).....	9
Figure 2.3 : Map of Turkey and surrounding regions showing configuration of tectonic plates, major structures (DSF: Dead Sea Fault; EAF: East Anatolian Fault; NAF: North Anatolian Fault; NAT: North Aegean Through), and motion of plates relative to Eurasia determined by GPS (red arrows) (Reilinger et al., 2006). White block arrows indicate the direction of extension in the Aegean.....	12
Figure 2.4 : Possible damage area and related submarine fault segments Are depicted by Parson (2004) for the 1500–2000 earthquake catalog of the Sea of Marmara region.	18
Figure 2.5 : (a) Map of the North Anatolian fault map plotted on shaded elevation image (SRTM-90 m) (b) Slip distribution along the North Anatolian fault during the 20th century earthquakes. Note the seismic gaps in Marmara and Yedisu that pose serious hazard its surroundings, particularly to Istanbul.....	20

Figure 2.6	: Focal mechanism solutions of small earthquakes (ML 1.6 to 4.1) between 2001 and 2003 (from Tan et al., 2008). Note the alignment of earthquakes along the submarine section of the North Anatolian fault.	21
Figure 2.7	: Centroid Moment Tensor solutions from Global CMT between 1976 and 2009.	21
Figure 2.8	: Proposed fault models for the North Anatolian Fault under the Sea of Marmara. A: Barka and Kadinsky-cade, 1988; B: Wong et al., 1995; C: Parke et al., 1999; D: Okay et al., 1999; E: Yaltrak 2002; F: Aksu et al., 2000; G: Le Pichon et al., 2001; Armijo et al., 2002.....	23
Figure 2.9	: Mechanical models (Muller and Aydin, 2005) based on three different fault configurations in the Sea of Marmara showing subsidence (blue areas) and uplift (red areas). a) Okay et al., 1999, b) Le Pichon et al., 2001, c) Armijo et al., 2002.....	27
Figure 2.10	: Observed (black) and modeled (red) GPS velocity field with %95 confidence ellipses in the Marmara region in Eurasian fixed reference. The region is divided into three blocks as Eurasia, Marmara and Anatolia by the northern and southern strands of the NAF. The fault model in the Sea of Marmara is the simplified version of that of Le Pichon et al. (2001) and Armijo et al. (2002). Blue circles show the nodes used to define the faults.	29
Figure 2.11	: Modeling results. (a) Variation of slip rates along the strands of the NAF and their kinematics in the Marmara region. (b) Fault parallel slip rates (i.e., strike-slip). (c) Fault normal slip rates (i.e., reverse or normal). Note the significant amount (12.3 ± 0.9 mm) of opening along the Northern Çınarcık fault (the purple color inc c).	30
Figure 3.2	: (a) Bathymetric map of the Çınarcık basin (contours every 20 m)	37
Figure 3.2	: (b) Morphotectonic map of the Çınarcık basin showing active faults and related submarine features.	38
Figure 3.3	: (a) Map of active faults and GPS vectors in eastern Marmara (relative to Eurasia) (from Reilinger et al., 2006). (b) Kinematic cartoon model showing westward motion of Anatolia relative to fixed Eurasia, which gives rise to opening in the Çınarcık basin. Black vectors show the direction and amount of the displacement given. Yellow and green arrows show, respectively, the fault parallel and fault normal components of displacement resolved on the North Çınarcık fault.....	40
Figure 3.4	: 3D NE oblique view of the Çınarcık basin showing the escarpment of the Northern Çınarcık fault sliced by landslides and arcuate faults, and the en-echelon faults at its base (ls: landslide, red arrows indicate fault traces).	42
Figure 3.5	: (a) 3D SW oblique view of the Çınarcık basin showing the escarpment of the Southern Çınarcık fault sliced by numerous small faults, triangular facets, debris flows and submarine fans. (b) 3D scheme showing how sediments are triggered by earthquakes.....	43

Figure 3.6 : Deep (down to ~10 km) seismic reflection profile SM36 crossing the Çınarcık basin in NE-SW direction (profile 36 in the inset map) from Laigle et al. (2008).....	45
Figure 3.7 : Bathymetry image of the Çınarcık basin with locations of the seismic lines.	46
Figure 3.8 : 3D, northwest view of the Çınarcık basin with a slice of multichannel seismic section (line 124; see Figure 3.7 for location) showing the deep depocenter of the Çınarcık basin bounded and cut by active synsedimentary faults.....	46
Figure 3.9 : Elastic dislocation model on a buried normal fault (red line) that results in warping of sediments on the hangingwall (in the area indicated by the ellipse), which is analogous to slip deficit on the upper portion of the fault (calculated using Coulomb 3 software of USGS).	48
Figure 3.10 : Multi channel seismic reflection section along the TMM 69 profile crossing the Çınarcık basin (see Figure 3.7 for the location).	50
Figure 3.11 : Marmarascarp Line C14 resolves recent sedimentary pile down to 70 ms. The vertical exaggeration is ~20, which helps to distinguish offsets of individual layers.....	51
Figure 3.12 : Selected north-south migrated profiles (134, 145,152) of the SEISMARMARA cruise from the western half of the Çınarcık Basin. Seismic profiles are re-interpreted after Carton et al. (2007). Red lines indicate the faults and colored dashed lines are to distinguish significant reflectors. Plio-Quaternary sedimentary units are drawn in yellow.	52
Figure 3.13 : 3D model of the Çınarcık basin merged with depth profiles from Carton et al. (2007) illustrates the match of mapped fault array with the faults at depth. Recent earthquakes from TUBITAK MAM network are also projected on both images.	53
Figure 3.14 : Schematic block diagrams depicting the structures of the Çınarcık and Hamner basins that appear to be similar.....	54
Figure 3.15 : Correlation of the 3D bathymetry map of the Central basin with the deep seismic reflection profile from SEISMARMARA cruise (Laigle et al., 2008) illustrates the structure of the basin at depth. It clearly demonstrates that what is seen on the basin floor from multibeam bathymetry penetrates see floor well below 5 km.....	56
Figure 3.16 : Morphology of the Central basin revealed by shaded multibeam bathymetry with (b) and without (a) interpreted faults. The similar scarp morphology with vertical throws (~10 m) is readily seen in the Profile B (Figure 3.18).....	57
Figure 3.17 : (a) 2D bathymetry map of the northern section of the Central basin (illumination from north). Black arrows indicate the morphological trace of the fault breaks. (b) Active faults mapped from the bathymetry (c) 2D bathymetry map of the southern section of the Central basin (illumination from south). Red arrows highlights the morphologic traces of the faults (d) Active faults mapped from the bathymetry.	58
Figure 3.18 : 3D view of the northern edge of the Central basin (illumination	

	from north). Profile A is taken from the sharp fault scarp that offset the outer basin floor and Profile B is taken from the northern edge of the inner pull-apart basin. Both fault scarps expose throws ranging from 10 to 40 m.....	59
Figure 3.19 :	Location of the selected 3.5 kHz seismic lines in the Central Basin.....	60
Figure 3.20 :	The 3.5 kHz profile (vertical exaggeration is 10) across the Central Basin. Sedimentary pile as defined by the high resolution 3.5 kHz profile (upper two panels; data without and with interpretation). Faults with normal slip at edges of inner pull-apart are readily seen.	61
Figure 3.21 :	Thousands meter scale topographic evolution of the (a) Central basin. (b) Large scale bathymetric profile across the Central basin depicting the nested graben morphology (c) Microbathymetry extract of the southern edge of the inner pull-apart (red box in Figure 3.21b. (white line indicates the profile location below) d) Microbathymetry profile resolves details of the morphology.	62
Figure 3.22 :	N-S 3.5 kHz profile along the Central basin that transects the inner pull-apart. Top panel illustrates the sedimentary horizons deduced from the chirp line. Subsidence of the inner basin is readily seen. Bottom panels are the chirp line with vertical exaggeration 20 and 10, respectively.	63
Figure 3.23 :	Comparison of the Central basin (right) with an analogue model (left panel) obtained by Wu et al., (2009). Note the similarities in the nested basins.	64
Figure 3.24 :	Shaded relief map of the Tekirdag basin combining multibeam bathymetry (25 m gridding) and SRTM 90 m onland. Red lines represent active faults determined from bathymetry and shallow seismic reflections. Those with uncertain recent activity are depicted with dashed redlines. Seismic-reflection profile MTA 05 (collected in the Sea of Marmara in September 1997 by MTA) is located with white dashed line.....	66
Figure 3.25 :	(a) Perspective view looking southwest of the western end of the Tekirdag Basin with combined onland topography and multibeam bathymetry. Schematic interpretation is based on profile in the lower panel and the map in Figure 3.24. (b) seismic-reflection profile MTA 05 is from Parke et al, 2003, and re-interpreted in this study. Profile reflects the basin asymmetry. The fastest subsidence is along the border fault, which is the northern branch of the NAF. Lines with colors indicate certain reflectors to illustrate the difference in layer thickness.	67
Figure 3.26 :	Chirp profile T04 from MARMARASCARPS (vertical exg. 10). Lower panel with Late Pleistocene-Holocene sediment layers. Note the minor vertical displacements on the antithetic faults in the NE part. Sediments are progressively thicker towards the border fault SW.....	68
Figure 3.27 :	Chirp profile T24 from the eastern part of the Tekirdag basin.....	68

Figure 3.28 : Sediment transport in to the deep basins of the Marmara Sea from the shelves.	71
Figure 3.29 : Bathymetry map of the Marmara Sea locating long cores (orange circles, MARMACORE cruise) and high-resolution mud-penetrator 3-5kHz profiles (white lines, MARMARASCARPS cruise) used to constrain recent sedimentation and faulting in the basins (Tekirdag, Central, Cınarcık from west to east). The profiles presented are a selection of all profiles.	73
Figure 3.30 : Synthetic core logs and correlations. The sediment description is indicated with ¹⁴ C calibrated age constraints (dated charcoal fragments, in ka and 95% confidence interval with OXCAL, ref). Comparison with adjacent echo sounding profiles, when available, is given. The dashed line denotes the transition from lacustrine to marine (blue overlay) sediments. The reference level encountered at the base of the sedimentary pile in the Central basin dates from 15.8 ka.	74
Figure 3.31 : Isopach map of Holocene deposits in the Marmara basin constructed from 3.5 kHz chirp profiles. Inset shows all the chirp lines collected during the Marmarascarps survey (2002).	76
Figure 3.32 : Marmarascarps line C14 images the sedimentary pile well down to 70 ms (see Figure 3.33a for its location). The vertical exaggeration is about 20; thickness is reported in second twtt with a constant velocity of 1700 m/s. Blue horizons represent Holocene marine sediments and the green horizon is the Late Pleistocene lacustrine fill.	77
Figure 3.33 : Location map of the selected chirp profiles (blue lines) from Çınarcık basin. MD Core 25 and 27 (yellow circles) are also projected.	78
Figure 3.34 : MARMARASCARPS 3.5 KHz chirp profile C15.	80
Figure 3.35 : Section across Central Basin (modified from Armijo et al., 2005). Upper Pleistocene and Holocene sedimentary pile as defined by the high-resolution 3.5 kHz profile (CB3) and enlarged core logs (lower panel; cores 31 and 29 from MARMACORE cruise, respectively 26- and 37-m-long) with sediment description and ¹⁴ C calibrated age constraints (dated wood fragments). Faults with normal slip at edges of inner pull-apart are readily seen (see location in Figure 3.37a).	81
Figure 3.36 : Cartoons illustrating the relationship between faulting and sedimentation (modified from Pondard, 2006). (a) Faulting occurs after the deposition of layers. (b) Faulting is synchronous with sedimentation (i.e. syntectonic sedimentation). Note the contrast in layer thicknesses within the hangingwall and footwall in b.	82
Figure 3.37 : (a) Sedimentation and faulting rates in the Central basin. Sedimentation-rate is averaged over the last 15800 years since deposition of the homogenite layer. (b) profile CB3 highlights the 90m cumulative offset of the homogenite layer used to derive the vertical throw rate. (c) Line CB04a indicates the	

	thickest part of the lake-marine transition as 48 m.	
	(d) Homogenite layer provides a reference level for assessing subsequent deformation. This layer is offset by several faults along the northern boundary faults on profile CB14.....	83
Figure 3.38 :	3.5 KHz chirp profiles across the Tekirdağ basin. Note the increase in thickness of Holocene sediment towards that south, indicating relatively stronger subsidence towards the southern boundary fault.....	84
Figure 3.39 :	Three-dimensional view of selected chirp profiles. Holocene sediments slightly gets thicker westward towards the depocenter. Inset shows the location the lines.....	85
Figure 3.40 :	Major segments of the NAF in the Sea of Marmara.....	86
Figure 3.41 :	Distribution of precisely located earthquakes between 2006 and 2010 in Marmara obtained by TÜBİTAK MRC (İnan et al, 2007) using hypoDD algorithm (Waldhauser ve Ellsworth, 2000). Depth distribution of the earthquakes plotted on the sides.....	87
Figure 4.1 :	Bathymetry of the Marmara Sea showing location of microbathymetry survey sites in black boxes along the submarine faults (red lines). The multibeam surveys were conducted along the fault scarps in a strip inside the boxes, not inside the entire boxes.....	90
Figure 4.2 :	ROV Victor 6000 was used during the MARMARASCARPS cruise to collect ultra high resolution bathymetry, push up cores and video imagery at the seafloor. Photo on the right exposes a carbonate crust that is offset by the fault in Tekirdag basin.....	92
Figure 4.3 :	Tectonic map of the Marmara region including the EM300 bathymetry of the Sea of Marmara, showing the active faults (from Armijo et al., 2002) and surface ruptures of the 1999 İzmit (red) and Düzce (purple) earthquakes (Barka et al., 2002) with focal mechanism solutions from Harvard CMT. Green lines with dates show the 20th century surface ruptures before the 1999 events. Red question mark with the dashed lines indicates the uncertainty of offshore extension of the 1999 İzmit earthquake rupture. Inset map depicts the tectonics of the eastern Mediterranean with arrows showing the movement of Arabia (Ar) and Anatolia (An) relative to Eurasia (Eu). (PIF: Princes Islands Fault, SCF: Southern Çınarcık fault).....	94
Figure 4.4 :	(a) Shaded relief map of the Mw 7.4 1999 İzmit earthquake rupture area east of Marmara Sea, showing fault segments in black lines and 1999 İzmit surface rupture in red lines (Barka et al., 2002). Red question marks denote the uncertainty concerning the submarine portion of the İzmit rupture. Yellow circles are $M_L > 2$ aftershocks recorded between August 20 and October 20 1999 by the TÜBİTAK permanent network (Özalaybey et al., 2002). Red star locates the epicenter of the 1999 İzmit earthquake. The blue-red bar below the map distinguishes individual fault segments that	

	<p>ruptured during the 1999 earthquake; red and blue bars indicate whether or not offsets are observed and measured along the fault rupture. (b) Aftershocks distribution at depth. The aftershocks extend in an uninterrupted continuation further west from Hersek delta along the axis of the İzmit Gulf up to the Çınarcık basin. (c) Slip distribution diagram of the 17 August 1999 İzmit surface rupture (after Barka et al., 2002). Slip values are extrapolated in dashed lines where there is no direct observation of slip along offshore segments.....</p>	96
Figure 4.5	<p>: Shaded (from North) relief image of the Gulf of İzmit mosaicked using SRTM (90 m) for land and multi beam bathymetry from Le Suroit (25 m), Odin Finder (10 m) and SHOD (~10 m). White and red lines show the active faults and the 1999 İzmit rupture, respectively.....</p>	97
Figure 4.6	<p>: (a) Bathymery map of western Gulf of İzmit. The active fault segments are indicated by black lines. The white thick line shows the track of ROV microbathymetry coverage in this area along the active fault strands. The Quaternary submarine canyon (black box enlarged in Figure 3b) meets the deep Çınarcık basin in its western extremity. (b) Morphology of the submarine canyon. Map combines multibeam bathymetry (10 m resolution) with the ROV microbathymetry (black outline) (0.5 m resolution, 0.1 m vertical accuracy). Faults (red lines) are identified from the high-resolution bathymetry.</p>	100
Figure 4.7	<p>: (a) Microbathymetry combined with multibeam bathymetry resolves the morphology of the canyon floor. Contours of every 10 m are plotted from the multibeam bathymetry and every 0.5 m from the microbathymetry (b) Enlargement of the microbathymetry extract of the canyon floor. A sharp, nearly linear fault break cuts across the bottom of the canyon. Note the offset of contour lines while crossing the fault trace. (c) Oblique 3-D microbathymetry view of the canyon floor. The fault trace is sharp and continuous. Shading from north exposes the south-facing scarp clearly. Red arrows highlight the rupture trace. White line displays the location of the topographic profile. White dashed lines indicate the eastern edge of the canyon offset right laterally by the fault (120 ± 10 m). B-B' represents the offset of the eastern edge of the topographic high (130 ± 10 m) (d) Enlarged profile across the scarp on the canyon floor. Profile resolves the fine-scale morphology of the south-facing scarp with an apparent throw of 50 cm (less than one contour line in the microbathymetry).....</p>	101
Figure 4.8	<p>: Morphology along the southern slope of the submarine canyon from the combined bathymetry as in Figure 4. (a) Central part of the submarine canyon. A continues fault break can be traced with left-stepping en echelon steps, secondary branches and a sag pond are also found.</p>	

	(b) Fault map deduced from the microbathymetry with contours at an interval of 1 m.....	103
Figure 4.8	: (c) Westernmost continuation of the microbathymetric strip. (d) Fault map deduced from the microbathymetry with contours at an interval of 1 m.....	104
Figure 4.9	: (a) Profiles constructed from the ROV microbathymetry with locations shown on the side map (same as Figure 8d). Note that all the scarps face southward. Vertical exaggeration is 2. (b) Profile constructed with combined bathymetry. The microbathymetry data (red line) resolves details of the scarp morphology that are not determined with the bathymetry background (blue crosses). Blue dashed line represents the initial slope morphology before faulting. Fault offsets the slope with a clear normal component. Apparent throw measured here is 6.2 m.....	105
Figure 4.10	: Coulomb stress changes on active faults due to the 1999 İzmit earthquake calculated using Coulomb 3.1 software (Toda et al., 2005) with a tapered slip distribution and a coefficient of friction of 0.4. Two possible rupture terminations for the İzmit earthquake were tested. In the first model (a) the rupture reaches to the entrance of Çınarcık basin as we interpret in this study whereas in the second model (b) it terminates just east of the Hersek delta. Note that in the first model the Hersek-Yalova segment, unlike the Princes Island fault, is not loaded by the İzmit earthquake.	106
Figure 4.11	: Schematic active fault map of the eastern Sea of Marmara showing the 10 km-wide step-over between İzmit and Central fault segments. Red line marks the western extension of the 1999 İzmit earthquake stopping at the entrance of Çınarcık pull-apart basin. (PIF: Princes Islands Fault, SCF: Southern Çınarcık fault).....	108
Figure 4.12	: The 1912 Ganos earthquake rupture area in western Marmara (Aksoy, 2009, fig. 5.2). The red line indicates coseismic rupture of the 1912 seismic sequence with the red stars pointing the location of the two main shock calculated by Ambraseys and Finkel, 1987 who provided the intensity map of the August shock shown in the inset. Note the rupture extending from the Gulf of Saros in the Aegean to the Central basin in Marmara Sea.....	110
Figure 4.13	: Photos showing surface deformation (landslides and surface ruptures) taken after the 1912 earthquake (Sadi 1912; Mihailovic 1927; Ambraseys and Finkel, 1987).	111
Figure 4.14	: Locations of the ultra-high-resolution bathymetry strips (white boxes). Inset map shows the offset measurements along the 1912 earthquake rupture (from Aksoy, 2009; fig 6.2). Box numbers are shown with red numbers.	113
Figure 4.15	: Microbathymetry of map showing the trace of the Ganos fault near the shore (box 34 in Figure 4.14).	114
Figure 4.16	: (a) Morphology of combined strike-slip and thrust scarps	

in the south-western Tekirdag Basin. The fault scarps are in a clear right-stepping en echelon array (Box 20 in Figure 4.14). (b) Corresponding side-scan sonar image. Encircled close-up identify sharp individual breaks s1 and s2 c) Micro-bathymetry profiles. Profile 1 show that the individual scarps are at the base of larger scarps with warped morphology, suggesting shortening associated with a component of north-eastward thrusting. Profile 2 shows a single cumulative scarp with convex shape. Individual scarp at its base (s1) is made of a steep escarpment about 10 m high (largely a free face) and a similar height of sediment talus..... 114

Figure 4.17 : Microbathymetry with Le Suroit bathymetry in the background and interpreted faults (red lines at lower panel) along the southern margin of the Tekirdağ basin (box 16-17 in Figure 4.14). 115

Figure 4.18 : Micro-bathymetry profiles. Profile 1 (upper panel) and Profile 2 (lower panel) shows that the individual scarps has composite normal and strike-slip component. (V for vertical throw). 116

Figure 4.19 : (a) Oblique 3D micro-bathymetry view of 10 m-high cumulative scarp and smaller individual break that is very linear and continuous over the sea-bottom. Contours every 0.5 m. Small red crosses locate detailed profile. Red arrows indicate fault trace (Armijo et al. 2005). (b) Enlarged profile across individual scarp with nearly vertical free face 1-1.5 m high. No vertical exaggeration. Dashed line suggests cumulative offset of initially flat bottom surface, possibly resulting from last two events. Location of active vent is indicated. 117

Figure 4.20 : Sea-bottom pictures of earthquake scarps in south-eastern Tekirdag Basin. (a) Fresh scarp corresponding to last event. Vertical free face 1-1.5 m high corresponds exactly to that seen in profile (Figure 4.19) locally the scarp reveals a thrusting component. Black bacterial mats with small white shells and brown authigenic carbonates (broken slabs) are seen at scarp base. Carbonate-cemented sediments and bacterial mats are also present on top of the scarp. View to SE. (b) Enlargement (box in a) shows slickensides with 15° rake substantiating dominant right-lateral motion and 4-6 m net slip for last earthquake rupture. Salient white objects are bivalve shells. View to South. (c) Cold seeps, black bacterial mats, authigenic carbonate slabs and active vent along break. The vent (location in Figure 4.19) is capped by white microbial mat. (d) Horizontal authigenic carbonate slab 10 cm thick appears associated with past seepage and venting. The carbonate slab has been broken by last earthquake rupture (right side). Vertical scarp to the left (1-1.5 m high) probably remains from penultimate event. View to SW. 118

Figure 4.21 : Successive microbathymetry strips from west to east (19 to 6) in the Tekirdağ basin (see Figure 4.14 for their locations).....	119
Figure 4.22 : (a) Morphology of EW-striking, purely strike-slip fault scarps across the Western High (for location see Figure 4.14 box w5). (b) Microbathymetry profile depicts the morphology of an individual scarp with a vertical throw of 2.6 m.	120
Figure 4.23 : (a) Easternmost microbathymetry extract at the Western high next to the entrance of Central basin. Morphology reveals a moletrack pattern with alternating pressure ridges and depressions all along the rupture zone. Inset indicate the location (b) contours from the microbathymetry every 1 m. Red line present the fault interpretation. (c) microbathymetry profile with a vertical throw of 3.5 m.	121
Figure 4.24 : Microbathymetry strips along the Western high (from west to east).....	122
Figure 4.25 : Bathymetry map shows sites of coring with ROV. A total of 96 short cores were collected around the vicinity of the fault scarps. Cores are indicated as circles with colors. Green lines are the route of the ROV Victor during the survey.....	125
Figure 4.26 : Sketch presents the logic of coring transect to the fault scarps. Cores were collected along transect through scarps.....	126
Figure 4.27 : Video capture photos by the ROV Victor (a) Coring in front of acarbonate slab in Tekirdag basin, which has been offset by the fault (b) A “black patch” at the foot of a scarp in Tekirdag basin, sampled with the push core. (c) Coring in Çınarcık basin along the slope of a scarp which is draped by hemipelagic sediments (d) Coring far field to the scarp to sample undisturbed sediments.....	127
Figure 4.28 : Schematic diagram of a well-type gamma detector.....	128
Figure 4.29 : Diagram simplifies the logic of ^{210}Pb and ^{137}Cs preservation in the sediments.....	129
Figure 4.30 : Bathymetry map of Tekirdag basin with core locations (blue circles). Two separate sites are simply names as site-A and site-B.....	131
Figure 4.31 : (a) Microbathymetry map (background Le Suroit bathymetry) of Site A. Two coring transects are 200 m apart. (b) Close up of the dashed box in Figure 7a. Yellow lines indicate microbathymetry profiles; cores are given in blue circles. Analyzed cores are blue circles. Red arrows highlight the fault rupture (c) Profile 1 shows the location of the collected cores with respect to the scarp. Scarp forms in a moletrack zone (d) Profile 2 with core locations.	132
Figure 4.32 : X-ray, profiles of mean grain size, ^{210}Pb and ^{137}Cs for site C4. Sedimentation rates were calculated using selected points of ^{210}Pb profiles.....	133
Figure 4.33 : The bathymetry map of the Western High locates the coring site C (orange box).....	135

Figure 4.34 : (a) Enlargement of the Site C (orange box in Figure 33). Cores are aligned N-S across the basin. (b) Microbathymetry profile across the sag pond. Core locations are indicated with blue boxes.....	136
Figure 4.35 : The $^{210}\text{Pb}_{\text{xs}}$ profiles for Cores 6 and 4. Sedimentation rates were calculated using selected points of $^{210}\text{Pb}_{\text{xs}}$ profiles.	136
Figure 4.36 : The bathymetry map of Central basin. Yellow boxes indicate survey areas. Lower panel depicts the location of the cores (yellow circles) from Site E.....	137
Figure 4.37 : (a) 3D view of the normal fault scarp at the southern boundary of the Central basin. Microbathymetry merged with Le Suroit bathymetry (background). (b) Profile depicts the normal fault morphology of an individual scarp (20 m). Cores are shown by red boxes. (c) X-ray images and logs of the Cores 7, 8 and 9. Note the sharp lithological contact that can be traced in all three cores. Sketch on the right illustrates the logic of coring at this site.	138
Figure 4.38 : X-ray, profiles of mean grain size, $^{210}\text{Pb}_{\text{xs}}$ for site E, cores 7 and 8. Sedimentation rates were calculated using selected points of $^{210}\text{Pb}_{\text{xs}}$ profiles. Top of both cores contain mixed layers.	139
Figure 4.39 : X-ray, profiles of $^{210}\text{Pb}_{\text{xs}}$ for site E, cores 7 and 8. Note that both cores are quite homogeneous.	140
Figure 4.40 : The bathymetry map of Çınarcık basin. Green boxes exhibit the microbathymetry enlargements with core locations.	141
Figure 4.41 : 3D microbathymetry of site H; cores are indicated by white circles. Cores 19 and 20 are highlighted.	142
Figure 4.42 : X-ray, granulometry and $^{10}\text{Pb}_{\text{xs}}$ profiles for Core 20. Note the sharp layer in Core 20.	142
Figure 4.43 : X-ray, granulometry and $^{210}\text{Pb}_{\text{xs}}$ profiles for Core 19. Red box highlights an erosional contact at the bottom of the core (right panel). Erosional contact is marked by red arrows.....	143
Figure 4.44 : (a) Microbathymetry map of site I. Three steps of individual scarps are observed. Cores are labeled with green dots. (b) Profile across three step-fault scarp with cores located.....	144
Figure 4.45 : X-rays and ^{210}Pb profiles of Cores 15 and 21.....	144
Figure 5.1 : (a) Map of the North Anatolian fault map plotted on shaded elevation image (SRTM-90 m) with location of offset measurements reported various researchers (A to I) along the fault (A: Koçyiğit et al., 1989; B: Barka, 1992; C: Şengör et al., 2005; D: Hubert-Ferrari et al., 2002; E: Barka and Hancock, 1984; F: Şaroğlu, 1998; G: Armijo et al., 1999; H: Koop, 1969; I: Koçyiğit, 1988). (b) Plot of cumulative offsets along the fault showing that the maximum offset appears to be 70-80 km and uniform between Karlıova and Tekirdağ.	149
Figure 5.2 : Geological map of Mudurnu valley and its surroundings (from MTA). Note the offset of volcanic and metamorphic	

	rocks across the southern branch of the NAF along the Mudurnu valley and south of Düzce plain.	151
Figure 5.3	: Geological map of the Dardanelles and Ganos region. Note the offset of Middle-late Eocene rocks on either side of the NAF (geology map modified from Armijo et al. 1999).....	152
Figure 5.4	: Offsets of morphological features on the sea floor. The ridge is offset by $\sim 3.5 \pm 0.1$ km across the Eastern High.....	152
Figure 5.5	: The ridge is offset 280 m right laterally with a vertical offset of 85 m. Note the white arrows in the upper panel which indicate motion vectors for an oblique displacement.....	154
Figure 5.6	: Reconstruction of of the Central basin reveals a 9 ± 1 km of right lateral offset.....	155
Figure 5.7	: Aksoy (2009) suggest that a large and deep incised valley which terminates abruptly at Gölcük, is offset 9 ± 1 km along the Ganos fault.	155

ACTIVE FAULTING AND EARTHQUAKE SCARPS ALONG THE NORTH ANATOLIAN FAULT IN THE SEA OF MARMARA

SUMMARY

The Sea of Marmara is located in the western part of the 1600-km long North Anatolian Fault Zone (NAF) and forms a 270-km long and 80-km wide intra continental marine basin between the Mediterranean Sea and the Black Sea. The Marmara Region is a highly active region in terms of earthquake faulting. Historical documents extending to the 5th century BC indicate more than 150 earthquakes causing damage to cities in the region. The dense seismicity is a reflection of the complex fault geometry of the NAF in the Marmara Region and particularly in the Sea of Marmara. The NAF is a major dextral transform fault (Ketin, 1948, McKenzie, 1972) that accommodates the westward motion of the Anatolian plate as a result of collision between Arabia and Eurasia in Miocene time. It ruptured during a well known propagating strike-slip earthquake sequence between 1939 and 1999 along a 900-km-long zone of continuous ruptures. The earthquake hazard has got public attention in Turkey after the devastating Mw=7.4, August 17, 1999 İzmit and Düzce earthquakes that caused tens of thousands of lives and cost more than 20 billion dollars to the Turkish economy. The İzmit earthquake was not a surprise to the earth scientists; rather it was expected since the westward migrating earthquakes stopped near Sapanca Lake at the entrance of Mudurnu Valley in 1967. The next one is now expected to strike the Marmara region within a couple of decades. The seismic risk is quite high in the region because about %30 of Turkey's population and about %50 of its industry are located in the Marmara region. The risk has become much higher since the population is nearly doubled within the last decades, particularly, in Istanbul, the most crowded city of Europe with its population of more than 15 million. The NAF enters to the Gulf of İzmit from the west and merges in Gaziköy (Tekirdağ) in the west. Two large earthquakes stroke these edges of the Marmara in 1912 and 1999. The submarine extension of these earthquakes is still poorly known because their surface rupture enters offshore in to the Sea of Marmara. Moreover, the location, geometry and kinematics of the NAF under the Sea of Marmara have been a matter of debate since 1940s. After the 1999 İzmit earthquake numerous scientific cruises have been carried out to investigate the active faults in the Sea of Marmara. The Turkish-French cruise of Ifremer R.V. Le Suroit obtained the first high-resolution complete bathymetric map of the deep basins of the Marmara Sea in 2000. The high-resolution bathymetry (~25 m), seismic reflection and side scan sonar imaging are used to map in fine detail the submarine active faults in the Marmara Sea. The side scan sonar towed 200 m above seafloor revealed particularly the presence of fault scarps. Several recent studies using these high-resolution geophysical data allowed detailed mapping of the submarine structure. Although the dataset and techniques used by these researchers are same and/or similar, their interpretations are rather different and conflicting. The MARMARASCARPS project (2002) was devoted to measurements of submarine

earthquake scarps with a Remotely Operated Vehicle (ROV), obtaining a ultra-high-resolution bathymetry, an extensive coverage with 3.5 kHz chirp profiles, an extensive sampling and coring of sediments close to the scarps, and a significant video and photo documentation of submarine earthquake ruptures.

In this study, several datasets from various cruises have been combined to better understand the 3D structure of the basins and the kinematics and evolution of the NAF in the Marmara Sea. Submarine morphotectonic features of the northern Marmara trough are described together with the deep seismic profiles, to consider the connection between the deep structure, surface morphology and related fault kinematics. 3.5 kHz chirp profiles that were acquired by an extensive survey during the MARMARASCARPS cruise are examined to understand the relation between sedimentation and faulting rates in the Late Pleistocene-Holocene. High resolution bathymetry and shallow and deep seismic reflections reveal that the Marmara contains 3 large deep basins (i.e., Çınarcık, Central and Tekirdağ) that appear to be opening under transtension, which is confirmed by analyses and modeling of the GPS velocity field.

The analysis of microbathymetry suggests that the 1999 İzmit earthquake rupture reached at least to 29.38°E longitudes about 10 km west of Hersek delta in the Gulf of İzmit. It is clearly expressed as a sharp fault break with a 50 cm apparent throw across the bottom of a submarine canyon. Further west, a pronounced and linear fault rupture zone is observed along with fresh en-echelon cumulative fault scarps. We infer that the seismic break continues to the west reaching a total length of ~145 km at around 29.24°E longitudes consistent with the 1999 rupture deduced from SAR interferometry. It appears to stop at the entrance of Çınarcık basin where normal faulting component prevails. In addition, a small fresh break 20-30 km long is identified in the NE Cınarcık Basin fault, which may be associated with the 18 October 1963 (Ms 6.4) earthquake or landslides that are common in this region. We suggest that fault complexity at the junction between dominant strike-slip faulting along the İzmit fault and significant normal faulting in the Çınarcık basin may acts as a barrier to rupture propagation of large earthquakes.

The submarine observation of fault scarps with microbathymetry and video imaging and ²¹⁰Pb dating suggest strongly that the August 9, 1912 Ganos earthquake reached at least the middle of the Tekirdağ basin (27.37.69"E 40.48.17"N) and most probably all the way to the Central basin, suggesting a total rupture of 120-150 km, similar to that of the 1999 İzmit earthquake. Consequently, the unbroken section of the NAF under the Sea of Marmara and thus the size of the Marmara seismic gap is therefore about 100 km, which implies an earthquake of M 7.3.

Taking into account the observations concerning the kinematics, geometry, morphology of the submarine faults and sedimentation rates, the northern branch of the NAF under the Sea of Marmara can be divided into 5 major segments (longer than 35 km). These are the Tekirdağ (45 km), Central (70 km), Prince's Island (35 km), Southern Çınarcık (55 km) and İzmit segments that accommodate a large portion of plate motion, hence have high slip rates, and generate large earthquakes. Of these, the Central and Prince's Island segments constitute the Marmara seismic gap. Considering their length and kinematics, it can be said that each of these segments is capable of producing earthquakes larger than magnitude 7. However, each one may be reactivated alone during an earthquake of M>7 or together with the neighboring 2-3 segments generating a much larger earthquake. In addition to these major segments, there are other minor segments, such as those bounding the outer

Çınarcık basin and İmralı basin. They have overwhelmingly normal slip component with lower slip rates and thus are mainly accommodation structures. They may also produce earthquakes but, of smaller size.

The Sea of Marmara is located in the western part of the 1600-km long North Anatolian Fault Zone (NAF) and forms a 270-km long and 80-km wide intra continental marine basin between the Mediterranean Sea and the Black Sea. The Marmara Region is a highly active region in terms of earthquake faulting. Historical documents extending to the 5th century BC indicate more than 150 earthquakes causing damage to cities in the region. The dense seismicity is a reflection of the complex fault geometry of the NAF in the Marmara Region and particularly in the Sea of Marmara. The NAF is a major dextral transform fault (Ketin, 1948, McKenzie, 1972) that accommodates the westward motion of the Anatolian plate as a result of collision between Arabia and Eurasia in Miocene time. It ruptured during a well known propagating strike-slip earthquake sequence between 1939 and 1999 along a 900-km-long zone of continuous ruptures. The earthquake hazard has got public attention in Turkey after the devastating Mw=7.4, August 17,1999 İzmit and Düzce earthquakes that caused tens of thousands of lives and cost more than 20 billion dollars to the Turkish economy. The İzmit earthquake was not a surprise to the earth scientists; rather it was expected since the westward migrating earthquakes stopped near Sapanca Lake at the entrance of Mudurnu Valley in 1967. The next one is now expected to strike the Marmara region within a couple of decades. The seismic risk is quite high in the region because about %30 of Turkey's population and about %50 of its industry are located in the Marmara region. The risk has become much higher since the population is nearly doubled within the last decades, particularly, in Istanbul, the most crowded city of Europe with its population of more than 15 million. The NAF enters to the Gulf of İzmit from the west and merges in Gaziköy (Tekirdağ) in the west. Two large earthquakes stroke these edges of the Marmara in 1912 and 1999. The submarine extension of these earthquakes is still poorly known because their surface rupture enters offshore in to the Sea of Marmara. Moreover, the location, geometry and kinematics of the NAF under the Sea of Marmara have been a matter of debate since 1940s. After the 1999 İzmit earthquake numerous scientific cruises have been carried out to investigate the active faults in the Sea of Marmara. The Turkish-French cruise of Ifremer R.V. Le Suroit obtained the first high-resolution complete bathymetric map of the deep basins of the Marmara Sea in 2000. The high-resolution bathymetry (~25 m), seismic reflection and side scan sonar imaging are used to map in fine detail the submarine active faults in the Marmara Sea. The side scan sonar towed 200 m above seafloor revealed particularly the presence of fault scarps. Several recent studies using these high-resolution geophysical data allowed detailed mapping of the submarine structure. Although the dataset and techniques used by these researchers are same and/or similar, their interpretations are rather different and conflicting. The MARMARASCARPS project (2002) was devoted to measurements of submarine earthquake scarps with a Remotely Operated Vehicle (ROV), obtaining a ultra-high-resolution bathymetry, an extensive coverage with 3.5 kHz chirp profiles, an extensive sampling and coring of sediments close to the scarps, and a significant video and photo documentation of submarine earthquake ruptures.

MARMARA DENİZİ'NDE KUZHEY ANADOLU FAYI BOYUNCA AKTİF FAYLANMA VE DEPREM SARPLIKLARI

ÖZET

Marmara Denizi 1600 km uzunluğundaki Kuzey Anadolu Fayı'nın batı kısmında oluşmuş 270 km uzunluğunda ve 80 km genişliğinde bir kıta içi denizel bir havzadır. Marmara bölgesi aktif faylarla sınırlanmış yüksek deprem riski taşıyan bir bölgedir. MS 5. yüzyıla kadar dayanan tarihsel deprem kayıtları bölgenin 150 den fazla sayıda depremle sarsıldığını göstermektedir. Deprem yoğunluğu, Kuzey Anadolu Fayı'nın (KAF) Marmara'daki kompleks fay geometrisinin bir göstergesidir. KAF, Avrasya ile güneydeki Arap levhasının çarpışmasıyla Anadolu levhasının batıya hareketi sonucu oluşmuş sağ yanal transform bir faydır. 1939-1999 yılları arasında 7 büyük deprem ile 900 km boyunca batıdan doğuya kırılmıştır. 1999 İzmit ve Düzce depremlerinin yarattığı binlerce can kaybı ve 20 milyar dolarlık ekonomik zarar sonrasında Türkiye'de deprem tehlikesi kamuoyunun dikkatini çekmiştir. İzmit depremi bilimadamları için bir sürpriz olmamakla birlikte KAF'nın doğudan batıya iyi bilinen deprem göçü nedeniyle sıranın 1967 Mudurnu depreminden sonra İzmit'e geleceği bilinmekte idi. Bugün 1999 İzmit depreminin ardından bir sonraki deprem Marmara Denizi içinde meydana geleceği herkes tarafından kabul edilen bir gerçektir. Bu durum Türkiye nüfusunun yüzde 30, endüstrinin yüzde 50'sinin yer aldığı Marmara bölgesi için büyük bir risk teşkil etmektedir. Marmara Denizi'ne İzmit körfezinden giren Kuzey Anadolu Fayı, karaya tekrar batıda Gaziköy (Tekirdağ) de çıkmaktadır. 1999'da İzmit körfezi boyunca kırılan KAF, batıda ise 1912 depremi ile kırılarak Marmara'nın batı ve doğusunu etkilemiştir. Bu depremlerin denizindeki devamları üzerinde çok fazla bilgi mevcuttur değildir. KAF'nın Marmara denizi içindeki segmentlerinin geometrisi, kinematığı ve konumları 1940'lardan beri bir tartışma konusudur. 1999 İzmit depremi sonrasında, Marmara Denizi içindeki fayları araştırmak için çok sayıda uluslararası deniz seferi organize edilmişti. 2000 yılında Fransız Le Suroit araştırma gemisi ile Marmara Deniz tabanının (yaklaşık 100 m'den derin olan) orta kesiminin yüksek çözünürlüklü (25 m) ilk derinlik haritası (batimetri) oluşturulmuştur. Bunun yanısıra yandan tarayıcı sonar (deniz tabanından 200 m yukarıdan) ve sismik yansıma ile elde edilen veriler sayesinde fayların çok detay haritalanması gerçekleştirilmiştir. Bu yeni veriseti kullanılarak denizaltındaki yapıların detaylı haritalatı üretilmiştir. Veriseti aynı olmasına rağmen değişik araştırmacılar birbiriyle çelişen, farklı fay modelleri ortaya sunmuşlardır. 2002 yılında diğer bir Fransız gemisi L'Atlante MARMARASCARPS projesi çerçevesinde, daha önce tespit edilen faylar üzerinde oluşmuş olan genç fay sarplıklarını tespit edebilmek için insansız uzaktan kumandalı bir denizaltı kullanarak çok yüksek çözünürlüklü (50 cm) mikrobatimetri verisi toplamış, sarplıklar boyunca video görüntüsü toplayarka kırık zonlarının net görüntülerinin tespit edilmesini sağlamış, bazı kırık zonları civarında kısa karotlar (35 cm) toplayarak deprem yaş tayini yapmayı hedeflemiştir. Ayrıca 600 km'lik 3.5kHz sığ sismik yansıma verisi (70 ms) de alınmıştır.

Bu çalışmada, MARMARASCARPS seferinde toplanan bu yüksek çözünürlüklü veriseti ve de diğer seferlerde toplanan veriler birleştirilerek, Marmara Denizi içindeki havzaların üç boyutlu yapısı ve kinematığı üzerine çalışılmıştır. Marmara Denizi kuzey havzalarının morfolojik yapısını anlayabilmek ve anlatabilmek için derin sismik kesitler ile taban morfolojisinin denetimi yapılmıştır. Bunun yanı sıra toplanan 3.5kHz sığ sismik kesitler incelenerek Geç Pleyitosen-Holosen dönemi sedimantasyon ve fay kayma hızlarının birbiri ile ilişkisi üzerine çıkarımlar yapılmıştır. Buna göre Marmara denizi içindeki üç derin havza (Çınarcık, Central and Tekirdağ) KAF'nın transtansiyonel tektonik rejimi altında aktif gerilmeli tektonik ile açıklanmaktadır. GPS hareket yönleri bu tip açılmayı desteklemektedir.

50 cm çözünürlüklü mikrobatimetri verisi, 1999 İzmit kırığının İzmit körfezi'ni takiben Hersek'in batısına (29.38°D) geçerek Çınarcık havzasının girişine kadar ilerlediği tespit edilmiştir. Hersek'in batısındaki denizaltı kanyonunun (-180 m) düz tabanı boyunca bir seri genç fay kırıkları görülmektedir. Kanyon tabanındaki sarplığın yüksekliği ise 0.5 m olup 1999 depremine ait olduğu tespit edilmiştir. Kanyonun güney eteği boyunca batıya doğru devam eden kırıklar Çınarcık çukurluğuna (29.24°D) kadar uzanarak sonlanmaktadır. Bu alandaki mikrobatimetri analizleri SAR interferometri verisinin İzmit depremi için verdiği 30 km'lik ek uzanımı desteklemektedir. İzmit deprem kırığı büyük olasılıkla Çınarcık havzasını kontrol eden transtansiyonel fay geometrisinin oluşturduğu geometrik bariyer sebebiyle burada sonlanmıştır. Ayrıca Adalar fayı önünde 20-30 km uzunluğunda genç görünümüne sahip fay sarplıkları gözlenmiştir. Bunların 18 Ekim 1963 (Ms 6.4) depremiyle ilişkili olabileceği gibi bu bölgede yaygın olan heyalanlarla da ilişkili olabileceği düşünülmektedir. Mikrobatimetri, video görüntüleri ve 210Pb analizleri, 1912 Ganos depreminin Tekirdağ havzasının güney kenarını kırdığı (27.37.69°D 40.48.17°K) ve muhtemelen Batı sırtın sonuna kadar ilerleyip Orta havzanın kenarına kadar ilerleyerek 120-150 km lik bir kırık oluşturduğunu ileri sürmektedir. Deniz içinde diğer kırılmamış fay kolları değerlendirildiğinde, Çınarcık havzası ile Orta havza arasında kalan 100 km'lik segmentin kırılması halinde en az M 7.3 büyüklüğünde bir deprem meydana gelecektir.

KAF'nın kuzey kolunun denizaltındaki kinematik, geometrik ve morfolojik özelliklerini göz önünde bulundurularak beş ana segmente ayırabiliriz. Bu segmentler, Tekirdağ (45 km), Orta (70 km), Adalar Fayı (35 km), Güney Çınarcık fayı (55 km) ve İzmit segmentleri olarak ayrılmıştır. Bu segmentler büyük oranda levha hareketlerini barındırdığından yüksek kayma hızları sahiptirler. Dolayısıyla tek başına ya da birlikte kırılarak büyük magnitudlü depremler oluşturabilirler. 1912 ve 1999 kırıklarının deniz altındaki devamından, Marmara Denizinde Orta segment ile Adalar fayı segmentinin sismik bir boşluk oluşturduğunu göstermektedir. Her iki segment de 7 ve üzeri büyüklükte deprem üretebilme kapasitesine sahiptir. Ana segmentlere ek olarak, havzaların kinematığına eşlik eden diğer normal bileşenli ikincil faylar da orta büyüklükte deprem üretebilirler.

1. INTRODUCTION

1.1 Scope of the study

The study area of this thesis is the Marmara region located in northwestern Turkey (Figure 1.1) along the North Anatolian Fault (NAF), one of the most active and important structures of the eastern Mediterranean region. The NAF with its conjugate East Anatolian Fault allows the Anatolian plate to escape westwards from the collision zone between the Arabian and Eurasian plates in eastern Turkey with an anticlockwise rotation with an Euler pole located in the Sinai peninsula in Egypt at an angular rate of $1.2^\circ/\text{m.a.}$ (Figure 1.1; McClusky et al., 2000). The Marmara region has many ancient cities (> 2000 years), such as Constantinople (modern İstanbul), Nicomedia (İzmit) and İznik (Nikea) and thus has a long record of earthquakes. Being the capital of Byzantine and Ottoman Empires, İstanbul, in particular, has a very long earthquake chronicle. Historical catalogues indicate that the city of İstanbul has been severely damaged by many earthquakes that appear to repeat every 200-300 years (Ambraseys, 2002). The 18th century earthquake cycle, May 1776, August 1766, 1894 and 1912, suggest that the next earthquake is well due and thus the seismic hazard in the study area is rather high (Ambraseys and Finkel 1987). The seismic risk is also very high in the region because about %30 of Turkey's population and about %50 of its industry are located in the Marmara region. The earthquake hazard has attracted public attention after the devastating 1999 Izmit and Düzce earthquakes that caused tens of thousands of lives and cost more than 20 billion dollars to the Turkish economy (official estimates [by DPT] for direct damage were 9-13 billion dollars). The İzmit earthquake was not a surprise to the earth scientists (Toksöz et al., 1979; Barka, 1992; Stein et al., 1997; Nalbant et al., 1998); rather it was expected since the westward migrating earthquakes stopped near Sapanca Lake at the entrance of Mudurnu Valley in 1967. The next one is now expected to strike the Sea of Marmara within a couple of decades (Parsons et al., 2000; Parsons 2004). The risk is much higher now since the population is nearly

doubled within the last decades, particularly, in Istanbul, the most crowded city of Europe with its population of more than 15 million.

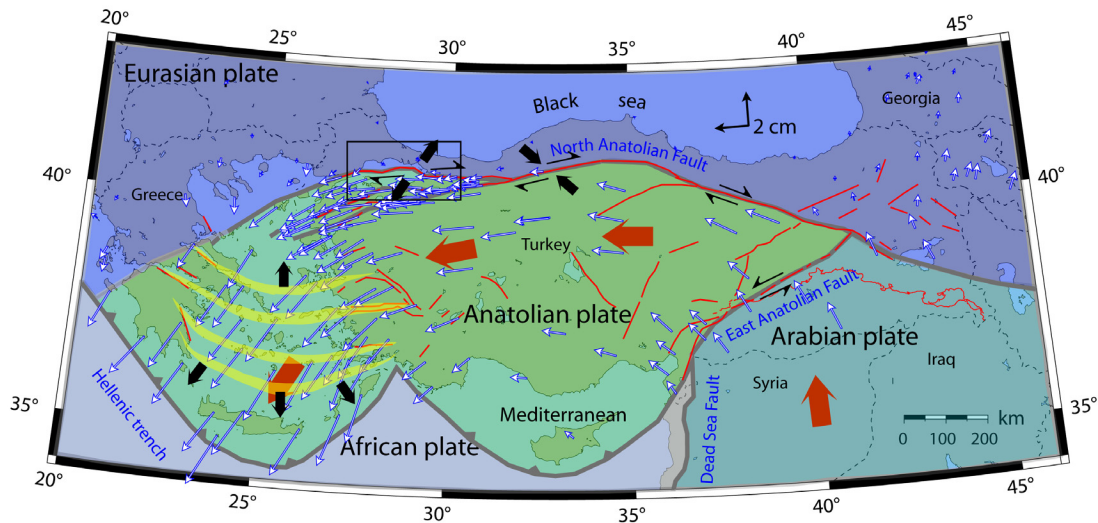


Figure 1.1 : Tectonic map of Turkey and its vicinity where four plates, i.e., the Arabian, African, Eurasian and Anatolian plates meet. Blue arrows with white fill are GPS vector that shows the anticlockwise rotation of Anatolia and Arabia relative to fixed Eurasia driven by the opening and seafloor spreading of the Red Sea (McClusky et al., 2000). The increase in GPS velocity towards the west demonstrates that the westward extrusion of Anatolia cannot be attributed to the collision between Arabia and Eurasia along the Bitlis-Assyrian suture in Eastern Turkey alone, and that the trench suction has an important contribution to anticlockwise rotation of Anatolia in the Aegean. Black block arrows show areas of local extension and compression. Red lines are active faults (from Şaroğlu et al., 1992). Yellow strips are showing schematically the Aegean extensional region.

The main source of seismic hazard in the Marmara region, is the NAF that splays into two major fault strands known as northern and southern NAF. The northern branch runs through the İzmit-Sapanca Lake, Gulf of İzmit and enters to the Sea of Marmara (Figure 1.2). As can be seen from the GPS data in Figure 1.1, most of the lateral motion appears to be transferred obliquely northward, from the main to the northern branch, across the Sea of Marmara basin that these two branches embrace. Thus the most active strand is the northern one that crosses the Sea of Marmara.

However, the location, kinematics and geometry of the submarine faults in Marmara were not known before the end of 1990s due to the paucity of geophysical surveys. Seismic exploration and limited side scan sonar imaging of the Marmara basins were conducted by MTA just before the 1999 İzmit earthquake (Parke et al., 1999).

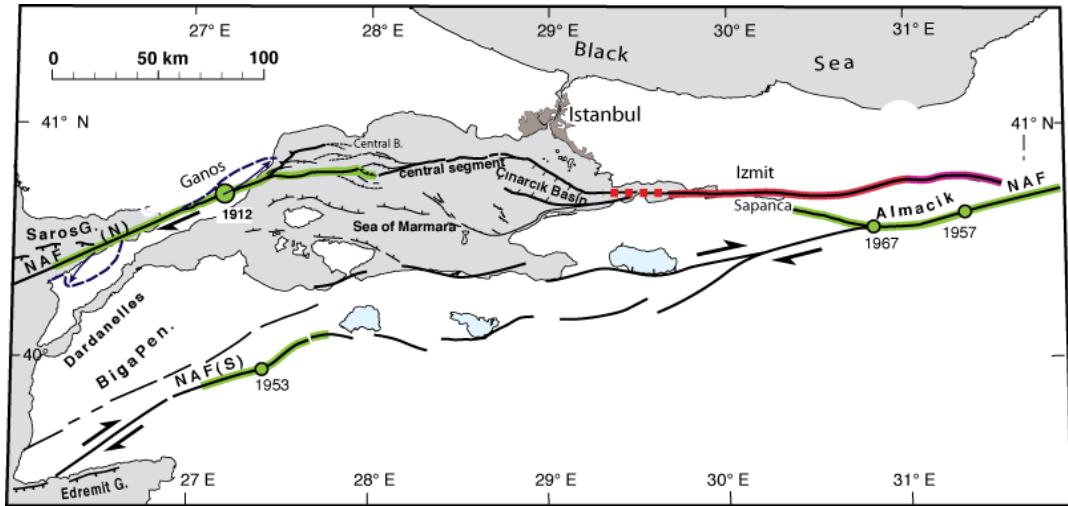


Figure 1.2 : Splays of the North Anatolian fault in the Marmara region. The northern splays runs through İzmit, the Sea of Marmara, Ganos and Saros bay while the southern branch runs through the İznik Lake, Bursa and Gulf of Edremit. Faults (black lines) with thick color shadows indicate earthquake ruptures in the 20th century. Fault map modified from Armijo et al. (2002).

These studies disclosed the first order characteristics of the NAF under the sea. After the 1999 İzmit and Düzce earthquakes it became unquestionable that the next earthquake would be in the continuation of the İzmit rupture in the Sea of Marmara. Therefore, the region has attracted interests of many scientists. As a result, numerous international scientific cruise missions have been performed (Armijo et al. 2002; Le Pichon et al. 2001; Armijo et al. 2005; Carton et al. 2007; Laigle et al. 2008; Géli et al. 2009) using numerous geophysical methods to unveil the extraordinarily fine details of the geological and morphological structure of the Sea of Marmara, which is now one of the best known submarine basins of the world.

In this study, we use data collected mainly during MARMARASCARPS scientific cruise in order to better understand the kinematics, geometry and segmentation of the NAF and recent submarine earthquakes on it. Complimentary data collected during other missions have also been used. The data sets used are multi-beam bathymetry, cores, shallow (0-80 m) and deep (> 5 km) seismic reflection and ^{210}Pb dating.

This thesis consists of 4 sections following the introduction:

In the second section, a brief summary of geological and paleotectonic settings of the study area is given. Then, the previous studies on the age, seismicity and some other

characteristics of the North Anatolian fault are discussed. Finally, the modeling results of the GPS velocity field in the study area are given.

In the third section, crustal-scale structures of the basins, and the relation between fault scarps crossing the seafloor and the structure at seismogenic depth are discussed. In addition, submarine active fault pattern, its geometry, segmentation and kinematics are addressed. Sedimentation rates and slip rates of normal faults are determined using chirp profiles, cores and radiocarbon dates.

In the fourth section the rupture history of large earthquakes associated with specific faults are inferred based on morphological analyses using ultra high resolution (0.5x0.5 m) microbathymetry collected with an ROV (Remotely Operated Vehicle) and ^{210}Pb dating. In particular, the western termination of the 1999 Mw 7.4 İzmit earthquake and the eastern termination of the 1912 Mürefte (Tekirdağ) earthquake were studied. Part of this section is discussed by Uçarkus et al. (in press).

In the fifth section the age and offset of the North Anatolian fault in the Marmara region and its implications are discussed. The last section provides a summary and conclusions of the thesis.

This work was carried out under the co-tutelle agreement between Istanbul Technical University (ITU) and Institut de Physique du Globe de Paris (IPGP) and supported by French Embassy of Ankara within the framework of the collaborative program on the seismic risk in the Istanbul and Sea of Marmara region coordinated by the Turkish TUBITAK and the French INSU-CNRS, with support from the French Ministry of Foreign Affairs (MAE). This thesis is co-supervised by Prof. Rolando Armijo (IPGP) and Assoc.Prof. Ziyadin Çakır (ITU).

2. GEOLOGICAL AND TECTONIC OVERVIEW OF THE SEA OF MARMARA REGION: STATE OF THE ART

2.1 Introduction

A better understanding of the characteristics of the tectonic regime in the Sea of Marmara region requires a good knowledge on the geologic, paleotectonic and seismological history of the study area and the North Anatolian fault. Therefore, in this section, first a brief summary of geological and paleotectonic settings of the study area is given. Then the previous studies on fault models, seismicity and some other characteristics of the North Anatolian fault are discussed. Finally the modeling results of the GPS velocity field in the study area are given.

2.2 Geology of the Marmara Region

The Sea of Marmara region has a complex basement geology consisting of several paleotectonic units of Turkey such as the Strandja and Istanbul zones in the north, the Sakarya zone in the south and Thrace basin in the west (Figure 2.1) (Okay, 1989). These zones constitute the main elements of the western Pontides. By the closure of the Intra-Pontide Ocean before the Lutetian (Şengör and Yılmaz, 1981; Okay and Tansel, 1992; Görür and Okay, 1996), a suture zone (i.e., Intra-Pontide) formed largely in the area where the Sea of Marmara developed (Figure 2.1). The Istanbul and Strandja zones are regarded as parts of the late Mesozoic Laurasian active continental margin and are separated by the Intra-Pontide suture from the Sakarya zone (Şengör and Yılmaz, 1981). The Intra-Pontide suture is closely followed by the North Anatolian Fault (Şengör and Yılmaz, 1981; Okay and Tansel, 1992; Okay and Görür, 1995).

The Strandja zone consists of granitic and gneissic rocks at the base, unconformably overlain by Lower Triassic to Middle Jurassic metamorphic rocks of the Strandja Massif that passes upward across an angular unconformity into sedimentary and volcano-plutonic assemblages of the Late Cretaceous (Görür et al., 1997). These

rocks are covered by Eocene to Miocene sediments of the Thrace Basin toward the Sea of Marmara (Pamir and Baykal, 1947; Sungurlu, 1971; Aydın, 1974; Doust and Arıkan, 1974; Şengör et al., 1984; Turgut et al., 1991; Kaşar and Okay, 1992). The Istrandja massif is separated from the Istanbul zone by a small area of undeformed Eocene sediments (Okay, 1989).

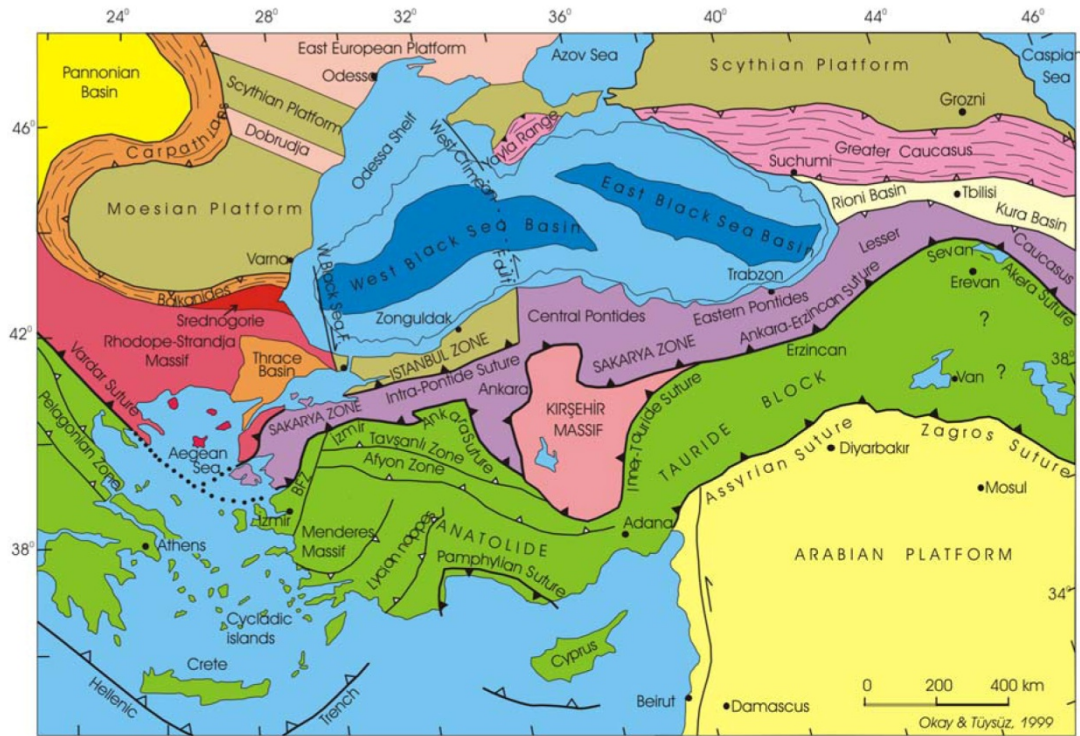


Figure 2.1 : Tectonic map of Turkey and its surroundings showing the major sutures and continental blocks (from Okay and Tüysüz, 1999).

The Istanbul zone consists of a late Precambrian crystalline basement characterized by gneiss, amphibolite, metavolcanic rocks, metaophiolite and voluminous Late Precambrian granitoids (Chen *et al.*, 2002; Yiğitbaş *et al.*, 2004; Ustaömer *et al.*, 2005) that are unconformably overlain by a continuous and well-developed Ordovician to Carboniferous sedimentary succession (Görür *et al.*, 1997; Dean *et al.*, 2000). The Paleozoic rocks are unconformably overlain by the uppermost Permian-lowermost Triassic continental red beds and limestones which are in turn succeeded unconformably by Upper Cretaceous to Lower Tertiary carbonates (Okay, 1989, Abdüsselamoglu, 1977; Saribudak *et al.*, 1989). The Istanbul zone is separated from the Sakarya terrane by the Intra-Pontide suture marking the trace of the Intra-Pontide Ocean (Şengör and Yılmaz 1981).

The Sakarya zone is a 120-km-wide continental fragment extending from the Aegean in the west to the Eastern Pontides in the east, described as a key zone to understand the Paleo-Tethyan evolution in Turkey (Figure 2.1). The basement of the Sakarya zone is divided into two tectonic assemblages: a lower assemblage of Paleozoic granitic and metamorphic rocks, and an upper assemblage of accretion-subduction units of the Paleo-Tethys, named as Karakaya complex (Okay et al., 1996). The basement is overlain with a sedimentary cover. In contrast to the Istanbul zone, the sedimentary sequence starts with Lower Jurassic sandstones and continues with Cretaceous clastics and carbonate rocks (Şengör et al., 1984; Okay, 1986), which rest on a complex basement.

The Thrace basin is a large Tertiary depression in northwest Turkey, which has formed at the complex junction between the Strandja, Rhodope, Sakarya and Istanbul zones (Figure 2.1). (Okay, 2008). Görür and Okay (1996) suggest that this basin was in a fore-arc position during the medial Eocene to Oligocene time, depending on the structural relationships between the Thrace Basin and the surrounding tectonic provinces. In the centre of the basin the thickness of the sedimentary rocks exceeds 8 km (Turgut et al., 1991; Görür and Okay, 1996). The sedimentary rocks are composed predominantly of an upward shallowing sequence of sandstone and shale. The sequence starts with deep marine turbidites of Eocene age and ends with continental Oligocene sandstone, shale and lignite (Okay, 2008). The middle Eocene to early Oligocene sedimentation within the basin was characterized by locally tuffaceous turbidites, whereas continental to shallow-marine clastics and carbonates with subordinate volcanoclastics were laid down both along the basin margins and on the bathymetric highs projecting into the basin interior (Turgut et al., 1991; Perinçek, 1991, Görür and Okay, 1996). Post-early-Oligocene sedimentation was mainly marginal marine to terrestrial represented by coal-bearing clastics and carbonates in part with some tuffaceous material (Doust and Arıkan, 1974; Turgut et al., 1991).

Middle Miocene collision of Arabia with Anatolia introduced very dramatic changes in the tectonic evolution of Turkey. Those remarkable changes created convenient marks to separate the country's neotectonic history from its paleotectonic history (Şengör et al., 1985). The present tectonic framework of Turkey has formed mainly as a result of closure of the multi-branched Neo-Tethyan Ocean during the Late Mesozoic and Cenozoic (Şengör and Yılmaz, 1981).

2.3 Tectonic Background

2.3.1 Paleo-tectonic setting of Turkey: A link to the present-day tectonics

Turkey is an amalgamated region that was assembled by the accretion of Gondwana-derived continental fragments to the southern rim of Laurasia as a result of the opening and northward subduction of the Tethyan oceanic plate (Şengör and Yılmaz, 1981). The palaeotectonic units of Turkey consist of six continental fragments: the Strandja, Istanbul and Sakarya zones, the Anatolide-Tauride and Kırşehir blocks, and the Arabian plate (Şengör and Yılmaz, 1981; Şengör et al., 1982). Four suture zones separate these continental fragments (Figure 2.1).

Tectonic and geologic history of Turkey is closely associated with the evolution of the Tethys Ocean (Figure 2.2). Palaeogeographic reconstructions show that the Tethys Ocean existed since 320 Ma as a large embayment between the two large continents of Gondwana Land in the south and Laurussia in the north (Figure 2.2). The Tethys Ocean is commonly subdivided into Neo-Tethys and Palaeo-Tethys, which partly overlap in time.

During the Permian the entire present area of Turkey constituted a part of the northern margin of Gondwana land facing Paleo-Tethys (Şengör and Yılmaz, 1981). The subduction of Paleo-Tethyan Ocean gave rise to the opening of the Karakaya marginal sea during the early Triassic that was later closed during the late Triassic. The Neo-Tethys began opening during the Late Permian interval (250 Ma) behind the Cimmerian continent that started to separate from northern Gondwanaland at that time (Şengör and Yılmaz, 1981). The opening continued through the Zagros Ocean all the way into the Himalayas, separating the Cimmerian continent from Gondwanaland. Meanwhile, the southern branch of the Neo-Tethys continued its growth while the northern branch originated as a Paleo-Tethyan marginal basin and extended into the present day Mediterranean area. The northern branch of Neo-Tethys included the Intra-Pontide, İzmir-Ankara, and the Inner Tauride oceans. In middle Jurassic the Paleo-Tethys was terminally closed, which resulted in the collision of the Cimmerian continent with the Scythian platform (south part of the East European Platform). Following the closure of the Paleo-Tethys, continued convergence led to crustal thickening and Tibetan-type volcanism throughout the eastern part of the eastern Pontides and the entire Caucasus area (Şengör and Yılmaz,

1981). Convergence between the African and Eurasian plates became dominant (~90 Ma) at all fronts and it started the development of severe geological events of Late Cretaceous, such as the opening of Black Sea behind the Rhodope-Pontide island arc and the extensive ophiolite obduction which took place throughout the Anatolide-Tauride platform and the northern Arabian platform (Şengör and Yılmaz, 1981). The Pontides formed at that time as an active island arc located in front of the opening Black Sea marginal basin (Şengör, 1979).

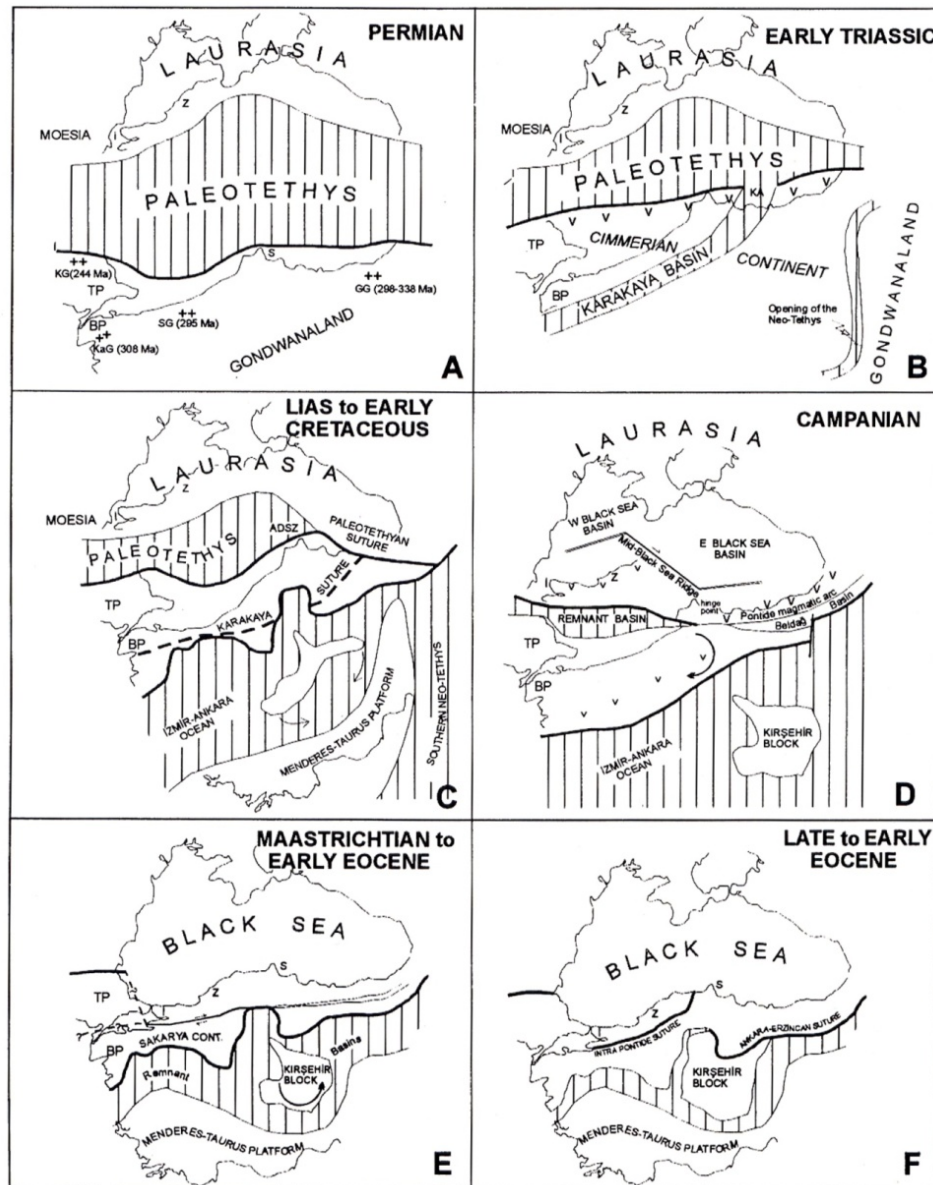


Figure 2.2 : Representative paleotectonic maps showing the tectonic processes that Turkey went through from Permian to Early Eocene (Yılmaz et al., 1997).

The northern branch of the Neotethyan Ocean was closed by the final collision and suturing of the Eurasian Plate in the north and Anatolian–Iranian platform in the south during Late Palaeocene–Oligocene (Şengör and Yılmaz, 1981; Seymen, 1975; Adamia et al., 1981). Meanwhile, the northward subduction of the southern branch of the Neotethys (Bitlis Ocean), running from southeastern Turkey to Cyprus, continued its evolution through late Middle Miocene. The Neotethyan Ocean closed entirely during the continent-continent collision between the Arabian and Eurasian Plates along the Bitlis–Zagros Suture zone (Şengör et al., 2008). The closure had very remarkable effects on the overall tectonics of Turkey. The eastern part of Anatolia has experienced a long-lasting intracontinental convergence between the late Middle Miocene and Early Pliocene, which resulted in crustal thickening and uplift, of the intervening Anatolian–Iranian plateau including the uplift of Cyprus (Bozkurt, 2001).

Under excessive thickening by shortening, an important part of Anatolia wedged out along two new plate boundaries, the North Anatolian and East Anatolian transform faults, and began to move westward on the oceanic lithosphere of the African Plate, thus giving birth to the “Anatolian block” (Ketin, 1948). Following the extinction of intracontinental collision across the Bitlis–Zagros Suture Zone, the earlier compressional-contractional tectonic regime in eastern Anatolia was replaced by a new compressional–extensional tectonic regime (tectonic escape/extrusion) by Early Pliocene (Bozkurt, 2001).

Middle Miocene collision of Arabia with Anatolia introduced very dramatic changes in the tectonic evolution of Turkey. Those remarkable changes created convenient marks to separate the country’s neotectonic history from its paleotectonic history (Şengör et al., 1985). The formation of the right-lateral North Anatolian and left-lateral East Anatolian transform faults, and the consequent westward escape of the Anatolian Plate along its boundary structures has resulted in the generation of present day neotectonic framework of Turkey (Figure 2.3).

2.3.2 The North Anatolian Fault

The North Anatolian fault (NAF) is a major dextral transform fault (Ketin, 1948, McKenzie, 1972; Şengör, 1979), which forms the tectonic boundary between the Eurasian and Anatolian plates (Figure 2.3). The ~1600-km-long fault zone, extending from the Karlıova triple junction in eastern Turkey to the tip of the Corinth Rift in Greece (Armijo et al., 1999), takes up the westward motion of the Anatolian plate as a result of collision between Arabia and Eurasia in Miocene time (Şengör, 1979; Şengör et al., 1985; Barka, 1992). The NAF is a very important active fault system because of its remarkable seismic activity and significance in the Eastern Mediterranean tectonic setting. The NAF has an extremely well developed narrow and simple trace from Karlıova in the east to Mudurnu valley to the west. This main part of the NAF comprises long fault segments separated by releasing step-overs (Barka and Kandinsky-Cade, 1988) and defines a large convex-northward arc that follows the Black Sea coast at distance of about 80 km (Barka, 1992). There are also several second order faults (Ezinepazarı fault, Esençay fault, Almus fault) that splay from the main fault zone into the Anatolian Plate.

The easternmost part of the NAF runs from Karlıova to Erbaa with a strike of N110°E, mostly as a continuous trace, but is disrupted by releasing step-overs which leads to the creation of various Neogene to Pleistocene extensional basins, such as the Erzincan, Suşehri and Niksar-Erbaa-Havza basins (Figure 2.5). In its central section between Ladik and Kargı, the NAF changes its strike from NW-SE through E-W to NE-SW. Neogene to Pleistocene Kargı and Tosya basins lie along this section of the fault. West of Kargı, the NAF runs N75°E in a fairly linear trend all the way to Bolu where it starts to widen and lose its simple, single trace. West of Mudurnu, the NAF splays into two major fault strands known as northern and southern NAF. The northern branch runs through İzmit-Sapanca Lake, Gulf of İzmit and enters to the Sea of Marmara. According to GPS data, most of the lateral motion appears to be transferred obliquely northward, from the main to the northern branch, across the large Sea of Marmara basin that these two branches embrace. The northern NAF is segmented with significant normal and strike-slip faults and interconnects the three sub-basins inside the northern Sea of Marmara with the onland strike-slip segments (İzmit and Ganos faults).

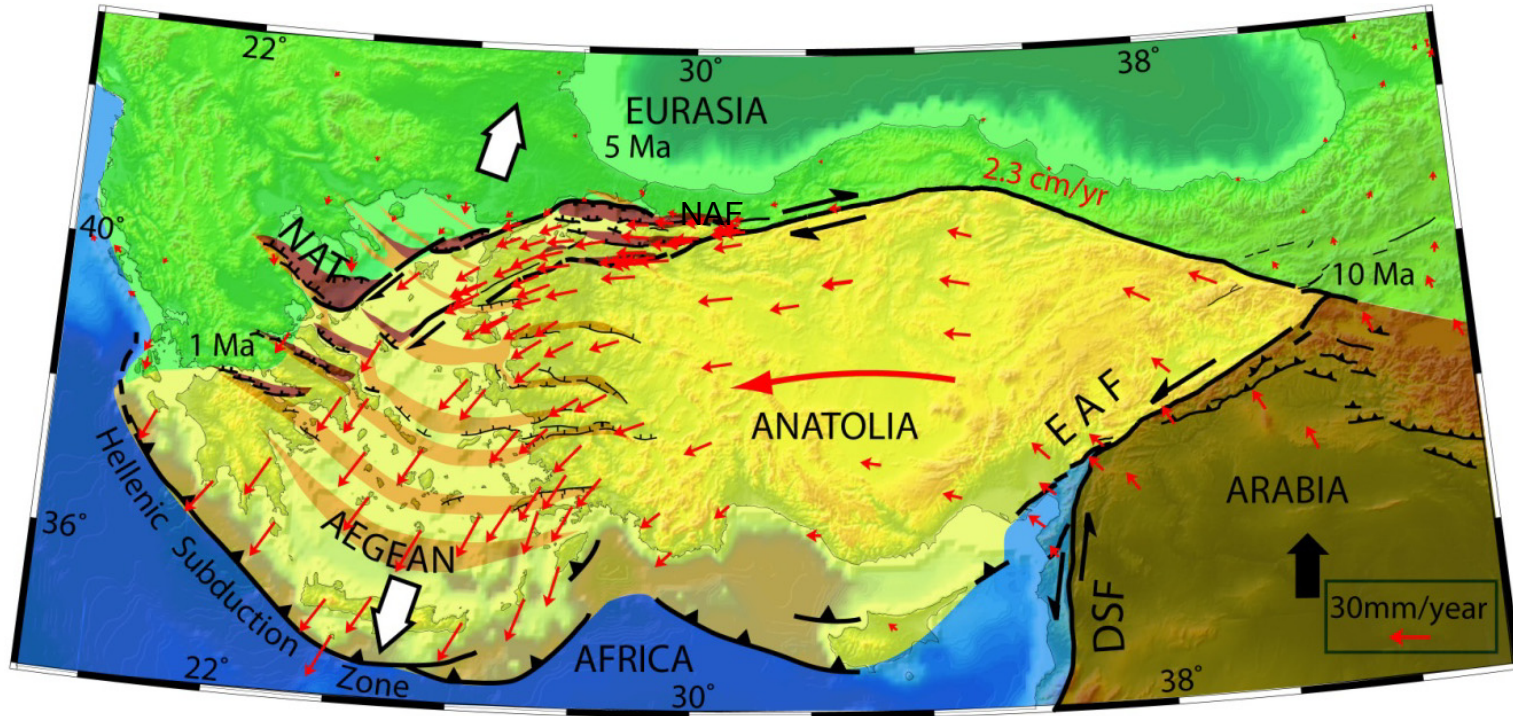


Figure 2.3 : Map of Turkey and surrounding regions showing configuration of tectonic plates, major structures (DSF: Dead Sea Fault; EAF: East Anatolian Fault; NAF: North Anatolian Fault; NAT: North Aegean Through), and motion of plates relative to Eurasia determined by GPS (red arrows) (Reilinger et al., 2006). White block arrows indicate the direction of extension in the Aegean.

Westward, the northern NAF re-appears onland between Ganos Mountain and Saros bay with a continuous strike-slip trace and runs offshore again through the Aegean Sea (Figure 2.5). Further west the NAF runs through the Northern Aegean trough and appears to die out within the Aegean Sea without reaching to Gulf of Corinth and finally the Hellenic arc (Figure 2.3). The southern NAF, as it diverts from the main fault zone, splits into two more strands. One of them defined as central NAF in previous studies extends westward following the southern margin of Iznik Lake and the Marmara Sea to the Kapıdağ Peninsula. The southernmost strand on the other hand extends towards Bursa, Ulubat and Manyas lakes entering to the Aegean near Gulf of Edremit.

2.3.2.1 Seismicity of the NAF in Marmara region

Historical Seismicity

The Marmara Region is one of the seismically most active region of Turkey. Numerous historical documents extending to the 5th century B.C. document more than 150 earthquakes causing damage to cities in the region (Guidoboni et al., 1994, 2005; Ambraseys and Finkel, 1995). The dense seismicity is a reflection of the complex fault geometry of the North Anatolian Fault in the Marmara Region and particularly in the Sea of Marmara. Although earliest records for earthquakes reach the 5th century B.C., the information available for these events is very poor and does not allow evaluating their location or even the magnitude accurately. Well-known events up to the 15th century A.D. are the 447, 460, 477/484, 740, 824, 926, 1063, 1343, 1344 and 1354. In this study, we focus on earthquake history of the last 500 years that are related to recent surface ruptures, which we possibly can observe at the seafloor in the Marmara Sea. Below we summarize earthquakes that occurred in corresponding time period (Figure 2.4)

1509, September 10:

In earlier studies, the 1509 event was considered as the largest and most destructive earthquake in the last five centuries in the Eastern Mediterranean and the damage was thought to be extending to a large area from Bolu to Gelibolu (Ambraseys and Finkel, 1990). However, although some sources express damage within the vicinities of Bolu, Edirne and Gelibolu, detailed and reliable descriptions of damage exist only for Istanbul.

Therefore, the damage distribution was revisited in recent studies (Ambraseys, 2001) where the major destruction has been limited to Istanbul. The number of destroyed houses is considered to be nearly 1000-1500 houses while 54,000 households are estimated for that time. Several churches and mosques including the Beyazid Mosque suffered from the shock. The Ottomans repaired some parts of the aqueducts. The loss of life is estimated to be between 1500 and 5000; among a population of 250,000 at that time in Istanbul. This corresponds to 0.4 – 2% of the city population. In previous studies the 1509 event was named as “Little Apocalypse” and a large magnitude was considered for the shock. However, Ambraseys, (2002) modified the magnitude of the event as $M_s = 7.2$ and the epicenter of the shock is suggested in the Central part of the NAF in the Sea of Marmara. The extend of this earthquake rupture is under debate, because Le Pichon, et al., (2001, 2003) consider that this event ruptured the entire fault section in the Sea of Marmara from Çınarcık Basin on the east to the Tekirdağ Basin on the west, while others suggest shorter rupture length (Armijo et al, 2005)

1719, May 25:

This is a large earthquake that occurred on the eastern part of the Sea of Marmara and caused damage to villages on either side of the Gulf of İzmit. The villages of Yalova, Pazarköy, Karamürsel, Kazıklı, Sapanca and also Düzce were destroyed (Ambraseys & Finkel, 1991). In Istanbul, some buildings, houses, and city walls also experienced damage. The destruction extends to Akviran, Çatalca, Çekmece, and Heybeliada. The earthquake is thought to have killed around 6000 people (Ambraseys & Finkel, 1991). The magnitude of the event is calculated as $M_s = 7.4$ and the epicentre is estimated to be east of the Hersek peninsula in the Gulf of İzmit (Ambraseys, 2002); very comparable with the characteristics of the 1999 Gölcük earthquake.

1754, September 2 :

A damaging shock caused considerable destruction in the vicinity Gulf of İzmit. The villages in the region were totally destroyed. The shock caused also damage to the lighthouse at Ereğli (Black Sea). In Istanbul, at Üsküdar and Balat the destruction was dense; houses, masonry houses, mosques and partly city walls collapsed. The loss of live in Istanbul is about 60, while about 2000 are considered in total. No damage is reported to the south of the Sea of Marmara. Some seismic sea waves

were reported, however they caused no damage. Ground openings are reported in İzmit, which possibly can be surface ruptures. The magnitude of the event is $M_s = 6.8$ and the epicenter is estimated at the Çınarcık Basin (Ambraseys, 2002).

1766, May 22:

A destructive earthquake occurred in the Sea of Marmara. The damage expanded to a wide area, from İzmit to Tekirdağ (E-W) and from Edirne to Bursa (N-S). Abundant amount of record provide descriptions on the results of the event, where Ottoman archives provide information for Istanbul and İzmit, whereas Greek sources provide for outer regions. Most of the damage is related to the structures within Istanbul. Mosques were destructed, where their minarets were mostly overturned and the some of the domes collapsed. Galata, Pera, Üsküdar and some other localities north along the Bosphorus experienced also damage. The land walls collapsed along most of their length. Some towers, rooms and walls were also collapsed at the Topkapı Palace. Damage occurred at a number of churches. The damage extended to Çatalca and Çekmece, where houses and walls were strongly demolished. The Effect expanded further into the Thrace causing loss at Kemerburgaz, Çorlu and Karışdırın. Edirne escaped only with slight damages. Further west at Tekirdağ, Ganos, Gelibolu and Çanakkale the effects of the shock are not clear and are possible related to the result of the earthquake in August 1766. On the east the damage was much stronger, where İzmit suffered badly and a seismic sea-wave caused heavy damage at the dockyards. South of the Marmara Sea, there was damage near Karamürsel and Bursa. Other sea wave intrusions were reported near Galata, Bosphorus and at Mudanya. Nearly 500 people died in Istanbul, while the number for other region in Marmara is unknown. The magnitude is estimated to be $M_s 7.1$ while the epicenter is given to be within the Çınarcık Basin (Ambraseys, 2002).

1766 August 5:

In August 1766 a second major shock occurred further west of the Sea of Marmara, ruining all damaged structures during the first shock in May 1766. The damage of the August shock extended to the west of the Sea of Marmara. Most of the destruction was localized between Tekirdağ and Mürefte. Gaziköy experienced damage so severely that only %10 of the houses remained. Destruction is also reported for the following villages: Avdin, Ganos, Gölcük, Hoşköy, Inceköy, Eriklice, Kalamış, Kestambol, Loupida, Güzelköy, Mürefte, Yeniköy, Palamut, Şarköy, Çınarlı,

Senduk, and Sternaköy. Particularly Hoşköy and Şarköy suffered much of damage. The castles in Seddülbahir and Kilidülbahir at Dardanelles collapsed extensively. Sultanhisar, south of Dardanelles suffered badly; the castle at Bozcaada needed extensive repair. Though affected many buildings the damage in Istanbul was less according to the May event. Some hans, Edirne kapusu, mosques and masonry buildings were ruined. There is also few information of destruction in Edirne, Izmit, Yalova, Karamürsel and Bursa.

1894 Jul 10:

A large earthquake struck the eastern part of the Sea of Marmara, as well some places west of Istanbul. The event is well described by Ambraseys (2001). The shock was widely felt in Bucharest, in Romania, on Crete, in Cide, Kastamonu, Ankara, Konya, Burdur and Aydın over an area of a radius of 440 km (Ambraseys, 2001). Most of the heavy damage is localized on the islands south of Istanbul; Büyük Ada, Kınalı Ada, Heybeli Ada, Burgaz Ada, and Yassı Ada. Almost all houses and buildings were reduced to ruins on these islands. The damage in Istanbul was also heavy in some regions. The some sections of the Covered Bazaar (Kapalı Çarşı) collapsed. Nearly all houses suffered in Fatih, Edirnekapı, Topkapı, and Balat. At Yesilkoy all stone houses and some other, a total of 250 houses were destroyed. However the monumental buildings such as the Hagia Sophia and the Fatih Mosque were just slightly damaged. Other cities around Istanbul suffered also from the earthquake. The easternmost damage is reported in Adapazarı, where 263 houses were destroyed and 600 turned inhabitable. The extensive damage is mostly related to poor ground conditions; a wide low alluvial plain. The damage between Adapazarı and Sapanca is less, where a church and a school were destroyed. The damage at Izmit is not well determined. Some villages along the Gulf of Izmit seem to have experienced severe destruction, however descriptions among accounts vary. A number of buildings and houses were also damaged at Gemlik and Mudanya, south of the Sea of Marmara. The total loss of life is 474 and 482 injuries (Öztin, 1994; Altınok and Ersoy, 2000) Some ground openings of 200 m long in NW direction are reported on the Prince Islands. Other fissures and cracks occurred along the coast of Yalova, at Karaköy, Pendik, and coast of Küçük Çekmece. The magnitude of the event is given as $M_s = 7.3$, while the epicentre is considered to within the Çınarcık Basin (Ambraseys, 2002).

1912 Aug 9:

The 1912 earthquake was a large shock felt not only in the eastern Balkans, but also in Bucharest and Vienna (Macovei, 1912; Mihailovic, 1927; Ambraseys & Finkel, 1987). The damage was centred between Çanakkale (Dardanelles) and Tekirdağ, but also reached to Istanbul, Edirne, Enez, Adapazarı, Ayvalık and Bursa (Ambraseys and Finkel, 1987; Mihailovic 1927). The maximum damage was localized between Tekirdağ and Mürefte. An IX-X MSK maximum intensity has been assigned for the region near the Mürefte village. The destruction and loss of life is described in several contemporary sources (Sadi, 1912; Macovei, 1912, 1913; Mihailovic, 1918, 1927, Agamennone, 1912,). A comprehensive description on the damage is available in Ambraseys and Finkel (1987). The damage killed 2800 and injured 7000 people About 12600 houses were destroyed, 12100 damaged beyond repair and 15,400 with serious damage (Ambraseys and Finkel, 1987)

The 9 August 1912 Mürefte earthquake (Mw 7.4) occurred with an epicenter near the Mürefte village according to Ambraseys and Finkel (1987). The earthquake was followed by a second large shock on 13 September 1912 that increased the damage towards west. The 9 August earthquake was accompanied with major surface faulting and co-seismic slip all along the onland section. In addition, some considerable amount of land-sliding occurred off the fault. Several recent studies provide ample description on the surface faulting, related offsets, seismic sea-waves and other consequences of the event (Aksoy, 2009; Altunel et al., 2000, 2004, Altınok et al., 2003a, b, Öztin, 1987; Tabban and Ateş, 1976 and Rockwell et al., 2001, 2009)

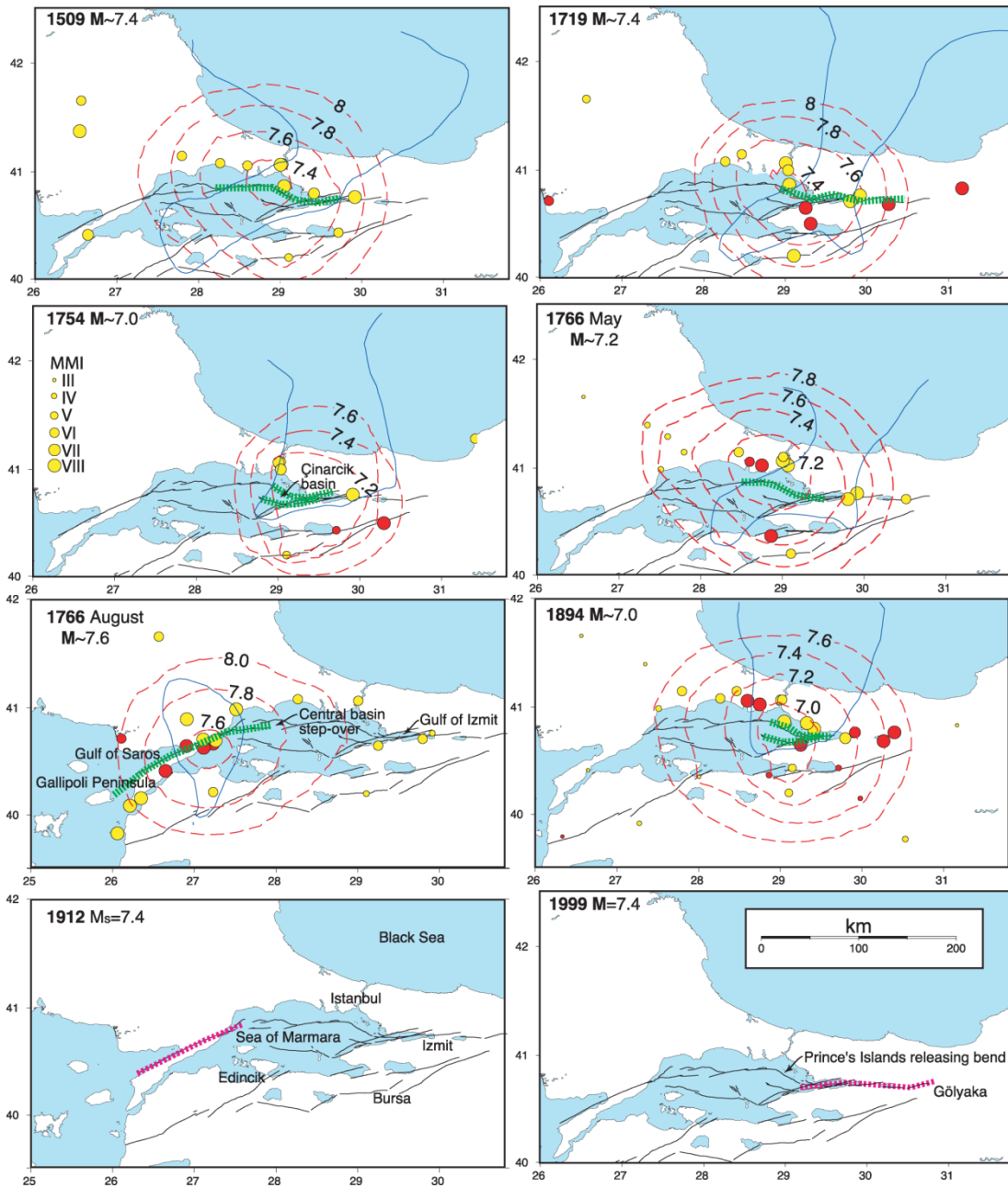


Figure 2.4 : Possible damage area and related submarine fault segments are depicted by Parson (2004) for the 1500–2000 earthquake catalog of the Sea of Marmara region.

2.3.2.2 Instrumental seismicity

The North Anatolian Fault has ruptured during a well known propagating strike-slip earthquake sequence between 1939 and 1999 along a 900-km-long zone of continuous ruptures. These earthquakes (and their rupture length and the maximum slip on them) are the M 7.9, 1939 Erzincan (360 km; 7.5 m), M 7.1, 1942 Erbaa-Niksar (50 km; 2 m), M 7.6, 1943 Tosya (280 km; 4.2 m), M 7.3, 1944 Bolu-Gerede (165 km; 3.5 m), M 7, 1957 Abant (30 km; 1.6 m), M 7.1, 1967 Mudurnu valley (80 km; 1.9 m), M 7.4, 1999 İzmit (160 km; 5.5 m) and M 7.2, 1999 Düzce (69 km; 5 m) earthquakes (Figure 2.5). Taking into account the M 7.4, 1912 Mürefte (Tekirdağ) earthquake to the west and the M 6.7, 1949 Karlıova earthquake to the east two large seismic gaps can be defined in the Marmara and Yedisu (Figure 2.5b). Following the 1999 Izmit event various earthquake scenarios for the historical earthquakes have been proposed and modeled by Hubert-Ferrari et al. (2000), Parsons et al. (2000, 2004) and Pondard et al. (2007) to evaluate seismic hazard and reveal fault interactions. All the studies indicate that a large earthquake ($M > 7$) will probably strike the Sea of Marmara region within couple of decades.

Focal mechanisms of 61 earthquakes with local magnitudes between 1.6 and 4.1 that took place between 2001 and 2003 in the Marmara Sea illustrate that the Marmara region is under transtentional stresses as the mechanisms are associated mainly oblique slip events (Figure 2.6) (Tan et al., 2008). The majority of the solutions are however nearly pure normal faulting. Distribution of earthquakes ($M > 5$) since 1976 show that the NAF is fairly quiet between the Karlıova triple junction and the Marmara region (Figure 2.7). This is obviously due to the stress drop caused by the successive events that occurred between 1939 and 1999. The seismic activity is concentrated in the Marmara region to the west and Karlıova region to the east.

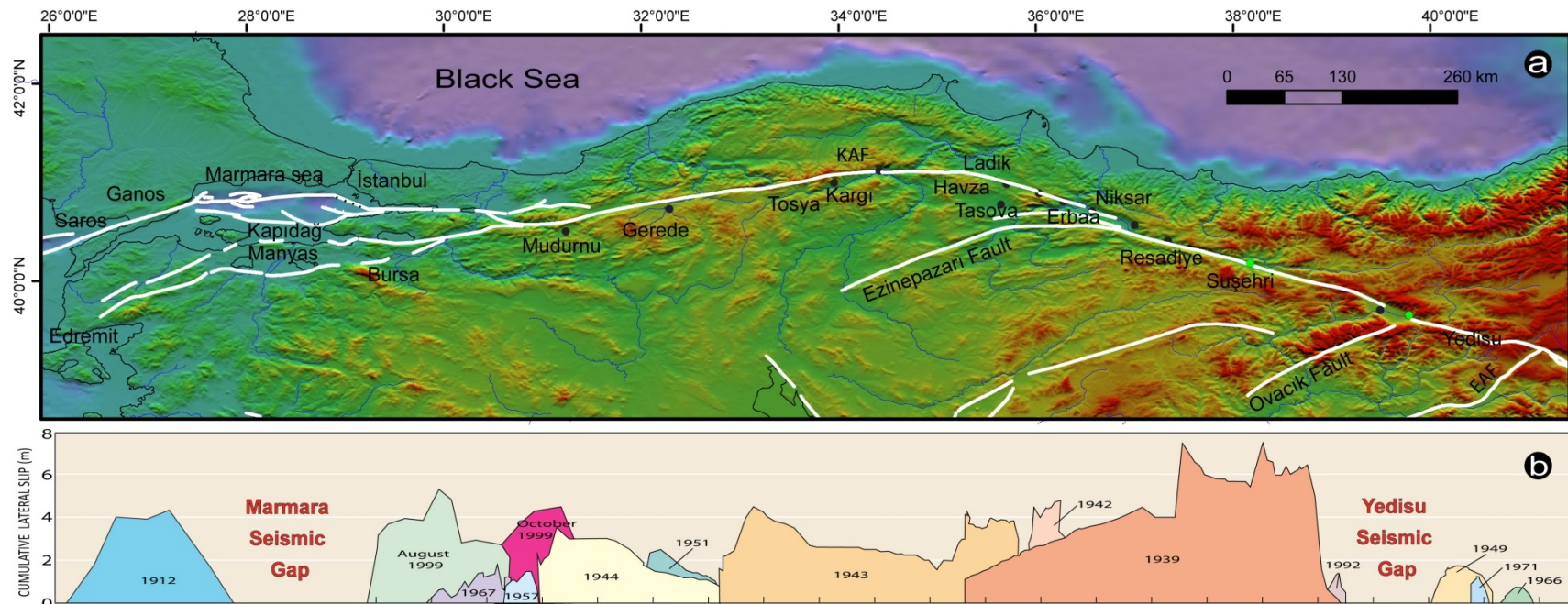


Figure 2.5 : (a) Map of the North Anatolian fault map plotted on shaded elevation image (SRTM-90 m) (b) Slip distribution along the North Anatolian fault during the 20th century earthquakes. Note the seismic gaps in Marmara and Yedisu that pose serious hazard its surroundings, particularly to Istanbul.

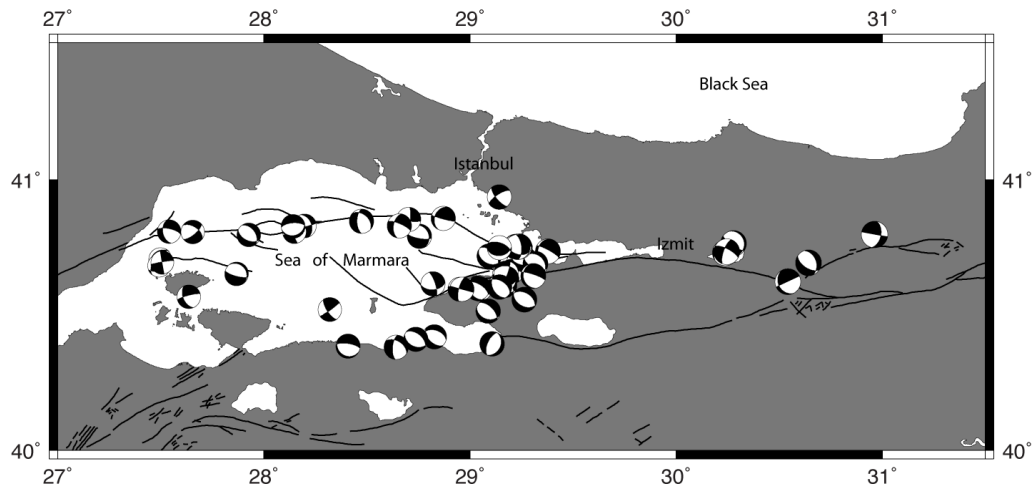


Figure 2.6 : Focal mechanism solutions of small earthquakes (ML 1.6 to 4.1) between 2001 and 2003 (from Tan et al., 2008). Note the alignment of earthquakes along the submarine section of the North Anatolian fault.

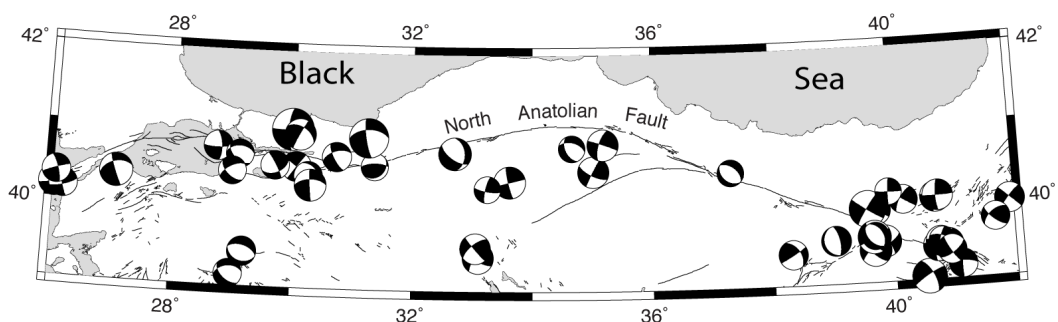


Figure 2.7 : Centroid Moment Tensor solutions from Global CMT between 1976 and 2009.

2.3.3 North Anatolian Fault in the Sea of Marmara

The Sea of Marmara is located in the western part of the 1600-km long North Anatolian Fault Zone and forms a 270-km long and 80-km wide intracontinental marine basin between the Mediterranean Sea and the Black Sea. It is connected to the low-salinity Black Sea via the Bosphorus and to the marine Aegean Sea via the Çanakkale Strait (Dardanelles). These two straits have sill depths of approximately 65 and 35 m, respectively. The NAF enters from the west in to the Gulf of İzmit and merges in Gaziköy (Tekirdağ) in the west. The location, geometry and kinematics of the NAF under the Sea of Marmara have been a matter of debate since 1940s. The following section provides a review of this issue.

2.3.3.1 Evolution of fault models in the Sea of Marmara

The geometry and distribution of active faults related to the NAF in the Sea of Marmara has long been a controversial issue. This controversy resulted in several fault models proposed in different kinematic and geometric constraints. As the NAF splay into several discontinuous segments in the Sea of Marmara region, it loses its evident single trace and does not illustrate a clear picture of its faulting pattern compared to its main part on land. Another fact is that most of the northern strand extends offshore creating uncertainties concerning the geometry and characteristics of active faulting in the Sea of Marmara. Most of the early works was limited in interpretation due to the lack of a detailed bathymetry map and high quality seismic data.

A large number of studies have focused on the NAF within and around the Sea of Marmara region during the last sixty years. Although the initial models for the evolution of the Sea of Marmara date back to the 1940s, the modern studies concerning the seafloor topography and seismic research have begun in late 1980s. The most important debates still are about the geometry of the faults cutting the sea floor despite the availability of widespread coverage of marine seismic and multi-beam data (Crampin and Evans, 1986; Şengör, 1987; Barka and Kadinsky-Cade, 1988; Barka, 1992; Ergun and Özel, 1995; Wong et al., 1995; Smith et al., 1995; Okay et al., 1999, 2000; Parke et al., 1999, 2002; Le Pichon et al., 1999, 2001, 2003; Aksu et al., 2000; İmren et al., 2001; Yaltrak et al., 2002; Armijo et al., 2002, 2005).

Pınar (1943) suggests two strands with unspecified nature crossing the Sea of Marmara where the northern strand followed the northern Marmara Sea basins and the southern one crossing Gemlik and Bandırma bays. Crampin and Evans (1986) interpreted the faulting pattern in the Sea of Marmara as an E-W trending single graben and introduced a wedge-shaped Marmara block from the seismicity pattern of the region. Şengör (1987) proposed a single strand in the Marmara Sea on which the Çınarcık basin was located as a pull-apart structure.

Barka and Kadinsky-Cade (1988) proposed three strands splaying from the NAF in the Marmara region based on field investigations and introduced a pull-apart origin for the three deep basins located within the northern half of the Marmara Sea (Figure 2.8A). According to that fault model, pull-apart basins are separated by NW-SW

strike-slip fault segments and bounded to the north and south by normal faults. Wong et al. (1995) and Ergün and Özel (1995) have adopted and slightly modified

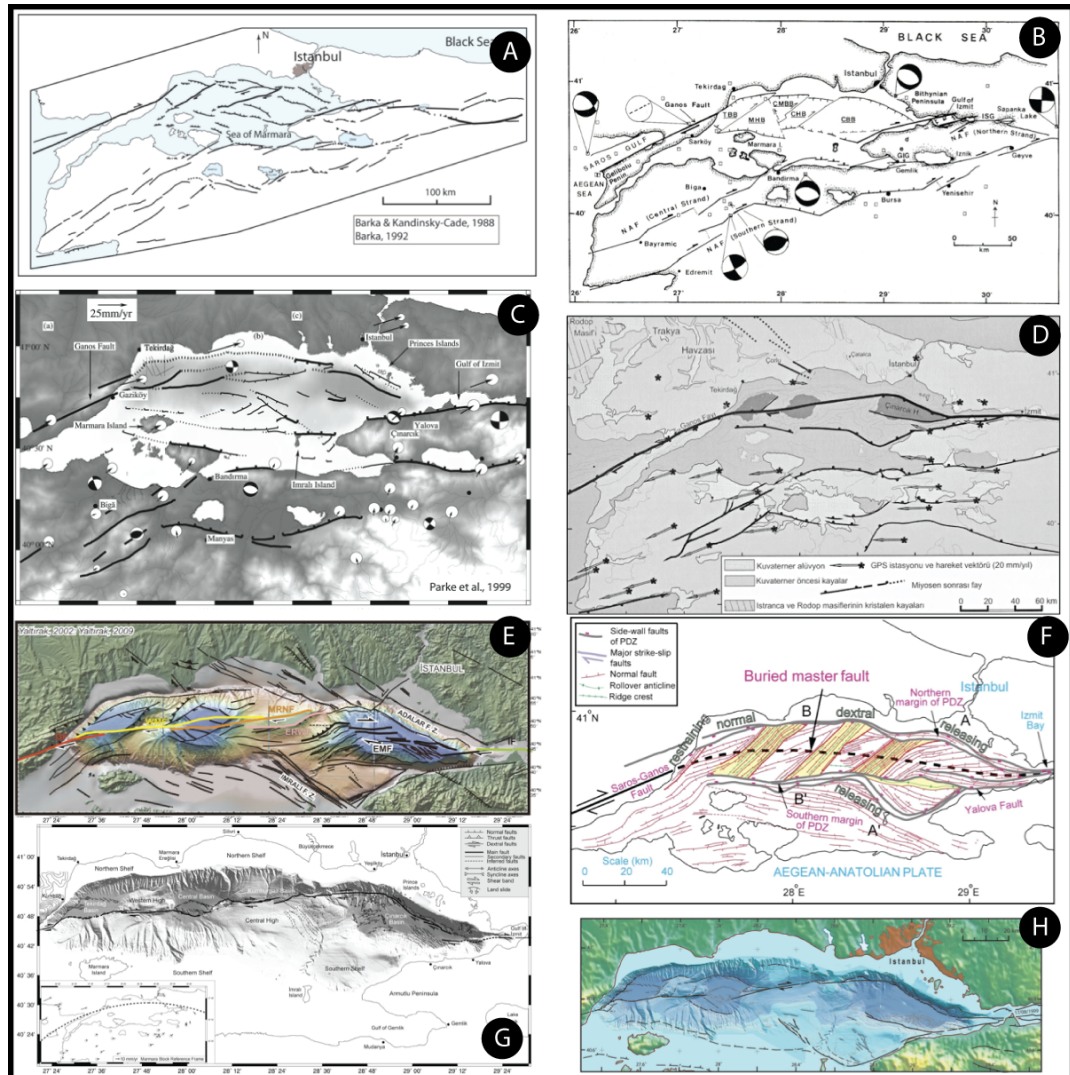


Figure 2.8 : Proposed fault models for the North Anatolian Fault under the Sea of Marmara. A: Barka and Kadinsky-cade, 1988; B: Wong et al., 1995; C: Parke et al., 1999; D: Okay et al., 1999; E: Yaltrak 2002; F: Aksu et al., 2000; G: Le Pichon et al., 2001; Armijo et al., 2002.

this model based on shallow seismic reflection data. According to Wong et al. (1995), the NAF in Marmara consists of overlapping master faults that partition the northern Sea of Marmara into an echelon blocks (Figure 2.8 B). Another interpretation by Smith et al. (1995) exhibited E-W, WNW-ESE trending normal faults from high-resolution sparker seismic reflection data, and proposed that the southern part of the Sea of Marmara basin is a half-graben.

In 1997, MTA collected 1500 line-km of seismic reflection data by R/V *Sismik-1*. Okay et al. (1999), Parke et al. (1999) and Le Pichon et al. (1999) interpreted this

dataset, each ending up with different fault models. According to Okay et al. (1999), Marmara basins have been forming along a very large releasing bend of NAF in the Sea of Marmara (Figure 2.8D). Whereas Parke et al. (1999) implied that the localized N-S extension dominated the tectonic regime in the Sea of Marmara due to the influence of Hellenic arc, and Sea of Marmara basins were controlled by en echelon faults with large normal component (Figure 2.8C).

Following the devastating Mw 7.4 August, 17th, 1999 İzmit earthquake, stress transfer analyses showed that the Sea of Marmara fault segments are the potential target to rupture with an $M > 7$ earthquake. This fact created an urgent need to obtain high-resolution submarine dataset in order to reveal the unknowns of the NAF in the Sea of Marmara. As described above, previous interpretations were limited to explain rupture and morphologic characteristics of the offshore fault system. For a better understanding of the seismotectonic activity in the Sea of Marmara, multinational and multidisciplinary research projects with high technology research vessels have started since then.

After the 1999 earthquakes, Le Pichon et al. (1999) have defined a continuous dextral strike-slip fault cutting across the entire northern Sea of Marmara, from Gulf of İzmit to Gulf of Saros. In their interpretation, there are no en echelon fault segments controlling the basins as proposed by previous authors. Their model of a thoroughgoing fault system crossing the entire northern Marmara basin was also pointing out a full rupture of the submarine fault system with an M 7.6 earthquake.

French-Turkish “MARMARA” cruise carried out on board RV Suroit in 2000, collected various sets of high resolution data which include a 25-m-gridded multibeam bathymetry, back-scatter and side-scan sonar imagery, and seismic reflection profiles. This new dataset provided precise location and extension of the active faults in the northern Marmara trough. Nevertheless, different fault interpretations came out from the same high-resolution dataset (Le Pichon et al., 2001; Armijo et al., 2002). Preliminary results of the Marmara cruise published by Le Pichon et al. (2001) persisted on a single through going fault across Marmara as proposed previously (Le Pichon et al., 1999, 2000; and İmren et al., 2001) (Figure 2.8G).

Different geometries have been offered successively following this hypothesis claiming that the pull-apart extension in Marmara is now inactive (Le Pichon et al., 2001; İmren et al., 2001; Le Pichon et al., 2003). It has also been claimed that the strike-slip faulting would have crossed the region recently (~200 ka), coevally with a major tectonic reorganization in the Sea of Marmara, due to a very young inception of the NAF. Hence, motion on the NAF in this region should have produced only minor total offset (4 km of right-lateral offset) (Le Pichon et al., 2003; Demirbağ et al., 2003; Rangin et al., 2004; Şengör et al., 2004). The origin of this hypothesis is linked to analysis of GPS velocity vectors. Le Pichon et al. (1999), Meade et al. (2002) and Le Pichon et al. (2003) deduce kinematic models defining a rigid “Marmara block.” While producing a good fit to GPS vectors those models appear kinematically inappropriate because the pure strike-slip motion they obtain within the extensional Marmara step-over produces a large compression across the strike-slip İzmit fault (up to 5–6 mm/yr), which is inconsistent with the well-known motion of that fault and with the best constrained earthquake mechanism available for the region (1999 İzmit earthquake; Mw 7.4). Clearly the GPS data alone do not provide a definite test.

Armijo et al. (1999, 2002, 2005) opposed the hypothesis of a single throughgoing fault system (Figure 2.8H). Accordingly, the Sea of Marmara pull-apart system has evolved between the conspicuous 70-km-wide step-over of the two well-known strike-slip faults on land (Ganos and İzmit faults), which have ruptured with purely right-lateral motion during recent earthquakes (Armijo et al., 2002, 2005). Long-term slip on the İzmit and Ganos faults puts the northern Marmara basin under an extensional regime that has caused significant overall subsidence (Armijo et al., 2002; Hirn et al., 2003; Muller and Aydin, 2005). Short-term GPS based models incorporating slip partitioning in the Sea of Marmara predict a right-lateral slip rate of about 18–20 mm/yr and extension of 8 mm/yr across the northern Marmara basin (Flerit et al., 2003; Armijo et al., 2003). At a smaller scale the oblique fault system within the northern Marmara step-over is formed by smaller steps bounding three deep basins with lozenge shape and active subsidence that is stronger than in the rest of Marmara (depth ~1200 m: Tekirdag, Central and Çınarcık Basins) (Barka and Kadinsky-Cade, 1988; Wong et al., 1995; Armijo et al., 2002; Okay et al., 1999, 2000; Hirn et al., 2003; Carton, 2003).

Another class of alternative tectonic interpretation emphasizes that the extension in Marmara is associated with the widespread extension in the Aegean not with the localized pull-apart stretching (e.g., Parke et al., 2002). However, the geology, the morphology and the GPS results at the regional scale exclude substantial Aegean extension as playing a significant role in the finite deformation of the Marmara Sea region (Armijo et al., 2002; Flerit et al., 2003, 2004).

Additional fault models with a different tectonic frame are proposed by Aksu et al. (2000) (Figure 2F) and Yaltırak (2002) (Figure 2E). Aksu et al. (2000) characterizes the crustal structure in Marmara Sea by a negative flower structure, bounded by two west-trending sidewall faults that are linked to a single vertical to steeply south-dipping master fault that extends to depths of > 30 km. The negative flower structure has an extremely complicated architecture consisting of relatively intact detached basal blocks, separated by southwest-trending ridges that serve as strike-slip transfer zones between the basins. Here, the basins and ridges are rotating counterclockwise.

2.3.3.2 Mechanical fault models

Despite the high quality geophysical data collected, there exist several interpretations for the fault geometry in the Sea of Marmara. Mechanical modeling methods are good approaches in order to test different fault geometries. Incorporating geophysical data with geomechanical modeling can show the best fitting solution to explain fault propagation through crustal lithosphere. Different numerical models are applied to examine the varying fault geometries within the Sea of Marmara and to predict the best fitting fault model (Muller and Aydın, 2005; Oglesby et al., 2008).

A remarkable numerical model by Muller and Aydın (2005) tests three proposed fault models by Le Pichon et al. (2001), Armijo et al. (2002) and Okay et al. (2000) (Figure 2.9). They evaluate the consistency of the proposed fault geometries with the observed geomorphology and structural deformation in the Sea of Marmara using mechanical modeling. Accordingly, if slip on faults in a given geometry produces surface deformation that resembles the morphology of the Sea of Marmara, then that fault geometry is considered to be mechanically consistent. They use a boundary element dislocation model an effective tool for relating fault geometry and regional loading conditions to observed topography (Armijo et al., 1996; Bilham and King, 1989; Dorbath et al., 1996; King et al., 1993). Muller and Aydın (2005) select the

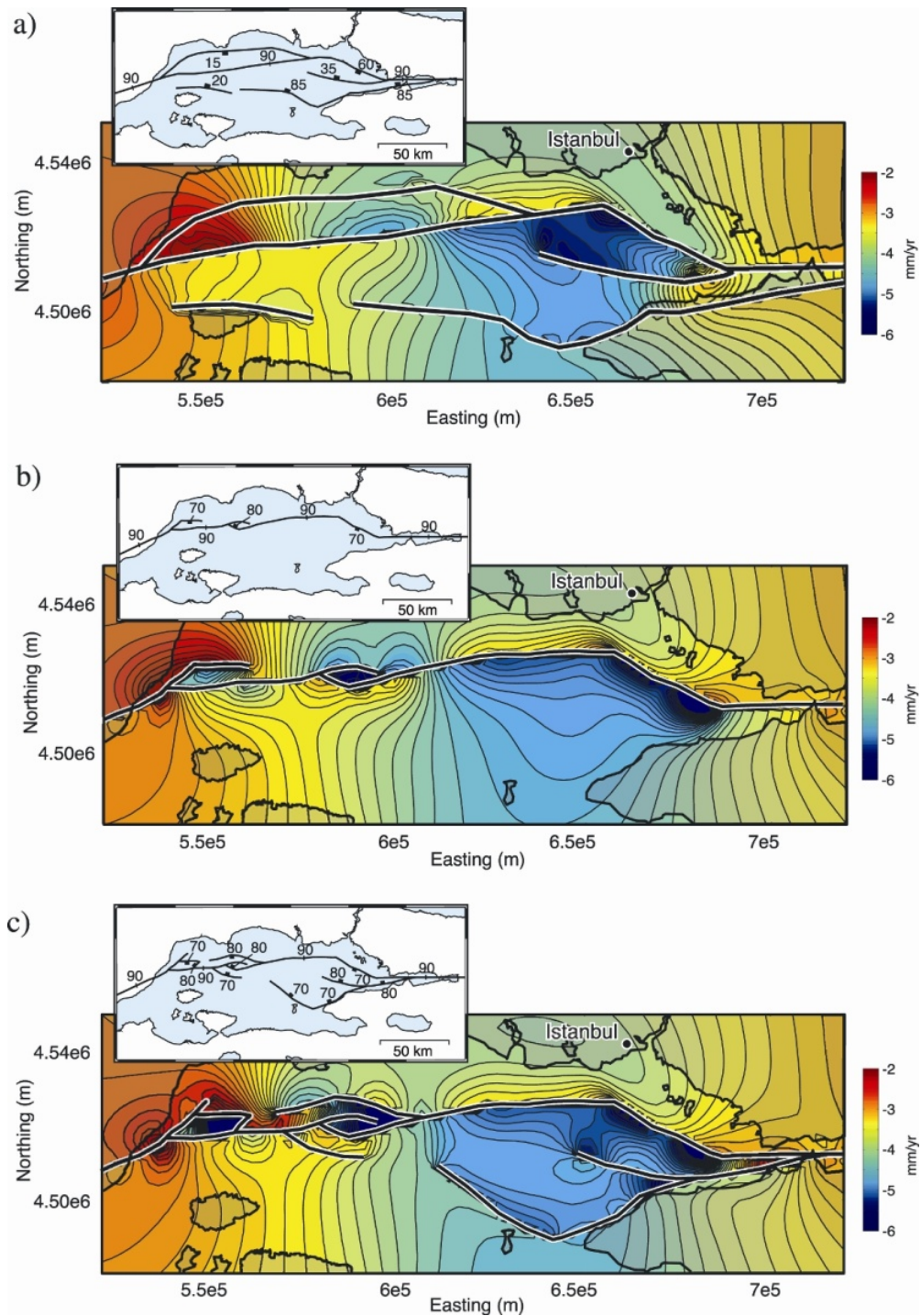


Figure 2.9 : Mechanical models (Muller and Aydın, 2005) based on three different fault configurations in the Sea of Marmara showing subsidence (blue areas) and uplift (red areas). a) Okay et al., 1999, b) Le Pichon et al., 2001, c) Armijo et al., 2002.

Armijo et al. (2002) and Le Pichon et al. (2001) models because they were both interpreted using the latest high-resolution bathymetry, and the Okay et al. (2000) model to represent the models that include northern and southern boundary faults in the Sea of Marmara (e.g., Parke et al., 1999). In the mechanical model, fault dips are

set to specific values where they are defined by seismic reflection surveys (Le Pichon et al., 2001; Okay et al., 1999, 2000).

The modeling results are shown in Figure 2.9. When deformation patterns of Okay et al. (2000) fault model is computed, it successfully produces some of the large scale basin structures within the northern trough in the general location of Çınarcık, Central and Imralı basins among which it best predicts subsidence pattern within the Çınarcık basin. Whereas it produces an asymmetric basin depth in Central basin where block subsidence is relatively uniform as observed from seismic reflection profiles (Armijo et al., 1999; Demirbağ et al., 2003; Parke et al., 1999; Wong et al., 1995). Okay et al. (2000) model also predicts a greater relative uplift in Tekirdağ basin than in the Ganos Mountain contrary to the observed morphology. Mechanical models based on the models of Le Pichon et al. (2001) and Armijo et al. (2002) overall look the same. Le Pichon et al. (2001)'s fault configuration predicts subsidence at the Çınarcık, Central and Tekirdağ basins but fails to explain the Imralı basin. Whereas the Armijo et al., (2002)'s model predicts successfully all the basins. Therefore, Muller and Aydın (2005) conclude that the best model is that of Armijo et al. (2002).

2.3.3.3 Present-day crustal movements: GPS constraints in the Sea of Marmara

GPS measurements in the Marmara region started in the early 1990s (Straub and Kahle 1997). A dense GPS network was formed with time since the region had been spotted to be prone to a large earthquake taking into account the westward migrating earthquakes that stopped near İzmit (Reilinger et al., 1997; Stein et al., 1997; Nalbant et al., 1998). As a result, the coseismic surface deformation due to the 1999 İzmit and Düzce earthquakes were well recorded by the Marmara GPS network run by TÜBİTAK Marmara Research Center (Reilinger et al., 2000). Analyses and modeling of the GPS velocity field have shown that the most active segment of the NAF in the Marmara region is the one that crosses the Sea of Marmara, that is, the northern strand. The measurements showed that while ~%80 of the plate velocity (16-17 mm/yr) is taken up by the northern strand, the southern segment accommodates ~%20 (3-4 mm/yr) (Straub, 1996; McClusky et al., 2000).

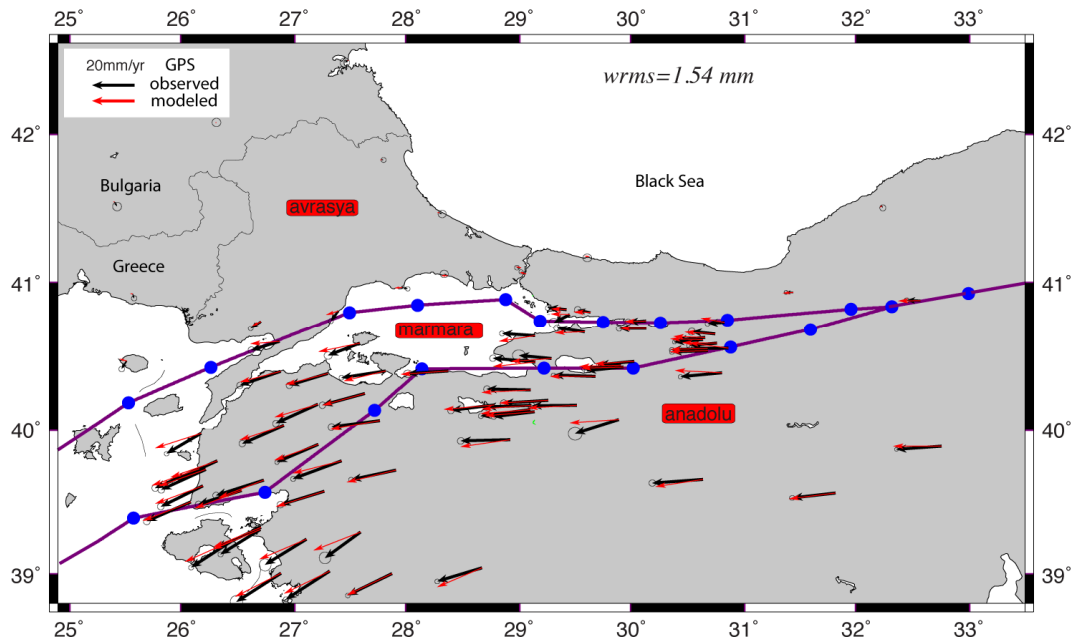


Figure 2.10 : Observed (black) and modeled (red) GPS velocity field with %95 confidence ellipses in the Marmara region in Eurasian fixed reference. The region is divided into three blocks as Eurasia, Marmara and Anatolia by the northern and southern strands of the NAF. The fault model in the Sea of Marmara is the simplified version of that of Le Pichon et al. (2001) and Armijo et al. (2002). Blue circles show the nodes used to define the faults.

Modeling the GPS velocity field using faults (Flerit et al., 2003) or fault-bounded blocks (Meade et al., 2002) have clearly demonstrated that the Marmara region is under a transtensional tectonic regime.

In this study, we model the GPS velocity field provided by Reilinger et al. (2006) assuming that the region is being deformed in a manner of rigid blocks bounded by active faults. The aim of our modeling is to demonstrate how the northern strand of the NAF running through the Sea of Marmara accommodates the motion of Anatolia observed by GPS. In other words, what the GPS measurements tell us about the kinematics and slip rates of the northern strand, as well the southern strand, will be deduced by elastic dislocation modeling. The region is divided into three tectonic blocks by the southern and northern strands of the NAF that splays off near Bolu (Figure 2.10). Faults bounding the blocks are defined by nodes from surface to the depth of 30 km. Then the GPS vectors are modeled by a combination of block rotations and back slip. The latter is used to simulate locking on the fault surfaces due to friction. The best fitting solution is obtained by inversion that uses a simulated

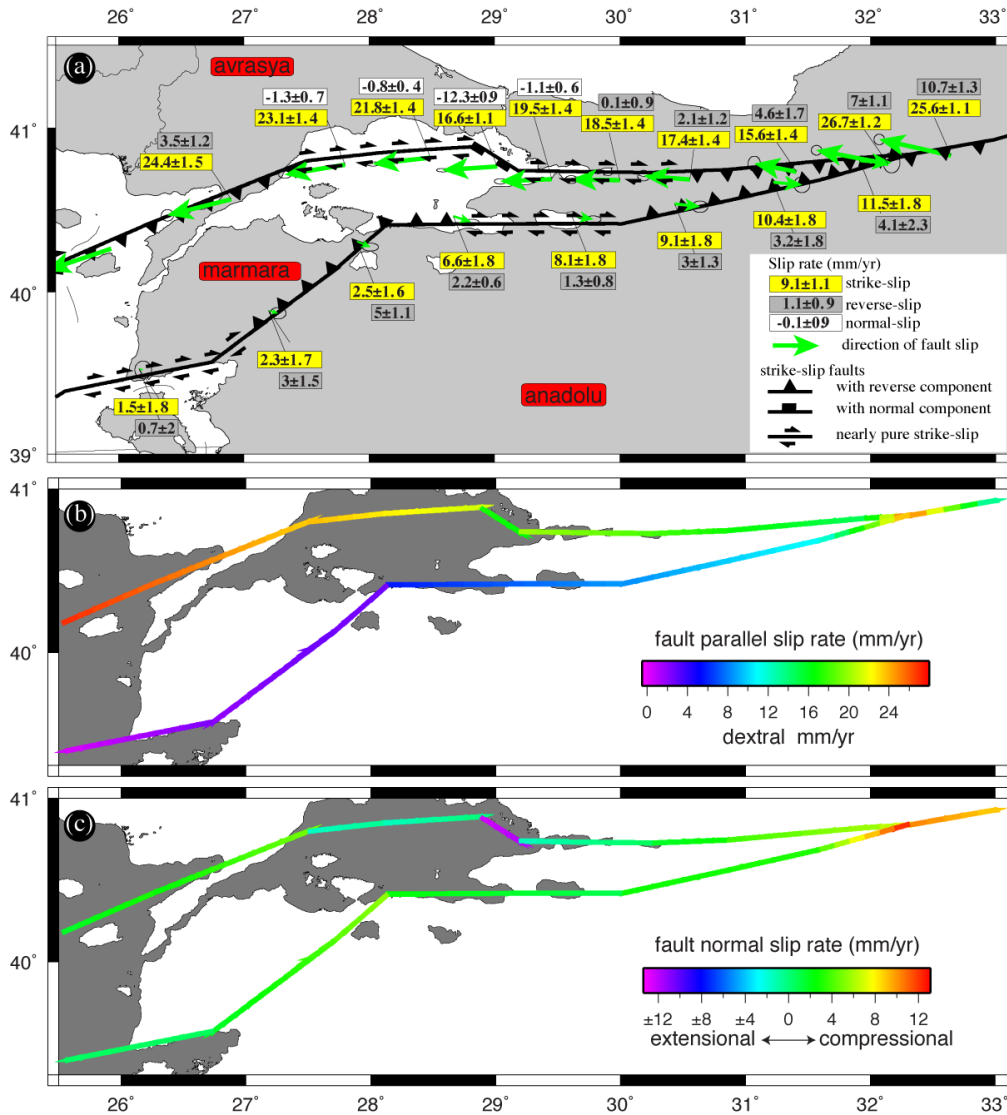


Figure 2.11 : Modeling results. (a) Variation of slip rates along the strands of the NAF and their kinematics in the Marmara region. (b) Fault parallel slip rates (i.e., strike-slip). (c) Fault normal slip rates (i.e., reverse or normal). Note the significant amount (12.3 ± 0.9 mm) of opening along the Northern Çınarcık fault (the purple color in c).

annealing algorithm (McCaffrey et al., 2002). Figure 2.10 shows the inversion results. As seen in the figure the model successfully predicts the observed GPS displacements with a reasonable fit (weighted root mean square misfit is 1.54 mm).

Figure 2.11 shows the variation of slip rates along the branches of the NAF in the study area. Both fault parallel (i.e., strike-slip) and fault normal (extensional or compressional) are inferred in the inversion. Those segments with fault normal component within ± 2 mm/yr are plotted as pure strike slip faults (couple arrows). Those with normal component lower than -2 mm are shown as normal faults (lines with white boxes on the hangingwall), and higher than 2 mm as reverse faults (lines with

triangles on the hanging wall). The model predicts successfully the kinematics of the faults such as the Ganos, Erdek-Edremit, and Karadere segments known to have compressional components. Most strikingly the model predicts extension on the submarine fault segments in the Sea of Marmara. The Northern Çınarcık fault, in particular, is inferred to have a significant normal slip component (12.3 ± 0.9 mm with a rake of 36°) due to its NW-SW strike. Extension along the fault segment between İznik and Erdek is not predicted by the model because of its E-W strike given in the model, suggesting that the fault pattern is probably more complicated and the fault strike should be more ENE-WSW subparallel to the Central Marmara segment. In summary, the GPS field requires transtension along the submarine section of the NAF in the Sea of Marmara.

3. CHARACTERISTICS OF ACTIVE FAULTING ALONG THE NORTH ANATOLIAN FAULT IN THE SEA OF MARMARA

3.1 Introduction

Before entering the Aegean westwards, the NAF splays into two major fault branches that are about 100 km apart in the Marmara region. According to available geological and geodetic data (Armijo et al., 1999; McClusky et al., 2000), most of the lateral motion appears to be transferred obliquely northward, from the main to the northern branch, across the large Marmara basin that the two branches embrace. At the northern part of the Marmara Sea, a deep trough (up to 1272 m) is formed by an oblique submarine fault zone which links two well known inland strike-slip branches on both sides that ruptured in 1912 to the west (Ganos segment) and in 1999 to the east (İzmit segment). This oblique submarine zone is here termed as the North Marmara Fault System (NMFS). Separated by NNE-SSW trending ridges, the deep northern Marmara trough (NMT) is composed of three smaller basins that are named, from east to west, the Çınarcık (1273 m), Central (1258 m) and Tekirdağ (1130 m) basins. Several recent studies using high-resolution multibeam bathymetry and seismic reflection profiles have proposed detailed maps of the submarine structure (e.g. Okay et al., 1999, 2000; Parke et al., 1999; İmren et al., 2001; Armijo et al., 2002; Le Pichon et al. 2003). Although the dataset and techniques used by these researchers are same and/or similar, their interpretations are rather different and conflicting.

In this study, several datasets from various cruises have been combined to better understand the 3D structure of the basins and the kinematics and evolution of the NAF in the Marmara Sea. Submarine morphotectonic features (based on the multibeam bathymetry) of the northern Marmara trough are described together with the deep seismic profiles, to consider the connection between the deep structure, surface morphology and related fault kinematics in the first section. In the second section, 3.5 kHz chirp profiles that were acquired by an extensive survey during the MARMARASCARPS cruise are examined to understand the relation between

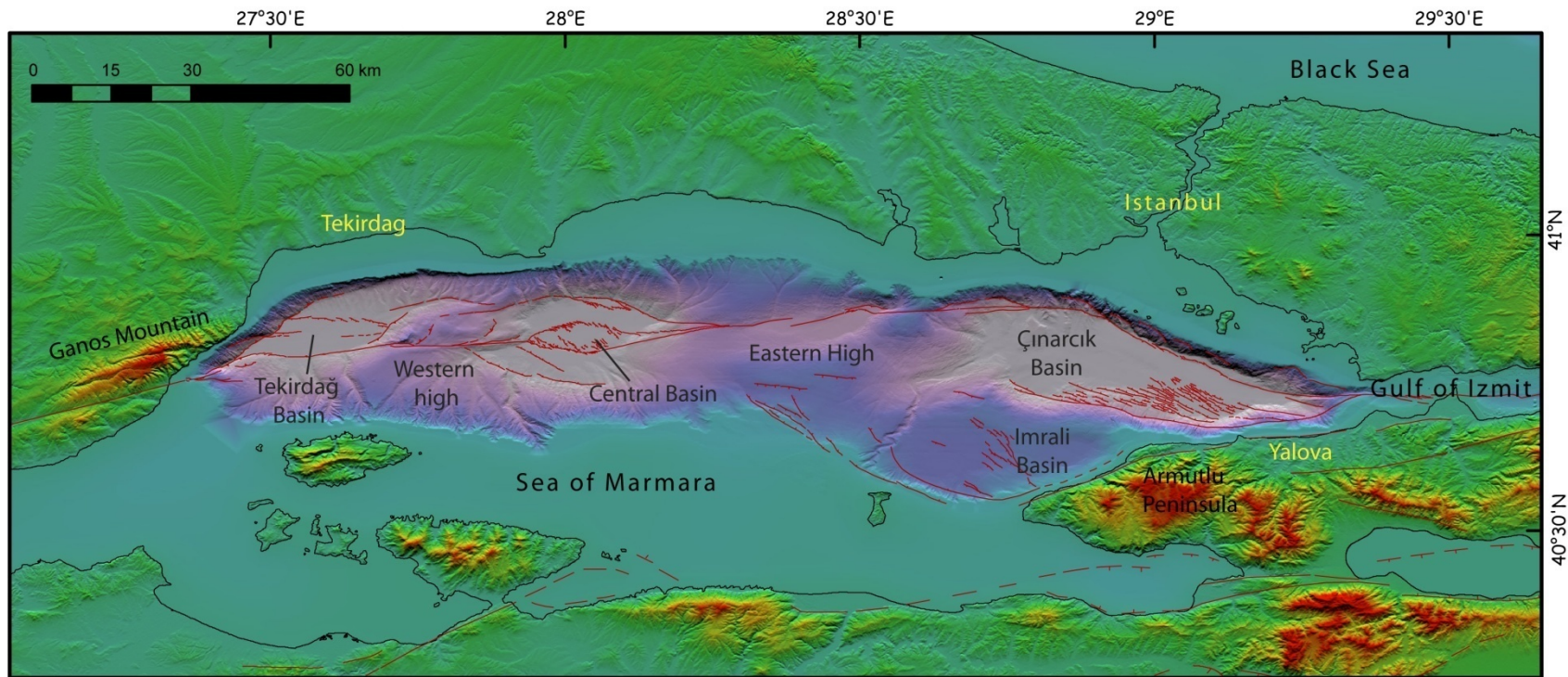


Figure 3.1 : Shaded elevation topography and bathymetry of the Marmara region showing the morphology shaped by active faults (red lines; modified from Armijo et al., 2002).

sedimentation and faulting rates in the Late Pleistocene-Holocene. The Sea of Marmara was isolated from both the Black Sea and the Aegean prevailed during the late Pleistocene glacial low sea level. The lacustrine period was followed by a sharp marine transgression. This important passage is a key time line to discuss competing tectonic and sedimentation processes subject to climatic change in the Sea of Marmara.

3.2 The Northern Marmara Fault System and associated active basins

The Sea of Marmara (Figure 3.1) is an important structure on the North Anatolian fault, but detailed study of this feature has only been possible with new data that comprise high resolution bathymetry, seismic and sonar soundings collected in the last 10 years. Nevertheless, the kinematics of the submerged part of the NAF beneath the Sea of Marmara is still a matter of debate. Two main fault model discussions diverge between crustal scale pull-apart tectonics (Armijo et al., 2002) and a single through-going strike-slip fault model suggesting now inactive extension (Le Pichon et al., 2001) along the Northern Sea of Marmara basin. The occurrence of large earthquake ruptures (1912 M 7.4 Ganos earthquake; 1999 Mw 7.4 İzmit and Mw 7.2 Düzce earthquakes) has provided examples of right-lateral slip increments corroborating the strike-slip morphology of the active faults on land. However, large earthquake ruptures are likely to occur within the next decades along the submarine faults beneath the Sea of Marmara (e.g. Hubert-Ferrari et al., 2000; Parsons et al., 2000; Parsons et al., 2004). In order to assess the nature of events threatening Istanbul, it is critical to have a correct understanding of segmentation in the Sea of Marmara.

The North Anatolian fault enters the Sea of Marmara through the Gulf of İzmit and emerges onland in the Gelibolu peninsula along the Ganos fault segment. In between these two strike-slip segments it follows significant submarine depressions and highs with alternating strike-slip and normal fault geometry. The submarine basins are aligned in an east-west direction with the Central basin bounded by two major ridges, namely, the Western and Eastern highs (Figure 3.1). The high-resolution bathymetry acquired by the Le Suroit clearly demonstrates that the basins get smaller towards the west (Figure 3.1) with their depths (although slight) also getting shallower. The gradual change in size towards the east may reflect the increase in normal faulting

component among the faults bounding the basins. The Marmara basin contains significant amounts of recent sediments (average thickness of 1-2 km), very thick in the deeper northern basins (> 6 km) and is cut by large normal faults, as observed in the seismic profiles (e.g., Parke et al., 1999, Carton et al., 2007, Laigle et al., 2008), suggesting that active subsidence is prominent in the Northern Marmara trough. The morphology of the active faults is well preserved on the seafloor. Fault scarps probably resulting from many seismic events can be followed over tens of kilometers. Individual breaks that may correspond to earthquakes in the recent past are also distinguishable. Most scarps show clear normal and strike-slip fault morphology, forming bends and pull-apart features at a range of scales. Active faulting along the NMT is segmented and appears to interconnect extensional basins (Çınarcık, Central and Tekirdağ Basins) with the İzmit and Ganos faults on land.

3.2.1 Tectonic and morphologic structure of the Çınarcık Basin

The Çınarcık basin is a wedge-shaped basin that narrows eastward where it meets the Gulf of İzmit (Figure 3.2a). It is bordered in the north by a narrow shelf, and in the south by a wide and deep shelf area that bears another depression, i.e., the İmralli basin (Figures 3.1 and 3.2a). The basin floor is fairly flat and lies at a depth of -1260 to -1120 m. The deepest part of the basin is -1272 m (from multibeam bathymetry) and located in the east. The basin widens westward and meets the Central high that separates it from the Central basin (Figure 3.1). Steep submarine slopes bound northern and southern margins of the Çınarcık basin and mark the active fault segments of the NNAF (Figures 3.2a and 3.2b). The northern slope is a distinct ~1000-m-high bathymetric feature which corresponds to a large, continuous, and south facing steep escarpment (25–30°). The southern slope of the Çınarcık Basin is wider, more irregular and less steep (15–20°) compared to the northern one.

Analyses of the high-resolution multibeam bathymetry and the seismic reflection data show that the strike-slip tectonic regime of the NAF significantly changes into oblique extension in the Çınarcık basin. The extensional behavior of the faults towards the west becomes evident particularly in the Gulf of İzmit. In the Çınarcık basin the oblique extension is taken up by the northern and southern margin faults that bifurcate from the NAF in Gulf of İzmit. The E-W trending İzmit fault segment along the axis of the Gulf of İzmit makes a sharp NW bend (30°) at the entrance of

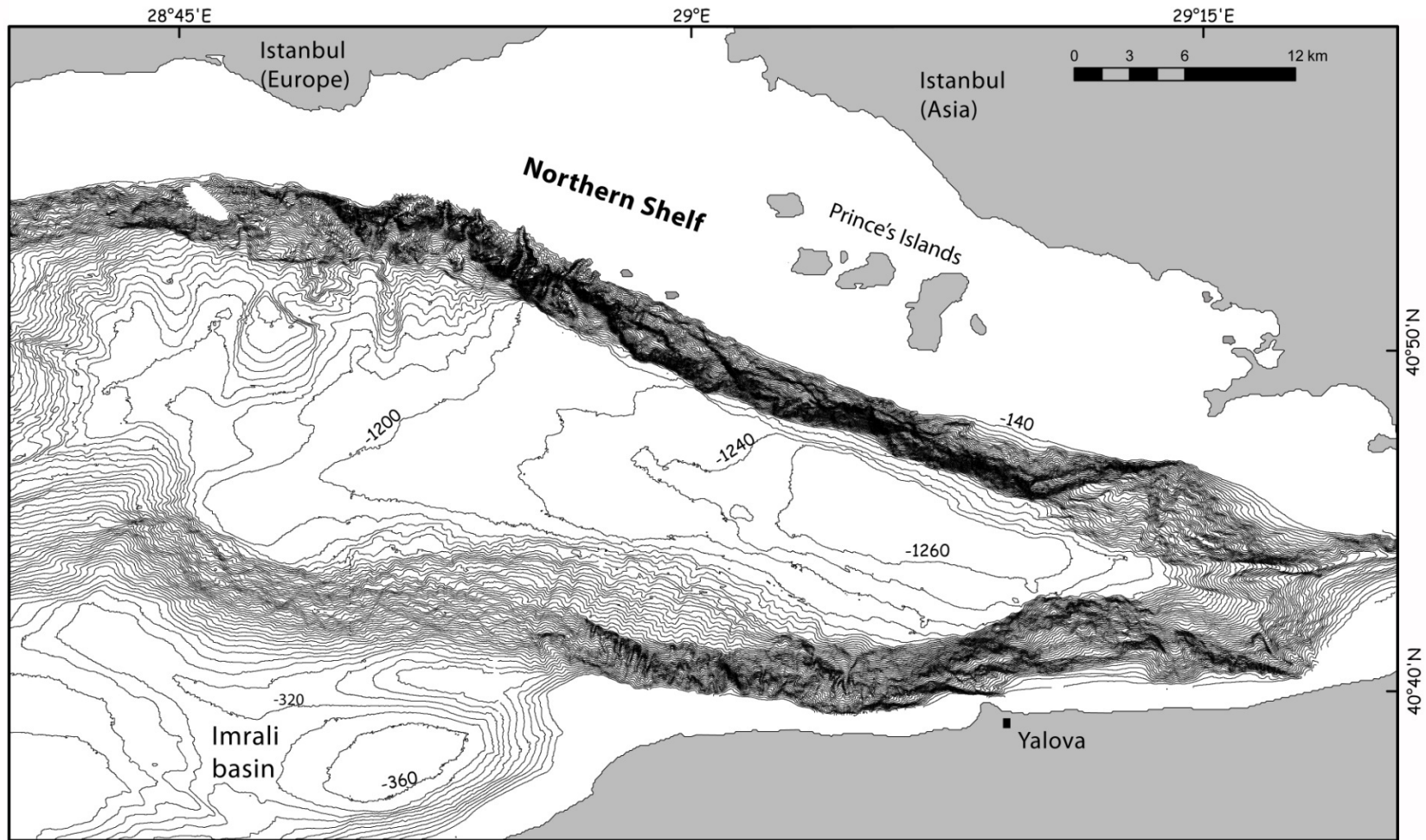


Figure 3.2 : (a) Bathymetric map of the Çınarcık basin (contours every 20 m)

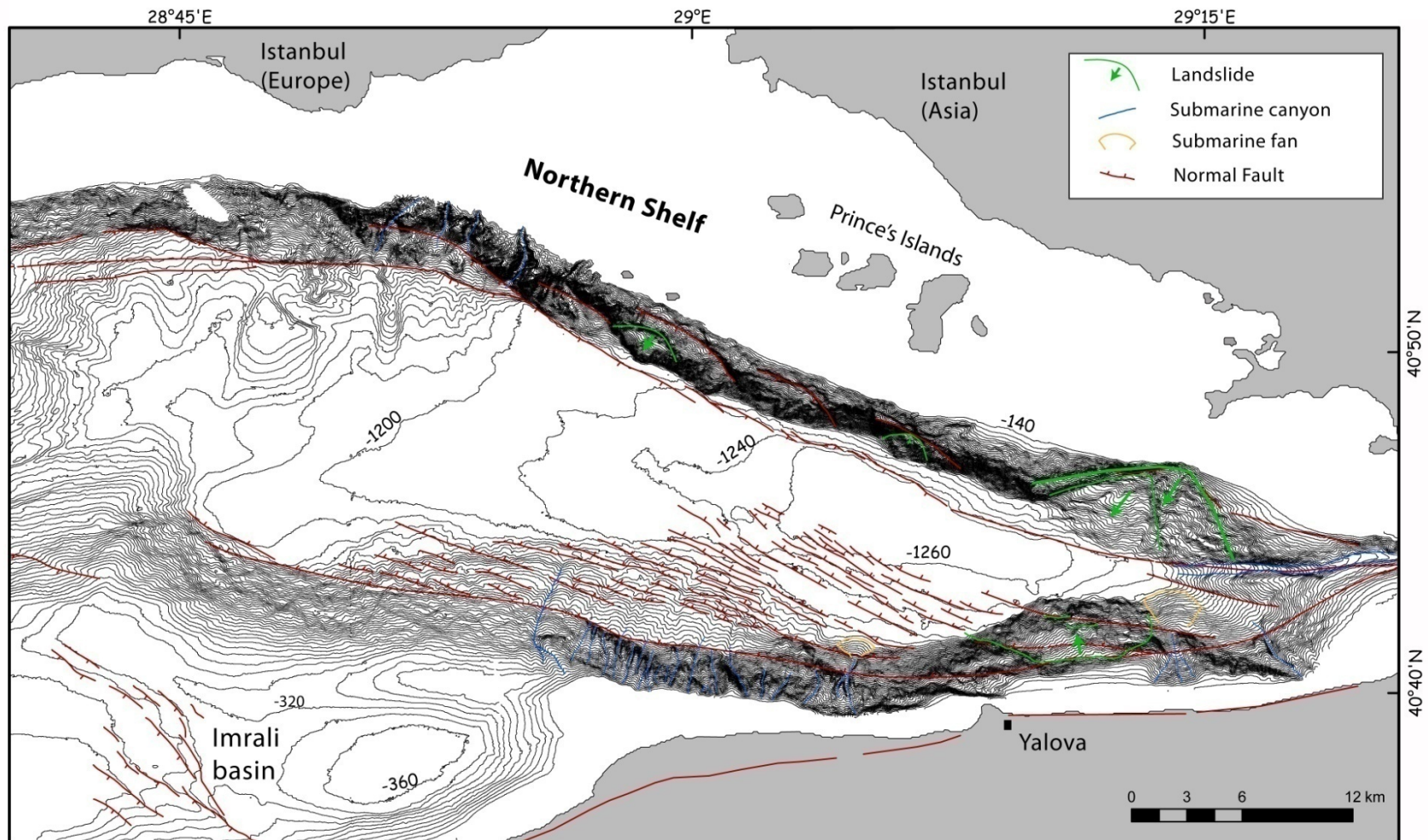


Figure 3.2 : (b) Morphotectonic map of the Çınarcık basin showing active faults and related submarine features.

the Çınarcık basin (Figure 3.3). This setting clearly presents a 14-km-wide releasing side-step between the E-W striking İzmit fault and the ENE-WSW striking faults that connect the Çınarcık and Central basins.

Such a configuration of faults necessarily requires a significant transtension in the Çınarcık basin. Indeed, deep seismic reflection studies (e.g., Carton et al., 2007) reveal a very thick (6-7 km) pile of sedimentary layers fanning towards the North Çınarcık fault, indicating a significant normal-slip component. As shown by the block modeling in the previous section, the other supporting evidence for the oblique motion on the Northern Çınarcık fault comes from the Global Positioning System measurements (Reilinger et al., 2006). The GPS vectors on the southern side (i.e., Anatolia) of the İzmit and Northern Çınarcık faults indicate 15-20 mm of westward motion relative to the northern side (i.e., Eurasia) (Figure 3.3). A simple cartoon model illustrates that by resolving the plate motion given by GPS on to the North Çınarcık fault gives strike-slip faulting with significant dip slip component (Figure 3.3).

The Northern Çınarcık fault on the seafloor presents an arrangement of left-stepping en-echelon faults that offset the basin floor at the foot of the large escarpment with throws of up to 100 m. Morphology and en-echelon pattern of these normal fault scarps supports our inference that the Northern Çınarcık fault indeed carries composite normal and strike-slip component. Analysis of the bathymetry shows that the escarpment of the oblique slip Northern Çınarcık fault is cut and displaced by numerous smaller and shallow synthetic faults of arcuate and en-echelon shape, which result in various landslides (Figure 3.4). In the hanging-wall of the Northern Çınarcık fault, seismic reflections reveal a major synthetic fault that merges with the main fault at depth (> 5 km) (Figures 3.6 and 3.7). Composite normal and strike-slip component of the both fault segment must be responsible for the creation of the 1000-m-high, 40-km-long, northern Çınarcık escarpment. Oblique slip may also be partitioned between these two segments.

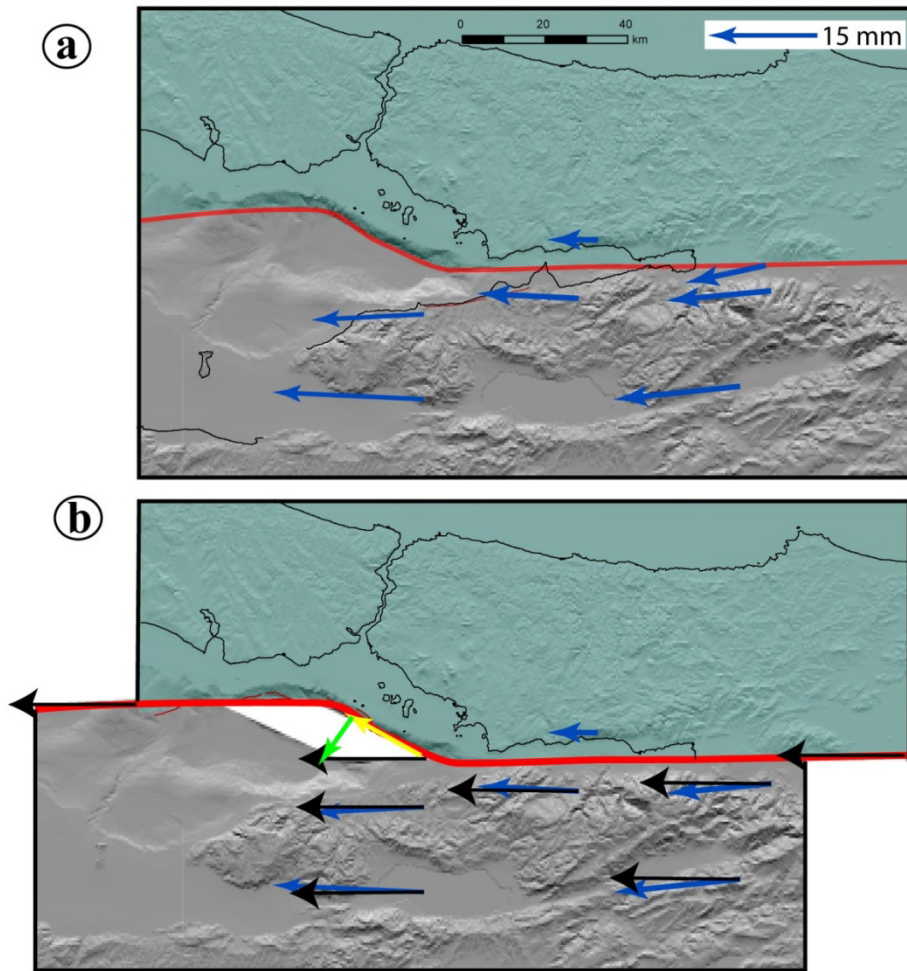


Figure 3.3 : (a) Map of active faults and GPS vectors in eastern Marmara (relative to Eurasia) (from Reilinger et al., 2006). (b) Kinematic cartoon model showing westward motion of Anatolia relative to fixed Eurasia, which gives rise to opening in the Çınarcık basin. Black vectors show the direction and amount of the displacement given. Yellow and green arrows show, respectively, the fault parallel and fault normal components of displacement resolved on the North Çınarcık fault.

The second fault segment which branches from the İzmit fault to the west, defines the southern margin of the Çınarcık basin north of the Armutlu Peninsula. Named as the Southern Çınarcık Fault (SCF) here, this fault is the main antithetic fault of the Çınarcık graben. Morphological and seismic reflection observations suggest that the SCF has a normal slip component. The southern slope is sculpted by several N-S running submarine canyons that are displaced vertically by the SCF. Triangular facets, typical geomorphologic features in extensional tectonics, are abundant along the southern slope as a result of active normal faulting (Figure 3.5). They bound small drainage basins within the footwall uplands of the fault line. Right-lateral offsets are hardly seen along these canyons, suggesting that the amount of strike-slip

component might be rather small along the SCF. The most prominent deformation style at the southern margin is the series of small en echelon oblique normal faults that splay out from the SCF towards the basin centre in a horsetail style. These NW trending (\sim N55°W on average) en-echelon faults are densely spaced especially at the southeastern side of the basin and but die fanning out towards the centre of the Çınarcık basin (Figure 3.2b). They create a step-like morphology on the sea floor with throws up to 25 m high at the bathymetry (Figure 3.7).

The surface expression of the faults bounding the Çınarcık basin can be projected downward well below many kilometers as seen in the deep multichannel seismic reflection profiles (MCS) acquired during the SEISMARMARA cruise Leg-1 and 2 (e.g. see Figure 3.8) (Carton et al., 2007; Laigle et al., 2008; Becel et al., 2009). The results of this cruise and their data acquisition parameters successfully resolved the structure of northern Marmara trough down to Moho (Laigle et al., 2008; Becel et al., 2009). Hence, a very profound MCS profile SM 36 (Laigle et al., 2009) improves our understanding of the structure at depth in the Çınarcık basin (Figure 3.6). Profile SM 36 transects the Çınarcık basin in NE-SW direction covering both northern and southern fault zones (Figure 3.6). It shows a clear basement reflector steeply dipping northeastward under the sedimentary basin.

During the SEISMARMARA Leg-1 (2001), a dense grid of multichannel seismic reflection profiles was collected covering the whole Çınarcık Basin and its margins (Carton et al., 2007). Along both northern and southern margins of the basin, seismic reflection data show deep-penetrating faults that have accommodated a large amount of extension since early Pleistocene. Line 124 from SEISMARMARA cruise is merged with the high-resolution bathymetry in 3D and it displays a successful correlation of surface morphology with the faults at depth (Figure 3.8). It shows that the basin is bounded on the northern side by two steep branches that appear to connect at depth into a single fault (Figure 3.8). To make a distinction, we name the fault bounding the large escarpment as F_{n1} and the fault that offset the basin floor as F_{n2} . F_{n1} must be the branch responsible for the long-term vertical displacement here. F_{n2} seems to have evolved afterwards.

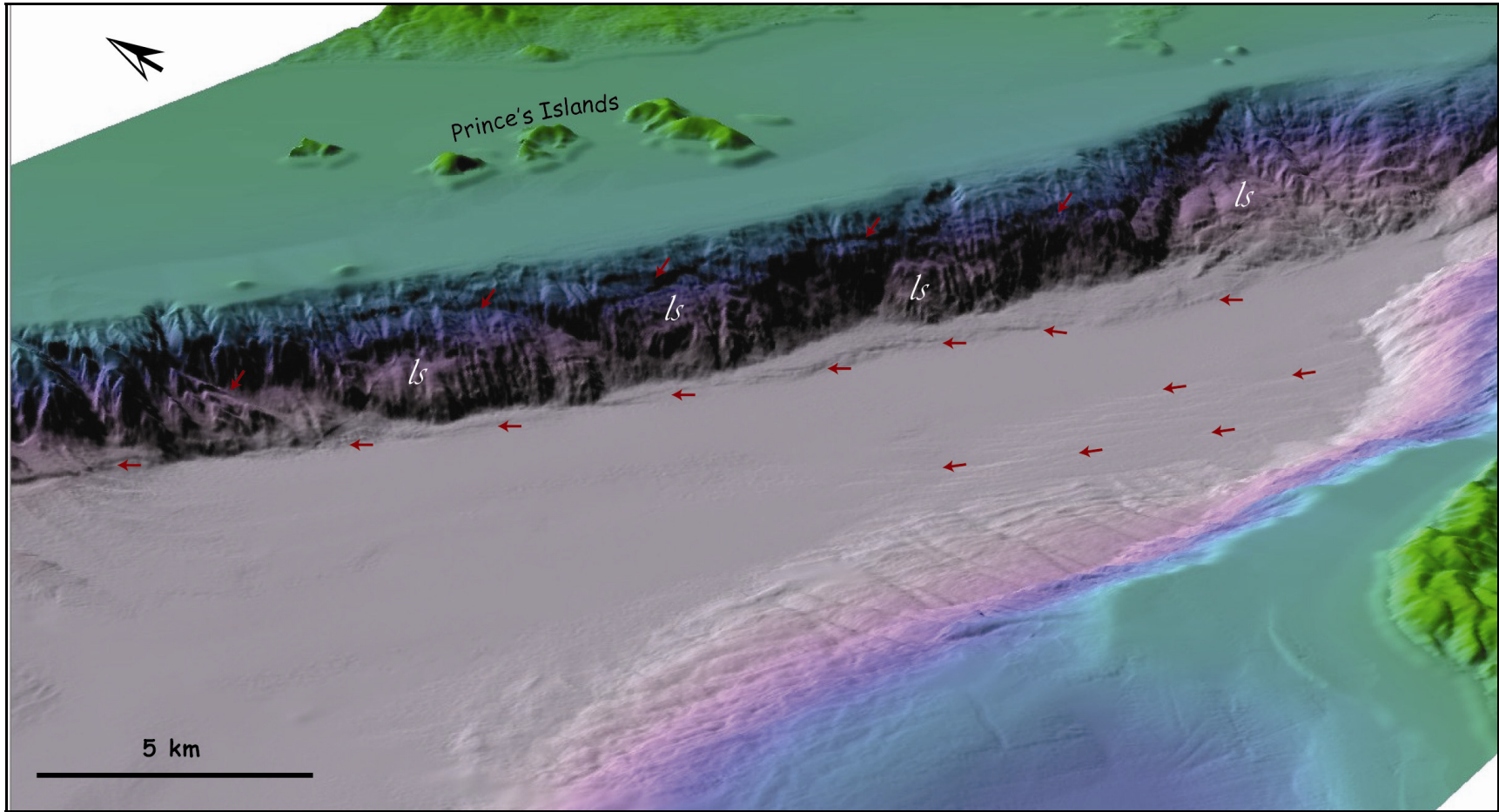


Figure 3.4 : 3D NE oblique view of the Çınarcık basin showing the escarpment of the Northern Çınarcık fault sliced by landslides and arcuate faults, and the en-echelon faults at its base (ls: landslide, red arrows indicate fault traces).

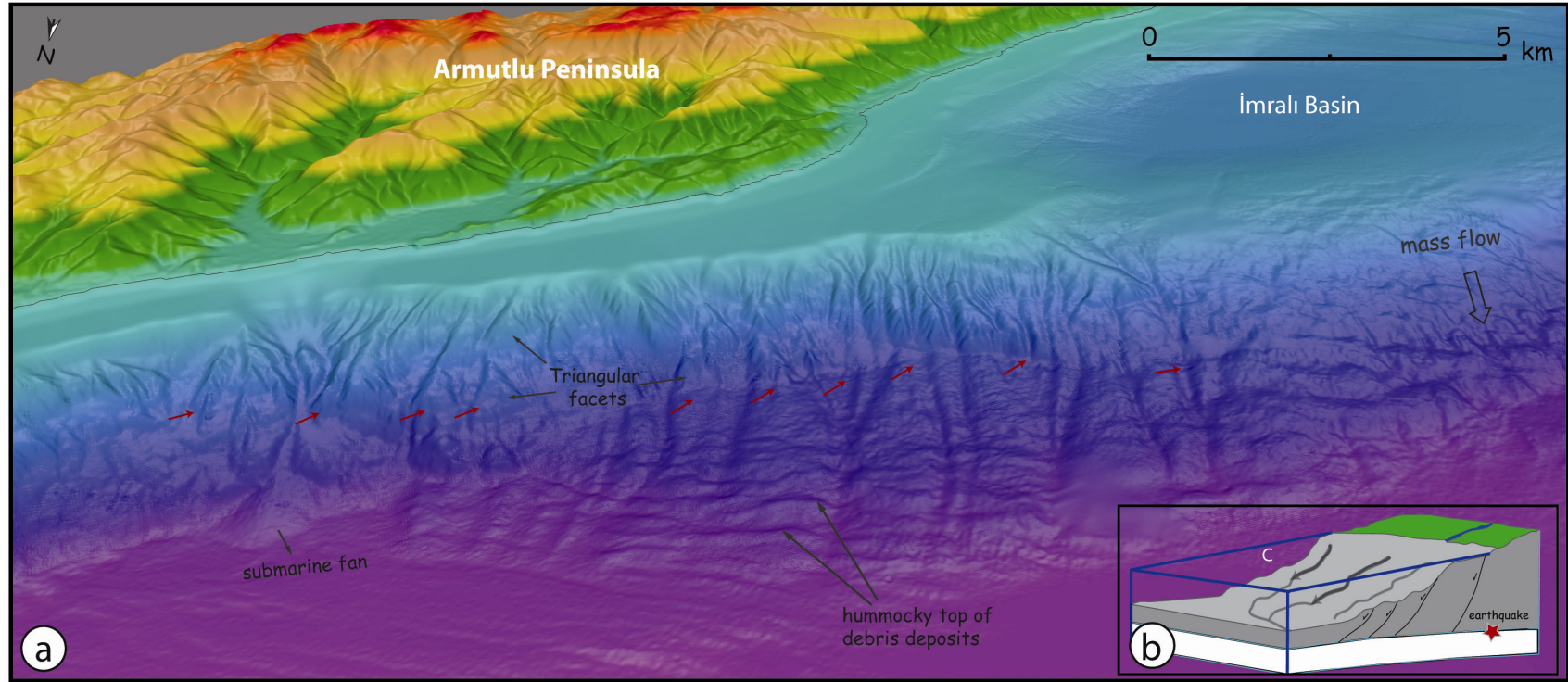


Figure 3.5 : (a) 3D SW oblique view of the Çınarcık basin showing the escarpment of the Southern Çınarcık fault sliced by numerous small faults, triangular facets, debris flows and submarine fans. (b) 3D scheme showing how sediments are triggered by earthquakes.

An interesting and peculiar feature of the sedimentary strata in the Çınarcık basin is the prominent downward warping of the layers tilted towards the Northern Çınarcık fault on the hanging wall of the F_{n2} (Figures 3.6 and 3.8). One mechanism that may explain this warping is the occurrence of relatively higher amount of slip at deeper depths. A simple elastic dislocation model has been calculated using normal slip on a buried normal fault. As shown in Figure 3.9, the model successfully produces the type of bending seen the Çınarcık basin. Decrease in differential stress with decreasing depth along active faults causes increase in fault dip and decrease in slip on the fault. During many earthquake cycles, this slip deficit on the shallow portion of the normal faults may result in sagging (and thus warping) in the hanging wall above the fault, as predicted by the elastic dislocation model.

On the steep southernmost margin, step-like morphology of the seafloor topography is interpreted as the evidence of normal faults although their evidence in the basement cannot be imaged in the seismic profiles (Carton et al., 2007). Further north into the flat portions of the basin, numerous small normal faults cut through the syn-kinematic sediments generally with little vertical displacements. These are synthetic faults located on the footwall of the major fault that offsets the basement at around 3 km of depth and bounds the deep basin fill to the south.

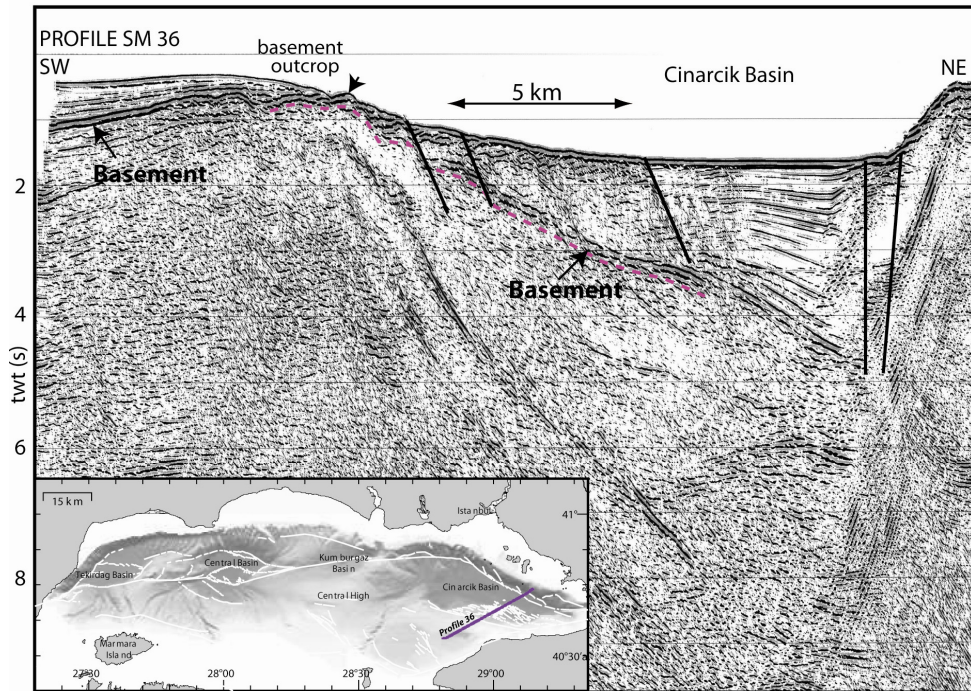


Figure 3.6 : Deep (down to ~10 km) seismic reflection profile SM36 crossing the Çınarcık basin in NE-SW direction (profile 36 in the inset map) from Laigle et al. (2008).

The orange horizon on the section 124 (Figure 3.8) is interpreted by Carton et al. (2007) to be the bottom of the Plio-Quaternary sedimentary fill that clearly thickens toward the NCF. These shallow sediments have low P-wave velocity ranging between 1.5 and 1.7 km/s as inferred from velocity analyses. Sediments below the syn-kinematic sediments have higher P-wave velocities, increasing downward from 1.7 to about 3.8 km/s (Carton et al., 2007). They correspond to Miocene and older pre-transform strata (Okay et al., 1999; Parke et al., 2002) in the Sea of Marmara. The distinction is made solely by the P-wave velocity differences. Therefore, these reflectors are not constrained in terms of lithological contrasts or of age due to the absence of wells in the Çınarcık Basin. The bottom of the basin is encountered at more than 5 s two-way time near the innermost branch of NCF. The maximum sedimentary thickness in the Çınarcık Basin is about 5–5.5 s twt (5–6 km using an

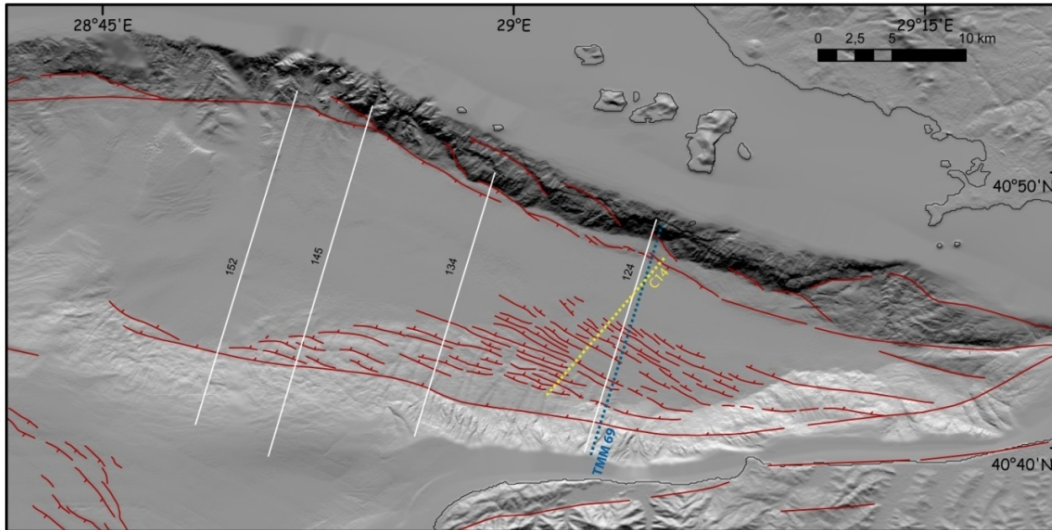


Figure 3.7 : Bathymetry image of the Çınarcık basin with locations of the seismic lines.

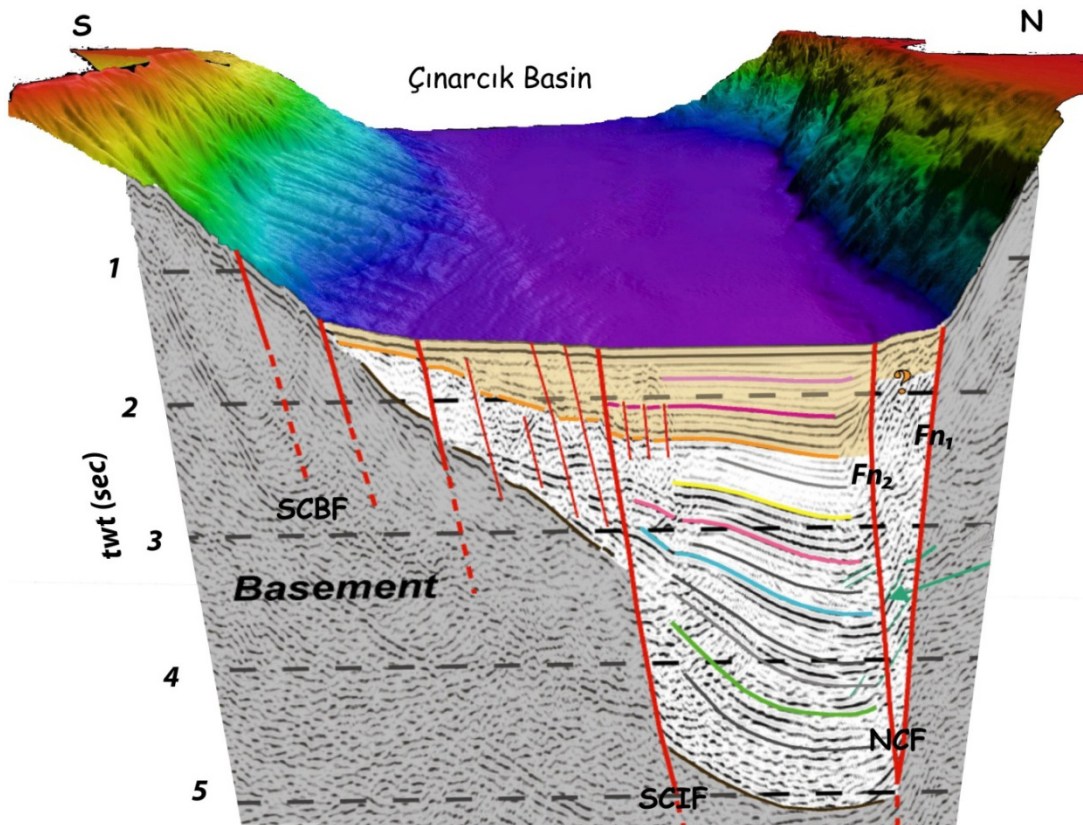


Figure 3.8 : 3D, northwest view of the Çınarcık basin with a slice of multichannel seismic section (line 124; see Figure 3.7 for location) showing the deep depocenter of the Çınarcık basin bounded and cut by active unconsolidated faults.

average velocity of 2–2.6 km/s) along the north-bounding fault, south and southwest of the bend in the northern escarpment.

Another high-resolution multichannel seismic profile, i.e., TMM 69, from TAMAM cruise (Steckler et al., 2008; Sorlien et al., 2008) highlights the above mentioned fault pattern (Figure 3.6 and 3.10). TMM 69 resolves very clearly the deformed sedimentary strata down to 2.6 s (~ 2 km). Vertical offsets of the faults bounding the basin at the seafloor are significant. The topographic steps seen at the bathymetry, match precisely with the normal faults at the southern half of the Çınarcık basin (Figure 3.10). Although the evidence for the basin margin faults are not very clear because of the complex reflections from the bedrock and debris deposits, some of the gravity collapses triggered by movement along this fault can still be distinguished (Figure 3.9). One particular gravity collapse is identified immediately in front of the southernmost boundary fault. Reflections are disrupted and deposits are unstratified, suggesting that they are the slump debris. The top of the debris is rather hummocky. Indeed, multibeam bathymetry data exhibits several hummocky features at the southern part of the basin floor. Probably, many triggered submarine slumps create the hummocky morphology here (Figure 3.4). Several turbidite horizons can be identified in TMM 69 section. These horizons are offset by the en echelon extensional faults. Hence, an average vertical displacement can be deduced for some of the faults in the profile. F_{n2} creates a topographic step (~100 milliseconds) that corresponds to a 75 m vertical offset (assuming a seismic velocity of about 1500 m/s for the shallow sediments) at the seafloor. The inner normal fault of the southern en echelon fault system creates a ~22 m vertical offset at the seafloor; evidently, the offset value increases (45 m, 60 m sec) at depth (note the offset of the blue reflector in Figure 3.10). Line TMM 69 reveals undoubtedly that both the main northern fault (NCF) and southern extensional fault system are very active structures and offset the entire Quaternary sedimentary pile.

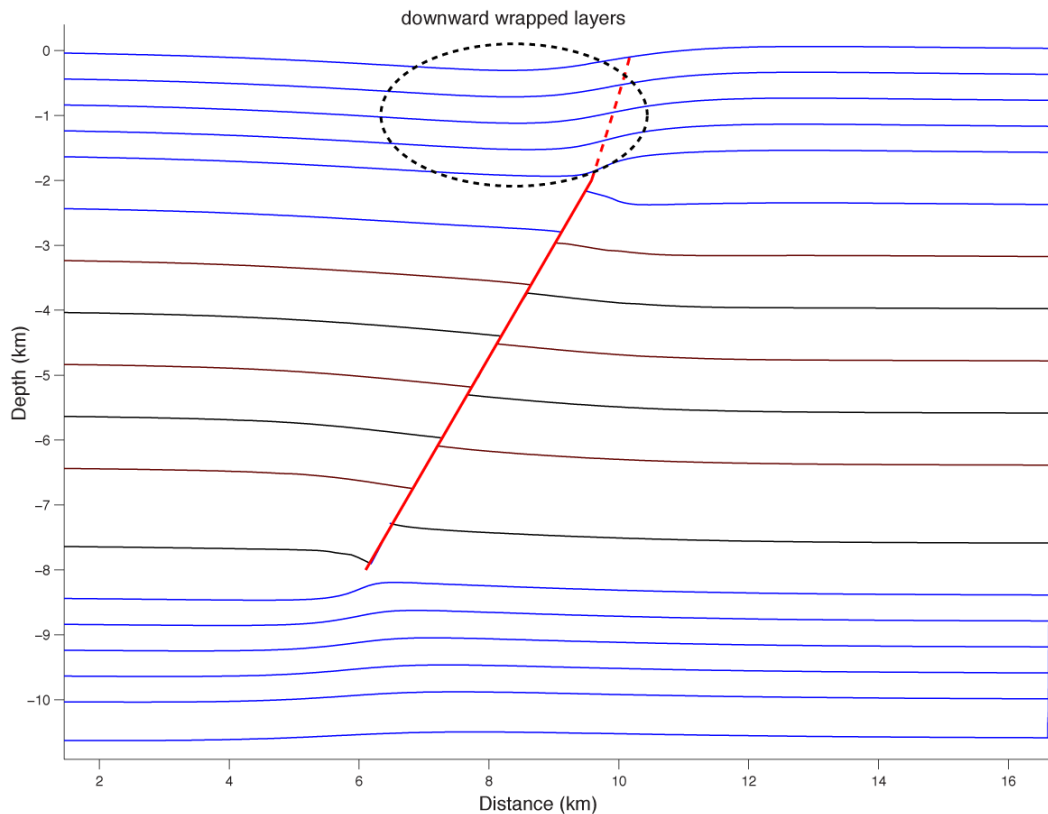


Figure 3.9 : Elastic dislocation model on a buried normal fault (red line) that results in warping of sediments on the hangingwall (in the area indicated by the ellipse), which is analogous to slip deficit on the upper portion of the fault (calculated using Coulomb 3 software of USGS).

The faults that are mapped at the eastern half of the Çınarcık basin from deep profiles can be resolved down to 50 m with 3.5 kHz chirp profiles at shallow depths. The near surface data shows that the vertical throws systematically grow with depth and faults progressively deform syn-kinematic sediments (Figure 3.11). Warping of sediments towards the F_{n2} observed down to the depths of 3-4 km (Figure 3.8) is revealed by the chirp profile to continue upward to very shallow depths (< 50 m), suggesting that what was happening in late Pliocene is still happening in Holocene. These sediments thicken significantly toward the F_{n2} supporting the high activity of this fault. Debris deposits that create hummocky features accumulated at the southern part of the basin cause certain reflections that produce resolution problems. Nonetheless, the turbidite horizons with high amplitudes can be resolved and the vertical throws that offset them can be illustrated.

As seen in several seismic lines of different depths, the eastern half of the Çınarcık basin is characterized by several en echelon faults offsetting its southern edge and a dominant northern boundary fault that creates the asymmetric sedimentary

deposition related to its strong normal faulting component. However, this pattern slightly changes towards western half of the Çınarcık basin as seen in the selected Seismarmara deep seismic profiles. The dense alignment of the normal faults at the eastern half slightly disappears. Line 134 confirms that two faults that bound the southern part of the basin are the deep basin faults that offset basement blocks. Previously the southernmost boundary fault was not distinguished clearly but line SM 134 shows a clear vertical offset of the contact between the basement and basin fill along this fault (Figure 3.12). One can also note that the basin sedimentary fill appears relatively symmetric in that section (hence slightly tilting towards south). Moreover, line SM 145 illustrates a new sub-basin evolving at the southern part of the basin. The slightly southward tilting sediments seen at the line SM 134 now clearly warps toward the southern inner boundary fault. This warping mostly seems to form a syncline in the sediment fill with a south dipping fault bounding the sub-basin (Figure 3.12). Both SM 145 and 152 transects the widest part of the Çınarcık basin westward. While the NE Çınarcık fault bends EW to connect to the Central strike-slip segment, its vertical-slip must be relatively less. In summary, the widest part of the Çınarcık Basin, south and southwest of the bend in the northern escarpment, seems to be the site of accumulation of the thickest sediments and thus probably the oldest part of the basin. A smaller subbasin is also imaged along the southern margin. There seems to exist another basin located on the western margin of the Çınarcık Basin toward Central High, filled by sediments up to 3–4 s thick and bounded to the south by a NNE-SSW trending fault.

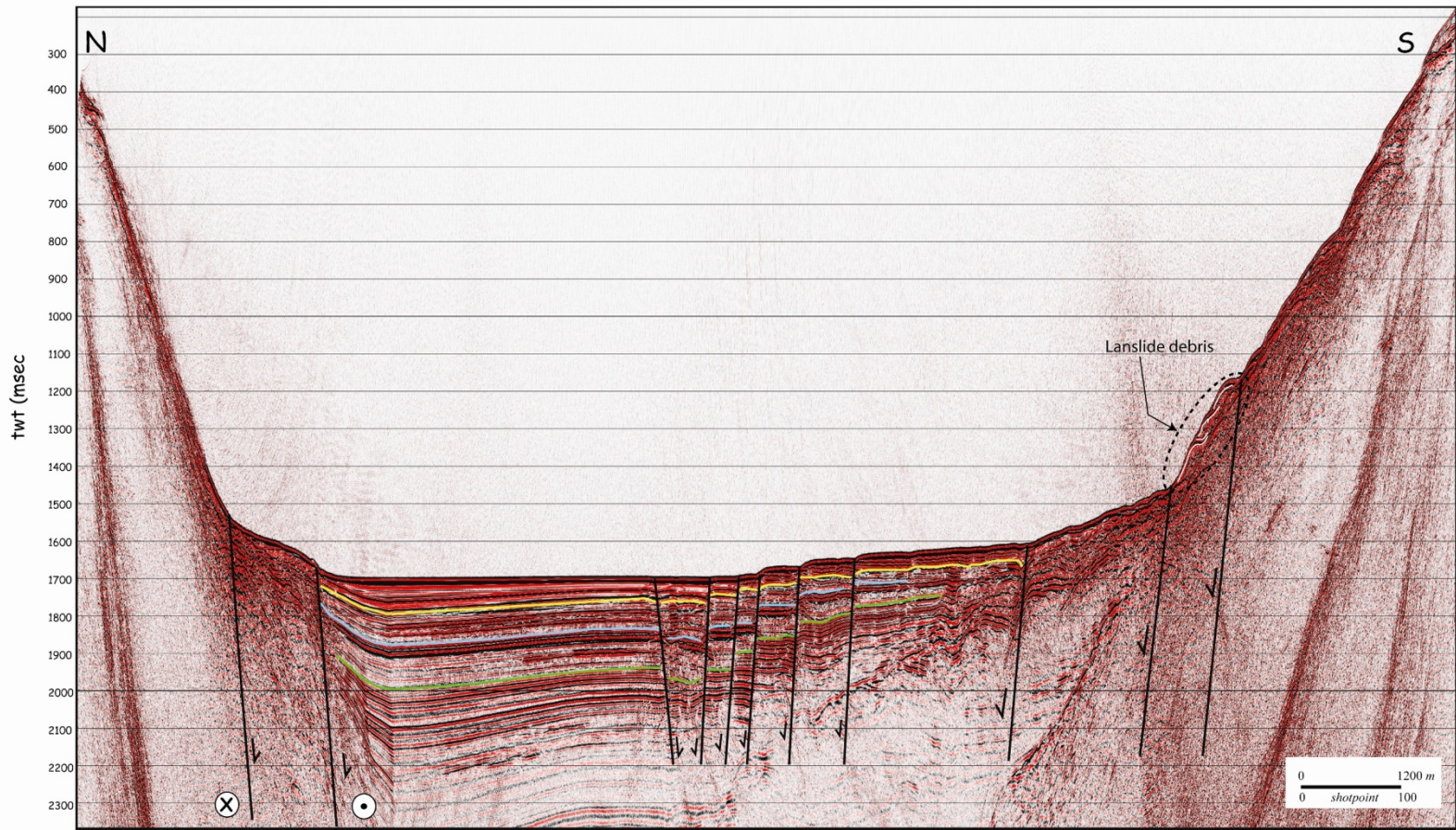


Figure 3.10 : Multi channel seismic reflection section along the TMM 69 profile crossing the Çınarcık basin (see Figure 3.7 for the location).

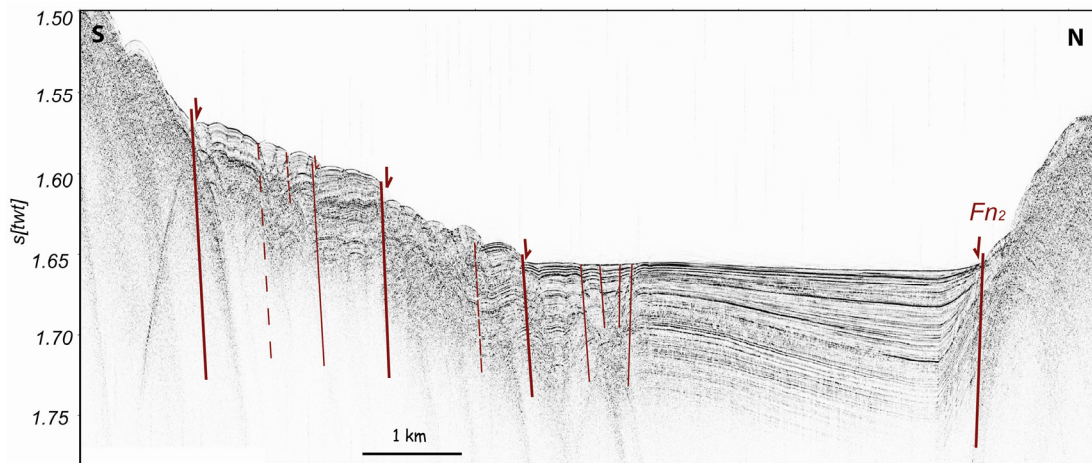


Figure 3.11 : Marmarascarp Line C14 resolves recent sedimentary pile down to 70 ms. The vertical exaggeration is ~ 20 , which helps to distinguish offsets of individual layers.

Correlation of the deep seismic lines of Carton et al. (2007) with the mapped faults from bathymetry illustrates an almost clear match of the structures (figure 3.13). Progressive thickening of the Plio-Quaternary depocenter eastward in the area where the NCF bends and the en echelon fault centered is quite notable in Figure 3.13.

The structural geometry and development of the Çınarcık basin does not fit exactly into the classical pull-apart models. Two strike-slip segments (i.e., the İzmit and Central Marmara segments) do not overlap, but are linked along the northwest margin of the basin by an oblique-normal fault, that is, by the Northern Çınarcık fault. The southern margin fault which bifurcates from the İzmit segment terminates in a manner similar to horse-tail splays in an array of en-echelon oblique normal faults. Seismic sections along the basin indicate that it is actively subsiding. It embraces a syn-kinematic sedimentary fill that thickens and dips northward towards the Northern Çınarcık fault. The vertical motion along the northern fault segment must be higher than the southern boundary fault, giving rise to the asymmetry of the basin. Therefore, the Çınarcık basin can be considered as a half graben. As shown above, deep seismic profiles reveal that the sedimentary fill is offset by normal faulting component both on its northern and southern margins.

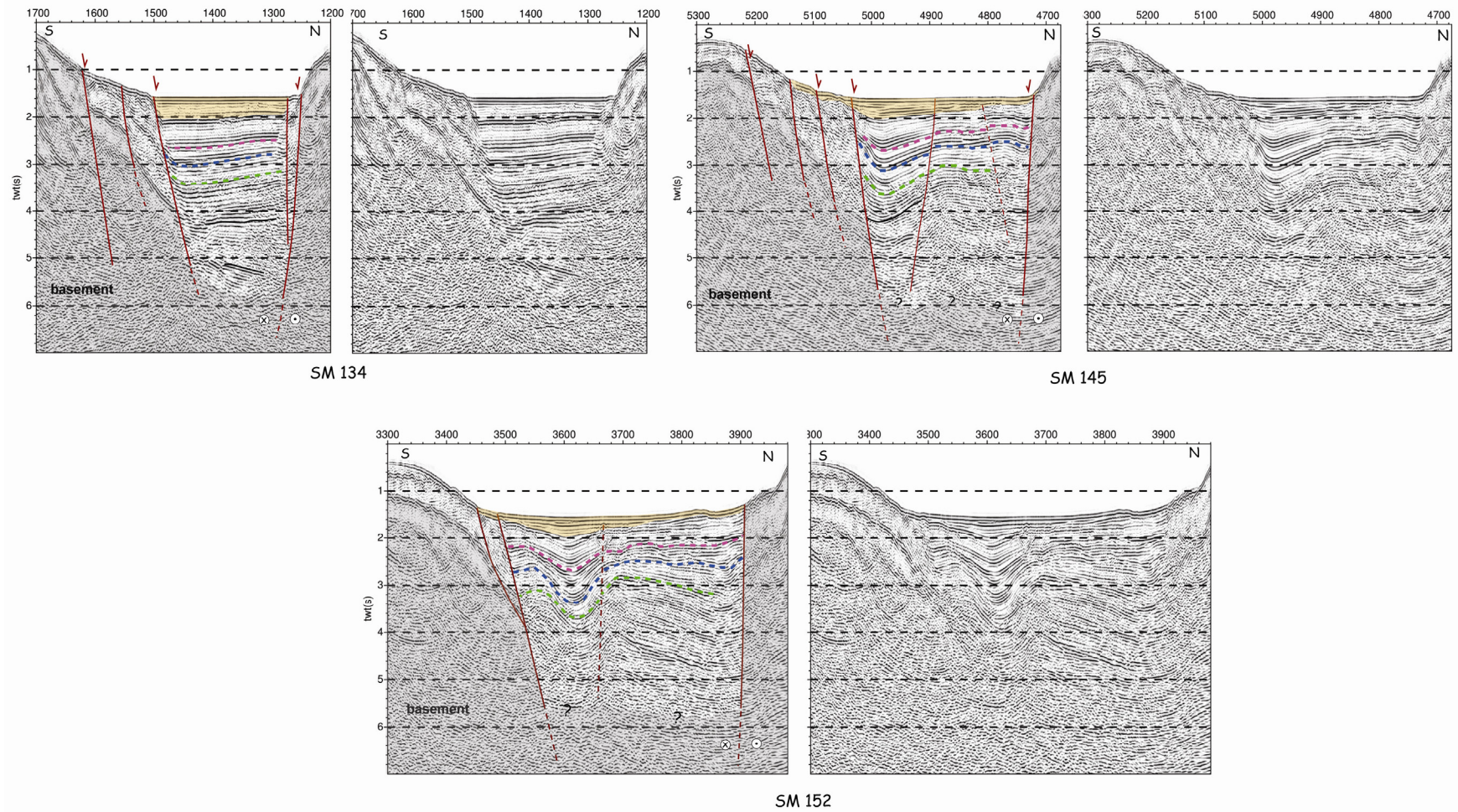


Figure 3.12 : Selected north-south migrated profiles (134, 145,152) of the SEISMARMARA cruise from the western half of the Çınarcık Basin. Seismic profiles are re-interpreted after Carton et al. (2007). Red lines indicate the faults and colored dashed lines are to distinguish significant reflectors. Plio-Quaternary sedimentary units are drawn in yellow.

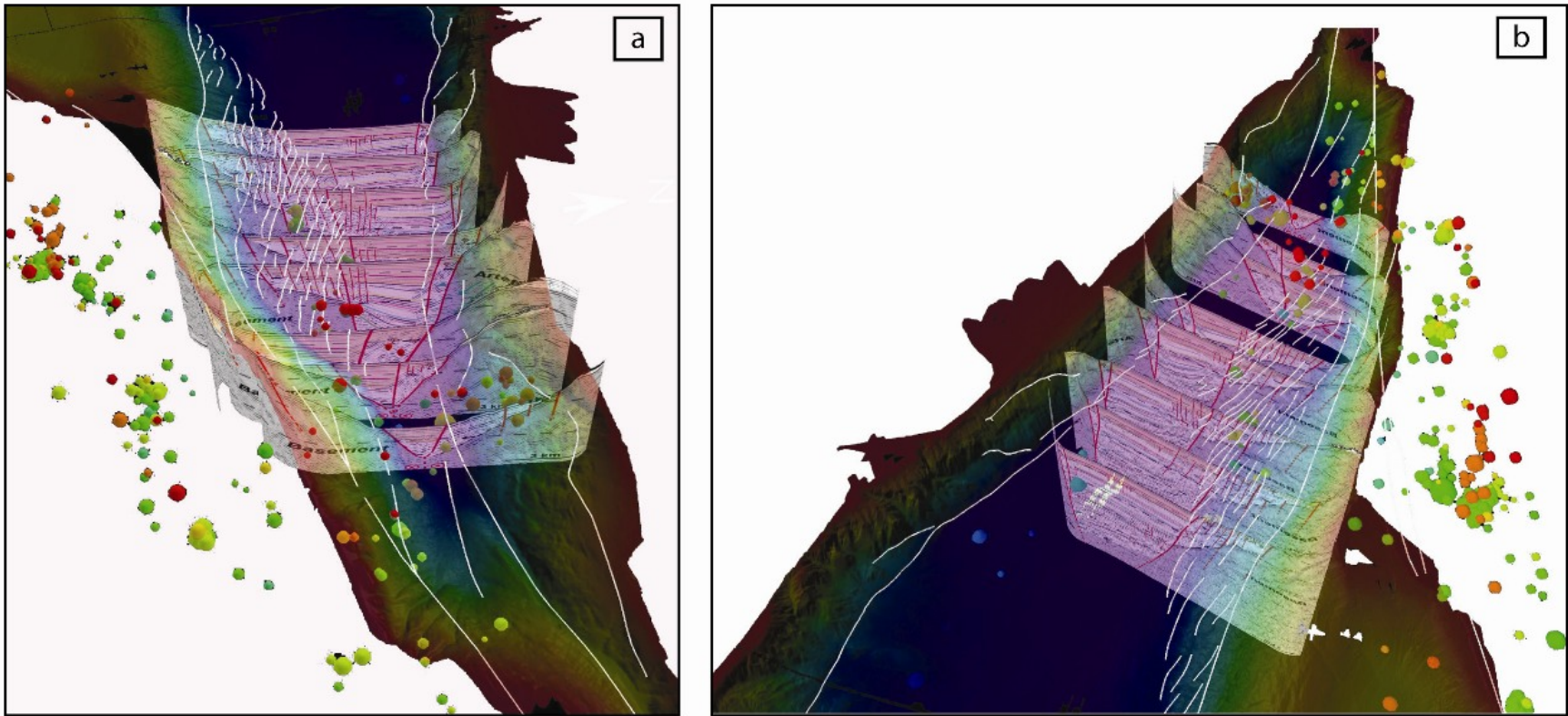


Figure 3.13 : 3D model of the Çınarcık basin merged with depth profiles from Carton et al. (2007) illustrates the match of mapped fault array with the faults at depth. Recent earthquakes from TUBITAK MAM network are also projected on both images.

As shown in Figure 3.12, in the eastern half of the basin, sedimentary depocenter with back tilted layers is located immediately in front of the Northern Çınarcık fault, indicating relatively more rapid subsidence along this fault (Figure 3.14b). However, towards the west the depocenter is shifted to the south along the Southern Çınarcık fault since the normal slip component along the Northern Çınarcık fault gets smaller towards this direction (Figure 3.12). Therefore, from east to west, the symmetry of the sedimentary basin changes with fanning direction changing from north to south. With the arrangement of the Southern and Northern Çınarcık and the İzmit faults that meet at a point west of Hersek, the Çınarcık basin appears to be a combination of fault-wedge and pull-apart basin (Figure 3.14a) very similar to the Hamner basin in New Zealand (Figure 3.14b) (Wood et al., 1994).

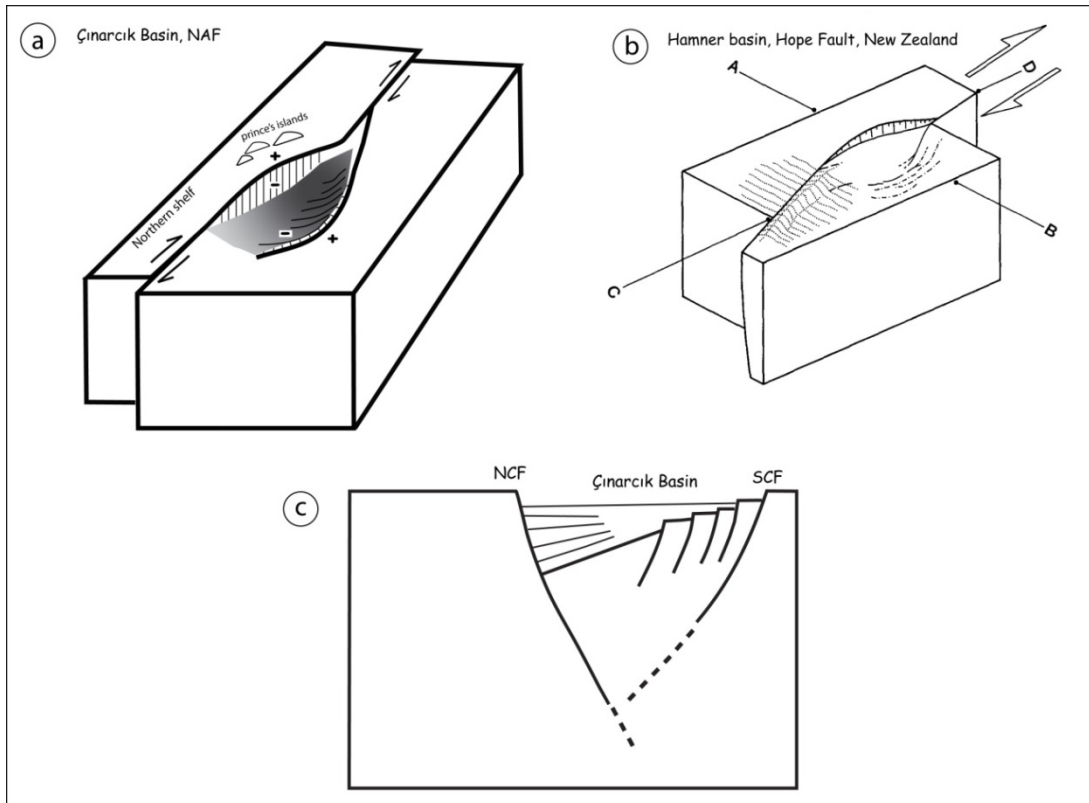


Figure 3.14 : Schematic block diagrams depicting the structures of the Çınarcık and Hamner basins that appear to be similar.

As discussed previously, the Northern Çınarcık fault runs oblique to the overall direction of the plate movement in eastern Marmara. Block modeling of GPS shows that this angle create significant dip-slip along the NCF. Oblique motion along tectonic boundaries is commonly partitioned into slip on faults with different senses

of motion. Partitioning can be explained by the upward elastoplastic propagation of oblique slip from a fault or shear zone at depth. The strain field ahead of the propagating fault separates into zones of predominantly normal, reverse, and strike-slip faulting (Bowman et al, 2003). In this context, it seems likely that the dip slip and strike slip are partitioned between the Fn1 and Fn2, respectively (Figure 3.8).

3.2.2 Tectonic and morphologic structure of the Central Basin

The Central basin is the second largest basin that aligns along the Northern Marmara fault system. In map view (multibeam bathymetry), it appears as a 16-km-wide structure consisting of two nested basins (Figure 3.16). Previous studies interpret this structure by different kinematic models. According to Armijo et al. (2002), the Central basin is a rhomb-shaped nested pull-apart structure comparable to rift-in-rift structures; whereas the single through-going fault model of Le Pichon et al. (2001) proposes a negative flower structure for the inner basin that evolves mainly by the clockwise rotation in the principle displacement zone. In the latter model, faults that bound the outer basin are neglected as they are assumed to be no longer active. However, as will be shown below, evidences from high-resolution seismic reflections and multibeam bathymetry suggest that these faults are still active.

Well-resolved seismic sections along the Central basin portray nested grabens that contain a thick sedimentary pile (> 6 km), suggesting that these faults are long-lived structures much older than the recent sediments (Figure 3.15). The northern and southernmost boundary faults seen in the deep seismic profile are the main faults that are responsible for the formation of the deep sedimentary trough (Figure 3.15). However, the inner graben nested inside the large basin must have evolved afterwards since the top most reflectors can be traced from the northern to the southern margin of the basin. Both the inner and outer faults of the Central basin carry normal components of slip and appear to splay, in map view, from linear right-lateral fault segments striking ENE-WSW located east and west of the Central basin (Figure 3.16).

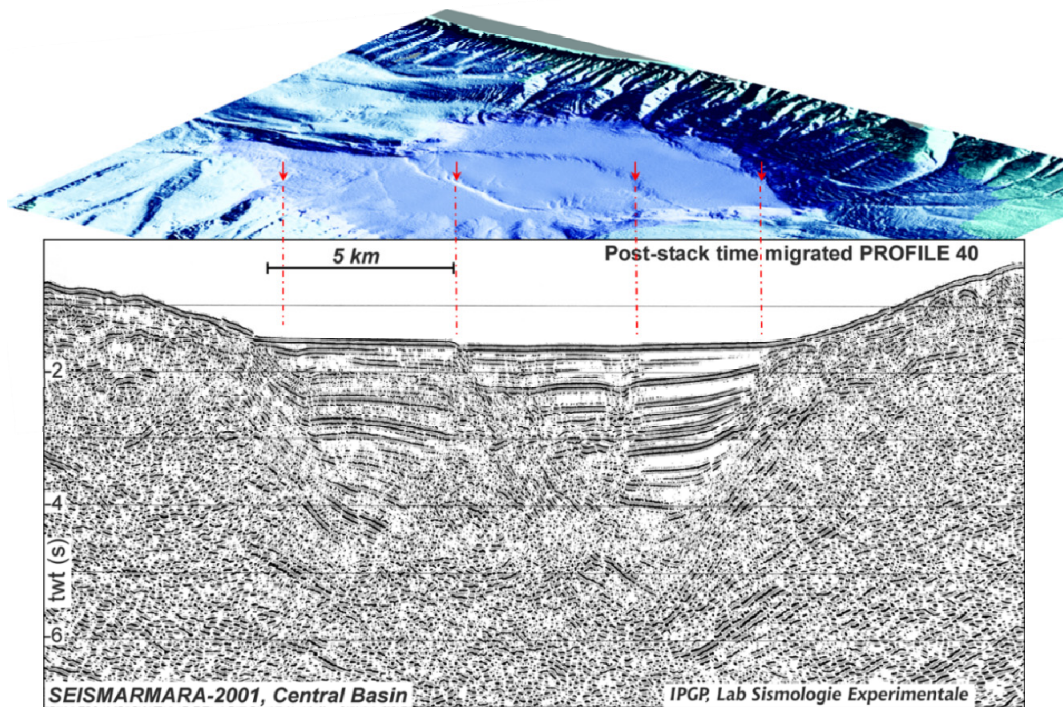


Figure 3.15 : Correlation of the 3D bathymetry map of the Central basin with the deep seismic reflection profile from SEISMARMARA cruise (Laigle et al., 2008) illustrates the structure of the basin at depth. It clearly demonstrates that what is seen on the basin floor from multibeam bathymetry penetrates see floor well below 5 km.

In the present day morphology, NW-SE striking faults mark the outer boundary of the Central basin at the base of a 1-km-high escarpment that appears eroded and drained by submarine valleys (Figure 3.17 and 3.19). These boundary faults embrace the flat floor of the Central Basin where sediments accumulate. They are oblique-extensional faults and present an arcuate trace in map view (Figure 3.16). At the northern edge, sharp young fault scarps with similar strike also run at the basin floor (Figure 3.17). They align in a left stepping en echelon arrangement and splay from the EW strike-slip segment that extends from the Eastern high. Their sharpness in the bathymetry suggests that they are most likely formed by active faults with composite normal and strike-slip faulting. This inference is supported by the shallow seismic profiles obtained with a 3.5 kHz sediment penetrator that illuminates and resolves with good accuracy the structure down to 70 ms (Figure 3.20).

The individual scarps strike NW-SE and display clear normal fault morphology across the most recent sediment (Figure 3.18). The topographic profile shown in Figure 3.18A resolves the morphology of an individual scarp with a throw of up to

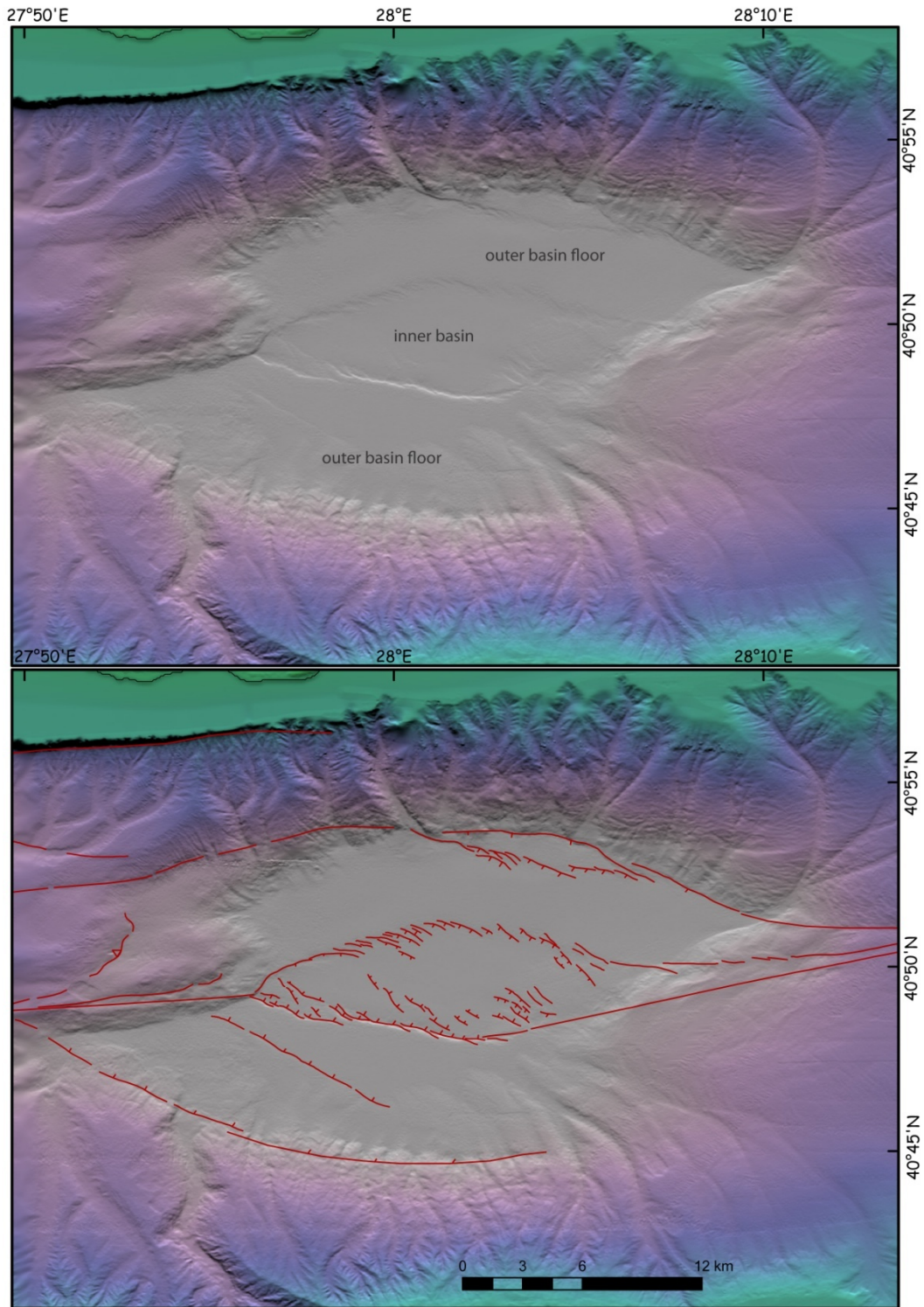


Figure 3.16 : Morphology of the Central basin revealed by shaded multibeam bathymetry with (b) and without (a) interpreted faults. The similar scarp morphology with vertical throws (~10 m) is readily seen in the Profile B (Figure 3.18).

40 m. Another set of NW-SE striking left-stepping en echelon faults bound the north of inner pull-apart basin.

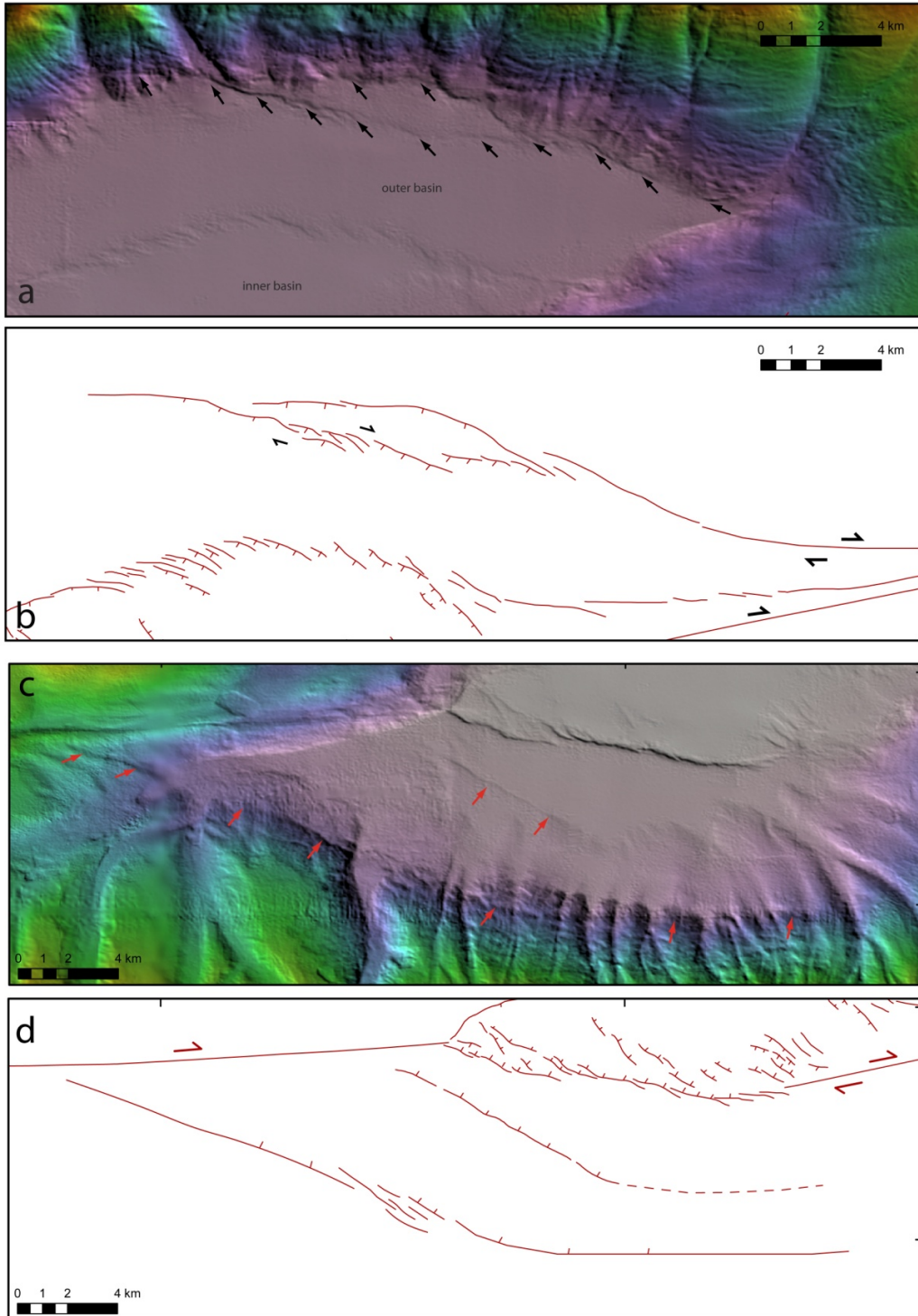


Figure 3.17 : (a) 2D bathymetry map of the northern section of the Central basin (illumination from north). Black arrows indicate the morphological trace of the fault breaks. (b) Active faults mapped from the bathymetry (c) 2D bathymetry map of the southern section of the Central basin (illumination from south). Red arrows highlights the morphologic traces of the faults (d) Active faults mapped from the bathymetry.

The southern oblique-extensional boundary fault has a relatively less pronounced trace on the bathymetry compared to the northern one. Nonetheless, the NW-SE striking boundary fault marks the base of the southern escarpment with a morphologic trace (Figure 3.19) and cuts the recent sediments as seen in the 3.5 kHz profiles (Figure 3.20). Many submarine canyons carve the slope and their related fans clearly exposed in the bathymetry.

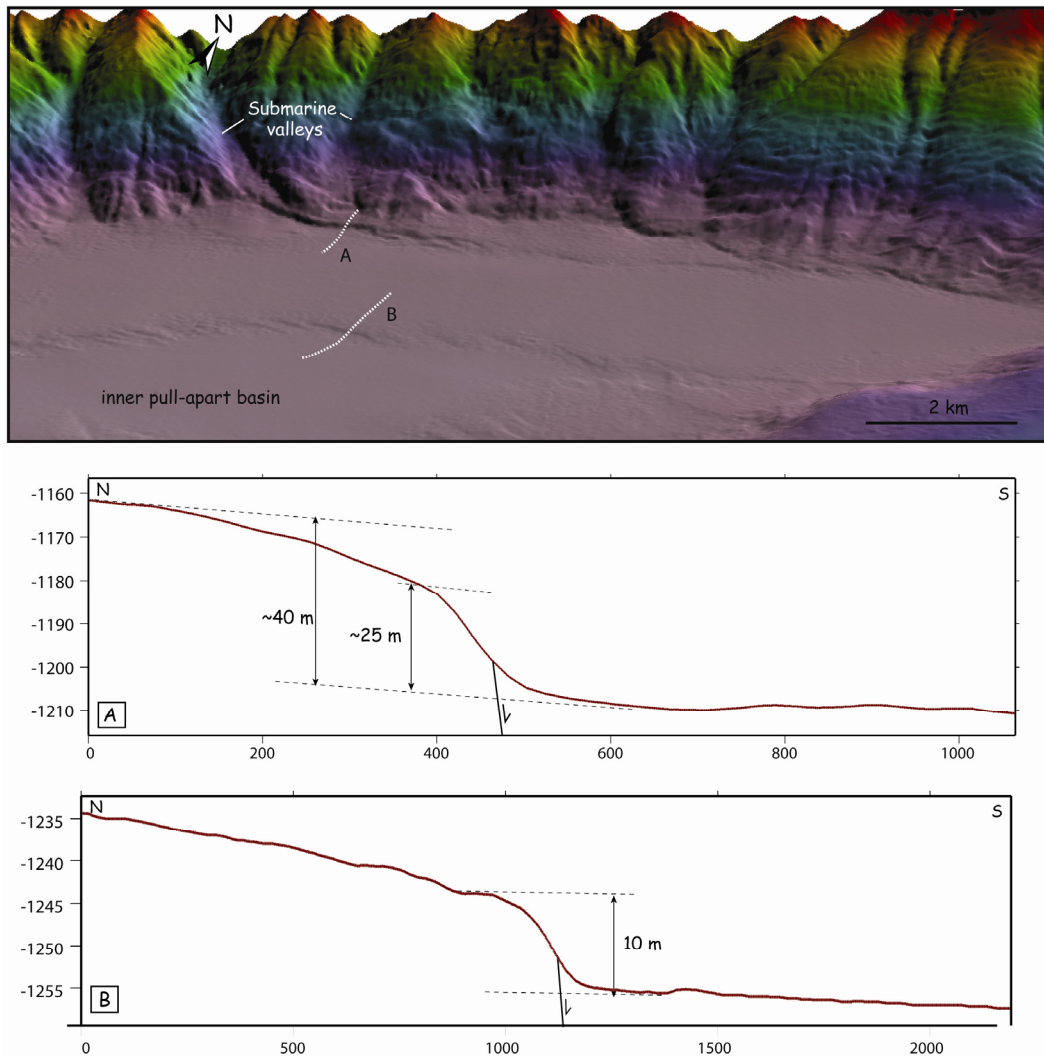


Figure 3.18 : 3D view of the northern edge of the Central basin (illumination from north). Profile A is taken from the sharp fault scarp that offset the outer basin floor and Profile B is taken from the northern edge of the inner pull-apart basin. Both fault scarps expose throws ranging from 10 to 40 m.

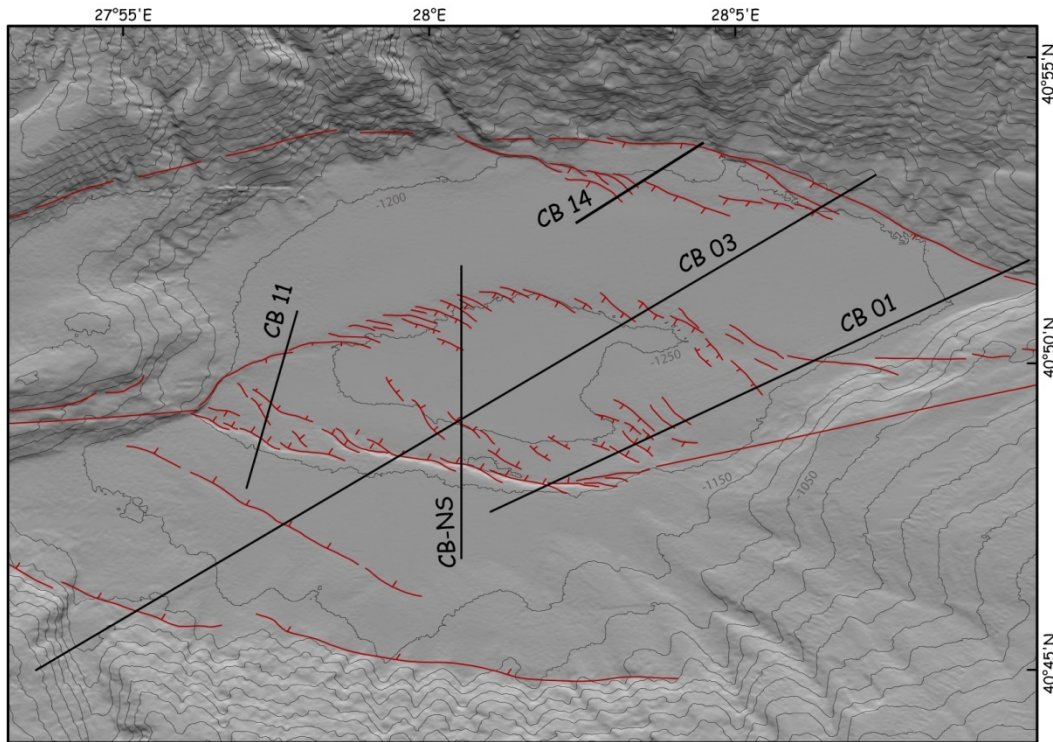


Figure 3.19 : Location of the selected 3.5 kHz seismic lines in the Central Basin.

In the middle of the Central Basin distinct en echelon fault scarps enclose a pull-apart basin with a characteristic rhomb-shape. The 5-km-wide inner pull-apart basin between two strike-slip segments (to the E and W) is bounded (to the NE and SW) by sharp normal fault scarps that offset the flat bottom of the basin. Between these two segments, the extensional step-over is about 4 km. The nested graben structure that characterizes the geometry of the subsiding Central Basin in cross section is well portrayed in the seismic profiles (Figure 3.20 and 3.21).

The fault scarps across the bottom strike mostly NW-SE and are formed by series of smaller (1-3 km long) left-stepping, en echelon segments, which attest to the nonetheless dominant, right-lateral motion across the overall fault zone. The individual scarps trend NW-SE and display clear normal fault morphology across the most recent sediments. They are on average 1-2 km long and the flat floor of the pull-apart is 20-60 m deeper than the surrounding sea floor. The cross section in Figure 3.22 illustrates the structure of the inner pull-apart; the lower inner floor appears flanked by the inner boundary faults and across them, by somewhat higher, flat shoulders.

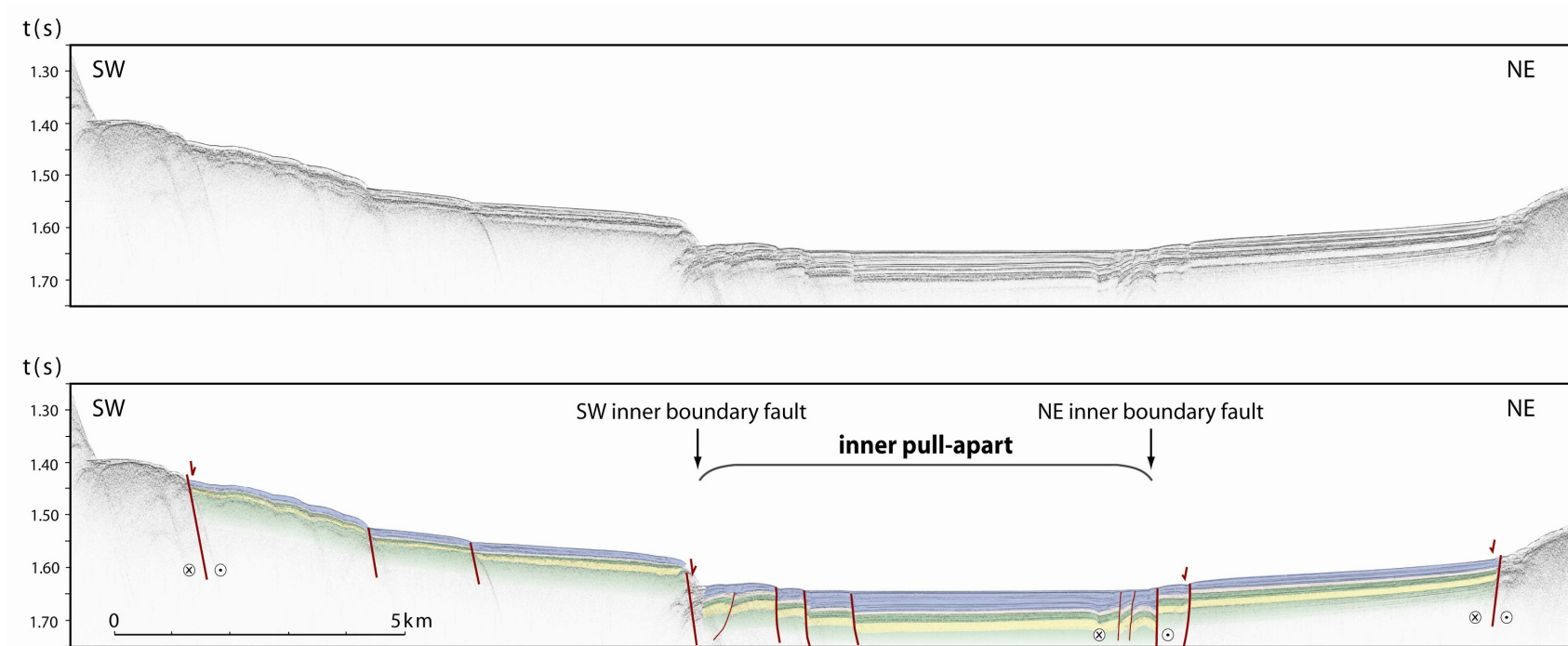


Figure 3.20 : The 3.5 kHz profile (vertical exaggeration is 10) across the Central Basin. Sedimentary pile as defined by the high-resolution 3.5 kHz profile (upper two panels; data without and with interpretation). Faults with normal slip at edges of inner pull-apart are readily seen.

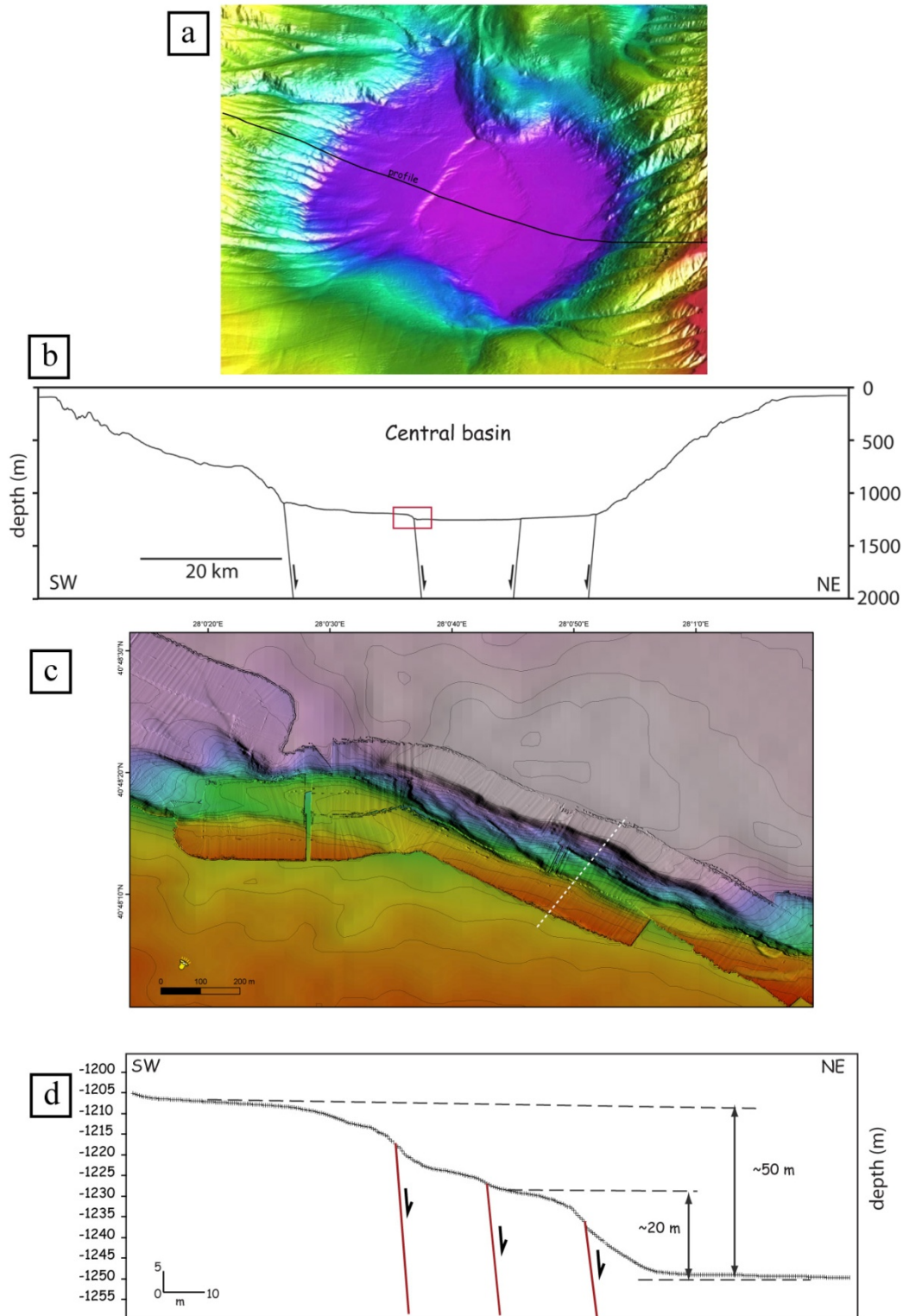


Figure 3.21 : Thousands meter scale topographic evolution of the (a) Central basin. (b) Large scale bathymetric profile across the Central basin depicting the nested graben morphology (c) Microbathymetry extract of the southern edge of the inner pull-apart (red box in Figure 3.21b. (white line indicates the profile location below) d) Microbathymetry profile resolves details of the morphology.

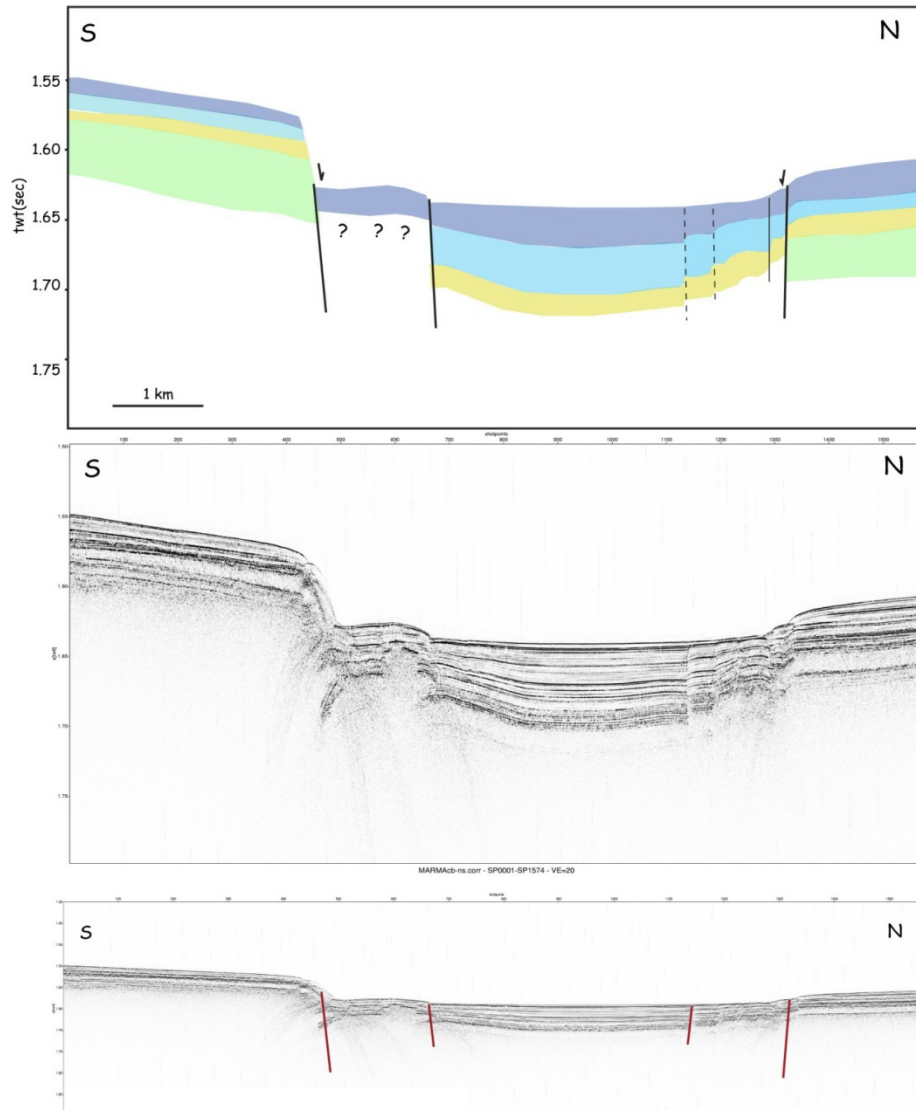


Figure 3.22 : N-S 3.5 kHz profile along the Central basin that transects the inner pull-apart. Top panel illustrates the sedimentary horizons deduced from the chirp line. Subsidence of the inner basin is readily seen. Bottom panels are the chirp line with vertical exaggeration 20 and 10, respectively.

The subsidence of the inner floor and the sediment distribution are both controlled by continuing activity of the inner boundary faults. The differences in sediment thickness in the floor of the Central Basin are related to the vertical motion on these faults (Figure 3.22). Cumulative fault scarps has formed at the SW boundary fault of the inner pull-apart with free faces seen in the ultra-high resolution bathymetry. Smaller-scale, sharp, steep scarps lacerate the larger cumulative (~50 m) scarps (Figure 3.21). The small-scale scarps cut obliquely across the slopes of the cumulative scarps, with a finer en echelon branching structure. This en echelon

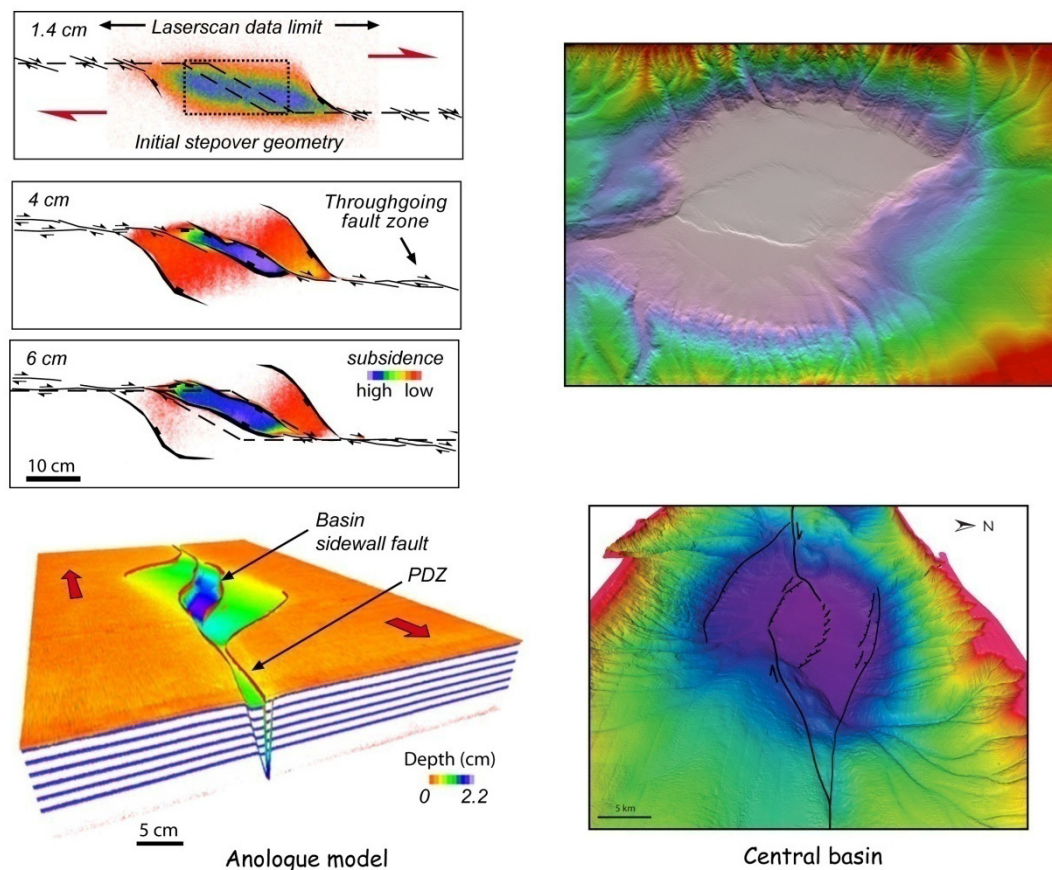


Figure 3.23 : Comparison of the Central basin (right) with an analogue model (left panel) obtained by Wu et al., (2009). Note the similarities in the nested basins.

arrangement of the SW inner boundary fault forms the terraced sidewalls of the inner basin, consistent with the basins that form in the analogue pull-apart models.

A recent analogue modeling by Wu et al., (2009) nicely illustrates that nested basins can develop in step over zones (Figure 3.23). As shown in Figure 3.23, one of their models with the outer and inner faults resembles very much the Central basin. Wu et al., (2009) define this structure as a pull-apart within a negative flower structure. Therefore, the Central basin can be considered both as pull-apart and negative flower. These two terms describe geometrically and mechanically similar structures. What comes first before the usage of correct terminology is to fully understand kinematics of the faults that bound and affect the Central or other basins in Marmara. Whether or not the Central basin is a textbook example of a pull-apart (Armijo et al., 2002) or a negative flower (Le Pichon et al., 2001), what cannot be denied is the fact that it is still experiencing rapid oblique extension.

3.2.3 Tectonic and morphologic structure of the Tekirdağ Basin

The 1120-m-deep Tekirdağ Basin is a rhomb shaped depression bounded by two topographic highs to the east and west (Western High, -550 m, Ganos Mountain, 924 m, respectively). In Tekirdağ basin, NAF forms a restraining bend between the N74E Ganos fault on land and the Tekirdağ segment which borders southern edge of the basin (Figure 3.24). Since the NAF has propagated westward across the Ganos-Dardanelles region, a series of folds involving Neogene sediments have formed successively at the Ganos bend, then transported southwestward along side the NAF (Ganos fault) by its continuing right-lateral motion (Armijo et al., 1999; 2002). Hence, the bend appears to be a long-lived structure. The Tekirdağ basin and the bend are critical complexities of the Ganos fault. The main strike-slip segment (Tekirdağ segment) bounds the basin to the south (Figure 3.24). The fault system at the southern edge has a large component of normal slip over the long term, as determined previously in the seismic sections (Parke et al 2002; Okay et al., 1999). This is a steep north-side-down fault, which slips obliquely with dip-slip component (Figure 3.25). The normal faulting appears as the main mechanism responsible for the Tekirdağ basin (Figure 3.25b), much like the other two deep basins in the Marmara Sea (i.e., Çınarcık and Central Basins).

The Tekirdağ basin appears as an oblique half graben structure filled with sediments tilted southwards to the fault (Figure 3.25a). Progressive tilting of syn-tectonic sediments implicates the NAF as the primary structure responsible for the Tekirdağ Basin (Figure 3.25b). The overall geometry of the Tekirdağ Basin is highly asymmetric, but also remarkably consistent through the sedimentary sequence, suggesting a uniform pattern of growth (Seeber et al., 2004). Seismic reflection profile MTA 05 (Parke et al. 2003) indicates clearly a steep dip in the upper reach of the fault. The fastest subsidence is along the Tekirdağ segment, which is the northern branch of the NAF (Figure 3.25b). The current turbiditic floor of the basin is nearly horizontal. Older turbiditic layers are progressively tilted toward the southwest, obliquely to the border fault.

Antithetic normal faults cross the basin floor in the northern side of the Tekirdağ basin. These faults are 1-3 km long and extend in a left stepping en echelon arrangement with their south side down. They create relatively minor vertical offsets

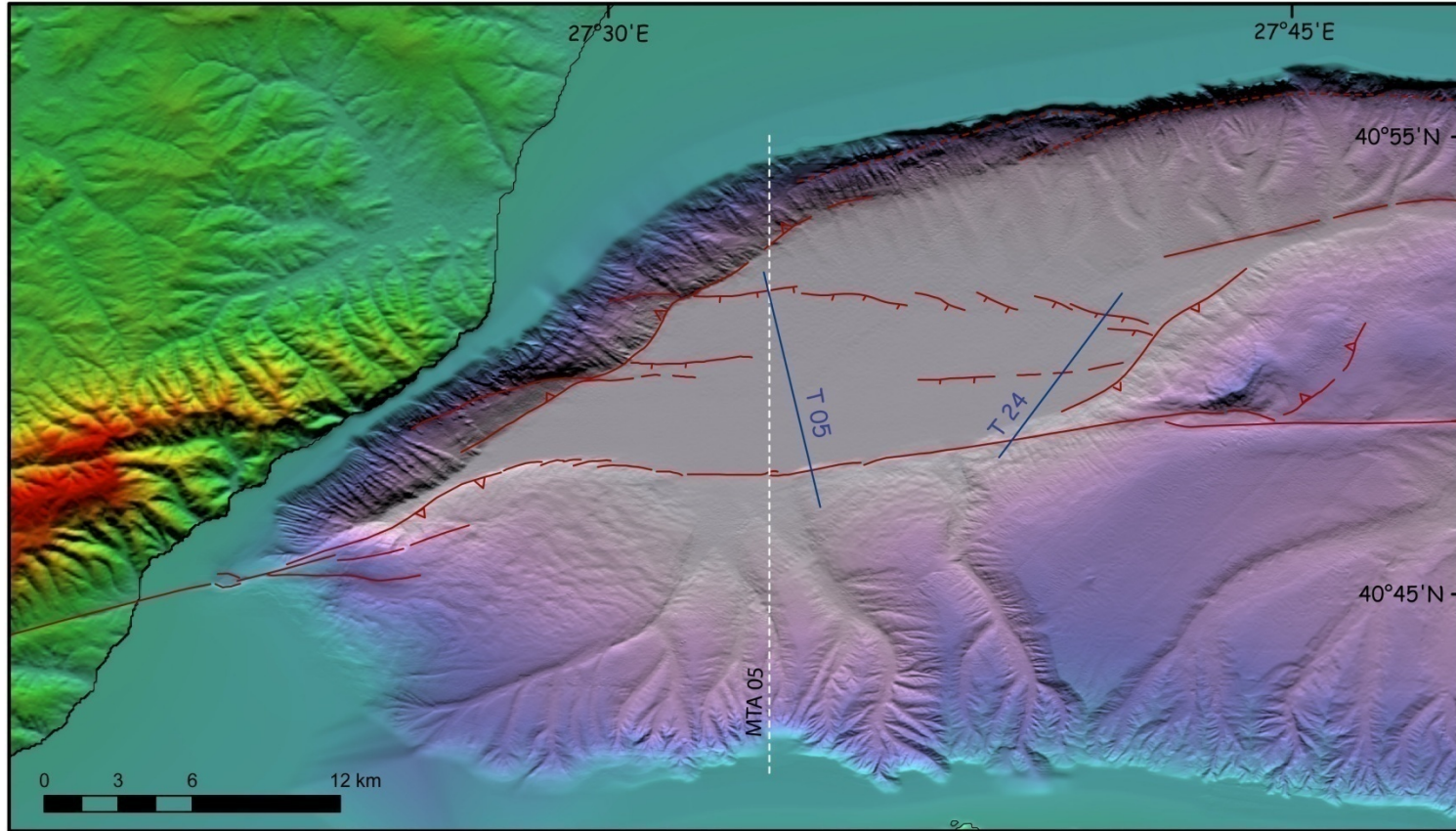


Figure 3.24 : Shaded relief map of the Tekirdag basin combining multibeam bathymetry (25 m gridding) and SRTM 90 m onland. Red lines represent active faults determined from bathymetry and shallow seismic reflections. Those with uncertain recent activity are depicted with dashed redlines. Seismic-reflection profile MTA 05 (collected in the Sea of Marmara in September 1997 by MTA) is located with white dashed line.

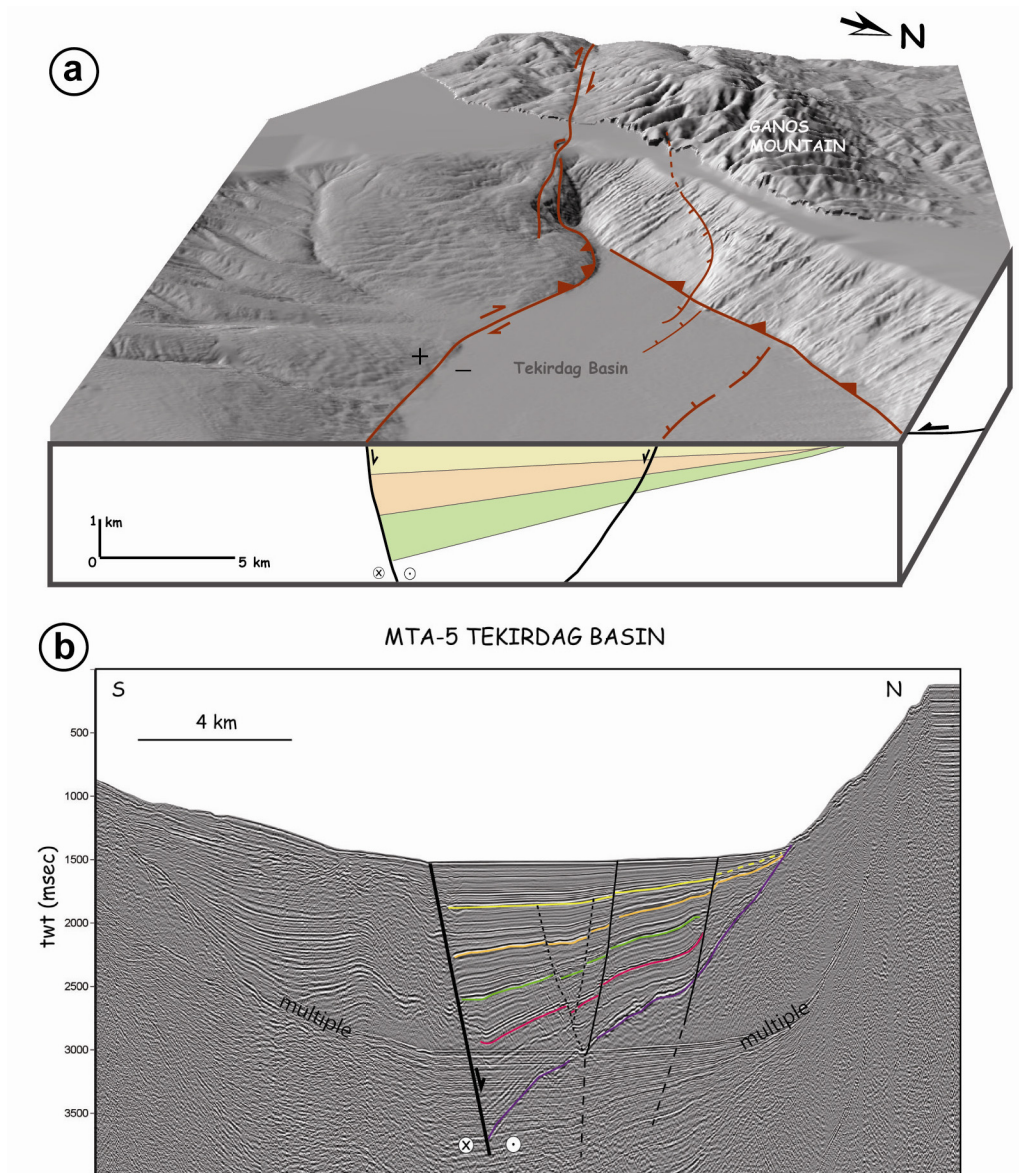


Figure 3.25 : (a) Perspective view looking southwest of the western end of the Tekirdag Basin with combined onland topography and multibeam bathymetry. Schematic interpretation is based on profile in the lower panel and the map in Figure 3.24. (b) seismic-reflection profile MTA 05 is from Parke et al, 2003, and re-interpreted in this study. Profile reflects the basin asymmetry. The fastest subsidence is along the border fault, which is the northern branch of the NAF. Lines with colors indicate certain reflectors to illustrate the difference in layer thickness.

in the syn-kinematic sedimentary deposits. These en echelon faults are best observed in the 3.5 kHz chirp profiles (Figure 3.26).

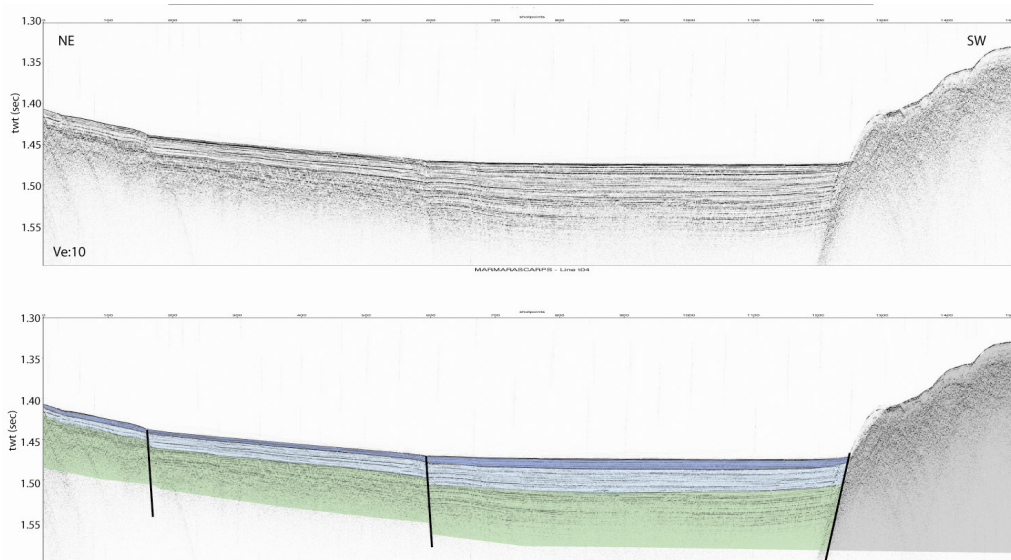


Figure 3.26 : Chirp profile T04 from MARMARASCARPS (vertical exg. 10). Lower panel with Late Pleistocene-Holocene sediment layers. Note the minor vertical displacements on the antithetic faults in the NE part. Sediments are progressively thicker towards the border fault SW.

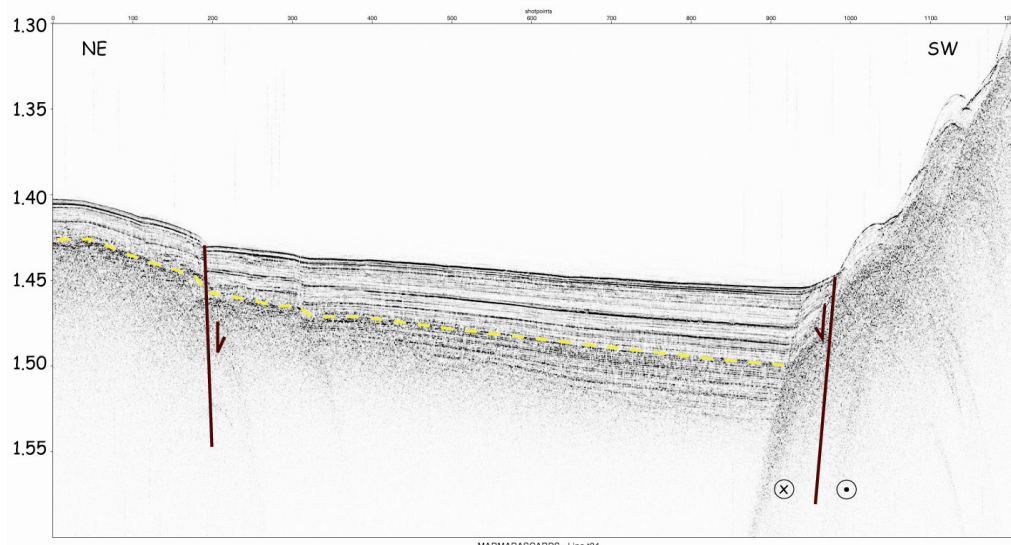


Figure 3.27 : Chirp profile T24 from the eastern part of the Tekirdag basin.

3.3 Late Pleistocene-Holocene subsidence and faulting rates in the Sea of Marmara

Northern branch of the North Anatolian fault system – with a set of recent high-magnitude earthquakes (Barka, 1996; Stein et al, 1997; Hubert-Ferrari et al, 2000; etc.) - is crossing the deep northern part of the Sea of Marmara.

The new geomorphologic and geologic evidence allows an accurate description of active submarine faults in the Sea of Marmara. Furthermore, ultra high-resolution microbathymetry data (50x50 cm spatial resolution) reveals set of fresh fault scarps associated with recent earthquakes. The origin of the submarine scarps under the context of competing tectonic, climatic and sedimentary processes is an interesting problem to understand. The answers of this problem are very much related with the major climatic and tectonic changes that affect the stratigraphic environments in the Sea of Marmara.

Sea-level oscillations during late Quaternary time (Chappell and Shackleton, 1986) were a major control on the paleogeography and stratigraphy of the Sea of Marmara. During the last glacial, when the global sea-level dropped below Dardanelles Sill (i.e., -85 m), the Marmara Sea was isolated from both the Black Sea and the Aegean becoming a fresh-brackish lacustrine environment during the Late Pleistocene (Stanley and Blanpied, 1980; Ryan et al., 1997, 2003; Aksu et al., 1999, 2002; Çagatay et al., 1999, 2000). This stage is followed by a sharp marine transgression (Çagatay et al., 2000; Polonia et al., 2004; Mercier de Lépinay et al., 2003). A record of the basin's reconnection to the global ocean is preserved in its sediments permitting the extraction of the paleoceanographic and paleoclimatic history of the region.

To characterize the stratigraphic environment and the sedimentary evolution of the deep Marmara basins, an extensive survey totaling 600 km of profiles with a 3.5 kHz sediment penetrator across the main deep basins (i.e., Tekirdağ, Central and Çınarcık basins) was undertaken during the MARMARASCARPS mission of 2002. The 3.5 kHz chirp profiles illuminate and resolve with good accuracy the structure down to 70 ms and hence, allowing to image the Late Pleistocene-Holocene sedimentary fill in the Marmara basins. The results from long sediment cores (35 m long) and calibrated ¹⁴C ages of wood fragments from cruise MARMACORE (performed in 2001) help us to construct the evolution of the morphology and the shallow sub-bottom stratigraphy during the last Glacial-Interglacial transition from lake to marine conditions in Marmara.

3.3.1 Relation between stratigraphy, climate change, and sedimentation rates in the Sea of Marmara

The main highland (made up of metamorphic and igneous units), representing potential terrigenous sources, are located on the southern side of the Sea of Marmara. The northern border has a lower relief and narrow drainage area, comprising Tertiary sediments and volcanic rocks. This situation is responsible for higher terrigenous input on the southern shelf (Ergin et al., 1991, 1999). The drainage pattern issued from the southern main relieves converge towards tributaries of the Sea of Marmara, while, north of it, the main drainage system flows westwards into the Aegean, avoiding significant input on the northern shelf.

As connecting the eastern Mediterranean (Aegean Sea) and the Black Sea through two shallow sills (Dardanelles and Bosphorus), the Sea of Marmara underwent the consequences of the last glacio-eustatic cycle (Ryan et al, 1997; Aksu et al, 1999; Çağatay et al, 2000, 2003; etc) and recorded the associated 120 m sea-level rise. Recent paleoenvironmental studies through coring and seismic imagery have been dedicated, by different teams, to the analysis of the Black Sea/Sea of Marmara connections and especially the last one considered as a major environmental change (Ryan et al, 1997). The last environmental modifications have been investigated through short gravity cores either in deep basins or shallow shelves positions (Çağatay et al, 2000, 2003); the lacustrine to marine change is considered to occur around 12 uncal. kyr BP as a sharp transgression base in shallow marginal sites, and more progressively in deep situations.

Following the sea-level fall during the late glacial period, river incisions took place on the continental shelf areas and carved their beds (increasing the sedimentation rate) forming the submarine valleys after the transgression. Sea level fall also activated submarine canyons thereby allowing large rivers to deposit their particulate load, via gravity flows, directly into the deep basins. Erosional unconformities developed across the entire shelf in connection with each regression culminating with a lacustrine lowstand. Flooding surfaces formed after each marine invasion and during the subsequent transgressions (Çağatay et al., 2009). These transgressions were relatively fast, because they coincide with the glacial terminations (Smith et al., 1995). The oscillation between sea and lake, modulated by global eustatic sea level,

has resulted in thick deposits of the marine sediments in seaward thickening wedges on the shelf.

Debris flows and turbidity currents are the main mechanisms of transport from the continental slope into the deep sea; these processes can be triggered by external forcing (e.g., an earthquake) or by the slope reaching a critical state as a result of ongoing deposition (Figure 3.28). In a tectonically active deep basin, such as the Sea of Marmara, turbidites related to earthquakes are expected to be common (Piper et al. 1988; Gorsline et al. 2000; Nakajima and Kanai 2000; Shiki et al. 2000; Sarı and Çağatay, 2006; McHugh et al., 2006). Basin margins in tectonically active areas typically contain turbidites that have been deposited from turbidity currents generated by seismic events (Nakajima and Kanai 2000; Shiki et al. 2000). Hence, the deep Marmara basins are bounded by steep margins that are controlled by the very active segments of the NAF.

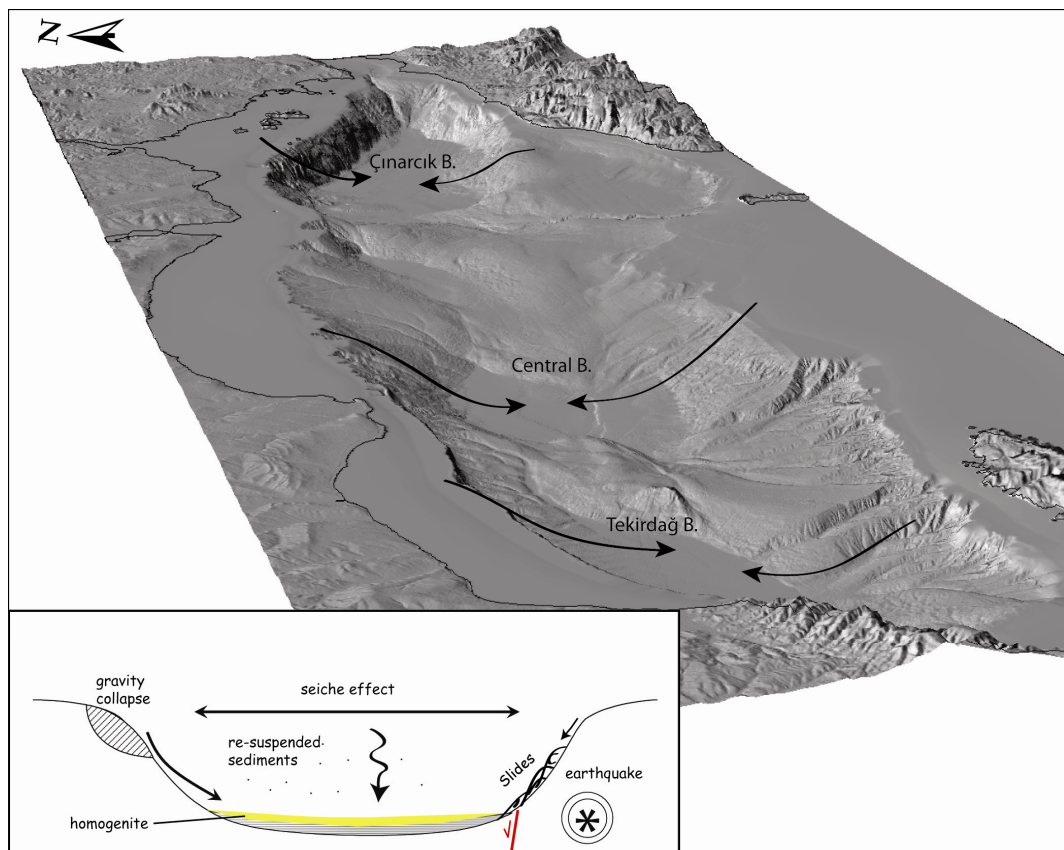


Figure 3.28 : Sediment transport in to the deep basins of the Marmara Sea from the shelves.

Historical seismicity of the Marmara Sea indicates that many destructive earthquakes ($M > 7$) occurred in the last 2000 years with relatively short recurrence intervals. As a

matter of fact, earthquake induced turbidites must be an effective component of sedimentation the Marmara Sea basins. The general configuration of the Sea of Marmara's sedimentary fill, as imaged by seismic reflection (Okay et al., 2000; Rangin et al., 2001; Le Pichon et al., 2001; Imren et al., 2001; Carton, 2003; Hirn et al., 2003; Demirbağ et al., 2003), clearly indicates a complete, long term, tectonic control on the sedimentary fill.

3.3.2 The 3.5 kHz chirp data and the correlation of ^{14}C dated cores

During the MARMACORE cruise (2001), 9 giant piston coring of ~35 m were collected to investigate especially the last 20 kyr of their sedimentary fill (non-marine before 12 kyr BP) and analyzed sections are correlated with 3.5 kHz chirp profiles collected during the MARMARASCARPS cruise (2002) (Figure 3.29). Most of these cores intersect the sedimentary markers of the lacustrine to marine transition. Analyzed sections of the cores (e.g., Beck et al., 2007) are basically composed of fine-grained terrigenous material with interlayered, sharply different sequences. The upper, marine, parts of the eight cores are almost entirely composed of faintly-layered clayey-silty, slightly calcareous mud (Beck et al., 2007). The background sedimentation is slightly variable with a high siliciclastic (clay–silt) and calcareous fraction, and is interrupted by only a few coarse turbiditic layers. These coarse turbiditic layers are correlated with a few high amplitude reflectors. Other reflections have variable amplitude and variable frequency (Figure 3.30).

In the lower part (lacustrine), the background sedimentation is finer-grained and with a more constant composition (siliciclastic with less biogenic material). This “hemipelagic-type” sediment often appears as clear thin intervals between numerous coarse turbiditic layers (Beck et al., 2007). Because they are intercalated within more constant background sediment, they produce constant amplitude and high frequency reflections (Figure 3.30). Thus, the separation of the upper marine period of sedimentation from the lower lacustrine (hemipelagic-type) can also be traced on the high-resolution seismic imagery.

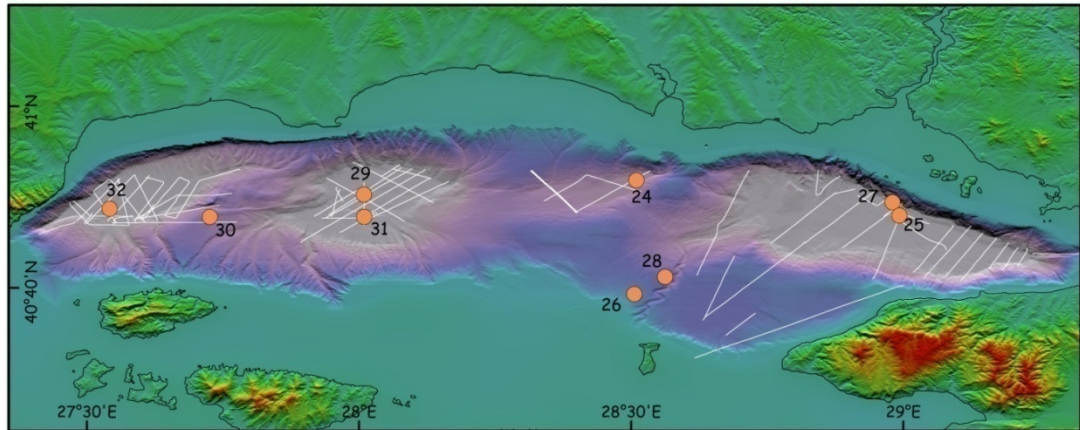


Figure 3.29 : Bathymetry map of the Marmara Sea locating long cores (orange circles, MARMACORE cruise) and high-resolution mud-penetrator 3-5kHz profiles (white lines, MARMARASCARPS cruise) used to constrain recent sedimentation and faulting in the basins (Tekirdag, Central, Cinarcik from west to east). The profiles presented are a selection of all profiles.

Turbiditic sequences are common in the deepest cores (MD 24, MD 25, MD 27, MD 29, MD 30) except for the Tekirdag Basin (Beck et al., 2007). They are almost entirely intercalated within the lower, lacustrine, part of the analyzed successions ranging from centimeter to decimeter thickness. Most of the cores appear to represent the Holocene and part of the Late Pleistocene. A.M.S. C14 analyses were performed on ten plant/wood or charcoal fragments. The youngest age constraint achieved from the lacustrine part is ~14 ka (Figure 3.30), which is in agreement with the lacustrine-to-marine transition age proposed by various authors around 12 uncal. kyr BP (Çağatay et al., 2000; Tolun et al., 2002; Çağatay et al., 2003).

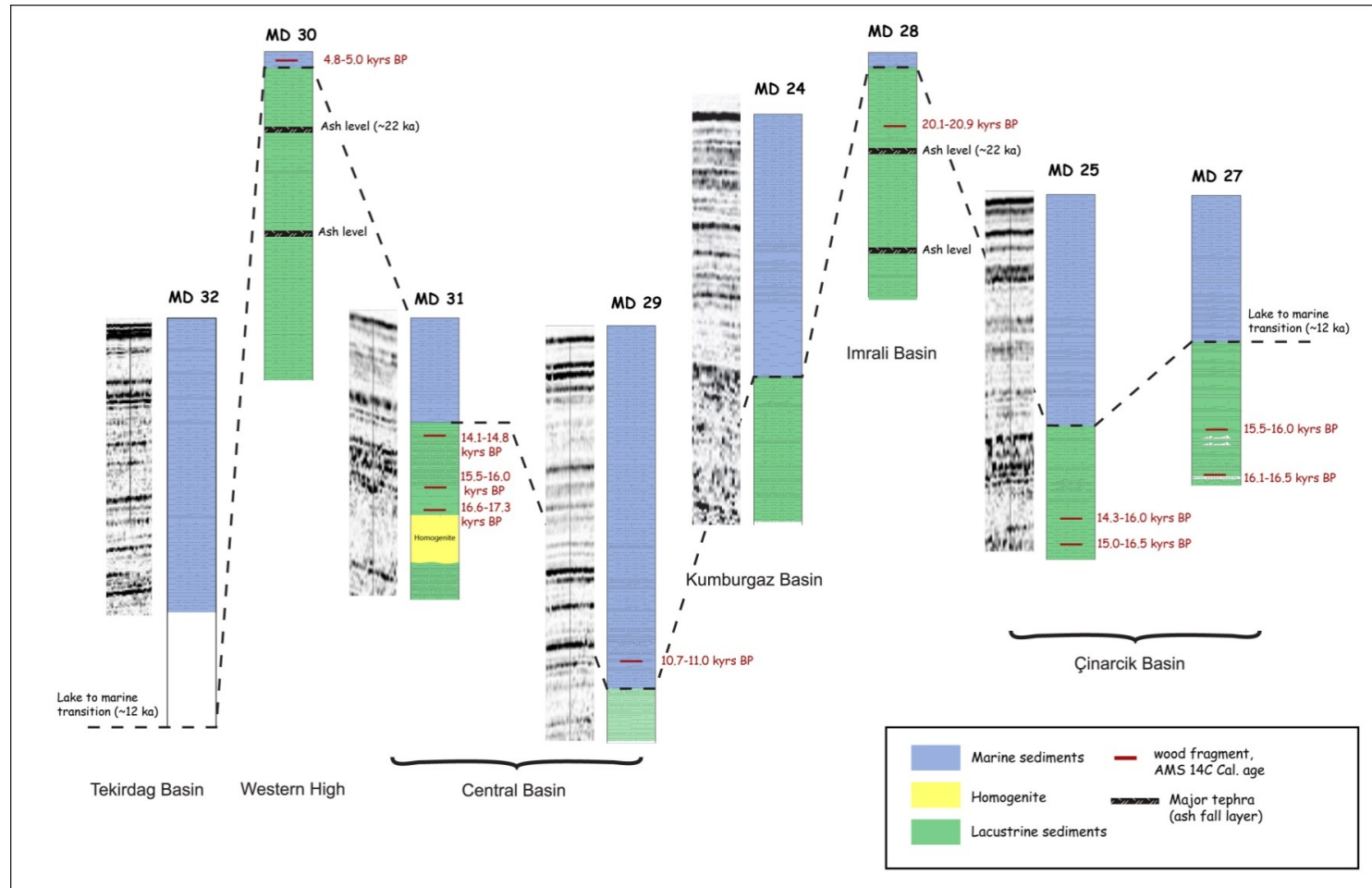


Figure 3.30 : Synthetic core logs and correlations. The sediment description is indicated with ^{14}C calibrated age constraints (dated charcoal fragments, in ka and 95% confidence interval with OXCAL, ref). Comparison with adjacent echo sounding profiles, when available, is given. The dashed line denotes the transition from lacustrine to marine (blue overlay) sediments. The reference level encountered at the base of the sedimentary pile in the Central basin dates from 15.8 ka.

3.3.3 Tectonic and stratigraphic implications on Late Pleistocene-Holocene subsidence and faulting rates

Active turbiditic surfaces in the Sea of Marmara basins are sharply bounded from the much steeper basin flanks, which typically receive only hemipelagic sediments. Turbidites are often bright reflectors and thus convenient markers of differential vertical deformation. Detailed observations from the chirp lines, allowed deciphering the marine upper part from the lacustrine lower sediments. The significant amplitude and high frequency reflections of the lacustrine sediments can be well imaged in most of the chirp profiles, hence providing detailed mapping of the lake-marine transition in the Sea of Marmara. Attitude of the uppermost sedimentary pile is well imaged down to 85 m (100 m.s.) depth. The vertical exaggeration of about 20 allows distinguishing offsets of individual layers. The adjacent MD cores have been projected onto profiles in order to correlate analyzed core sections with the reflections in the profiles. Hence, we achieve a good match in terms of mapping the lake-to-marine transition in the Sea of Marmara basins. Thus, an isopach map of the lacustrine-marine transition is constructed from 3-5kHz mud-penetrator profiles for the Marmara Sea basins (Figure 3.31). The map illustrates the thickness of lacustrine-marine transition, which also indicates the thickness of Holocene deposits. Analysis of the chirp profiles shows that Late Pleistocene-Holocene (LPH) sedimentary fill is strongly affected by the tectonic activity along the submerged NAF segments. The isocontours in the map (Figure 3.31) illustrate the depocenter of the Holocene sediments in the three deep basins coinciding significantly with zones where subsidence due to normal faulting prevails.

In Çınarcık basin, the depocenter is located at eastern part where NAF makes a sharp 30° transtensional bend. Here the basin is also bordered to the south by a dense network en echelon normal faults contributing to overall subsidence. The main fault that delimits the northern margin of the Çınarcık basin carries important amount of normal faulting component as inferred from the deep seismic sections. The chirp line C14 in Çınarcık basin, confirms the vertical deformation in the LPH sedimentary towards the main south facing fault scarp (Fn₂) at the base of the Çınarcık escarpment. At the southern part of the basin, vertical offsets are distinguishable in

Isopach Map of the Lacustrine/Marine Transition Horizon

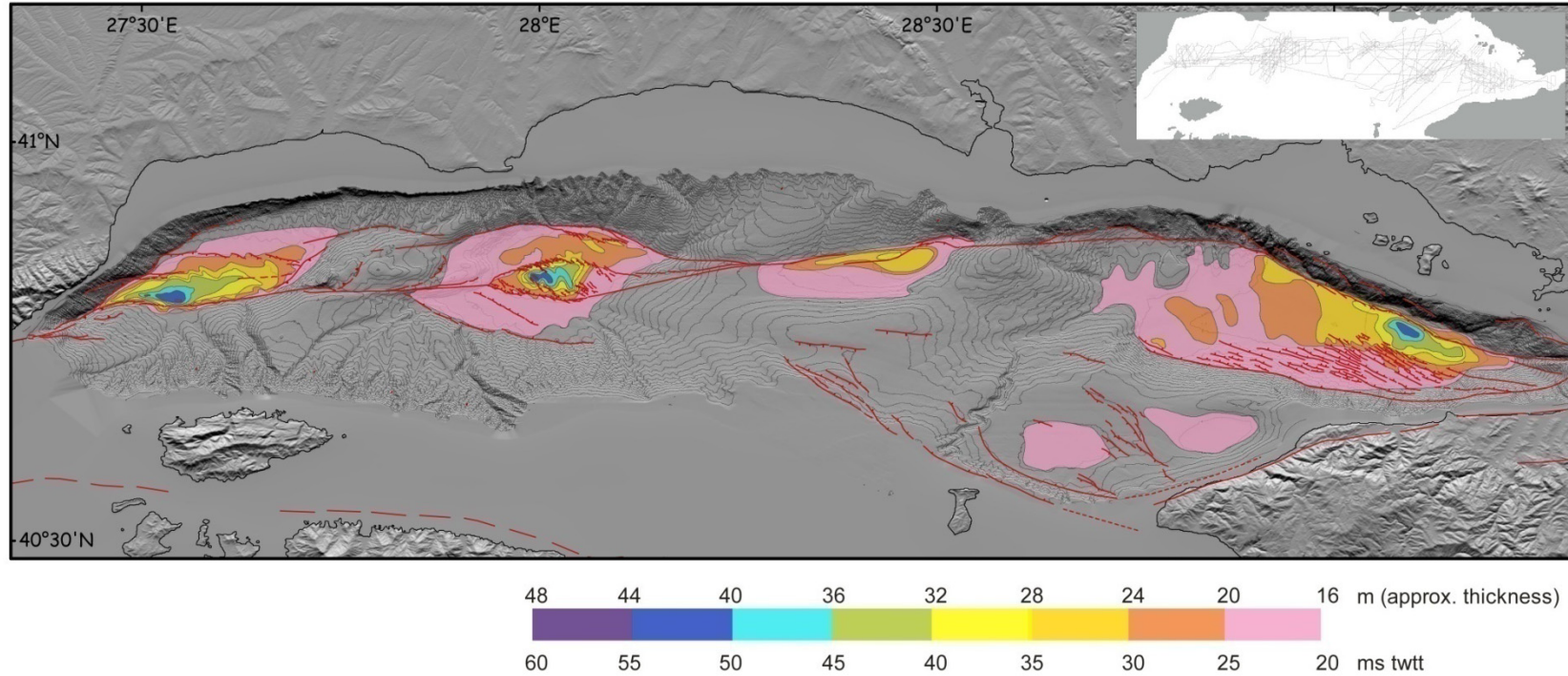


Figure 3.31 : Isopach map of Holocene deposits in the Marmara basin constructed from 3.5 kHz chirp profiles. Inset shows all the chirp lines collected during the Marmarascarp survey (2002).

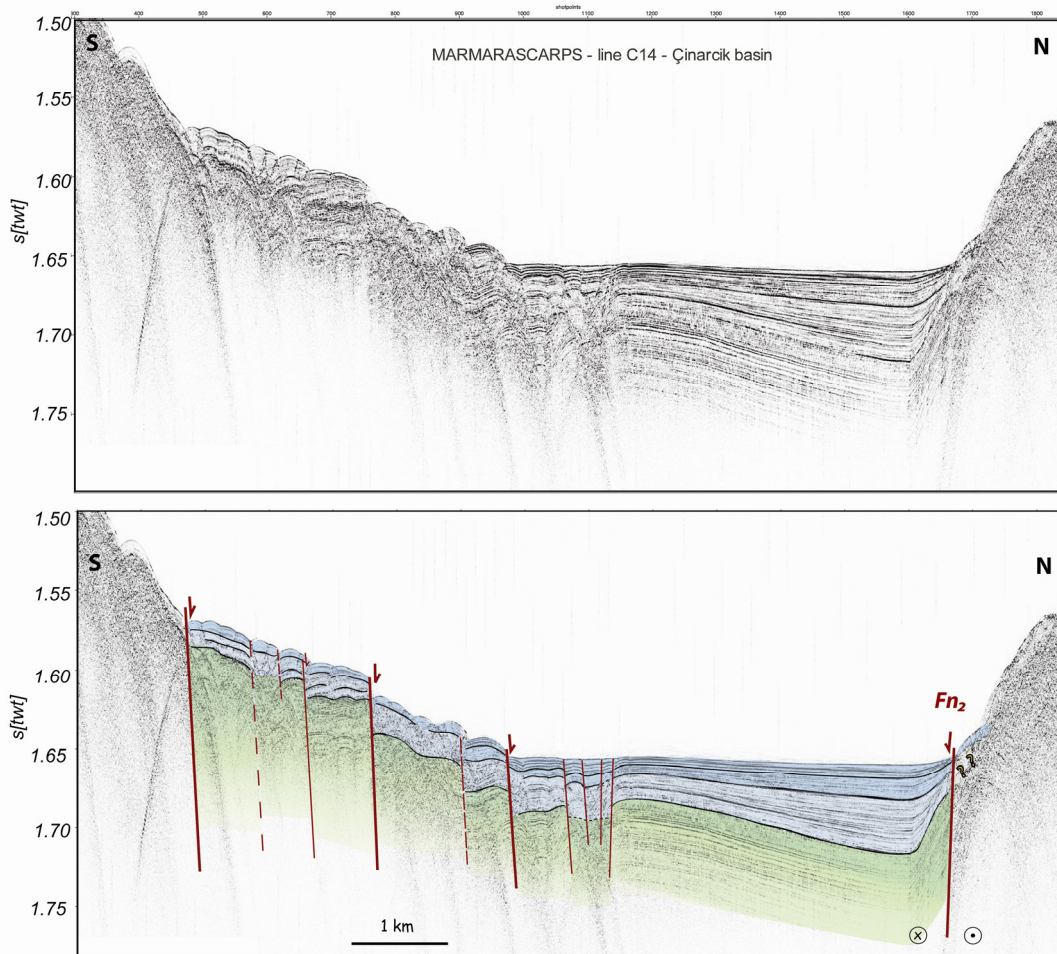


Figure 3.32 : Marmarascarp line C14 images the sedimentary pile well down to 70 ms (see Figure 3.33a for its location). The vertical exaggeration is about 20; thickness is reported in second twtt with a constant velocity of 1700 m/s. Blue horizons represent Holocene marine sediments and the green horizon is the Late Pleistocene lacustrine fill.

significant reflectors along the dense en echelon normal faults at this site. Here, some horizons are less visible because of the reflections coming from the hummocky morphology of the debris deposit. Nevertheless, certain horizons (e.g., top of the lacustrine sequence) can be distinguished with confidence. As a result of the fanning due to the normal component of the Northern fault, thickness of the top marine part increases from 24 m to 50 m (60 m s) towards Fn_2 (Figure 3.32).

Faults with normal slip offset the entire LPH sedimentary fill. The sequence observed in the line 14 is resolved together with the cores MD 25 and 27, which are correlated with the nearest chirp line C10 (Figure 3.33). The high frequency reflections of coarse-grained turbiditic sequences of the lacustrine fill are best seen on profile C10 (Figure 3.33d).

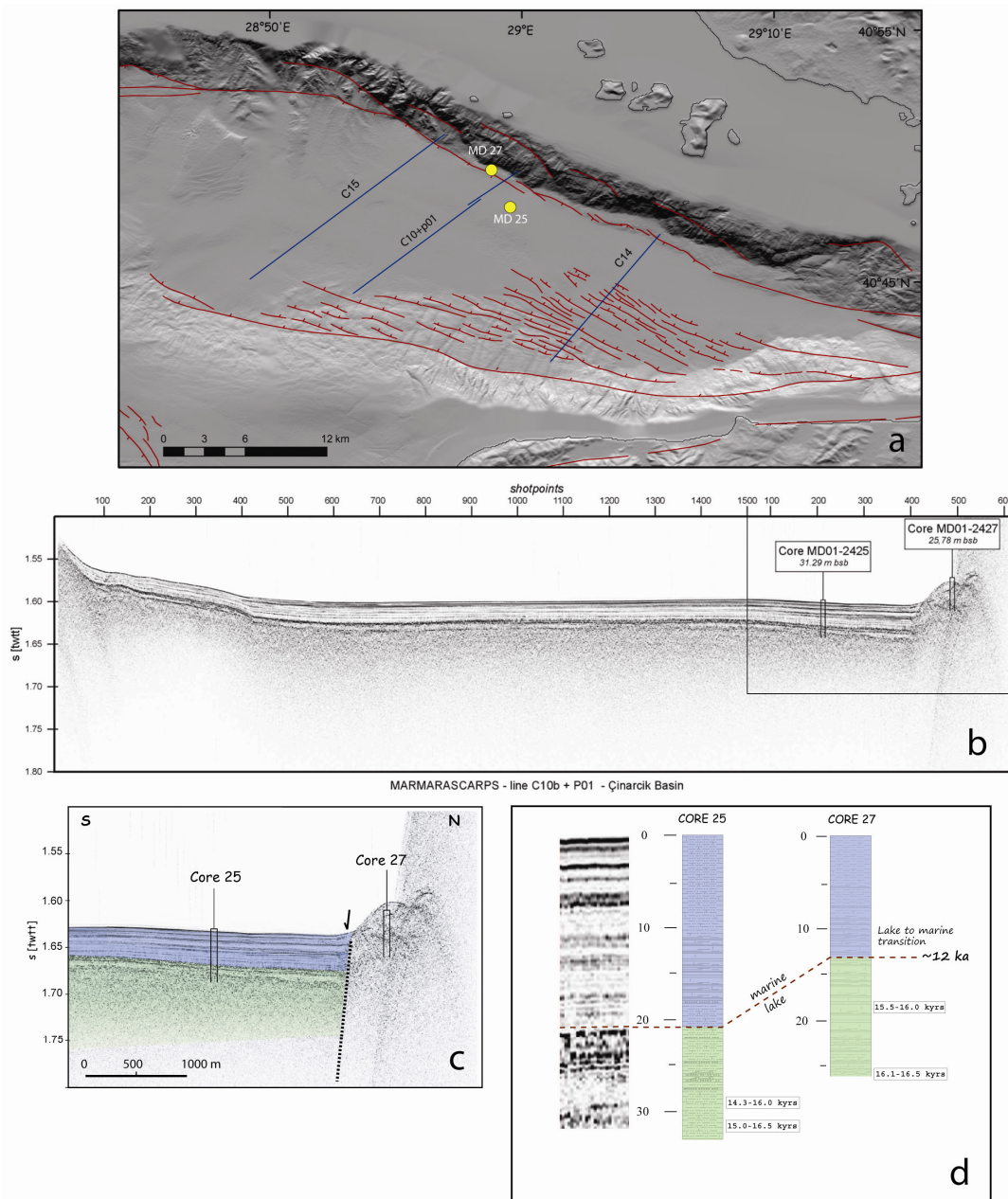


Figure 3.33 : Location map of the selected chirp profiles (blue lines) from Çınarcık basin. MD Core 25 and 27 (yellow circles) are also projected.

Analysis show that upper 10 m of Core MD 25 consists of poorly stratified clayey silt, 10-18 m more laminated with few sand layers. The lithology between 18-28 m is poorly stratified and darker (sulfurous) with coarse turbidites; lower part is homogenous clayey silt. Top 9 m of Core 27 also consists of poorly stratified clayey silt and 9-17 m is regularly laminated. The 17-23 m (lacustrine part) is laminated and darker (sulfurous) with thick coarse turbidites; lower part is homogenous with coarse turbidites.

Thickness of the marine units varies in both cores. While the thickness of the top marine part in core 25 is 21 m, it is 13 m in Core 27. The same applies to the cores in Central basin where significant thickness differences appear both in chirp profiles and core sections due to the vertical motion across normal faults. The total mean sedimentation rate deduced from the cores MD 25 and 27 is about 1.5 mm/yr in Çınarcık basin and 0.9 mm/yr over the northern shoulder.

Line C15 (Figure 3.34) confirms that the thickness of the Holocene sediments gradually decrease westward in the Çınarcık basin, which is readily seen from the isocontours in the isopach map. Here, Holocene deposits are thickest in front of the northern fault (Fn₂) where dip-slip component is higher, ~36 m, whereas they are 18 m thick towards south of the line C15.

The differences in sediment thickness at the floor of the Central Basin are sharp. They must be accounted for by vertical motion across normal faults, especially across the larger inner boundary faults, which have significant continuity in map view (Figure 3.36a). In the Central basin, line CB3 shows a inner basin nested between larger outer faulted edges (Figure 3.35). The subsidence of the inner floor and the sediment distribution are both controlled by continuing activity of the inner boundary faults. That dependence is readily seen in the profile. Line CB3 is correlated with cores MD 31 and 29, which provide the complete record of hemipelagic and turbiditic sediments deposited from the late Pleistocene to the present. About 35 m of marine sediments (see enlargement with Core 29 in Figure 3.35) have accumulated since the transgression over the inner floor of the Central Basin and only 10 m (see enlargement with Core 31 in Figure 3.35) over its SW shoulder (south of the boundary fault), at minimum average sedimentation rates of 2.6 mm/yr and 0.7 mm/yr, respectively. These rates are substantially faster than sedimentation rates previously found in shallower parts of the Marmara basin ($\leq 0.3-0.5$ mm/yr in the shallow shelves at depths ≤ 100 m; 0.1-0.2 mm/yr at intermediate depths of 300-700 m (Çağatay et al., 2000)).

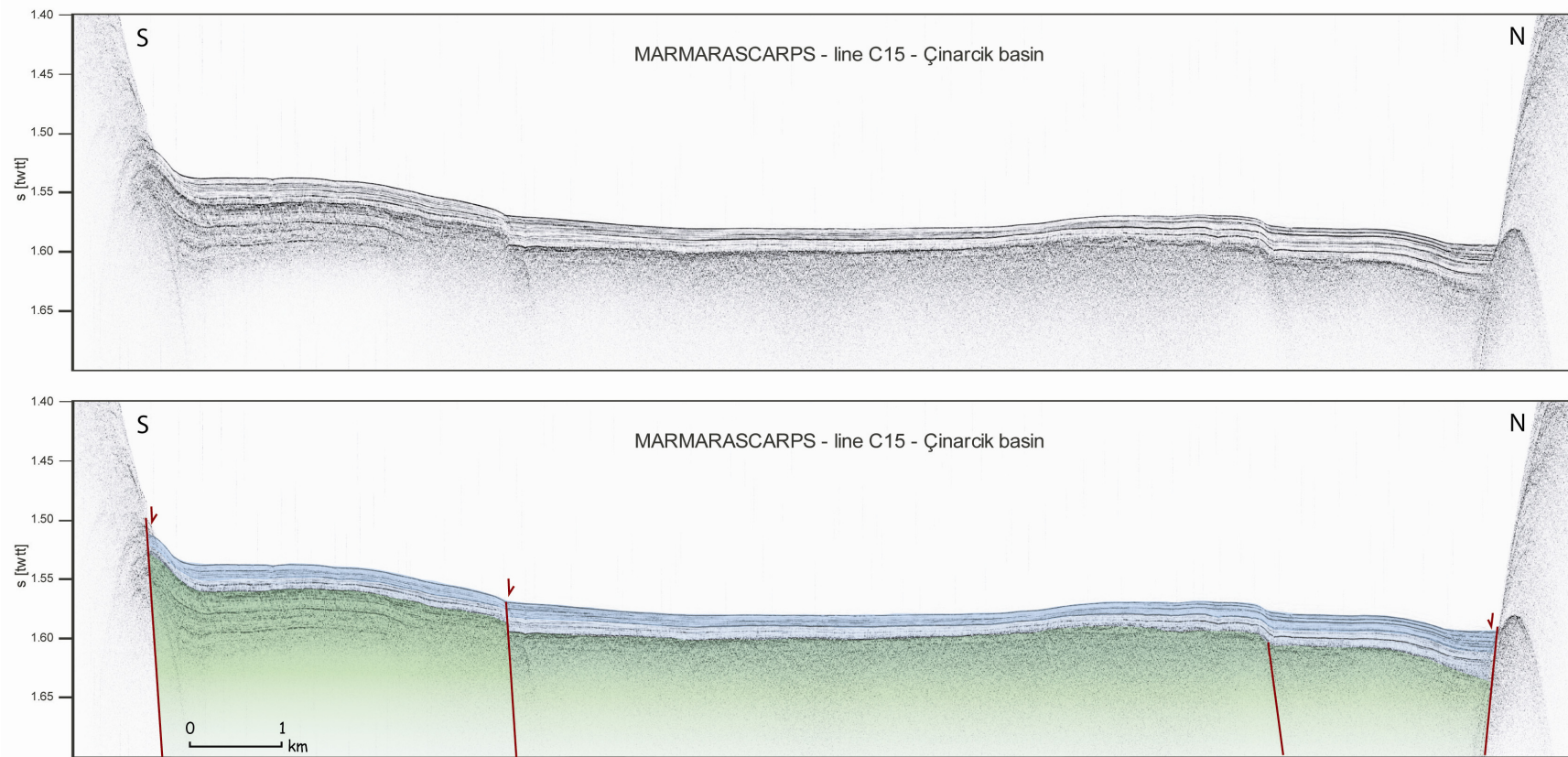


Figure 3.34 : MARMARASCARPS 3.5 KHz chirp profile C15.

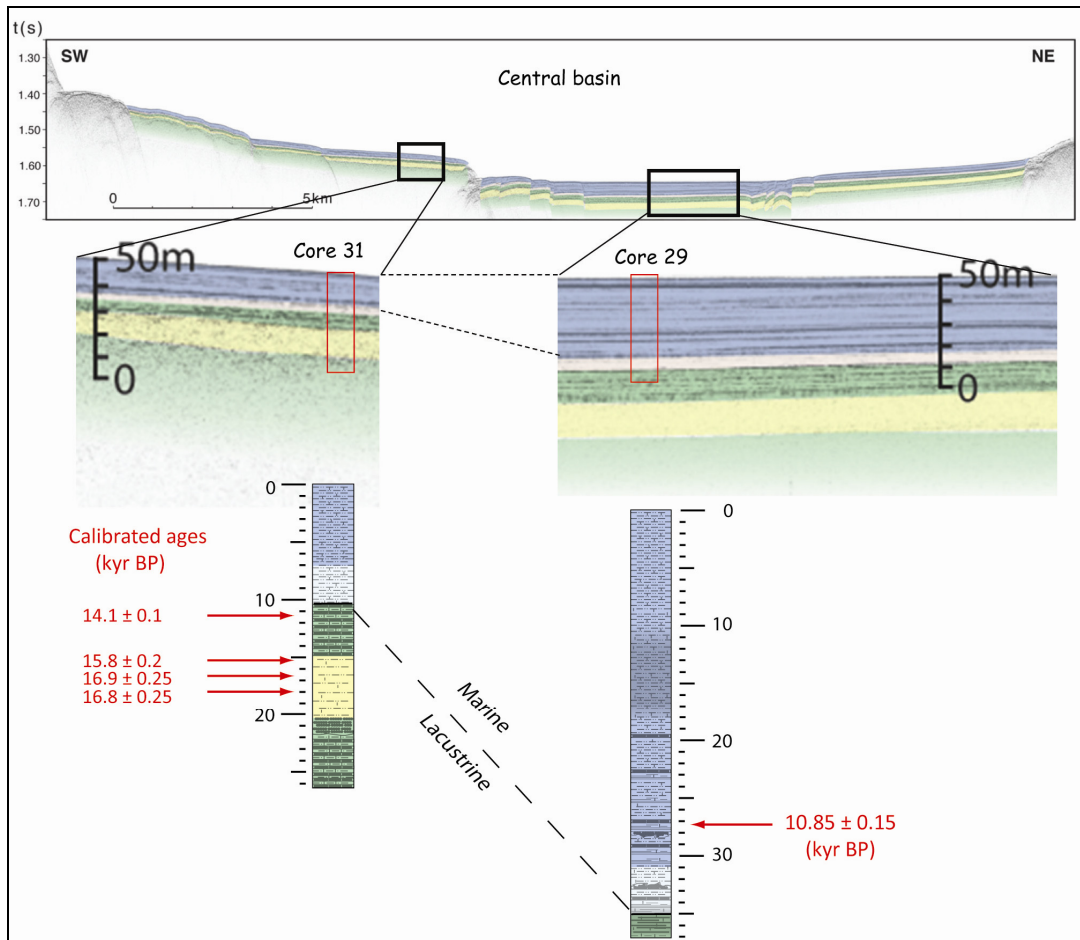


Figure 3.35 : Section across Central Basin (modified from Armijo et al., 2005). Upper Pleistocene and Holocene sedimentary pile as defined by the high-resolution 3.5 kHz profile (CB3) and enlarged core logs (lower panel; cores 31 and 29 from MARMACORE cruise, respectively 26- and 37-m-long) with sediment description and ^{14}C calibrated age constraints (dated wood fragments). Faults with normal slip at edges of inner pull-apart are readily seen (see location in Figure 3.37a).

As seen in CB3 profile shown in Figure 3.35, some sedimentary packages can be identified and traced across the entire basin both in the inner basin and on the shoulders from north to south. When examining the sections carefully it becomes clear that the same layers are thicker inside the inner basin. This is a strong evidence for the activity of fault being synsedimentary and extensional. If the layers had been deposited on a flat seafloor and faulted later on, the thickness of the layers should have been the same everywhere (Figure 3.36). Therefore, the faults do not postdate the uppermost section of the sedimentary pile and the faults bounding the inner basin have significant normal component. Most remarkable horizon found on line CB3 is the homogeneous transparent acoustic layer (Figures 3.37b and d) described as a

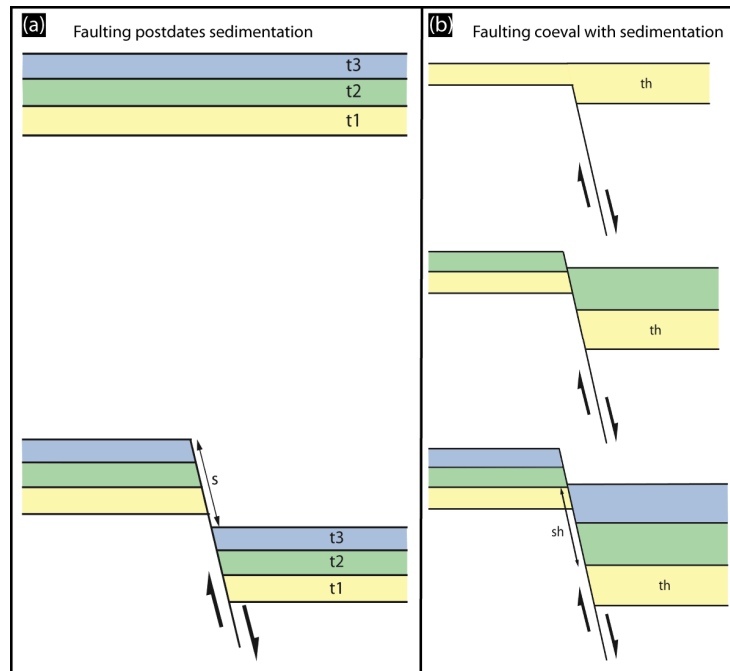


Figure 3.36 : Cartoons illustrating the relationship between faulting and sedimentation (modified from Pondard, 2006). (a) Faulting occurs after the deposition of layers. (b) Faulting is synchronous with sedimentation (i.e. syntectonic sedimentation). Note the contrast in layer thicknesses within the hangingwall and footwall in b.

very fine-grained unit in Cores 29 and 31 (Beck et al., 2007) corresponding to a pre-Late Glacial Homogenite (Figures 3.35 and 3.37). Core MD 31 completely crosses this homogenous layer that must be deposited as a suspended load. A 6 to 9 m thick homogenite layer marked as a yellow horizon interlayered within the lacustrine deposits (green horizon in Figure 3.35) providing a reference level for assessing subsequent deformation. The wood fragment sample from the lacustrine sediments yields a 15.8 ± 0.2 cal. kyr BP age and thus, dating the top of the homogenite. The 90 m vertical offset of this significant layer in line CB3 allows us to deduce a vertical throw rate of 5.5 mm/yr for the SW inner boundary fault whereas we deduce a vertical offset of 35 m for the homogenite layer by the NE inner boundary fault, providing a vertical throw rate of 2.25 mm/yr (Figure 3.37a and b). This inference indicates that the vertical-slip along the SW fault is relatively higher than the northern one. While stratigraphic offsets indicating these larger faults are very active, they have also created sharp scarps in the bathymetry. Conversely, smaller secondary faults with less continuity in map view have less stratigraphic offset, less morphologic expression and thus appear less active (≤ 1 mm/yr throw rate) (Figure 3.37a). It appears that vertical motion associated with normal faulting and sediment

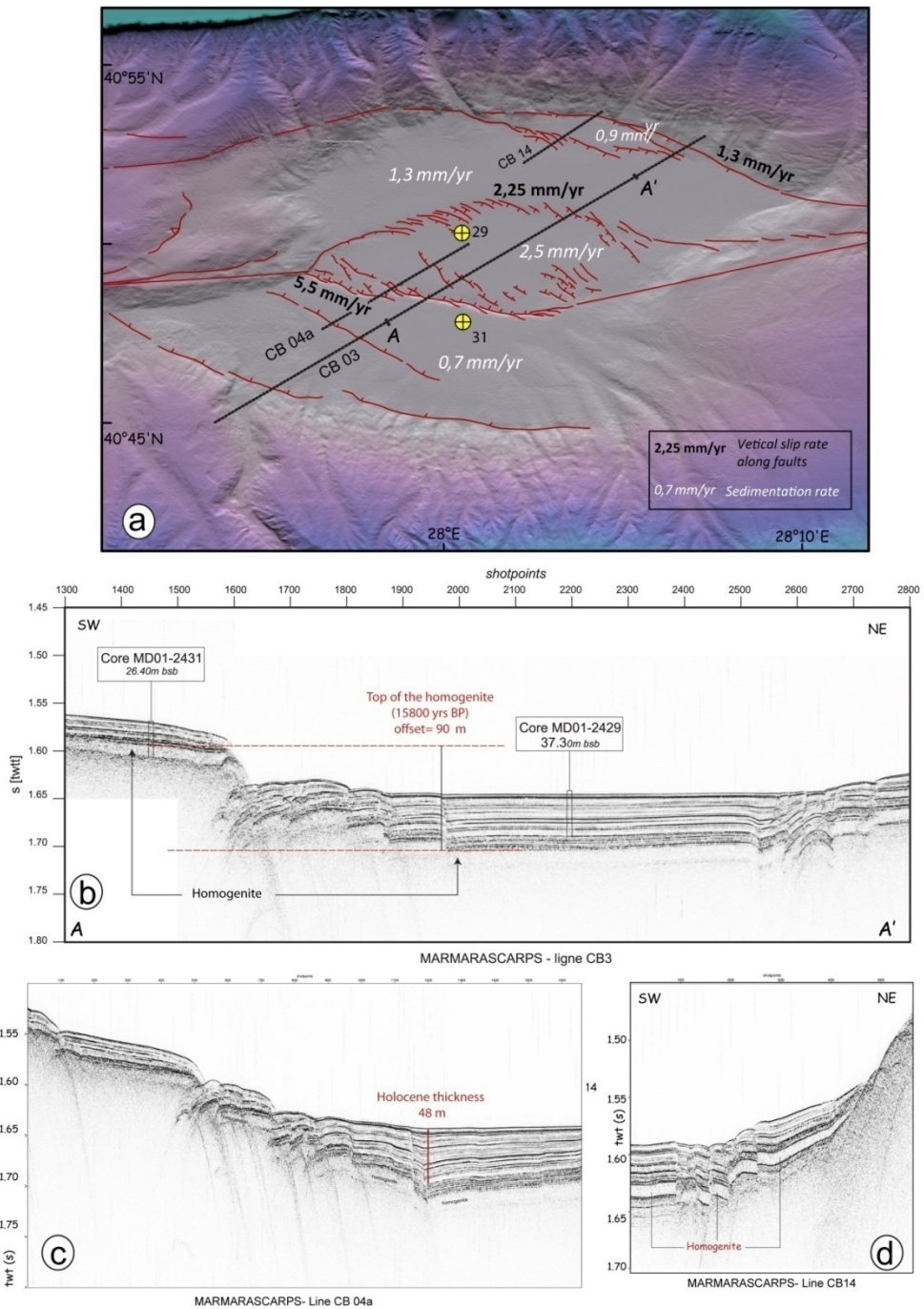


Figure 3.37 : (a) Sedimentation and faulting rates in the Central basin. Sedimentation-rate is averaged over the last 15800 years since deposition of the homogenite layer. (b) profile CB3 highlights the 90m cumulative offset of the homogenite layer used to derive the vertical throw rate. (c) Line CB04a indicates the thickest part of the lake-marine transition as 48 m. (d) Homogenite layer provides a reference level for assessing subsequent deformation. This layer is offset by several faults along the northern boundary faults on profile CB14.

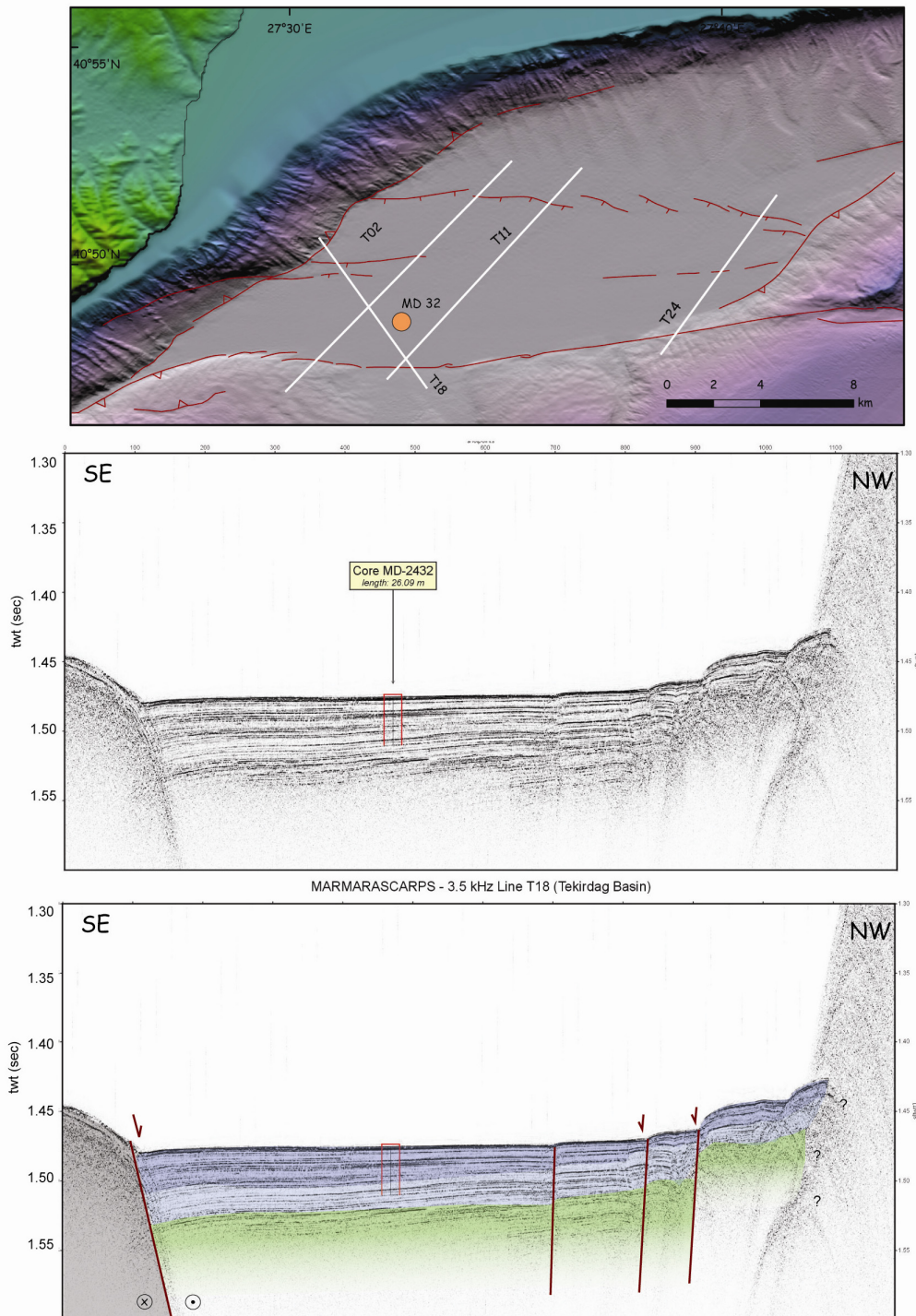


Figure 3.38 : 3.5 KHz chirp profiles across the Tekirdağ basin. Note the increase in thickness of Holocene sediment towards that south, indicating relatively stronger subsidence towards the southern boundary fault.

accumulation are the basic competing processes explaining both the late Pleistocene-Holocene stratigraphy variations and the morphology of the Central Basin floor. In Tekirdag basin, LPH sediments appear asymmetric due to fault-normal tilting toward southern main boundary fault in Tekirdag basin. Lacustrine-marine transition is well

observed in the chirp lines as in Central and Çınarcık basins. Accordingly, the thickness map of LPH transition in Tekirdag depicts that the depocenter is located near at the narrow end of the basin near the restraining bend (Figure 3.31).

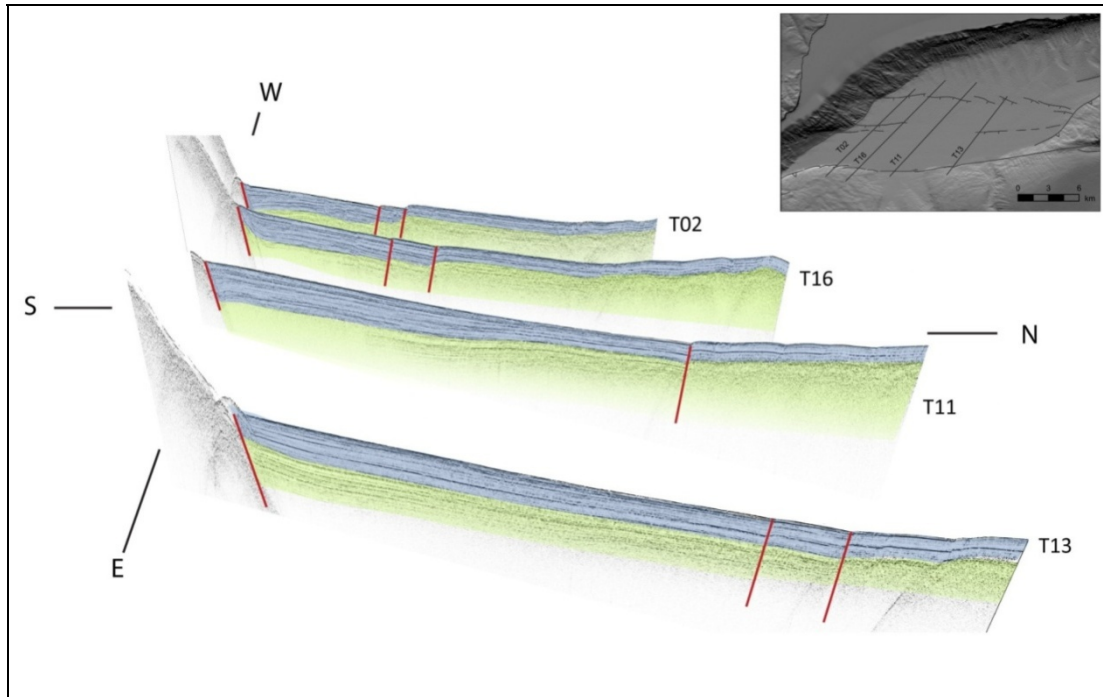


Figure 3.39 : Three-dimensional view of selected chirp profiles. Holocene sediments slightly gets thicker westward towards the depocenter. Inset shows the location the lines.

One remarkable observation derived from the chirp profiles, is the distinct vertical offsets of the secondary faults at the northern part of the Tekirdag basin (Figure 3.38). These faults cut across the entire Holocene sedimentary fill up to the seafloor. It is clear that these are active antithetic faults. The northernmost antithetic fault has relatively larger vertical displacement. The offset of the lacustrine transition is ~32 m on the northernmost fault depicting a 2-2.6 mm/yr vertical slip rate (based on the transition taking place around 12-14ka).

3.4 Discussion

Taking into account the observations concerning the kinematics, geometry, morphology of the submarine faults and sedimentation rates, the northern branch of the NAF under the Sea of Marmara can be divided into 5 major segments (longer than 35 km). These are the Tekirdağ (45 km), Central (70 km), Prince's Island (35 km), Southern Çınarcık (55 km) and İzmit segments that accommodate a large portion of plate motion, hence have high slip rates, and generate large earthquakes.

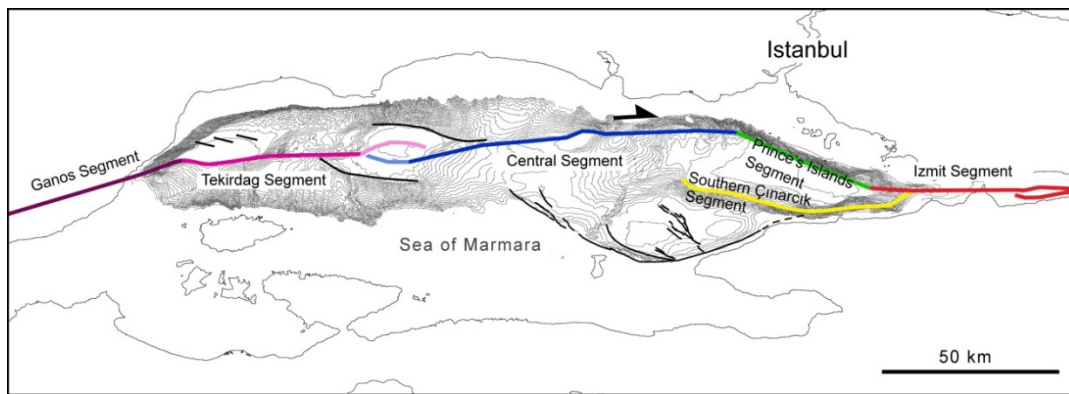


Figure 3.40 : Major segments of the NAF in the Sea of Marmara

Considering their length and kinematics (Wells and Coppersmith 1994), it can be said that each of these segments is capable of producing earthquakes larger than magnitude 7. However, each one may be reactivated alone during an earthquake of $M > 7$ or together with the neighboring 2-3 segments generating a much larger earthquake. In addition to these major segments, there are other minor segments, such as those bounding the outer Çınarcık basin and İmralı basin. They have overwhelmingly normal slip component with lower slip rates and thus are mainly accommodation structures. They may also produce earthquakes but, of smaller size. Precise location (< 1 km) of earthquakes between 2006 and 2010 by TÜBİTAK Marmara Research Center provides insights about the geometry, location and deep structure of the submarine faults in the Sea of Marmara (Figure 3.41). Earthquakes in eastern Marmara (Figure 3.41a) are located along known active fault segments, mostly between 2 and 15 km of depths. The Prince's Islands fault, in particular, is well defined by the seismic activity. Earthquakes in eastern Çınarcık basin are however distributed in the basin and appear to be located both on the main boundary fault to the north and on the distributed normal faults to the south. It is interesting to

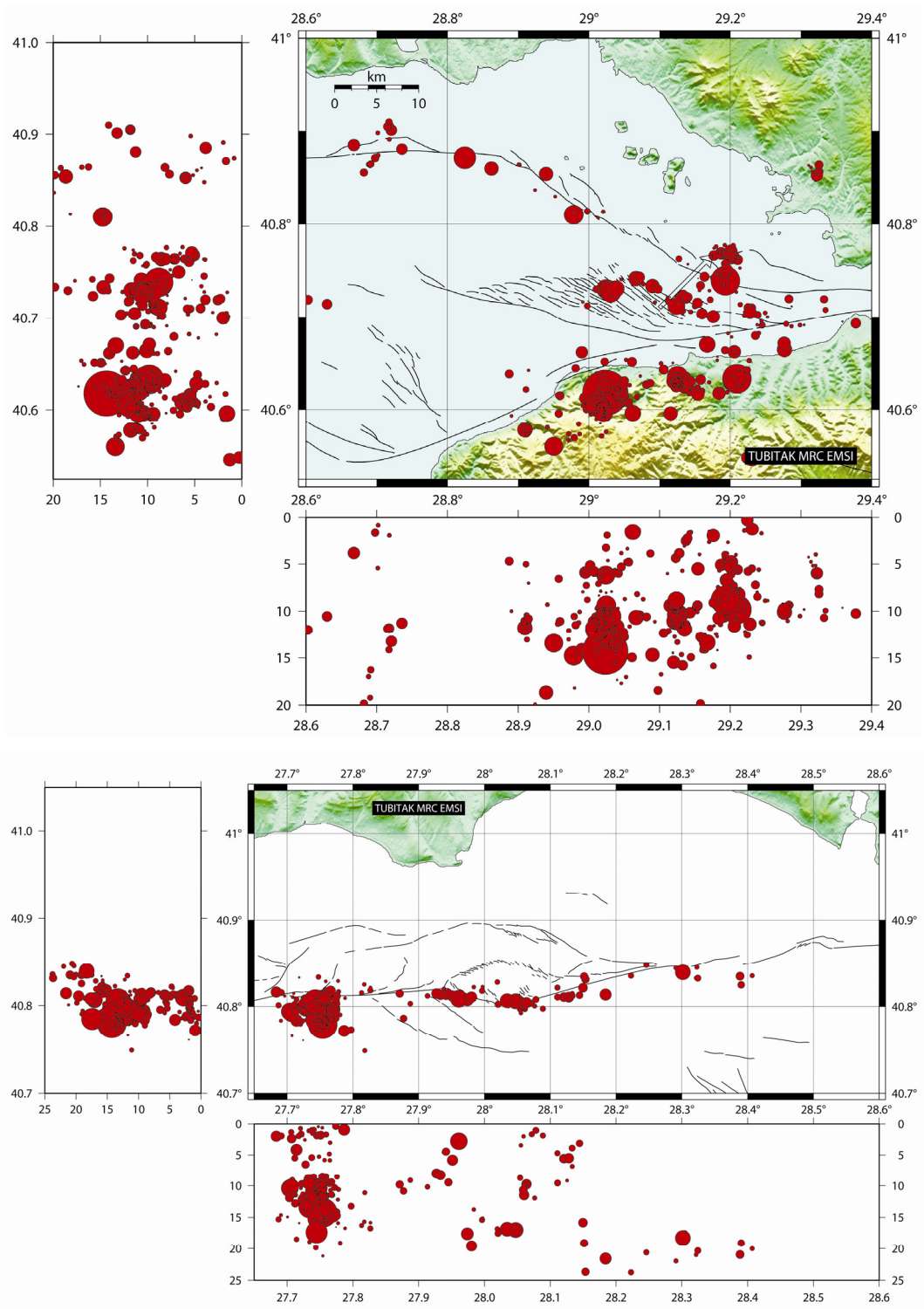


Figure 3.41 : Distribution of precisely located earthquakes between 2006 and 2010 in Marmara obtained by TÜBİTAK MRC (İnan et al, 2007) using hypoDD algorithm (Waldhauser ve Ellsworth, 2000). Depth distribution of the earthquakes plotted on the sides.

note that the earthquakes in the Central basin are located only along the southern margin of the inner basin (Figure 3.41b).

4. EARTHQUAKE SCARPS IN THE SEA OF MARMARA

4.1 General introduction

Earthquake scarps record the instantaneous deformation of landforms as the surface expression of earthquake faults. The morphological characterization of earthquake scarps establishes the knowledge of fault rupture kinematics, slip rate and earthquake cycle related to a significant active fault. Moreover, mapping the geometry of rupture traces and assessing the surface slip distribution of large earthquakes proved to be a steady source of reference in development of seismic hazard methodologies worldwide (Schwartz and Coppersmith, 1984; Wald and Heaton, 1994; Barka, 1996; and many others). While these studies are well established for land, they are at the pioneering stage for submarine environments. Recent advances in high-resolution submarine imaging and sampling techniques now provide opportunities for reconstructing the earthquake records in the submarine environments.

As the North Anatolian Fault bifurcates into two main branches in eastern Marmara region, its northern most active branch goes offshore under the Sea of Marmara. Consequently, there has been a decisive need to explore offshore segments of the NAF. With that purpose, the MARMARASCARPS cruise performed in 2002 collected high-resolution data to characterize the submarine morphology along the northern branch of the NAF. The dataset includes micro-bathymetry, photo/video imagery and shallow sediment coring acquired with a ROV (Remotely Operated Vehicle) with systematic coverage of the most prominent fault scarps in the northern Sea of Marmara. The micro-bathymetry data together with the video imagery revealed clear morphologic evidence of recent faulting activity along several segments of the northern Marmara fault system. Along some of the faults, fine, outstandingly well-preserved scarps were discovered, most probably associated with recent earthquake breaks. The preliminary results (Armijo et al., 2005) show that: (1) An outstanding break extends offshore eastward of the Ganos Fault, between that fault and the Central Basin. (2) A very fresh break is seen where the Izmit fault

enters westward into the Cinarcik Basin. It corresponds very probably to the underwater extension of the 1999 Izmit earthquake rupture. (3) Small fresh breaks cut along the NE edge of the Cinarcik Basin over several kilometers. They can be associated tentatively with the Ms 6.4 1963 earthquake (4) No young break could be detected between the Central Basin and the Cinarcik Basin.

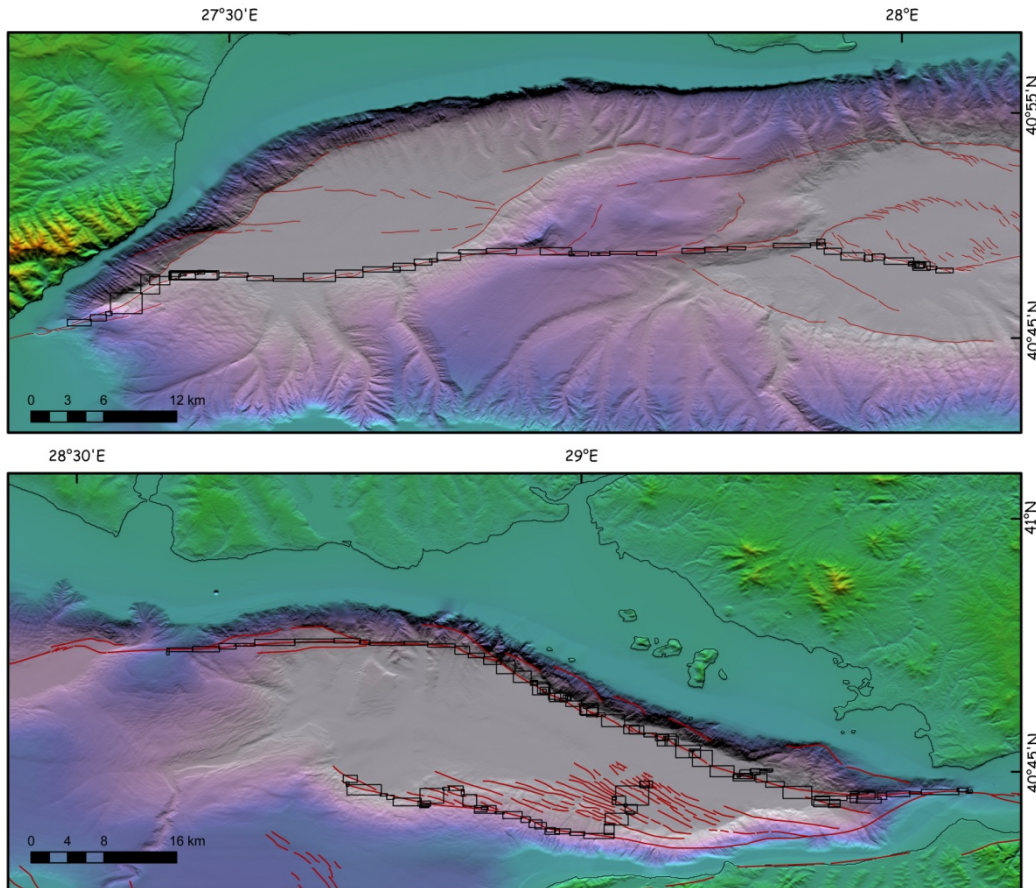


Figure 4.1 : Bathymetry of the Marmara Sea showing location of microbathymetry survey sites in black boxes along the submarine faults (red lines). The multibeam surveys were conducted along the fault scarps in a strip inside the boxes, not inside the entire boxes.

Accordingly, the goals of this chapter are to characterize young earthquake ruptures and the morphological evolution of scarps, seeking to unravel first-order fault segmentation and significant geometrical barriers to rupture propagation. Some submarine breaks can be correlated with recent events or older historical earthquakes. It has been proposed that large historical earthquakes (1509, 1719, May 1766, August 1766, 1894) ruptured totally or partially segments under the northern Sea of Marmara (Ambraseys and Finkel, 1991; Parsons, 2004). Particularly, the set of well-preserved earthquake scarps which extend offshore from the Ganos and Izmit

faults on land can be attributed to the submarine ruptures of the purely strike-slip 1999 Izmit (Mw 7.4) and the 1912 Ganos (Ms 7.4) earthquakes and this will be examined in detail in the following sections. This problem is addressed by describing the rupture length and possible slip distribution associated with recent earthquakes recorded by particularly well-preserved submarine scarps.

One important question is how to determine the age of the last submarine earthquake break which is relatively difficult to assess directly with dating approaches. However, recent sedimentation rates can provide information on the age of the sediment covering the scarps. With that purpose, the interface cores (35 cm) collected by ROV are investigated to identify sedimentary sequences. Geochronological control is obtained using ^{210}Pb ($T_{1/2} = 22.3$ years) method, measured by gamma counting. This critical issue concerning the dating of the earthquake scarps will be discussed in the last section of this chapter.

4.2 Method: Seafloor Observations in the Sea of Marmara and the new dataset

After the 1999 İzmit earthquake numerous scientific cruises have been carried out to investigate the active faults in the Sea of Marmara. The Turkish-French cruise of Ifremer R.V. Le Suroit obtained the first high-resolution complete bathymetric map of the deep basins of the Marmara Sea in 2000 (Le Pichon et al. 2001; Armijo et al. 2002). The high-resolution bathymetry (~25 m), seismic reflection and side scan sonar imaging are used by Armijo et al. (2002) to map in fine detail the submarine active faults in the Marmara Sea. The side scan sonar towed 200 m above seafloor revealed particularly the presence of fault scarps.

MARMARASCARPS (2002) was devoted to measurements of submarine earthquake scarps with a Remotely Operated Vehicle (ROV), obtaining a ultra-high-resolution bathymetry, an extensive coverage with 3.5 kHz chirp profiles, an extensive sampling and coring of sediments close to the scarps, and a significant video and photo documentation of submarine earthquake ruptures.

The campaign was conducted in 2002 to study the detailed geology and geomorphology of these submarine seismic scarps associated with the 1999 Izmit and other recent and historical large earthquakes (i.e., 1912 Ganos, 1894 Çınarcık earthquakes) in the Sea of Marmara. During the campaign, video and photo imaging

and ultra-high-resolution bathymetric mapping of the sea floor were carried out with an unmanned submersible since other methods such as seismic reflection, side scan sonar or multi beam bathymetry could not resolve surface fault ruptures of individual earthquakes. These observations allowed successfully the identification of the fault scarps associated with the 1912 Ganos earthquake on the western side of the Marmara Sea (Armijo et al., 2005).

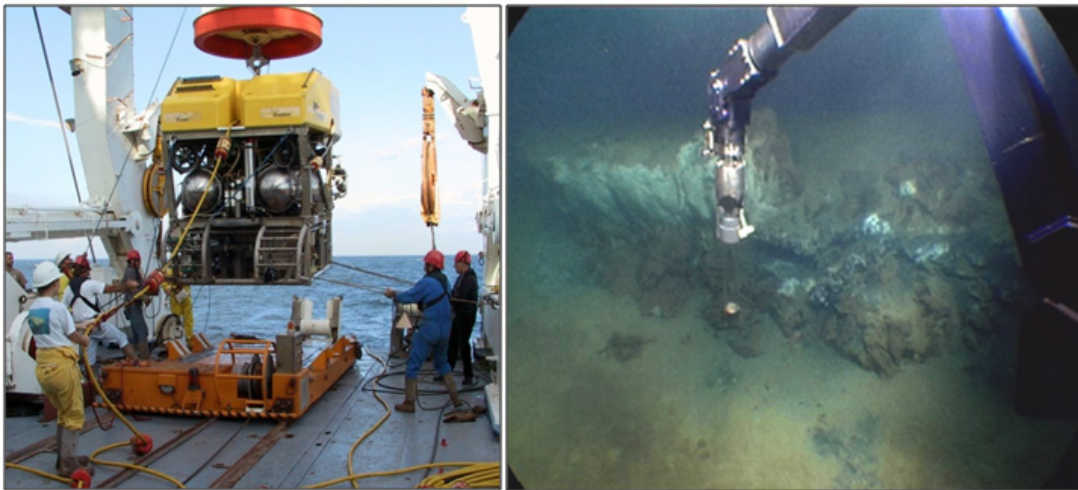


Figure 4.2 : ROV Victor 6000 was used during the MARMARASCARPS cruise to collect ultra high resolution bathymetry, push up cores and video imagery at the seafloor. Photo on the right exposes a carbonate crust that is offset by the fault in Tekirdag basin.

During the MARMARASCARPS campaign, the unmanned submersible ROV Victor 6000 and the oceanographic vessel Atalante were used to perform an ultra-high resolution, high-precision bathymetric survey (microbathymetry) of the main submarine faults in the northern Sea of Marmara (Figure 4.2). The ROV was operated with a Seabat 8101 multibeam sounder to survey faults over a total length of about 300 km with an average horizontal resolution of 0.5 m and a vertical accuracy of 10 cm, using a high-precision submarine navigation system (less than 10 m of uncertainty) based on a DGPS positioning of the vessel. Exploration at low altitude over the sea bottom (2 m) was made in specific sites to make direct visual observations of the fault breaks. The point wise micro-bathymetric data were gridded and plotted using Generic Mapping Tools (Wessel & Smith, 1995). In this study, we also use complementary data from other cruises led by R/V Odin Finder and R/V Urania. During these two cruises, multibeam bathymetry data were collected in western and central basins of the Gulf of Izmit in 2000 and 2001 (Polonia et al. 2004;

Cormier et al. 2006). The multibeam bathymetry west of Hersek is combined with the microbathymetry data from Marmarascarps cruise.

4.3 Western Termination of the Mw 7.4, 1999 İzmit Earthquake Rupture: Implications for the Expected Large Earthquake in the Sea of Marmara

The Mw 7.4, August 17, 1999 İzmit earthquake ruptured ~100 km-long onland section of the North Anatolian Fault (NAF) in eastern Marmara region, causing loss of more than 20000 people and extensive destruction. However, the western termination and total length of the earthquake rupture is still a matter of debate because the surface rupture enters offshore in the Gulf of İzmit after displaying a coseismic displacement of ~5 m. Such a high amount of slip implies that the fault rupture must certainly continue significantly westwards on the sea floor, but where exactly it terminated is difficult to determine. This issue is critical for determining the size of the Marmara seismic gap, south of Istanbul. Therefore, to explore the fault scarps associated with the 1999 rupture on the sea floor, we have studied the ultra-high resolution bathymetry (0.5 m resolution) acquired with a remotely operated submersible during the MARMARASCARPS cruise, an innovative approach proved to be useful in searching earthquake surface deformation on the sea floor.

4.3.1 Seismotectonic background

The right-lateral North Anatolian transform fault between the Eurasian and Anatolian plates is one of the most prominent and seismically active structures of the Eastern Mediterranean (Figure 1) (Barka, 1996; Armijo et al. 1999; Şengör et al., 2005). The NAF has an extremely well developed narrow and simple trace from Karlıova in the east to the Mudurnu valley in the west. However, west of Mudurnu, the NAF splays into two major fault strands known as northern and southern NAF. The northern branch runs through the İzmit- Sapanca Lake and enters into the Sea of Marmara, while the southern branch runs south of the Biga and Armutlu peninsulas through Iznik Lake, Bursa and Gemlik bay. According to GPS observations, most of the lateral motion appears to be transferred obliquely northward, from the main fault to the northern branch, across the Sea of Marmara basin (Figure 1.1) (McClusky et al., 2000; Armijo et al., 2002; Reilinger et al., 2006).

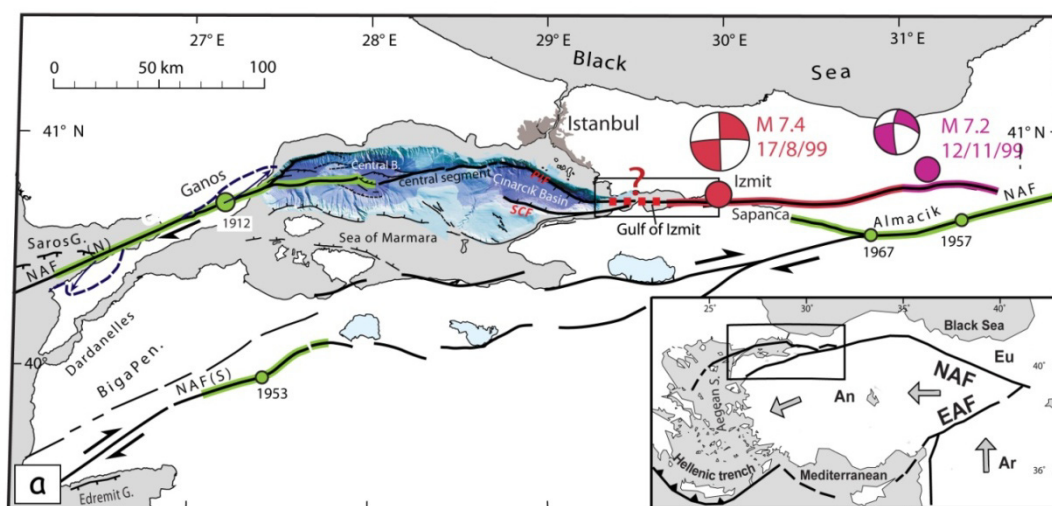


Figure 4.3 : Tectonic map of the Marmara region including the EM300 bathymetry of the Sea of Marmara, showing the active faults (from Armijo et al., 2002) and surface ruptures of the 1999 Izmit (red) and Düzce (purple) earthquakes (Barka et al., 2002) with focal mechanism solutions from Harvard CMT. Green lines with dates show the 20th century surface ruptures before the 1999 events. Red question mark with the dashed lines indicates the uncertainty of offshore extension of the 1999 Izmit earthquake rupture. Inset map depicts the tectonics of the eastern Mediterranean with arrows showing the movement of Arabia (Ar) and Anatolia (An) relative to Eurasia (Eu). (PIF: Princes Islands Fault, SCF: Southern Çınarcık fault).

The Sea of Marmara is characterized by the 70-km-wide step-over between two well known strike-slip faults, İzmit and Ganos, which have ruptured during the 1999 İzmit and 1912 Ganos earthquakes and appears to be among the clearest examples of pull-apart basins in the world (Armijo et al., 2002). The Neogene and Quaternary tectonics puts the northern Marmara basin under an extensional regime that has caused significant overall subsidence (Armijo et al., 2002; Hirn et al., 2003; Muller & Aydin 2005). The northern Marmara step-over is formed by smaller steps bounding three deep basins (Tekirdağ, Central and Çınarcık Basins) with active subsidence that is stronger than in the rest of Marmara (Barka & Kadinsky-Cade, 1988; Wong et al., 1995; Armijo et al., 2002).

The northern branch of the NAF enters the Sea of Marmara through Gulf of İzmit and its purely strike-slip regime already becomes slightly transtensional forming two interconnected basins (i.e., Karamürsel and Gölcük) (Figure 4.4). These are depressions, bounded by short, en-echelon, extensional and strike-slip segments (Polonia et al., 2004). The bathymetric mapping indicates that the NAF branches into

two segments west of the Hersek delta (Figure 4.4a); the E-W trending Hersek-Çınarcık and the ENE-WSW trending Hersek-Yalova. The latter segment runs parallel to the coast and branches into numerous smaller normal faults that bound partially the south of Çınarcık basin. The 25-km-long Hersek-Çınarcık segment connects to the Princes Island fault (PIF) that bounds the Çınarcık basin to the north (Figure 4.4a). Here, it makes a ~10-km-step to the north and continues westward along the Central segment in the Sea of Marmara (Figure 4.4a). Analyses of the high-resolution bathymetric data and seismic profiles show that the largest step-over along the northern branch is located offshore in the Çınarcık Basin (Armijo et al., 2002). The strike slip motion between Hersek-Çınarcık and Central segments is transferred with the NW-SE trending Princes Islands fault. Oblique opening along this fault results in the formation of the deep Çınarcık extensional basin filled with sediments of up to 5 km thick (Carton et al., 2007) and represents a major structural complexity along the NAF where the transcurrent tectonics transfers into an oblique extension resulting in significant thinning in the brittle crust.

4.3.2 The Mw 7.4, 17 August 1999 İzmit earthquake

The Mw 7.4, 17 August 1999 İzmit earthquake (M_0 1.7-2.0 x 10²⁰ Nm) was not a surprise because westward migrating earthquakes had already taken place along the North Anatolian Fault (NAF) all the way from Erzincan to the İzmit region breaking ~1000 km-long section of the NAF since 1939 (Toksöz et al., 1979; Barka 1996; Stein et al., 1997). As for the falling dominos, these triggered earthquakes reached the İzmit region following the southern boundary of the Almacık block (Figure 4.3) (Barka, 1996). The İzmit and November 12, 1999 Düzce (Mw 7.2) earthquakes ruptured together almost entirely the northern boundary of the Almacık block and the İzmit fault segment (Figure 4.3).

The 1999 İzmit earthquake nucleated on the NAF south of İzmit with bilateral rupture propagation to the west and east breaking four fault segments, (i.e., the Karadere, Sakarya, Sapanca, Gölcük segments) with a total length of ~100 km on land (Figure 4.4). They are separated by up to 4 km wide stepovers with both releasing and restraining bends (Barka et al., 2002). The maximum horizontal offset produced along the surface break was 5.5 m on the Sakarya segment, immediately east of Sapanca Lake (Figure 4.4) (Barka et al., 2002). Active faults in the vicinity of

the İzmit rupture, particularly around the rupture tips, are now loaded with high static stress whose peak value is equivalent to tens of years of stress accumulation at a normal tectonic rate (Hubert-Ferrari et al., 2000; Çakır et al., 2003a). An accurate estimation of static stress changes caused by an earthquake on the neighboring active faults depends heavily on the source parameters of the earthquake itself. Therefore, the rupture parameters of the 1999 İzmit earthquake need to be well constrained to assess the seismic hazard in the Istanbul.

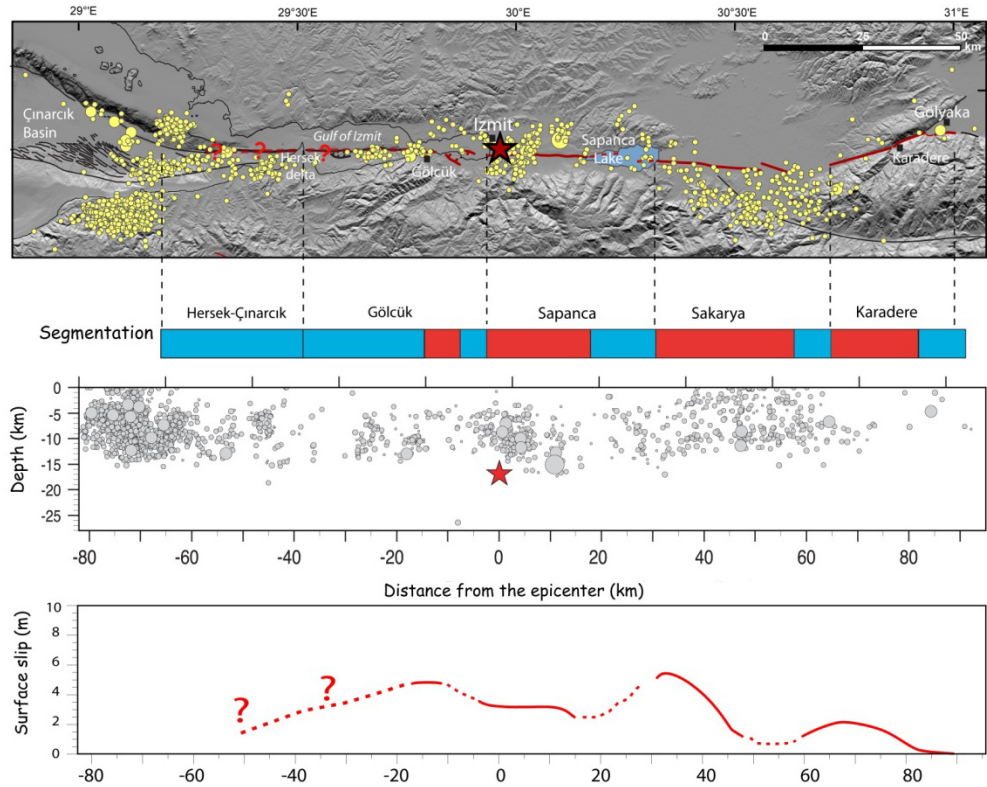


Figure 4.4 : a) Shaded relief map of the Mw 7.4 1999 İzmit earthquake rupture area east of Marmara Sea, showing fault segments in black lines and 1999 İzmit surface rupture in red lines (Barka et al., 2002). Red question marks denote the uncertainty concerning the submarine portion of the İzmit rupture. Yellow circles are $M_L > 2$ aftershocks recorded between August 20 and October 20 1999 by the TÜBİTAK permanent network (Özalaybey et al., 2002). Red star locates the epicenter of the 1999 İzmit earthquake. The blue-red bar below the map distinguishes individual fault segments that ruptured during the 1999 earthquake; red and blue bars indicate whether or not offsets are observed and measured along the fault rupture. (b) Aftershocks distribution at depth. The aftershocks extend in an uninterrupted continuation further west from Hersek delta along the axis of the İzmit Gulf up to the Çınarcık basin. (c) Slip distribution diagram of the 17 August 1999 İzmit surface rupture (after Barka et al., 2002). Slip values are extrapolated in dashed lines where there is no direct observation of slip along offshore segments.

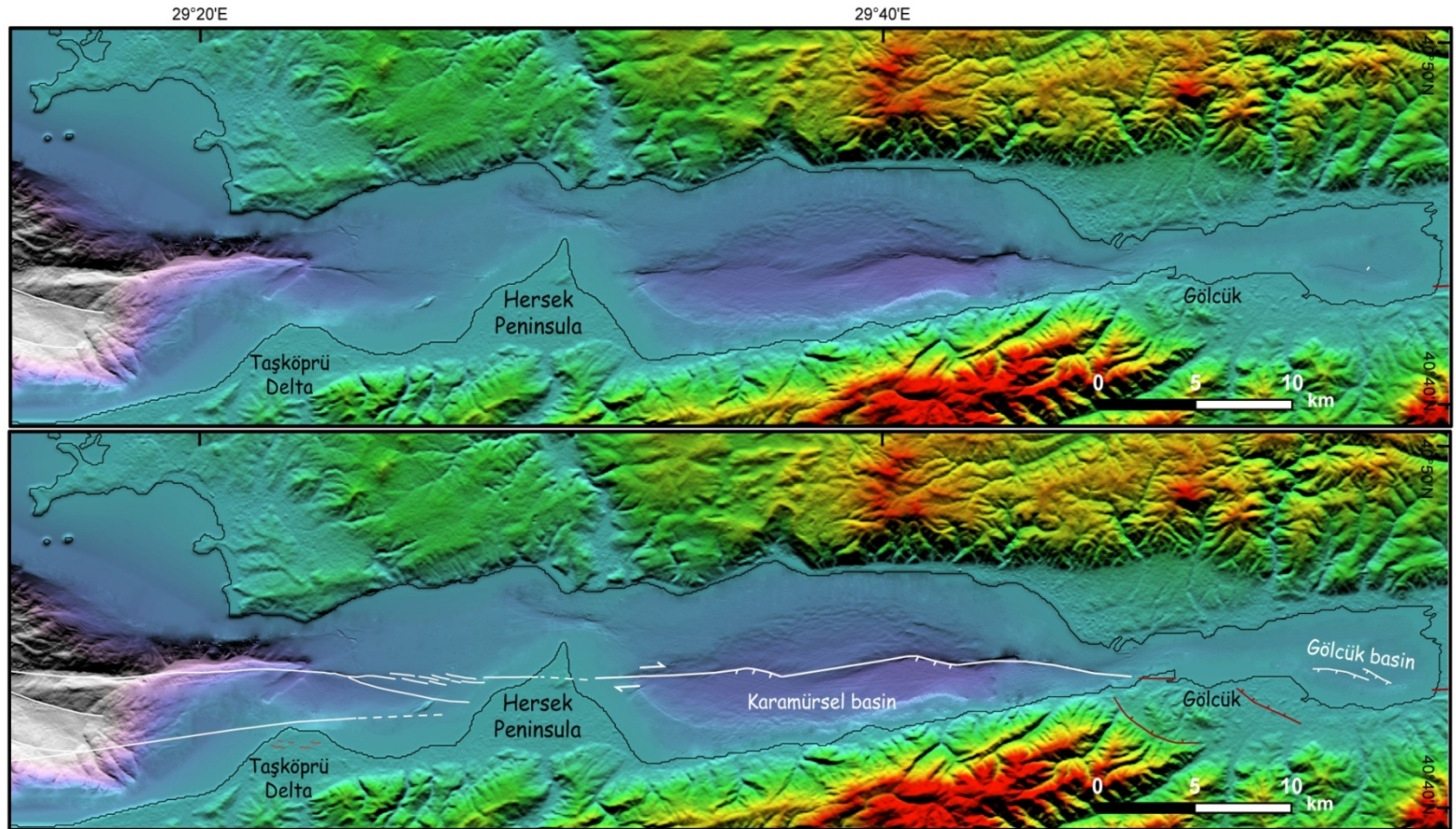


Figure 4.5 : Shaded (from North) relief image of the Gulf of İzmit mosaicked using SRTM (90 m) for land and multi beam bathymetry from Le Suroit (25 m), Odin Finder (10 m) and SHOD (~10 m). White and red lines show the active faults and the 1999 İzmit rupture, respectively.

Although the surface rupture of the 1999 earthquake was very well documented onland, the offshore continuation in the Gulf of İzmit still remains ambiguous because the coseismic surface faulting of the İzmit earthquake disappears offshore to the west of Gölcük, immediately after displaying a right-lateral offset of about 5 m (Figure 4.5) (Barka et al., 2002). Further west, field observations did not reveal any evidence for a surface rupture in the Hersek Delta except some ground cracks and open fissures, suggesting that the rupture propagation must have stopped somewhere between Gölcük and Hersek within the Karamürsel basin (Pınar et al., 2001; Lettis et al., 2002; Cormier et al., 2006; Kozacı et al., 2002). However, GPS and InSAR modeling (Çakır et al., 2003b; Reilinger et al., 2000; Wright et al., 2001; Delouis et al., 2002) together with the analysis of aftershock distribution (Özalaybey et al., 2002; Karabulut et al., 2002), suggest that the rupture most probably continued westward beyond the Hersek peninsula along the Hersek-Çınarcık segment.

4.3.3 Submarine fault scarps west of Hersek: evidence for the 1999 İzmit earthquake rupture

The westernmost section of 1999 İzmit earthquake surface rupture was observed onland west of Gölcük where the fault rupture crosses the Navy base with a 4.7 m right-lateral offset (Barka et al., 2002) and enters the Gulf of İzmit. From this point forward, the fault entirely runs offshore and thus it becomes difficult to identify the rest of the surface rupture (Figure 4.4). However, Polonia et al. (2002) present towed camera images of fresh-looking polygonal cracks offshore Gölcük filled by black and yellowish mud possibly related to fluid or gas escape during 1999 earthquake. Such evidence of gas seepage was also introduced by Kuşçu et al. (2005) from chirp profiles acquired during a post-earthquake cruise offshore Gölcük. Further west, faulting becomes transtensional in the Karamürsel basin by composite strike-slip and normal faulting (Figure 4.4).

Cormier et al. (2006) describe here a series of lineaments that strike subparallel to the main fault branch east of Karamürsel basin and interpret them as open cracks or mole tracks. No other significant inferences have been made for the 1999 fault break in Karamürsel basin except a small slump which was probably triggered by the 1999 İzmit earthquake (Cormier et al., 2006). No ground rupture was observed in the

Hersek delta although the Hersek lagoon reportedly subsided by about 20–30 cm (Lettis et al., 2002).

The absence of surface rupture across the Hersek delta can be explained by the attenuation of faulting within the deltaic sediments (Gülen et al., 2002). The most likely scenario, however, is that the amount of right-lateral slip across the Hersek Delta is rather small and distributed or absent since it is located at the western end of the Gölcük segment, as observed also in the Akyazi bend where there is a gap in surface rupture between the Sakarya and Karadere segments (Barka et al., 2002). Sets of E-W striking, en-echelon, open cracks with throws up to 25 cm were mapped in Taşköprü delta west of Hersek (Figure 4.6) (Barka et al., 2002; Gülen et al., 2002; Emre et al., 2003). These fractures are probably due to lateral spreading of unconsolidated deltaic sediments. North of the Taşköprü delta, the multibeam bathymetry exposes a prominent Quaternary submarine canyon that is offset right-laterally by the Hersek-Çınarcık segment. Polonia et al. (2004) infer a ~100 m right-lateral offset from the sea-floor reflectivity based on CHIRP sonar data. However, our estimates based on the displacements of the eastern edge of the canyon floor and the topographic high to the west suggest an offset 20-30% higher than that estimated by Polonia et al. (2004) (Figure 4.7).

The submarine canyon runs towards south, but as it deepens it makes a sharp westward turn towards the Çınarcık basin (Figure 4.6). It has a relatively flat bottom (at 180 m depth), suggesting that it is now inactive and filled with Holocene sediments. The canyon was active during the Last Glacial sea-level lowstand until about 11 kyr BP when it was merged by the Holocene sea-level rise (Çağatay et al., 2003, Polonia et al., 2004).

The flat floor of the canyon represents the ideal place to search for the sea floor rupture of the 1999 İzmit earthquake, since its leveled surface could preserve only the last earthquake rupture. The ultra high-resolution bathymetry data from the MARMARASCARPS campaign systematically cover the extent of the Hersek-Çınarcık segment aiming to detect the continuation of the surface rupture (Figures 4.6a and 4.6b). Indeed, the microbathymetry shows a remarkable linear rupture across the canyon floor with a south facing sharp scarp (Figures 4.7). The scarp illustrates an apparent throw of 50 cm and appears to have the morphology similar to “bumps” that form along the mole tracks (Figure 4.7). Such mole tracks with

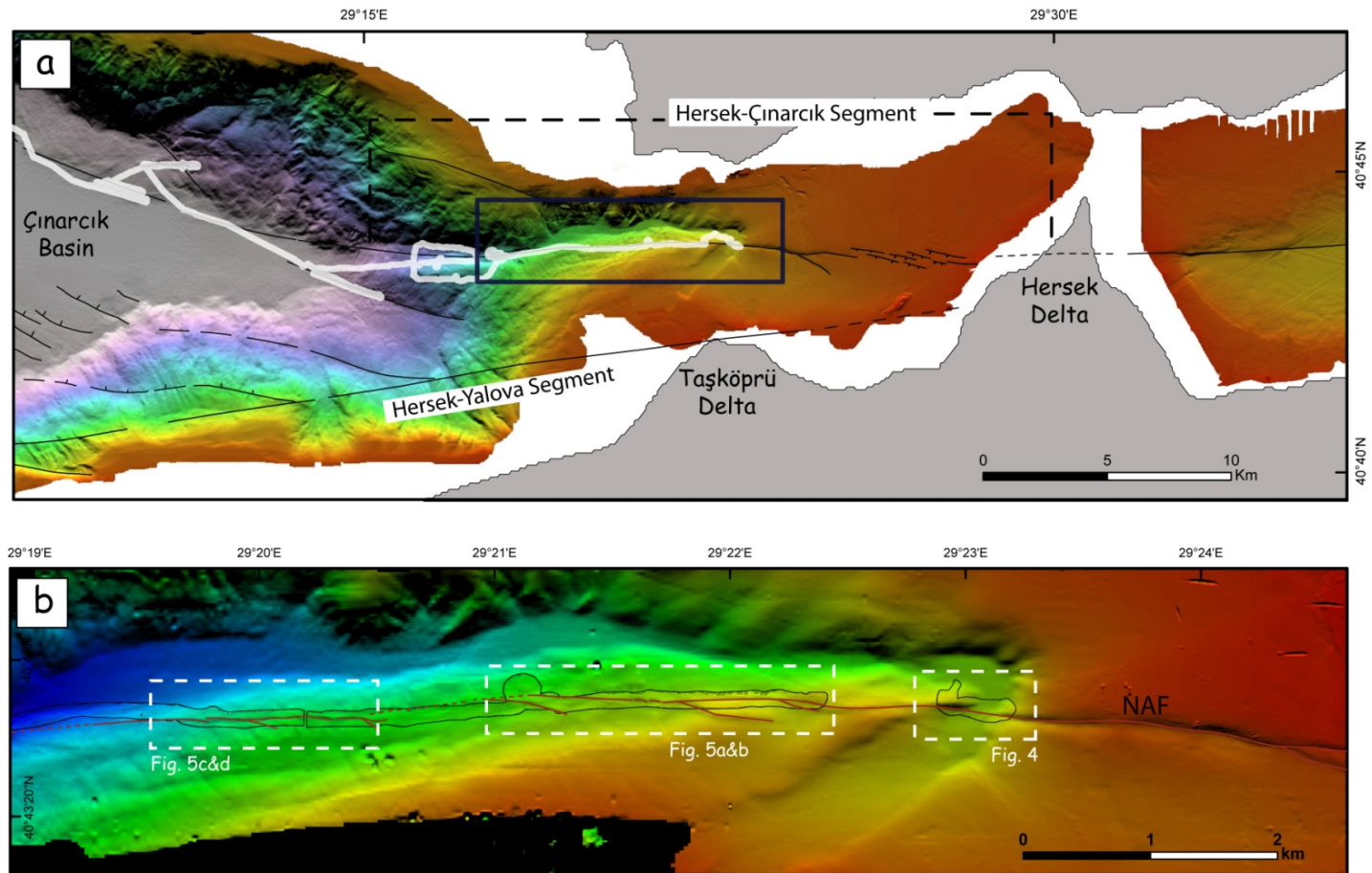


Figure 4.6 : (a) Bathymetry map of western Gulf of İzmit. The active fault segments are indicated by black lines. The white thick line shows the track of ROV microbathymetry coverage in this area along the active fault strands. The Quaternary submarine canyon (black box enlarged in Figure 3b) meets the deep Çınarcık basin in its western extremity. (b) Morphology of the submarine canyon. Map combines multibeam bathymetry (10 m resolution) with the ROV microbathymetry (black outline) (0.5 m resolution, 0.1 m vertical accuracy). Faults (red lines) are identified from the high-resolution bathymetry.

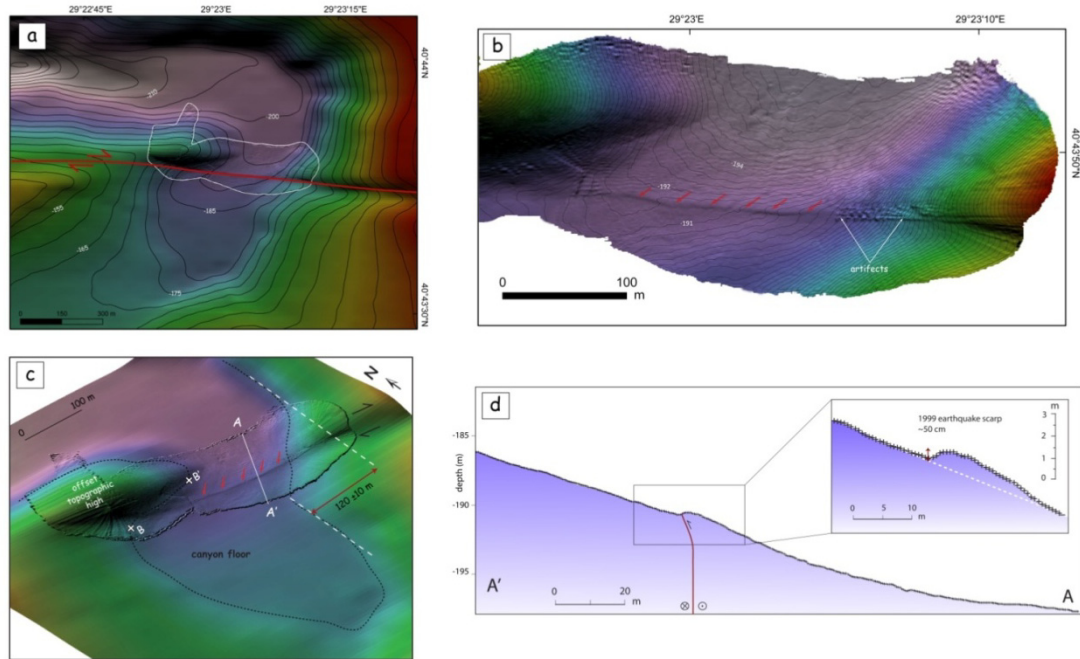


Figure 4.7 : (a) Microbathymetry combined with multibeam bathymetry resolves the morphology of the canyon floor. Contours of every 10 m are plotted from the multibeam bathymetry and every 0.5 m from the microbathymetry (b) Enlargement of the microbathymetry extract of the canyon floor. A sharp, nearly linear fault break cuts across the bottom of the canyon. Note the offset of contour lines while crossing the fault trace. (c) Oblique 3-D microbathymetry view of the canyon floor. The fault trace is sharp and continuous. Shading from north exposes the south-facing scarp clearly. Red arrows highlight the rupture trace. White line displays the location of the topographic profile. White dashed lines indicate the eastern edge of the canyon offset right laterally by the fault (120 ± 10 m). B-B' represents the offset of the eastern edge of the topographic high (130 ± 10 m) (d) Enlarged profile across the scarp on the canyon floor. Profile resolves the fine-scale morphology of the south-facing scarp with an apparent throw of 50 cm (less than one contour line in the microbathymetry).

alternating topography, generally not exceeding 50 cm were produced on land during the İzmit earthquake (Barka et al., 2002; Ferry et al., 2004). Slope-degrading processes, such as gravity collapse, sliding, talus creep, are expected to be more effective along the canyon compared to other places at the sea bottom. Therefore, sediment transport must be high enough to bury any individual event and thus the scarp at the bottom of the canyon is most likely associated with the 1999 İzmit earthquake. The InSAR modeling indicates a minimum of 2 m horizontal displacement in this area (Çakır et al., 2003b), suggesting $\sim 14^\circ$ rake giving the 0.5 m throw on the canyon floor. Similar vertical and horizontal offsets are common

especially along the Sakarya segment of the 1999 İzmit rupture (see Table 1 in Lettis et al., 2002). However, it is rather difficult to assess the individual horizontal offset related to the 1999 rupture from the ROV bathymetry due to the lack of required markers on the seafloor (comparable to man-made features on land). The cumulative right lateral offsets measured in the canyon are 120 ± 10 m in its eastern edge and 130 ± 10 m in its western edge (Figure 4.7).

Further west, the ROV microbathymetry reveals a set of significant fault breaks mostly in a left-stepping en echelon arrangement, running parallel to the E-W section and southern slope of the canyon (Figures 4.6 and 4.7). This pattern is typical in dextral displacement zones (Biddle & Christie-Blick 1985; Woodcock & Schubert 1994).

The fine-scale morphology of these submarine scarps is very well preserved and can be continuously traced in the microbathymetry over ~ 5 km. Morphological features typical of strike-slip faulting such as oblique secondary fault branches, sag ponds and push-ups (Figure 4.8), accompany the main fault trace here. Push-up ridges and sag ponds alternate at segment ends or at slight fault bends (Figures 4.8a-d). The dimensions of these features (50-80 m long; 20–30 m wide) suggest that they may have resulted from cumulative movements of past events. Topographic profiles constructed from the microbathymetry at this site resolve the fine-scale morphology of these scarps (Figure 4.9a). As in the canyon floor, nearly all the scarps face upslope to the south and their heights range between 0.5 to 6 meters. However, to calculate a more precise throw we combine the microbathymetry with the Odin Finder (2000) multibeam bathymetry (Figure 4.9b) to take into account the slope in the far field. The maximum vertical throw is measured as ~ 6.2 m along this section (Figure 4.9b). Vertical offsets of up to 2.6 m were observed along the surface rupture on land but, large vertical displacements are located only on extensional jogs mainly in Gölçük and Sapanca (Figure 4.5). Vertical throws along the main rupture zone are however much lower as expected. Therefore, vertical displacements of up to 6.2 m along the Hersek-Çınarcık segment represent at least three or more earthquakes. The fresh fault scarp morphology in the canyon slope suggests that they were most probably re-activated by a recent event that can be attributed to the western extension of the 1999 rupture.

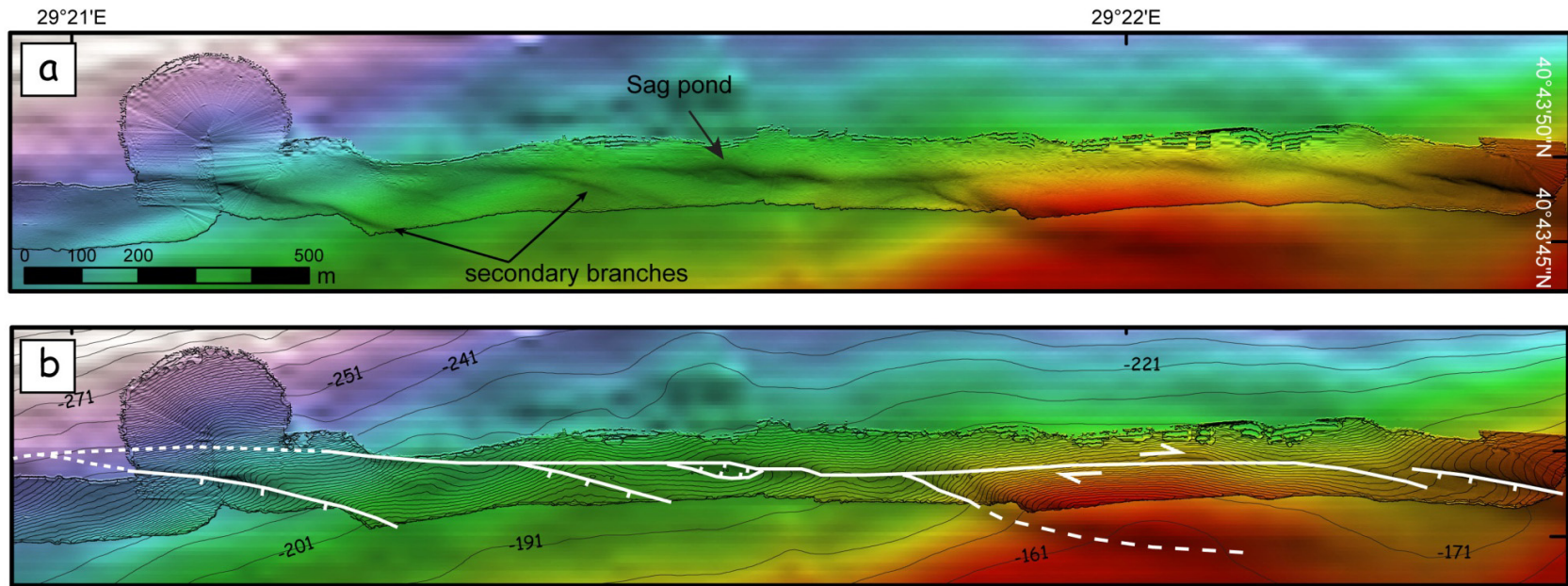


Figure 4.8 : Morphology along the southern slope of the submarine canyon from the combined bathymetry as in Figure 4. **(a)** Central part of the submarine canyon. A continues fault break can be traced with left-stepping en echelon steps, secondary branches and a sag pond are also found. **(b)** Fault map deduced from the microbathymetry with contours at an interval of 1 m.

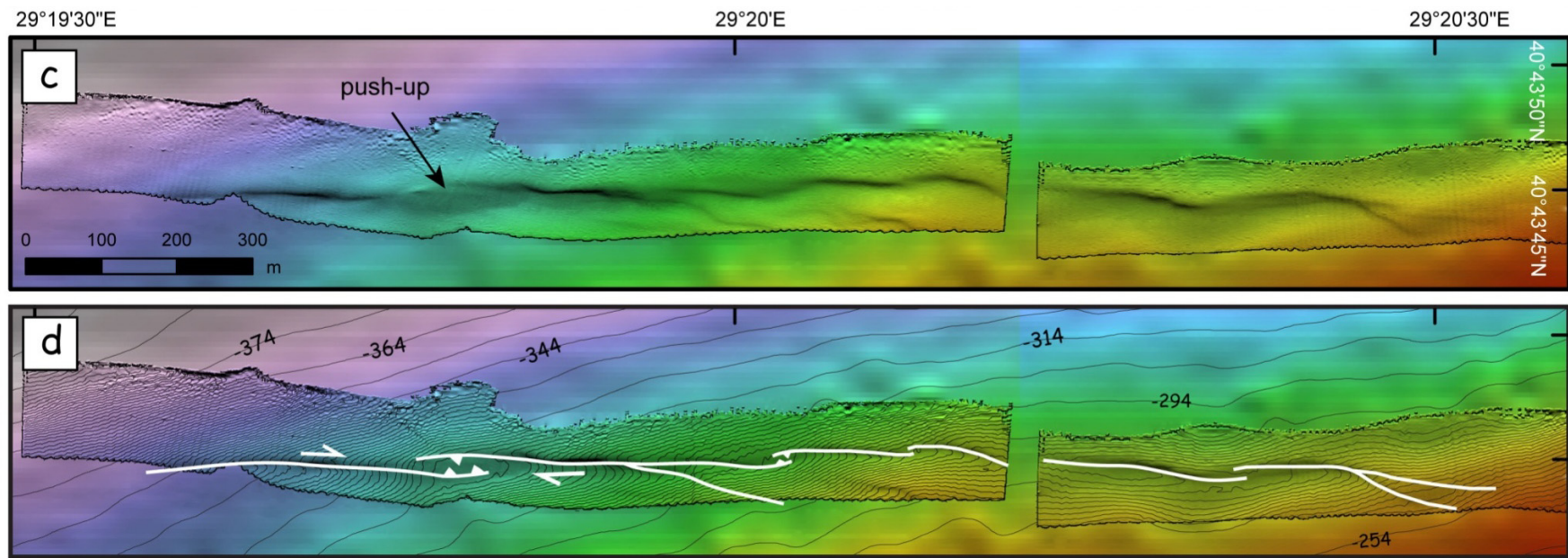


Figure 4.8 : (c) Westernmost continuation of the microbathymetric strip. (d) Fault map deduced from the microbathymetry with contours at an interval of 1 m.

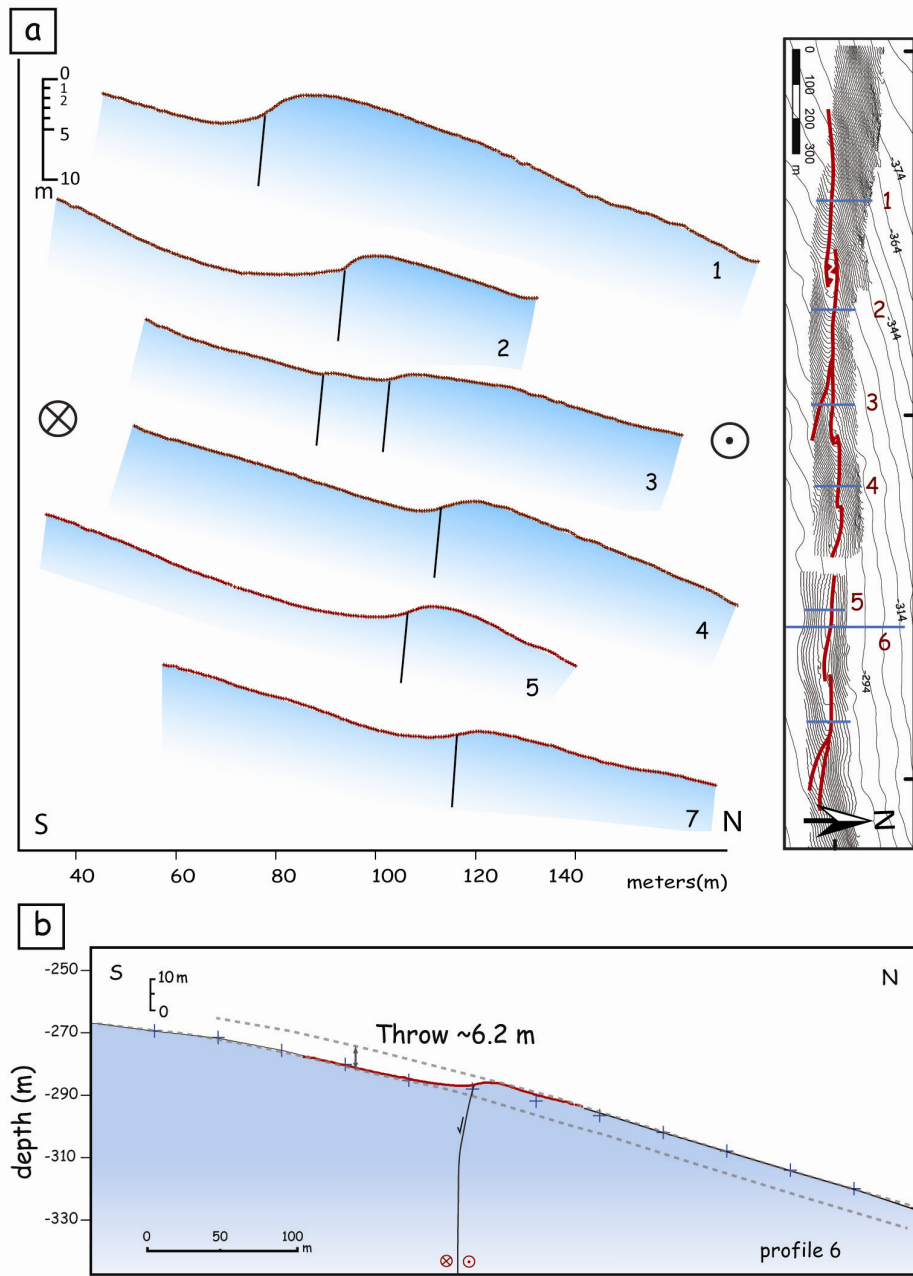


Figure 4.9 : (a) Profiles constructed from the ROV microbathymetry with locations shown on the side map (same as Figure 8d). Note that all the scarps face southward. Vertical exaggeration is 2. (b) Profile constructed with combined bathymetry. The microbathymetry data (red line) resolves details of the scarp morphology that are not determined with the bathymetry background (blue crosses). Blue dashed line represents the initial slope morphology before faulting. Fault offsets the slope with a clear normal component. Apparent throw measured here is 6.2 m.

These cumulative scarps can be associated with some of the historical earthquakes that are thought to have taken place on this segment, e.g., 1509, 1719, 1754 and 1894 (Ambraseys and Finkel 1991, 1995; Ambraseys 2002).

4.3.4 Coulomb stress modeling of the 1999 İzmit earthquake

We have conducted Coulomb stress modeling in order to understand how the active faults in the eastern Sea of Marmara were affected by the static stress transfer due to the 1999 İzmit earthquake.

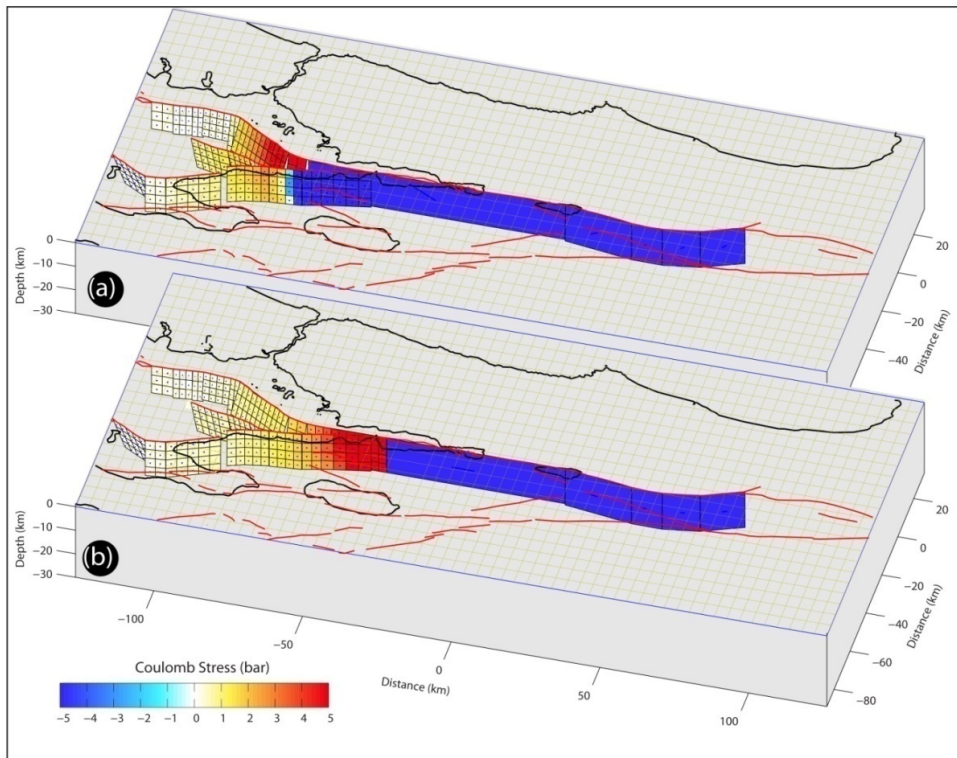


Figure 4.10 : Coulomb stress changes on active faults due to the 1999 İzmit earthquake calculated using Coulomb 3.1 software (Toda et al., 2005) with a tapered slip distribution and a coefficient of friction of 0.4. Two possible rupture terminations for the İzmit earthquake were tested. In the first model (a) the rupture reaches to the entrance of Çınarcık basin as we interpret in this study whereas in the second model (b) it terminates just east of the Hersek delta. Note that in the first model the Hersek-Yalova segment, unlike the Princes Island fault, is not loaded by the İzmit earthquake.

We calculate Coulomb stress change on faults considering two scenarios; rupture terminating (1) near Hersek on the eastern side of the delta at the tip of Gölcük segment or (2) near Yalova about 30 km west of Hersek at the tip of the Hersek-Çınarcık segment. We calculate the static stress resolved on the active faults of

Armijo et al. (2002) using Coulomb 3.1 software developed in United State Geological Survey (Toda et al., 2005). In the first model, the rupture tip is placed at the western end of the Gölcük segment located east of Hersek Peninsula around the tip of the Karamürsel basin. We use a model fault of ~120 km long with distributed (tapered) slip (equivalent of $M_w=7.4$) and a coefficient of friction of 0.4. As illustrated in Figure 4.10a, this model predicts that the İzmit earthquake causes to the highest static stress changes on to the Hersek-Çınarcık and Hersek-Yalova segments. However, if the İzmit rupture is extended 30 km further west rupturing the Hersek-Çınarcık- segment, the stress on the Hersek-Yalova segment does not increase, but decreases significantly becoming negative. On the other hand, the Princes Islands fault receives 3-4 bars more static stress (Figure 4.10b). Therefore, in this scenario, while the earthquake potential on the Hersek-Yalova segment is reduced by the termination of İzmit rupture at the entrance of Çınarcık basin, the area of high static stress increase moves further west, bringing the southern and northern boundary faults of the Çınarcık basin closer to failure.

4.3.5 Discussion and conclusions

The analysis of the ultra-high resolution bathymetry data gathered during the MARMARASCARPS cruise presents evidence that the 1999 İzmit earthquake rupture extends in Gulf of İzmit further west of the Hersek delta and continues with the Hersek-Çınarcık segment. The supporting evidence is the presence of a fresh fault scarp with a relatively small vertical offset (i.e., 50 cm) across the floor of a Quaternary submarine canyon located ~10 km west of Hersek at 29.38° E longitude (Figure 4.7). Westward, distinctive fault breaks with higher throws (up to 6.2 m) are traceable over 5 km in the extracts of microbathymetry up to 29.326° E (Figure 4.6).

Although the 1999 break could not be pointed out individually as clearly as in the canyon floor, the fine scale morphology of these fault scarps implies that the rupture continues up to the entrance of the Çınarcık basin reaching a total length of ~145 km at around 29.24°E. Instead of stopping in the middle of the straight Hersek-Çınarcık fault segment, the rupture must have propagated all the way to the entrance of the Çınarcık pull-apart basin where the strike-slip tectonic regime of the NAF significantly changes into the oblique extension (Figure 4.11) (Armijo et al., 2002). Our microbathymetry extracts at the easternmost section of the Çınarcık basin do not

present any evidence for a recent surface rupture, suggesting that 1999 İzmit earthquake rupture did not proceed further west.

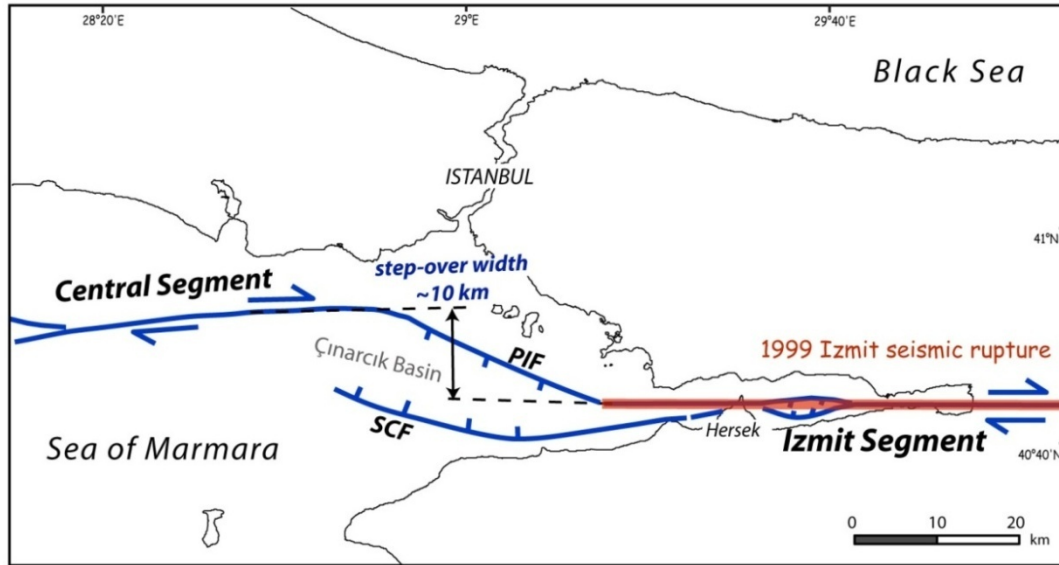


Figure 4.11 : Schematic active fault map of the eastern Sea of Marmara showing the 10 km-wide step-over between İzmit and Central fault segments. Red line marks the western extension of the 1999 İzmit earthquake stopping at the entrance of Çınarcık pull-apart basin. (PIF: Princes Islands Fault, SCF: Southern Çınarcık fault).

Dynamic rupture studies of earthquakes as well as the historic observations show that large step-overs (> 4 km wide) play a crucial role on earthquake rupture termination (Barka and Kadinsky-Cade; 1988; Harris and Day, 1993a; 1999; Oglesby 2005; Wesnousky 2006; Elliott et al., 2009). In a recent study, Elliott et al. (2009) suggest that the gradual increase in complexity toward a stepover will incrementally reduce the rupture energy, causing a gradual decrease of the coseismic slip and prevent the rupture propagation through the step-over. Therefore, we consider that the Çınarcık pull-apart basin between the large step-over (~ 10 km wide) of the strike-slip İzmit and Central segments in the Sea of Marmara most probably acted as a barrier to the rupture propagation and induced the termination of the 1999 İzmit earthquake (Figure 4.11).

We conclude that the 25-km long Hersek-Çınarcık segment was broken as the fifth segment during the 1999 İzmit earthquake together with the other segments (i.e. Karadere ~ 30 km, Sakarya ~ 25 km, Sapanca ~ 30 km, Gölcük ~ 35 km) mapped in the field (Barka et al., 2002). Consequently, the static stress transferred by the İzmit earthquake on to the faults bounding the Çınarcık basin is now significantly (3-4

bars) higher than that could have caused by the rupture termination east of Hersek (Figure 4.10b). On the other hand, the İzmit earthquake does not promote failure of the Hersek-Yalova segment since it is located mostly in the stress shadow (i.e. areas of stress increase). Because the Hersek-Çınarcık segment is broken during the İzmit earthquake, it is unlikely that the future earthquake can nucleate around Hersek and propagates westward, breaking both the Princes Islands and Central segments.

4.4 1912 Ganos earthquake rupture in the Sea of Marmara: rupture geometry and morphology of the scarps

4.4.1 Introduction

The 9 August 1912 Ganos (Mürefte) earthquake ruptured the Ganos segment of the NAF, creating widespread damage and important loss of life (Ambraseys and Finkel, 1987) (Figure 4.12). Due to the world primitive seismograph network of the time, an accurate instrumental location, hence the exact magnitude of the earthquake is not established. However, a reliable surface-wave magnitude calculation by Ambraseys and Finkel (1987) gives a surface Richter magnitude (M_s) of 7.4 ± 0.3 for the 1912 earthquake, indicating a large rupture event similar to the M_w 7.4, 1999 İzmit earthquake. Ambraseys and Finkel (1987) suggest a co-seismic faulting that crossed all the land between the Gulf of Saros and Sea of Marmara with a total rupture length of 50 km. Although previous studies agree that the earthquake involved at least 45 km of surface rupture along-strike during 1912 earthquake, the total length of the co-seismic fault segment and the slip distribution along whole strike are poorly known. However, it is crucial to gather this information in order to determine the long-term behavior of the Ganos fault zone and hence to constrain the seismic gap in the Sea of Marmara.

Small tsunami waves suggesting a possible submarine extension of the rupture are reported along the shores of the Sea of Marmara at the time of the 1912 event but quantification of the phenomenon appears difficult (Mihailovic, 1927; Ambraseys and Finkel, 1987). The tsunami and macroseismic effects suggest that the rupture may have extended at least several tens of kilometers under the western Sea of Marmara although.

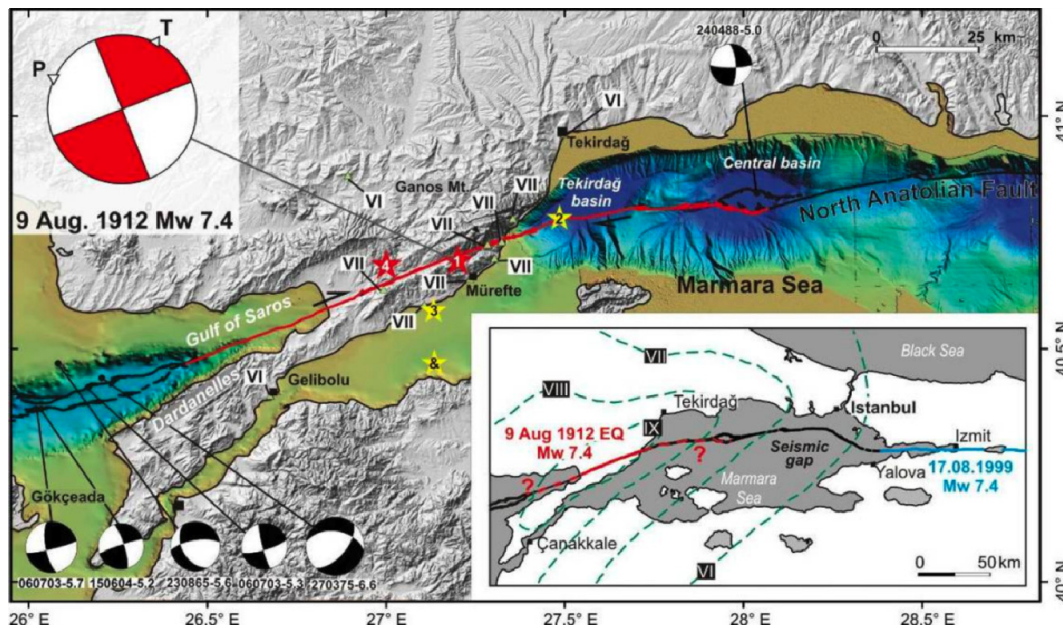


Figure 4.12 : The 1912 Ganos earthquake rupture area in western Marmara (Aksoy, 2009, fig. 5.2). The red line indicates coseismic rupture of the 1912 seismic sequence with the red stars pointing the location of the two main shock calculated by Ambraseys and Finkel, 1987 who provided the intensity map of the August shock shown in the inset. Note the rupture extending from the Gulf of Saros in the Aegean to the Central basin in Marmara Sea.

4.4.2 Field observations of the 1912 Ganos earthquake rupture on land

Field studies on the surface rupture of the 1912 earthquake can be divided into two groups. First group of field reports were the contemporary ones, which generally provide information on the amount of damage and loss of life right after the 1912 Ganos earthquake. The surface faulting is described in a more general way as “cracks” and is not distinguished as surface deformation types. But numerous field photos from the reports illustrate ground ruptures between Gulf of Saros and Gaziköy with surface faulting typical of strike-slip earthquakes and allow us to identify the type of co-seismic deformation (Sadi 1912; Mihailovic 1927). Accordingly, the coseismic features of moletracks, normal fault scarps and large landslides can easily be seen from these photos (Figure 4.13). The length and continuity of the fault breaks confirms the large-scale surface faulting. Mihailovic (1927) reports a 2.6-km-long crack at Gaziköy consisting of short sections, which longest is 840 m with an opening of 50-60 cm and a depth of 1.80 m. He notes that the southeastern block of this crack has subsided for 40 cm. Liquefaction has been reported at many parts of the Ganos and Gelibolu region.

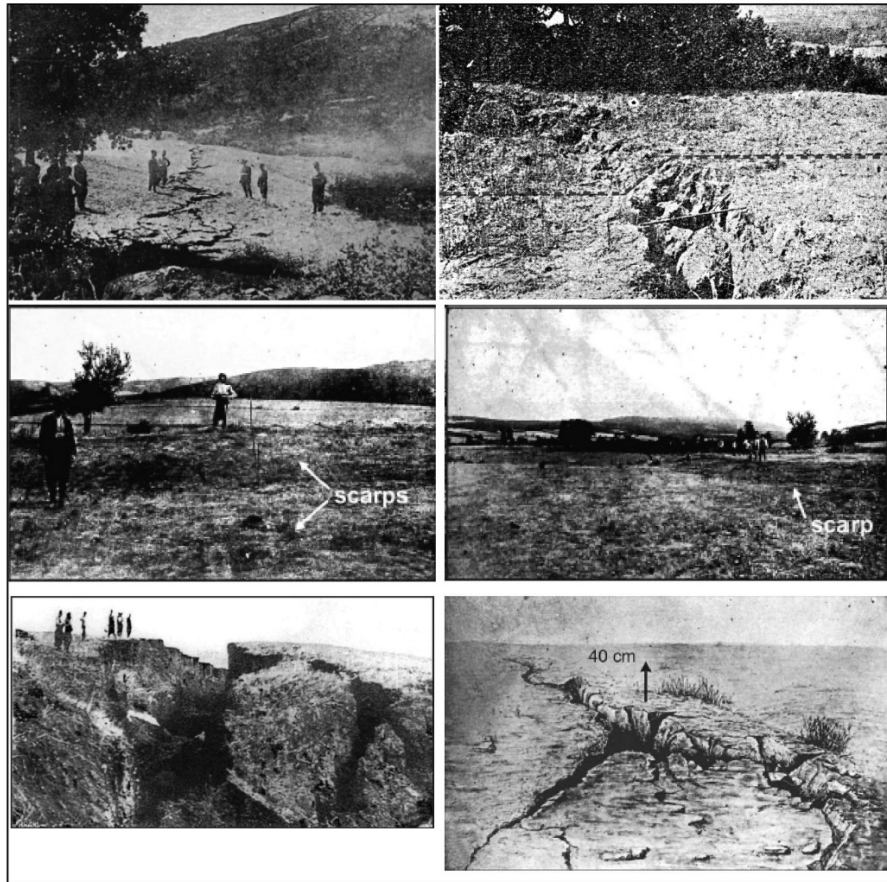


Figure 4.13 : Photos showing surface deformation (landslides and surface ruptures) taken after the 1912 earthquake (Sadi 1912; Mihailovic 1927; Ambraseys and Finkel, 1987).

Field investigations carried out along the Ganos fault indicate that offset features associated with the 1912 event can still be identified (Altunel et al., 2000; Altınok et al., 2003; Aksoy et al., 2009). The offset measurements along the Ganos fault show slip as much as 5.5 m close to the shoreline and about 5 m just before the fault enters in to the sea in Gaziköy. This, as in the case of Gölcük, suggests strongly that the rupture must have continued significantly towards the east on the sea floor of the Sea of Marmara. Base on the offset measurement, it is also suggested that the whole onshore section of the fault ruptured during 1912 earthquake (Altunel et al., 2000; Aksoy et al., 2009). Surface deformations of the 1912 earthquake were described in contemporary reports as “cracks” (Macovei, 1912; Mihailovic, 1927; Sadi, 1912). No fault rupture was reported as such, but pictures of mole-tracks and en echelon cracks clearly suggest prevalent right-lateral slip (Ambraseys and Finkel, 1987).

About a month after the 9 August 1912 Ganos event ($M_s=7.3$), another large earthquake ($M_s = 6.8$) struck again the area between Saros bay and Marmara Sea on 13 September 1912. Aksoy et al. (2009) have retrieved a relative source time function by analyzing the seismic waveforms of the 13 September and 9 August shocks digitized from old seismograms. They deduced source duration of 40 seconds for the 9 August earthquake. Taking an average unilateral rupture propagation of 3 km/s, this duration implies a rupture length of 120 km, consistent with the earthquake size of $M_w 7.4$, similar to the 1999 İzmit earthquake on the other side of the Sea of Marmara. Assuming a rupture length of 30 ± 10 km for the second shock in September, Aksoy et al. (2009) infer a total rupture length of 150 ± 20 km for the 1912 seismic sequence. They suggest that the 1912 rupture extend most likely from the Saros Trough towards east and reach the Central Marmara Basin, consistent with major geometric complexities along this section of the North Anatolian Fault, and in agreement with Armijo et al. (2005) (Figure 4.12). If the 1912 rupture indeed went all the way to the Central basin then this should be recorded on the sea floor morphology and sedimentation. Therefore in this study, using short interface cores and the ultra high-resolution microbathymetry acquired by ROV Victor along the fault zone between Ganos and Central basin (Figure 4.15), we analyze the fine detail morphology of submarine fault scarps and sedimentation rates from ^{210}Pb to find clues about the 1912 earthquake rupture.

4.4.3 Morphology of submarine fault scarps in Tekirdağ and Central basins

Map of submarine active faults from Le Pichon et al. (2001) and Armijo et al. (2002) shows that the Ganos fault enters into the Sea of Marmara striking NE-SW with the same strike on land and continues another 15 km before making a relatively sharp and important bend in south west of the Tekirdağ basin. This section of the fault is partly covered by the multibeam microbathymetry survey during the MARMARASCARPS cruise as shown in Figure 4.15.

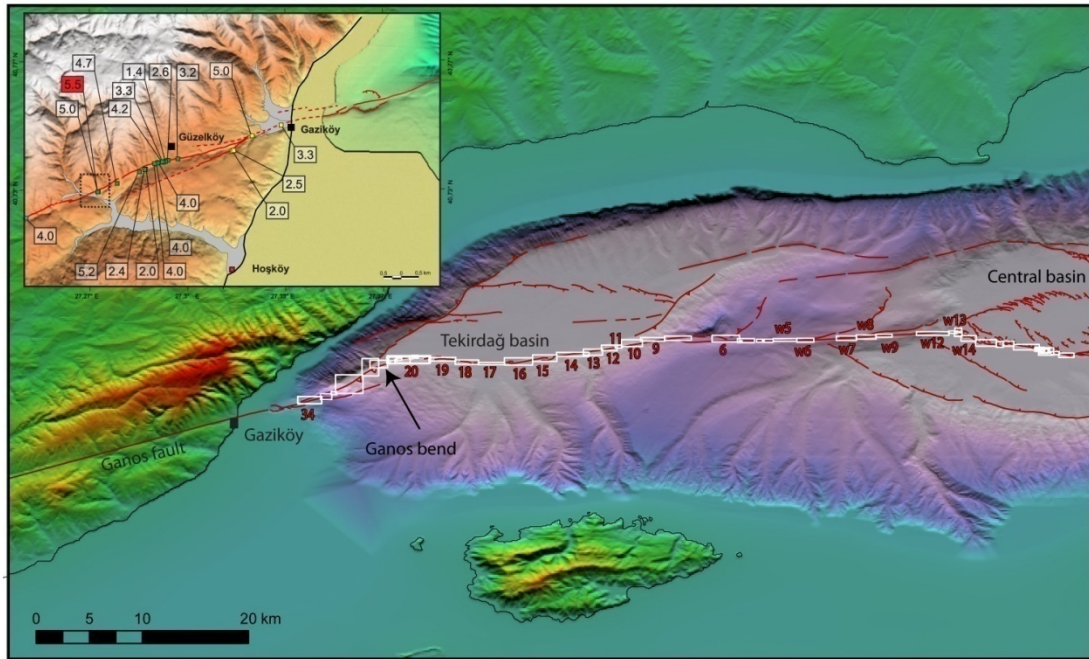


Figure 4.14 : Locations of the ultra-high-resolution bathymetry strips (white boxes). Inset map shows the offset measurements along the 1912 earthquake rupture (from Aksoy, 2009; fig 6.2). Box numbers are shown with red numbers.

The microbathymetry data (0.5 m) are merged with 25 m gridded multi beam bathymetry acquired by Le Suroit (Le Pichon et al., 2001; Armijo et al., 2002). The closest microbathymetry to the shore is shown in Figure 4.15. A sharp and linear fault break is immediately seen in the first microbathymetry strip (Box 34 in Figure 4.14) where Ganos fault enters the Sea of Marmara west of the compressional bend. This NE-SW fault break creates scarp facing SE. Fault scarps are measured to be reaching up to 5 m. Further northeast the fault break could not be traced up to the Tekirdağ restraining bend where en echelon faults with thrust component are observed both in microbathymetry and side scan sonar images (Figures 4.16 and 4.17). The geometry of scarps at the Ganos restraining bend in the south-western Tekirdag Basin is illustrated in (Figure 4.16). Fault segments about 500-800 m long and striking NE on the average are disposed in a regular right-stepping en echelon array. One-to-one correspondence between scarp features seen in the microbathymetry and in the side-scan sonar images is very striking. NE-striking, right-stepping en echelon structure here associated with transpression provides support to the inference of a component of NW-SE shortening expressed by north-westward directed thrusting as the south Tekirdag fault veers into the Ganos retraining bend. As the fault veers EW along the southern margin of the Tekirdag basin, fault scarps

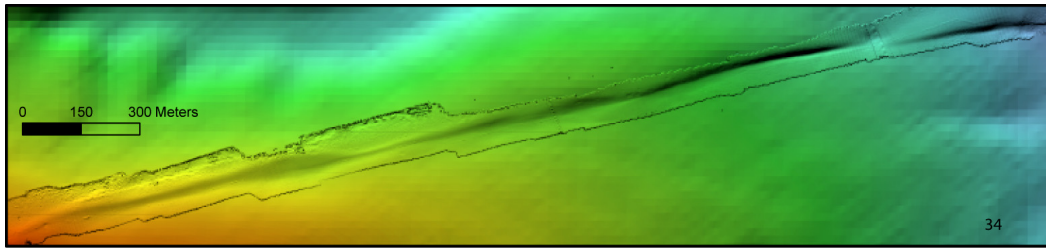


Figure 4.15 : Microbathymetry of map showing the trace of the Ganos fault near the shore (box 34 in Figure 4.14).

present features of typical of strike-slip faulting. From this point forward up to the entrance of Central basin, fault scarps can be continuously traced from the microbathymetry strips presenting remarkable rupture morphology.

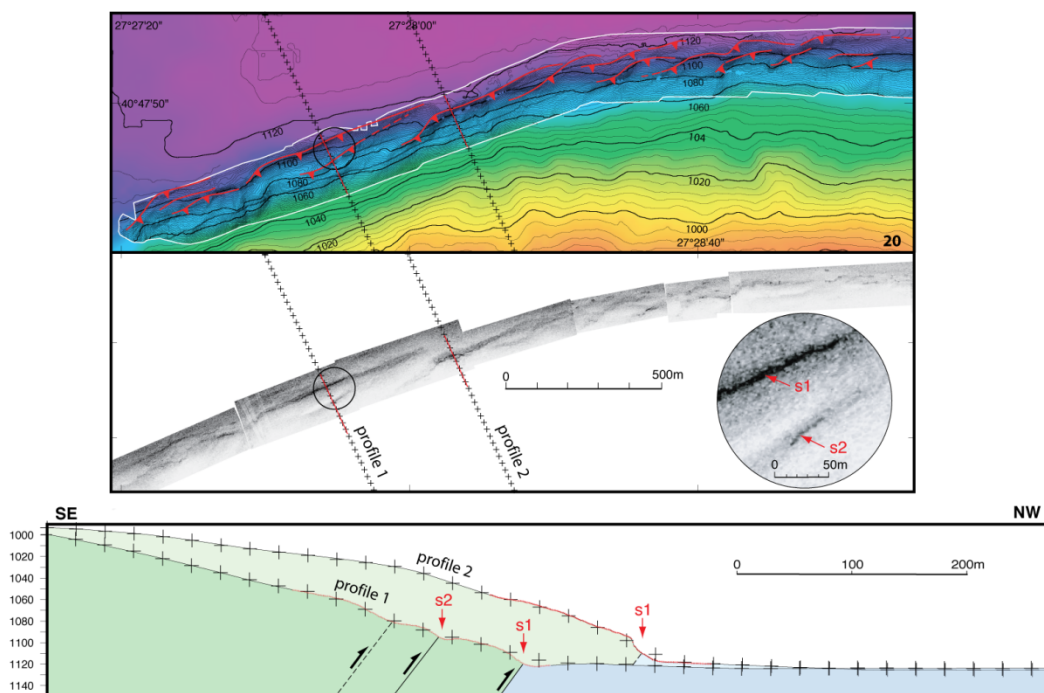


Figure 4.16 : (a) Morphology of combined strike-slip and thrust scarps in the southwestern Tekirdag Basin. The fault scarps are in a clear right-stepping en echelon array (Box 20 in Figure 4.14). (b) Corresponding side-scan sonar image. Encircled close-up identify sharp individual breaks s1 and s2 c) Micro-bathymetry profiles. Profile 1 show that the individual scarps are at the base of larger scarps with warped morphology, suggesting shortening associated with a component of north-eastward thrusting. Profile 2 shows a single cumulative scarp with convex shape. Individual scarp at its base (s1) is made of a steep escarpment about 10 m high (largely a free face) and a similar height of sediment talus.

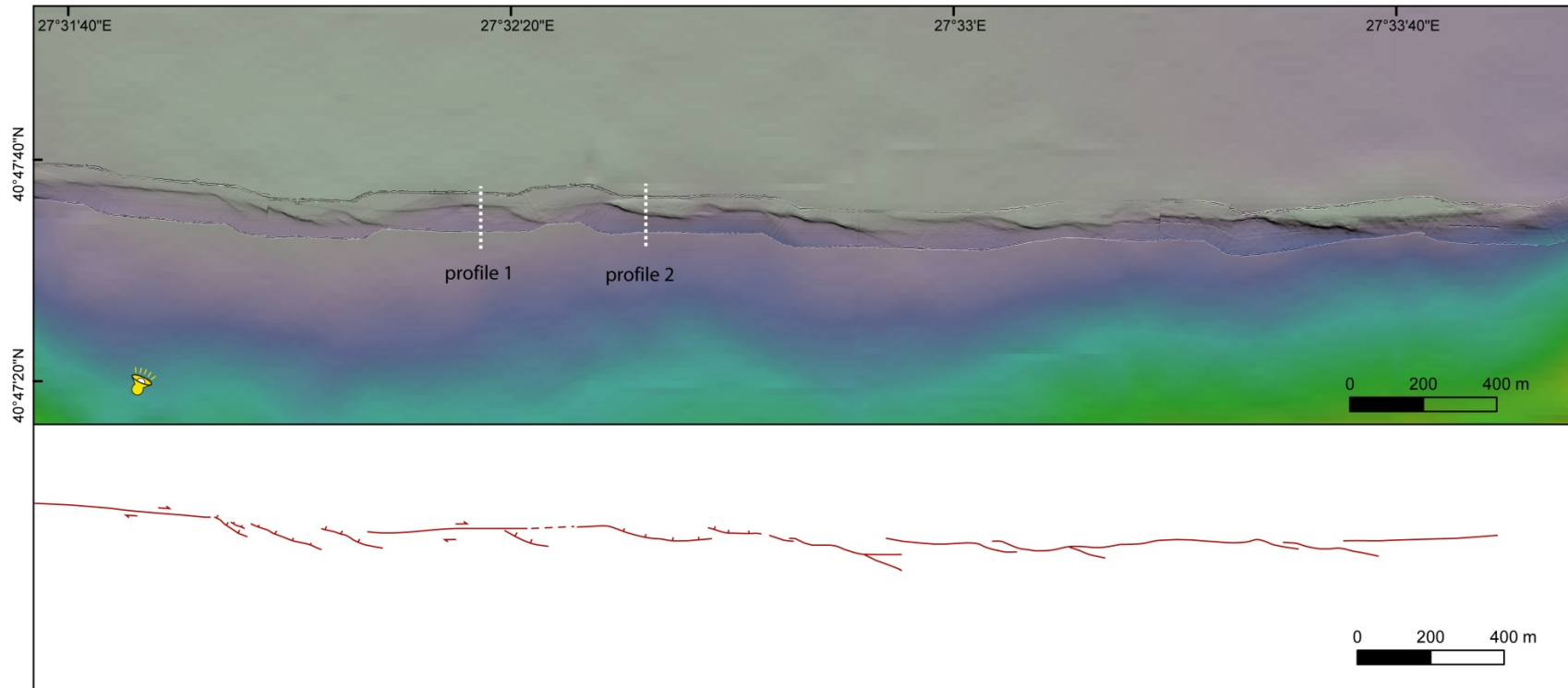


Figure 4.17 : Microbathymetry with Le Suroit bathymetry in the background and interpreted faults (red lines at lower panel) along the southern margin of the Tekirdağ basin (box 16-17 in Figure 4.14).

The micro-bathymetry in Figure 4.17 reveals an outstanding rupture zone comparable to the 1999 earthquake rupture features on land. Here, we observe a rupture zone with antithetic normal faults and left-stepping fault arrays. Two topographic sections are constructed from the microbathymetry (Figure 4.17 and 4.18). The scarp morphology expose that the fault carries composite normal and strike-slip component. Profile 1 resolves the morphology of the fault scarp with a total throw of 2.6 m (Figure 4.18).

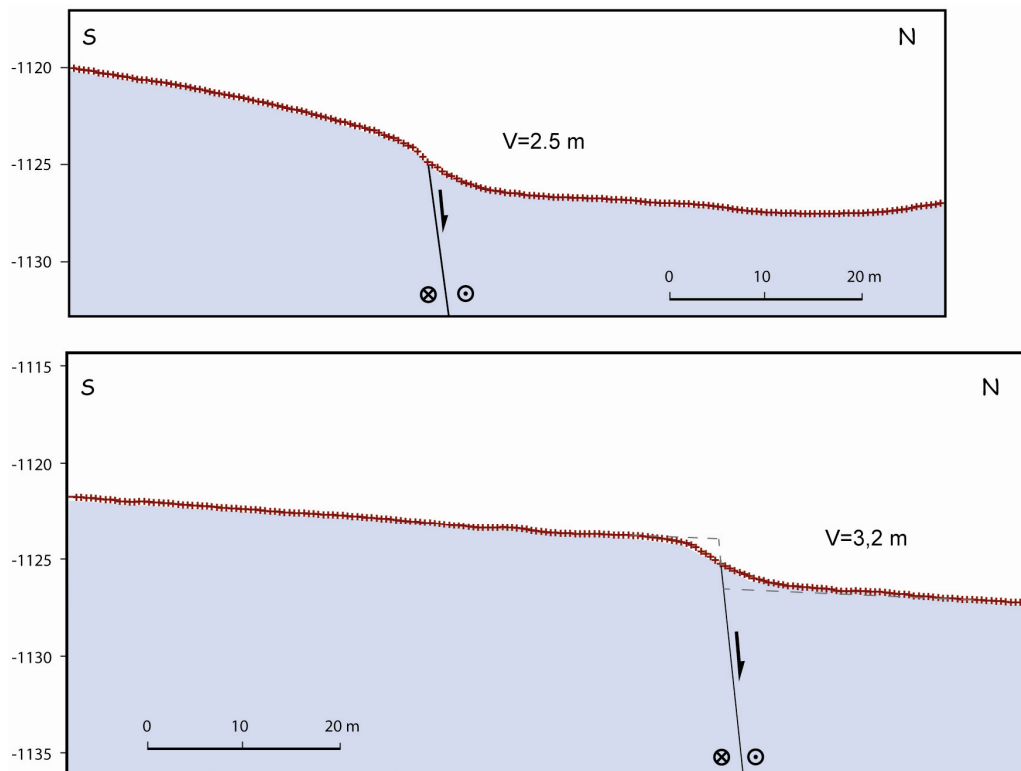


Figure 4.18 : Micro-bathymetry profiles. Profile 1 (upper panel) and Profile 2 (lower panel) shows that the individual scarps has composite normal and strike-slip component. (V for vertical throw).

Profile 2 is taken along the antithetic fault and presents a vertical thros 3.2 m consistent with its normal faulting component (Figure 4.18). The morphology of the scarps shows that they are draped by sediments, but the overall geometry looks quite well preserved and less eroded. Similar throws are observed on land after the 1999 Izmit and Düzce earthquakes. A remarkable 3.7 m vertical throw (Akyüz et al., 2002) was measured right after the 1999 M 7.2 Düzce earthquake. Nevertheless, these throws may possibly comprise at least two events as well. Hence, another sharp, linear break at the base of a cumulative scarp about 10 m high is found where the fault crosses a submarine valley outlet (Figure 4.19). There, the flat bottom surface

appears to have been recently beveled (possibly by strong downward currents and sediment transport along the channel), producing an excellent marker for the last faulting events. The profile in Figure 4.19 b shows a vertical free face about 1-1.5 m high flanked by a talus slope to the north and by an eroded scarp crest to the south. Therefore the scarp associated with the last event does not explain the total vertical offset of about 2-3 m observed for the originally flat surface. This suggests that a previous event with similar throw has contributed to the total offset.

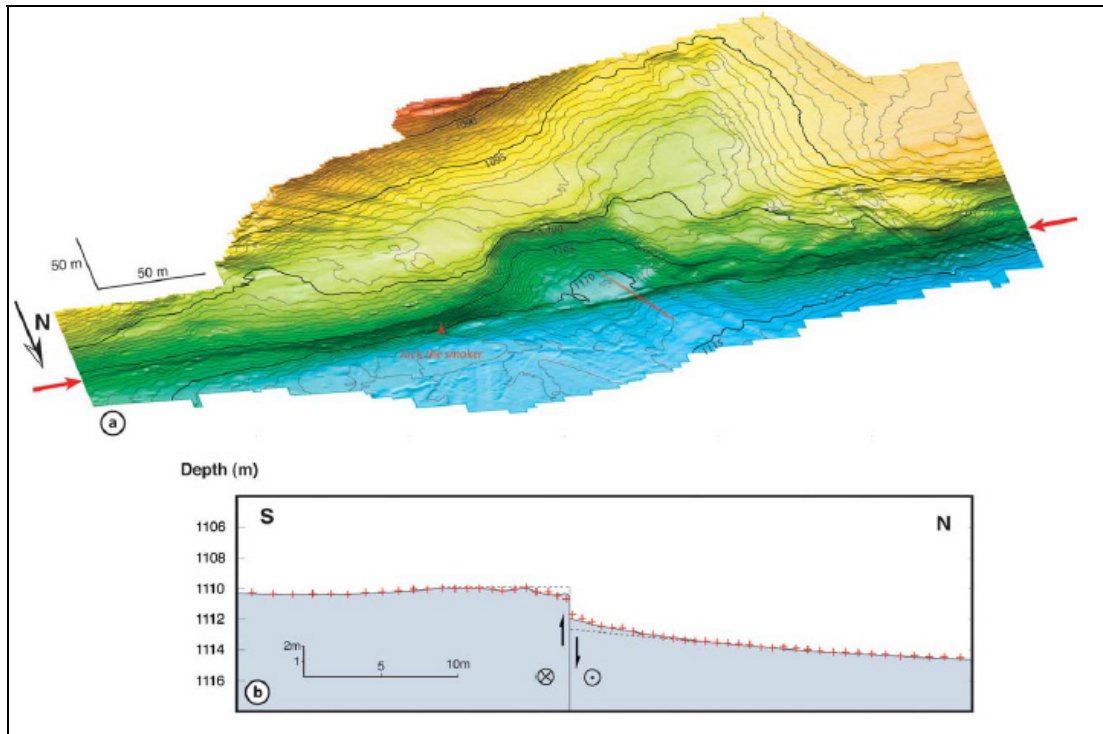


Figure 4.19 : (a) Oblique 3D micro-bathymetry view of 10 m-high cumulative scarp and smaller individual break that is very linear and continuous over the sea-bottom. Contours every 0.5 m. Small red crosses locate detailed profile. Red arrows indicate fault trace (Armijo et al. 2005). (b) Enlarged profile across individual scarp with nearly vertical free face 1-1.5 m high. No vertical exaggeration. Dashed line suggests cumulative offset of initially flat bottom surface, possibly resulting from last two events. Location of active vent is indicated.

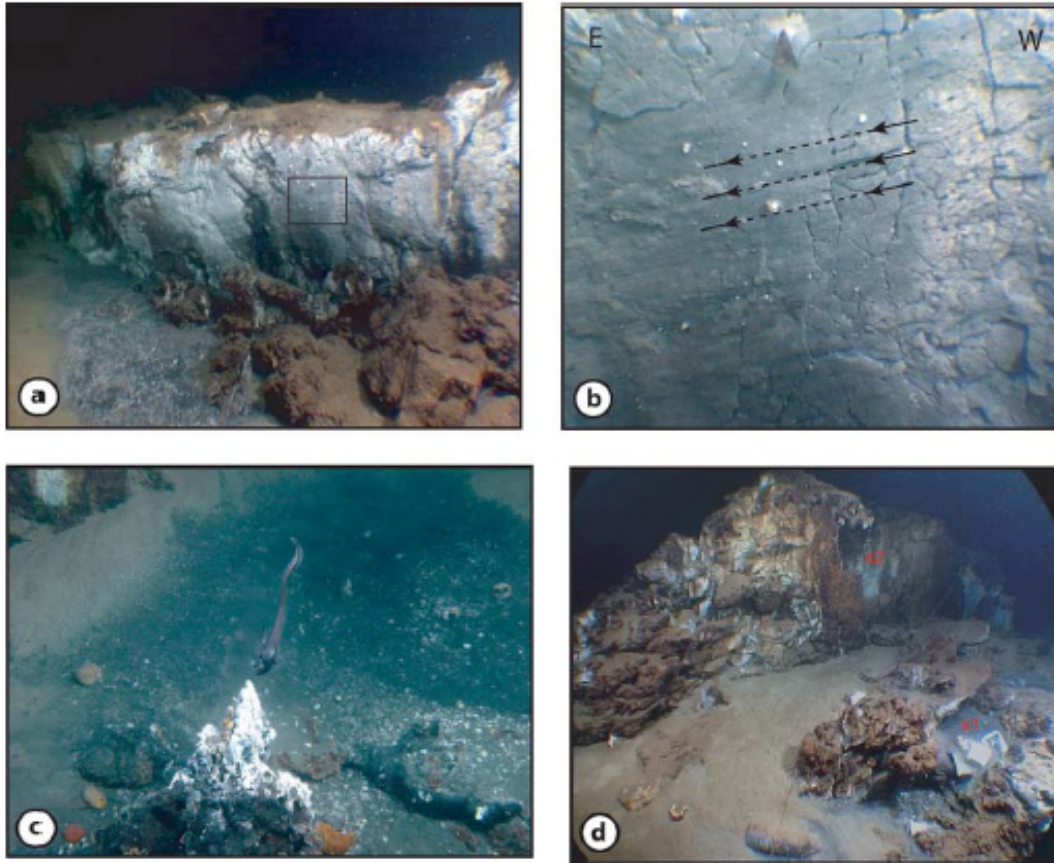


Figure 4.20 : Sea-bottom pictures of earthquake scarps in south-eastern Tekirdag Basin. (a) Fresh scarp corresponding to last event. Vertical free face 1-1.5 m high corresponds exactly to that seen in profile (Figure 4.19) locally the scarp reveals a thrusting component. Black bacterial mats with small white shells and brown authigenic carbonates (broken slabs) are seen at scarp base. Carbonate-cemented sediments and bacterial mats are also present on top of the scarp. View to SE. (b) Enlargement (box in a) shows slickensides with 15° rake substantiating dominant right-lateral motion and 4-6 m net slip for last earthquake rupture. Salient white objects are bivalve shells. View to South. (c) Cold seeps, black bacterial mats, authigenic carbonate slabs and active vent along break. The vent (location in Figure 4.19) is capped by white microbial mat. (d) Horizontal authigenic carbonate slab 10 cm thick appears associated with past seepage and venting. The carbonate slab has been broken by last-earthquake rupture (right side). Vertical scarp to the left (1-1.5 m high) probably remains from penultimate event. View to SW.

Locally the scarp appears in overhanging attitude, which suggests a secondary thrusting component. A close-up of the free face reveals slickensides attesting to the prevailing right-lateral motion (Figure 4.20a). A net oblique slip of 4-6 m is required

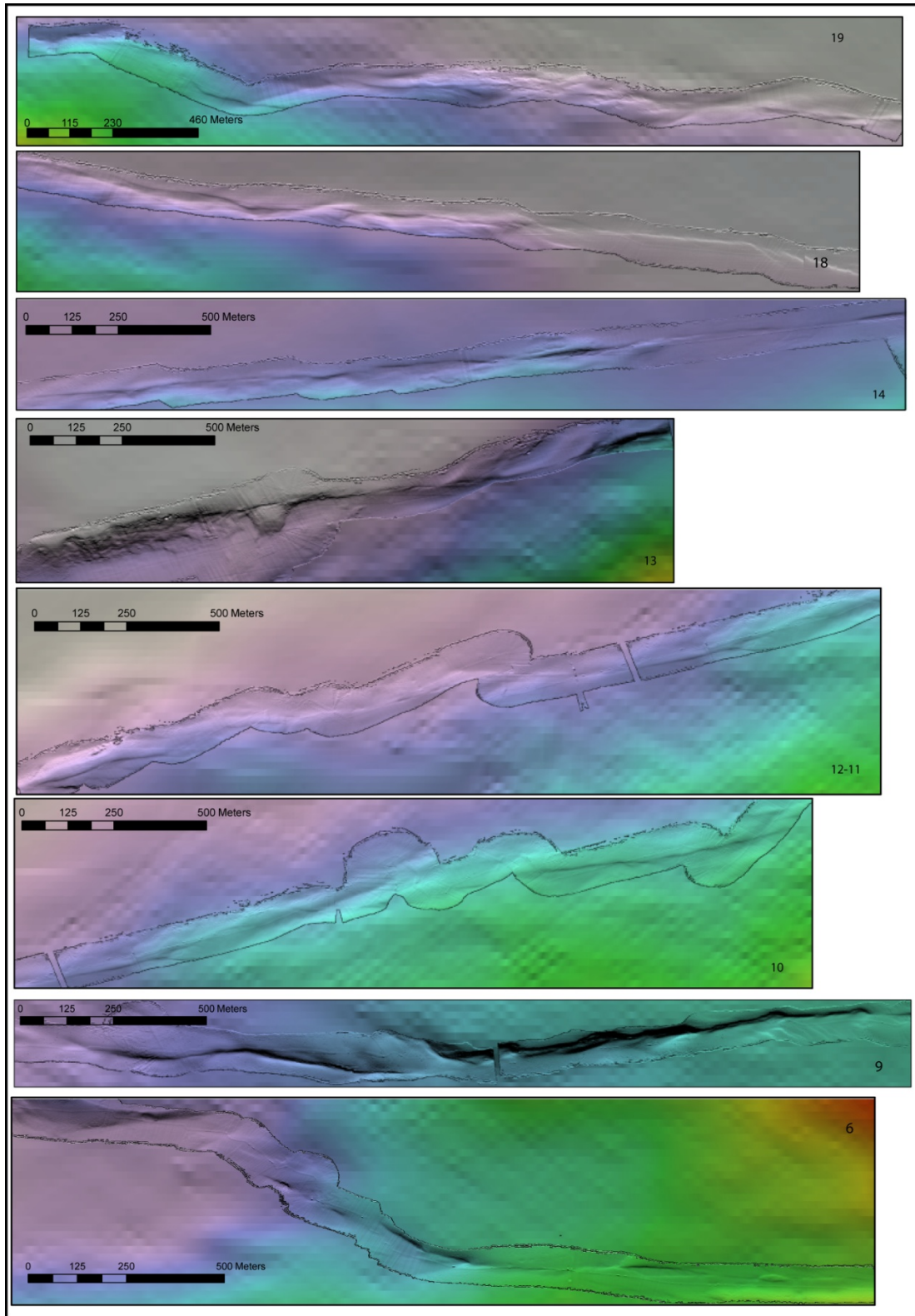


Figure 4.21 : Successive microbathymetry strips from west to east (19 to 6) in the Tekirdağ basin (see Figure 4.14 for their locations).

for the last faulting increment to be consistent with both the exposed free face and the slickensides, and about twice this amount to explain the total vertical offset of the flat surface. Conspicuous zones of cold fluid and methane seepage with associated bacterial mats, authigenic carbonate crusts and symbiotic life were discovered with the ROV in close spatial association with the submarine fault scarps, suggesting that the active fault zones control the fluid circulation within the sedimentary pile (Figure 4.20c, d). These morphologically sharp and well-preserved scarps that found at the floor of the Tekirdag basin can be followed continuously for almost 20 km to the east of the Western high. The micro-bathymetry also shows that opposite north- and south-facing scarps alternate along strike, attesting that there is no systematic vertical offset of the morphology; thus the prevailing motion across the fault is strike-slip.

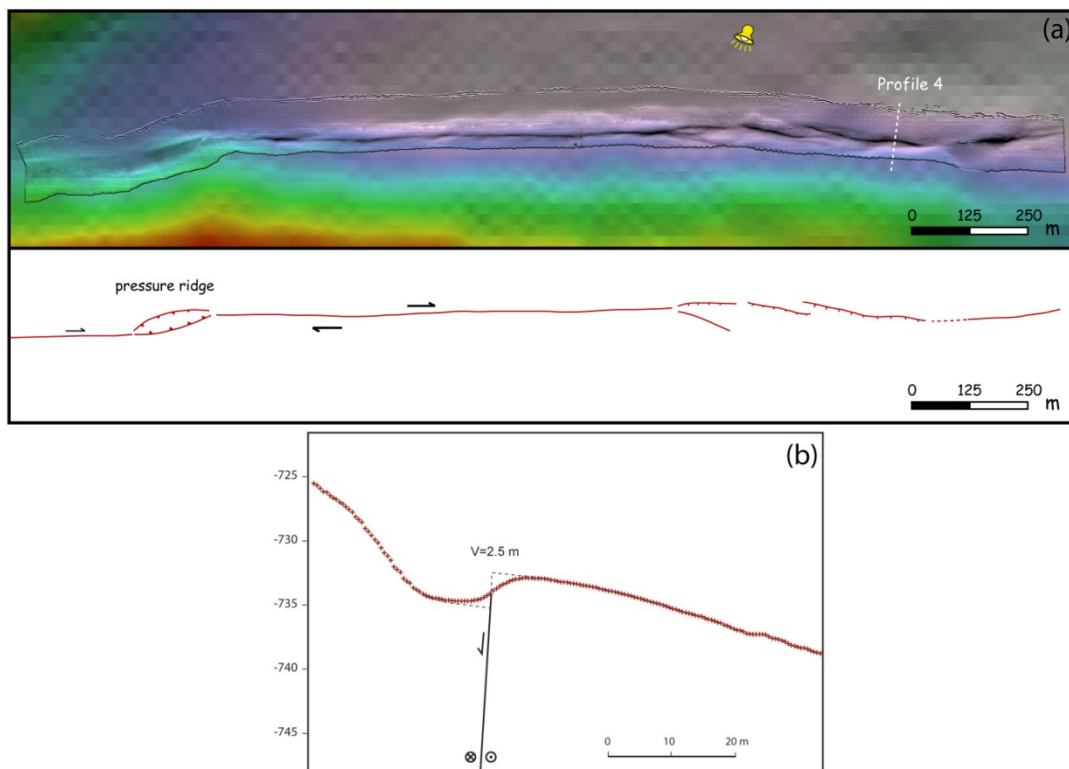


Figure 4.22 : (a) Morphology of EW-striking, purely strike-slip fault scarps across the Western High (for location see Figure 4.14 box w5). (b) Microbathymetry profile depicts the morphology of an individual scarp with a vertical throw of 2.6 m.

Continuous and linear scarps can also be traced in Western high (Figure 4.22). This set of continuous individual scarps comes into sight in the micro-bathymetry as a sharp cut made into the soft sediments covering the smooth topography of the Western High. Visual inspection with the ROV proved that the small-scale scarps are mantled with a thin drape of soft pelagic sediments and no free-face was found. For

comparison strike-slip earthquake ruptures on land are generally associated with mole-tracks in the places where the fault rupture crosses unconsolidated sediments. A very distinctive fault rupture is seen in Figure 4.22. Microbathymetry reveals a distinct pressure ridge along a small restraining bend of the fault rupture in the eastern section of the map. Other alternating bends create sagging areas such as the antithetic normal faults seen at the western section of the microbathymetry. Profile 4 illustrates very clearly this sagging area along one of the antithetic normal faults. Vertical throw is measured as 2.6 m

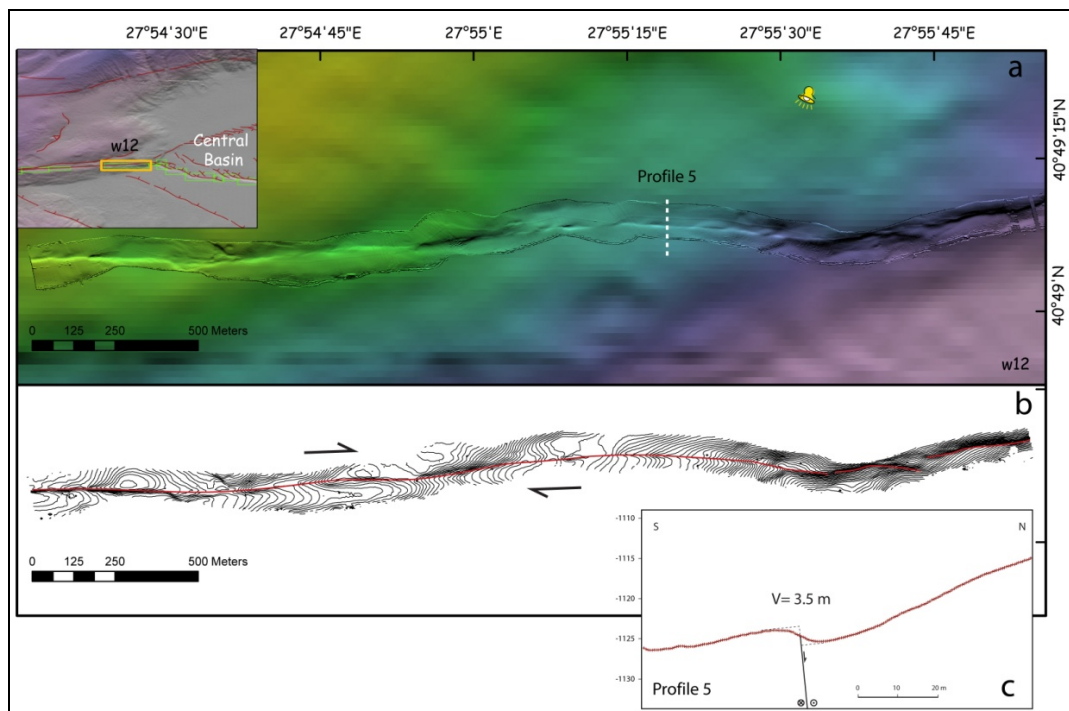


Figure 4.23 : (a) Easternmost microbathymetry extract at the Western high next to the entrance of Central basin. Morphology reveals a moletrack pattern with alternating pressure ridges and depressions all along the rupture zone. Inset indicate the location (b) contours from the microbathymetry every 1 m. Red line present the fault interpretation. (c) microbathymetry profile with a vertical throw of 3.5 m.

The easternmost microbathymetry image (Figure 4.23) illustrates a typical mole track pattern with alternating highs and lows, pressure ridges and open cracks, with small scarplets facing alternatively the two sides of the fault. Microbathymetry profile shows a north facing scarp with a 3.5 m throw (Figure 4.23c). It reveals a well preserved morphology which stands at the bottom of a slope. At the easternmost part, the fault break meets cumulative faults that delimit the westernmost edge of the Central basin.

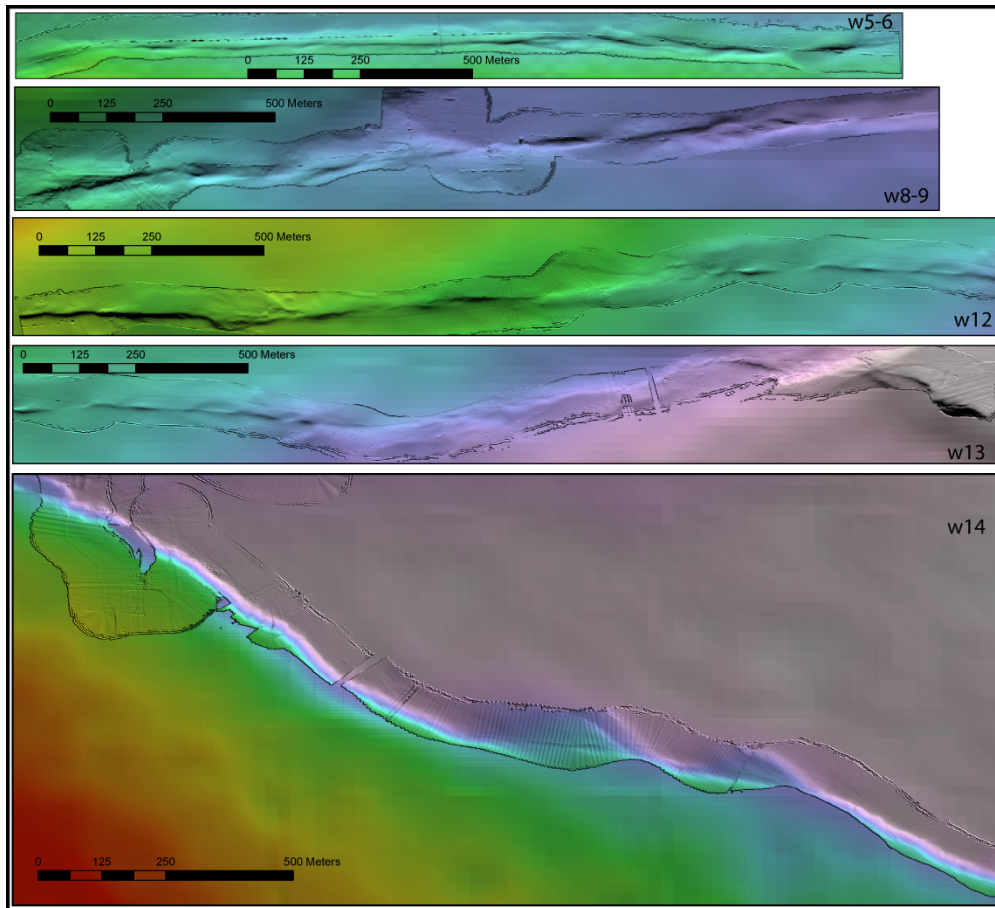


Figure 4.24 : Microbathymetry strips along the Western high (from west to east)

The continuous fresh and distinctive scarp morphology that is observed from the westernmost part of the Tekirdag bend up to the easternmost side of the Western high diminishes at the entrance of the Central basin where large cumulative normal faults scarps prevail (Figure 4.24, w14). Relatively moderate (1- 4 m) throws determined from the microbathymetry suggest that they may be associated with a single or two events (1912 and 1766b). The fact that such sharp scarps are absent along the Central fault segment (which is thought to be associated with the 1766a event) suggest that it is the increments of 1912 earthquake rupture which creates this significant and continuous morphology along the Tekirdag segment (Figure 4.21 and 4.24).

4.4.4 Conclusions

A well-preserved rupture appears continuous over 60 km between the Ganos bend and the Central Basin, involving fault segments with different kinematics (transtension, nearly pure strike-slip and transpression).

The submarine observations of fault scarps along the Tekirdağ segment from Gaziköy in the east to the Central basin in the west reveal that they are extremely well preserved and look fairly fresh on the contrary to the Central segment, along which almost no young scarps were observed. This implies that Tekirdağ segment must have experienced an earthquake relatively recently compared to the Central segment. The most recent destructive earthquakes that affected western Marmara are the August 1776 and August 1912 events (Ambraseys, 2005). The fast sedimentation rates in the deep Marmara basins strongly suggest that this youthful rupture is associated with the 9 August 1912 (Ms 7.4) earthquake. Evidence for a more concealed scarp associated with a large penultimate event in the same submarine region could correspond to rupture of the 5 August 1766 (M~7.4) earthquake.

Visual exploration of the area shows that the individual fault scarps are often marked by the occurrence of black bacterial mats and by small scarplets that are difficult to discriminate from the over steepened basal slopes. Exceptionally the occurrence of broken and offset authigenic carbonate slabs along the fault trace allowed us to see clear reactivation scarps about 0.5 m high.

The slickensides on the fault scarp shown in Figure 4.18 and the ^{210}Pb analyses discussed in section 4.5 indicates strongly that the 1912 rupture reached at least to the middle of the Tekirdağ basin (27.37.69"E 40.48.17"N). The Tekirdağ segment running from the restraining bend in the west to the Central basin in the east is a fairly straight section of the NAF.

The direct observations of submarine scarps in the Marmara Sea establish clearly that the last large scarp-forming earthquake ruptured a set of discrete segments limited to the western Sea of Marmara and that the rupture was arrested at the Central Basin step-over. Once the 1912 earthquake rupture arrived to the middle of this segment it must have continued and reached the closest barrier, that is, the Central basin. Whether the earthquake ruptured the oblique slip faults bounding the southern side of the Central basin (Armijo et al., 2005) or stopped in the entrance of the Central basin (Aksoy et al., 2009) could not be clearly determined.

4.5 Re-constructing the the history of earthquakes in the the Sea of Marmara over the last century based on 210Pb geochronology

Paleoseismologists, who trench across faults, document evidence of paleoearthquakes large enough to rupture the fault at the ground surface. By exhuming the top few meters of an active fault, paleoseismologists may find disturbed ancient soil layers or other traces left by past earthquakes (Sieh et al., 1984; Rockwell, 1987; Meghraoui et al., 1988; Pantosti et al., 1993; Okumura, 1994; McCalpin, 1994; McCalpin and Shlemon, 1996, etc.). Disturbed layers can be attributed to historical earthquakes by using several dating methods (^{14}C , Pb ^{210} , etc.). While paleoseismic methodologies are well established onland, they are at the pioneering stage for the submarine environments. Recent advances in high-resolution submarine imaging and sampling techniques provide opportunities to study the submerged portions of continental transforms offshore. The deformation and earthquake record over the entire transform basin history is uniquely preserved in syntectonic sediment with good spatial coverage and long temporal span. With that perspective, an ultra-high-resolution bathymetric survey with an extensive sampling and coring of sediments close to the scarps was conducted during the MARMARSCARPS cruise in 2002. Major goal of this survey was to unravel the earthquake history of the submarine segments of the North Anatolian Fault in the last century.

Direct observations from the the video imagery and microbathmetry data succesfully characterize the geometry of the fault scarps in the Sea of Marmara. These well-preserved scarps are related to recent earthquake ruptures at the seafloor. The Marmara Sea region has a well-known historical seismicity (Ambraseys and Finkel, 1995; Ambraseys and Jackson, 2000). Major earthquakes were reported for the last 150 yrs that took place at the submarine section of the NAF, e.g 1963, 1912, 1894. To determine the age of the last submarine earthquake break is relatively difficult to assess directly with dating approaches. However, recent sedimentation rates can provide information on the age of the sediment covering the scarps. With that purpose, ROV push cores (35 cm) are collected to identify disturbed sedimentary sequences around the vicinity of the scarps to establish the geochronologic match with known historical events. Geochronological control is obtained using ^{210}Pb ($T_{1/2}$

= 22.3 years) method, measured by γ counting, which spans continuous sedimentation over the past 150 years.

4.5.1 Strategy and methods

Observations from visual exploration and ultra-high resolution bathymetry data exposed sets of well-preserved earthquake scarps and several fine-scale fault breaks at the bottom of Marmara Sea (Armijo et al, 2005). Those breaks extend eastward of the Ganos fault and can be followed continuously along the Tekirdag basin and Western High up to the Central basin over 60 km. Other sites of fresh scarps were discovered at the NE edge of Çınarcık Basin and the submarine canyon at the west of Hersek Peninsula. These submarine seismic scarps are thought to be associated with the 1999 Izmit, 1912 Ganos, 1894 or 1963 Çınarcık earthquakes. In order to test this inference, ROV collected 96 cores from the sites that are selected based on the analysis of the microbathymetry (Figure 4.25).

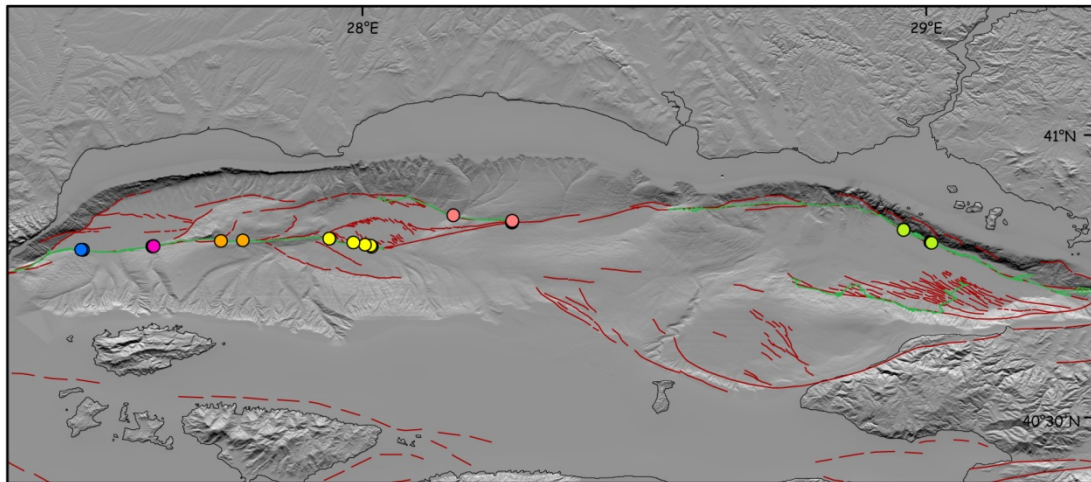


Figure 4.25 : Bathymetry map shows sites of coring with ROV. A total of 96 short cores were collected around the vicinity of the fault scarps. Cores are indicated as circles with colors. Green lines are the route of the ROV Victor during the survey.

The age of the last earthquake break is difficult to assess directly with dating approaches. However, recent sedimentation rates can provide information on the age of the sediment covering the scarps. We will use the ^{210}Pb method to determine the accumulation rate of sediments. In a typical application, the average accumulation rate over a period of 100 - 200 years is obtained. From the accumulation rate, the age of sediment from a particular depth in the sediment column can be estimated.

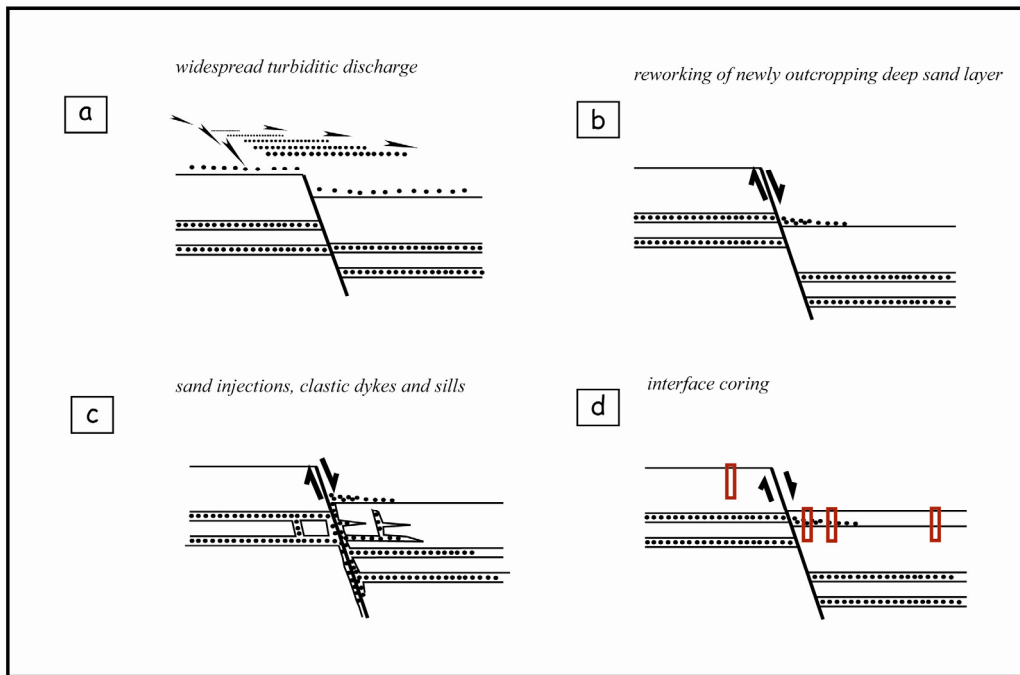


Figure 4.26 : Sketch presents the logic of coring transect to the fault scarps. Cores were collected along transect through scarps.

Cores are collected along transect to the scarps. The logic was to sample cores from the foot of the scarps (to sample disturbed sediments) and far from the scarps (to sample undisturbed sediments). Mechanisms such as reworking of previously deposited turbiditic layers or direct deposition of scarp-derived (comparable to colluvial wedges on land) coarse sediments are expected to form during a submarine fault rupture (Figure 4.26). Especially, sites of normal fault scarps-like in Central basin are adequate sites to observe disturbed sediments in the cores (Figure 4.27).

As the study focuses on events over the last century, ^{210}Pb geochronology technique is used to obtain sedimentation rates which would guide us to measure the time elapsed since some particular event (past earthquakes). It would give us a rate to assess the evolution of the morphology of the scarps in the last 100-150 years. Recent sedimentation rates can provide information on the age of the sediment covering the scarps.

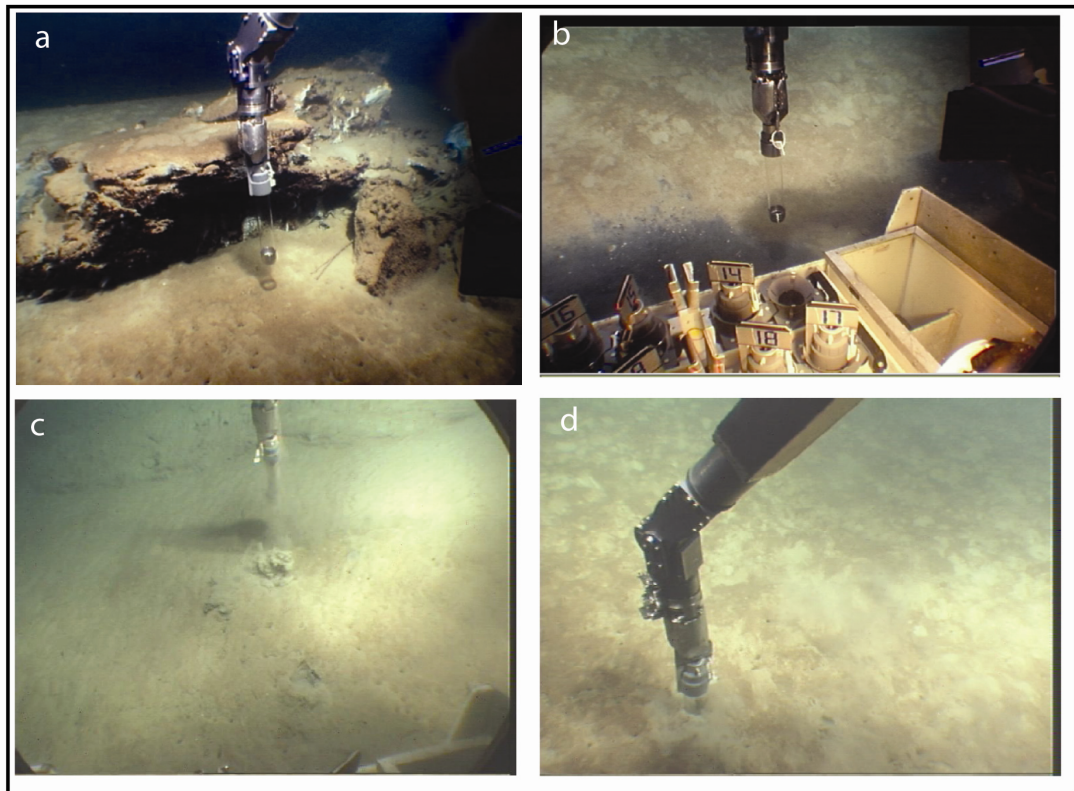


Figure 4.27 : Video capture photos by the ROV Victor (a) Coring in front of a carbonate slab in Tekirdag basin, which has been offset by the fault (b) A “black patch” at the foot of a scarp in Tekirdag basin, sampled with the push core. (c) Coring in Çınarcık basin along the slope of a scarp which is draped by hemipelagic sediments (d) Coring far field to the scarp to sample undisturbed sediments.

96 push cores up to 35-cm-long were collected during the MARMARASCARPS campaign. Selected cores are investigated for the present study. Cores were opened, described, photographed, sliced longitudinally for radiographical study and sampled centimeter for granulometry analyses in collaboration with University of Bordeaux, EPOC. Radiographic imaging was performed with a classical X-ray equipment (SCOPIX) coupled with CEGELEC radioscopy instrumentation (Migeon et al. 1998). This technique was used to identify sedimentary structures and textures (presence of reworking by burrowing organisms, consolidated or unconsolidated sediment, and change in grain size). It helped in the selection of layers for ^{210}Pb , ^{226}Ra and ^{137}Cs analyses. After X-ray examination, selected cores were sampled for

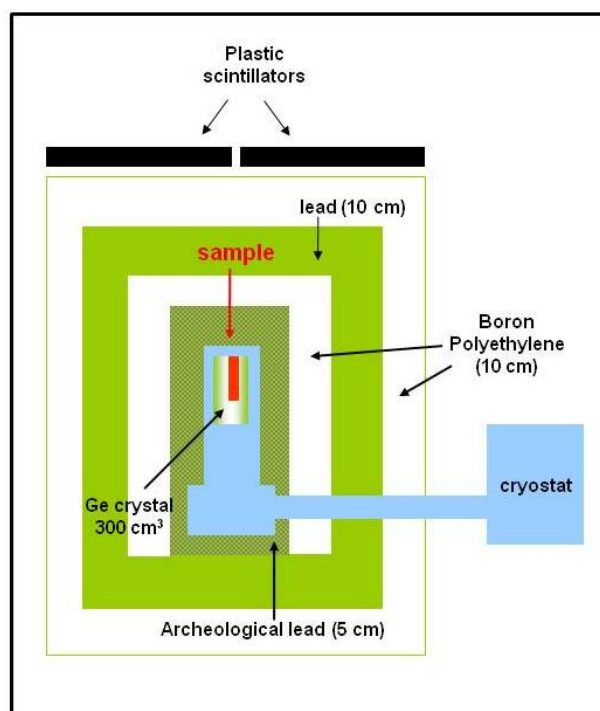


Figure 4.28 : Schematic diagram of a well-type gamma detector.

grain size and ^{210}Pb measurements. The sediment was dried at 60°C , crushed in a mortar, prior to radionuclide analysis. ^{210}Pb measurements were established using two detectors: a semi-planar germanium detector and a well-type germanium detector (Schmidt et al., 2007; 2009) (Figure 4.28).

4.5.2 Use of ^{210}Pb geochronology in sediment dating

Undisturbed, laminated sediments record the changes in the water column and the discharge area. If the age of each sediment layer can be determined, analysis of sediments can be used for tracking events from the past. Lead-210 (^{210}Pb) geochronology is an isotopic method of age estimation based on the radioactive decay of ^{222}Rn and ^{210}Pb (Noller, 2000). Because of the relatively short half-life of ^{210}Pb (~22 years), it is used to estimate sedimentation rates for the past century or a little more. The ^{210}Pb method can be applied in paleoseismic studies by dating organic-rich sediments to confidently estimate the age of an earthquake within the past 150 years. The method is widely used in the determination of sedimentation rates in lacustrine and marine depositional records.

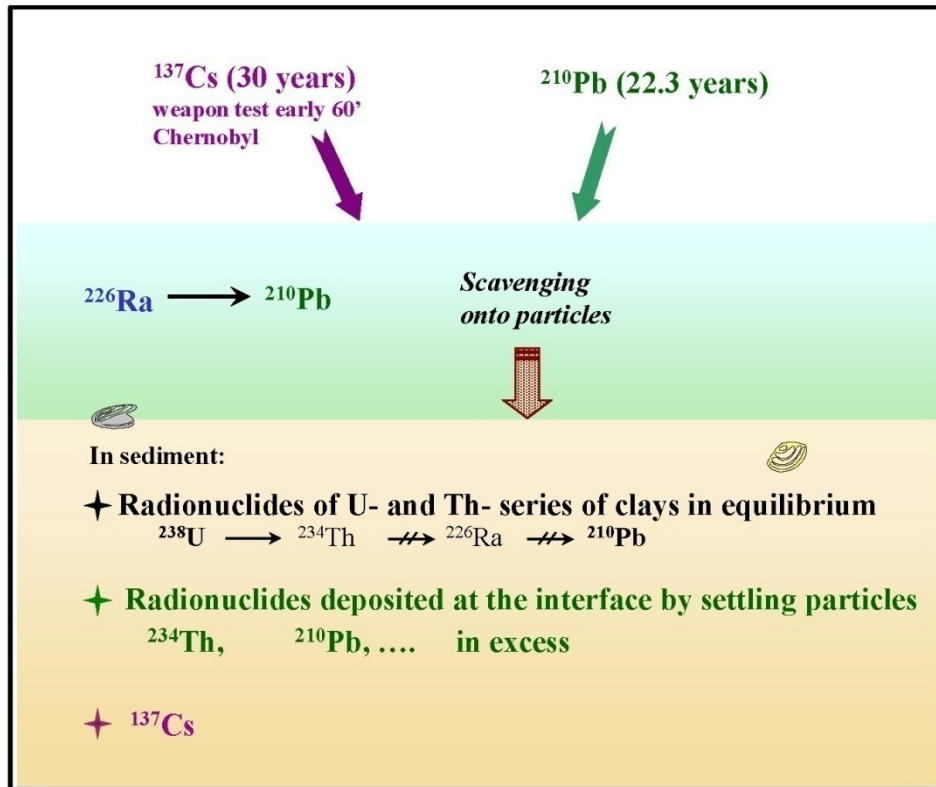


Figure 4.29 : Diagram simplifies the logic of ^{210}Pb and ^{137}Cs preservation in the sediments.

^{210}Pb is a naturally occurring radioactive element that is part of the Uranium-238 radioactive decay series (Figure 4.29). The radioactive element uranium has an almost infinite half-life (4.5×10^9 yr) and for these purposes can be considered to be present at an unchanging concentration (over time) in the earth's crust. Although the concentration of uranium varies from location to location, it is present essentially in all soils and sediments, at least at some low level. Over time the uranium-238 very slowly decays into uranium-234 (half-life = 248,000 yr) which decays into thorium-230 (half-life = 80,000 yr) which decays into radium-226 (half-life = 1620 yr). Radium-226 in the soil exhibits the same level of radioactivity as uranium-238 from which it was originally derived, because of a natural phenomenon called secular equilibrium. The overall result is that radium-226 is found at low and essentially unchanging levels in soils everywhere. When radioactive radium-226 decays, it produces the radioactive inert gas radon-222 (half-life = ~ 3.8 days). Radon (Rn) gas can escape to the atmosphere before it decays into the next radioactive element (a nonvolatile metal), if it is produced in soils close to the air-soil interface. This radon emanation is a normal occurrence and thereby causes the terrestrial atmosphere to contain a low but fairly constant level of radioactive gas. After several days

residence time in the atmosphere, the ^{222}Rn naturally decays to polonium-218, a metallic radionuclide which, over a period of hours/days, falls to the earth with dust and rain. A number of subsequent radioactive decays occur over a period of minutes and ^{210}Pb (half-life = 22.3 yr) is produced. The ^{210}Pb which falls into a lake or ocean tends to end up in the sediments over the next few months and becomes permanently fixed on the sediment particles (Figure 4.29). Within 2 years, polonium-210 (^{210}Po), the granddaughter of ^{210}Pb , is in secular equilibrium (i.e. the same activity) with the ^{210}Pb . It is actually the ^{210}Po that we measure because it provides more accurate estimates of the ^{210}Pb than will direct measurements of ^{210}Pb .

The ^{210}Pb method is based on the measurement of the unsupported (excess) ^{210}Pb activity, which is added into the sediment by settling particles that scavenge ^{210}Pb produced in the water column and from atmospheric fallout. Once incorporated into the sediment, unsupported ^{210}Pb decays with depth, equivalent to time, in the sediment column according to its known half-life (22,26 yrs). In applying this principle, it is assumed that the specific activity of newly deposited particles at a given site is constant with time. Therefore, sediment accumulation rate can be derived from ^{210}Pb , based on two assumptions: Constant flux and constant sediment accumulation rate (CF:CS model):

The decrease of $^{210}\text{P}_{\text{xs}}$ with depth is described by the following relation (4.1):

$$[^{210}\text{Pb}_{\text{xs}}]_z = [^{210}\text{Pb}_{\text{xs}}]_0 \exp[-\lambda z/S] \quad (4.1)$$

Z is the depth, λ is the decay constant of the nuclide and S is the sediment accumulation. $[^{210}\text{Pb}_{\text{xs}}]_z$, 0 are the activities of ^{210}Pb at surface, or base of the mixed layer (Schmidt et al, 2005).

4.5.3 Results and Discussion

4.5.3.1 Tekirdag Basin cores

The 1912 earthquake rupture on land continues eastward entering offshore along the southern edge of Tekirdag basin. Dominantly strike-slip scarps with variable dip-slip component are observed along the submarine fault trace. Two separate sites are chosen for coring in the western and eastern part of the Tekirdag basin (Figure 4.30).

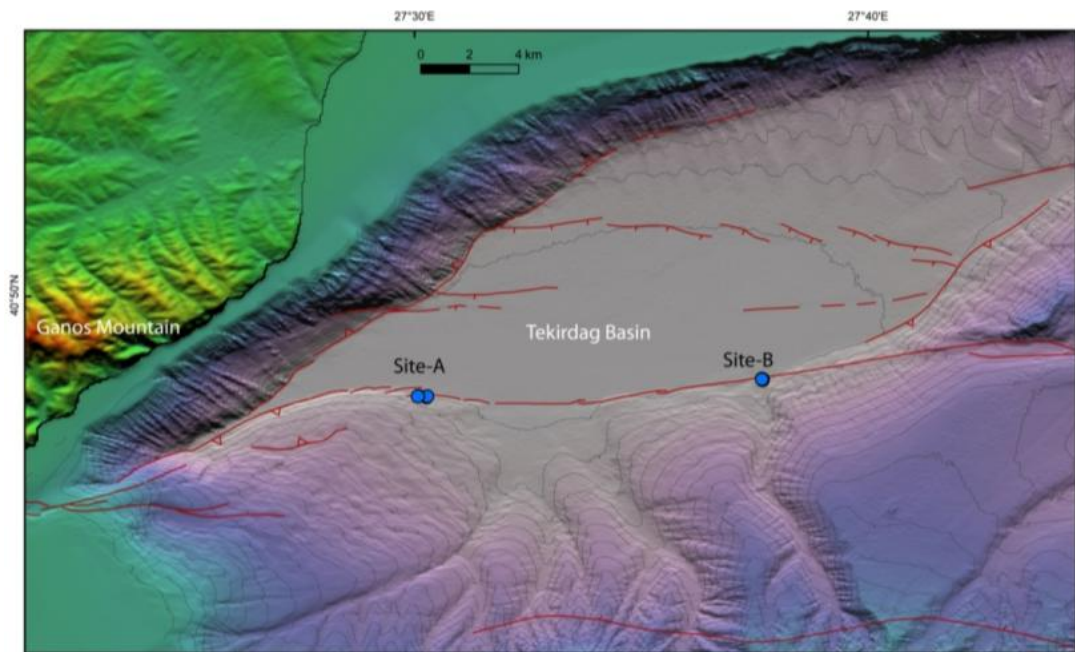


Figure 4.30 : Bathymetry map of Tekirdag basin with core locations (blue circles). Two separate sites are simply names as site-A and site-B.

Site A is located east of the compressional bend along the Tekirdag segment (Figure 4.30). Fault rupture is observed as a 100 m-wide deformation zone at this site cutting a slope. Rupture morphology is mainly strike-slip associated with mole tracks (Figure 4.31b, 4.31c, 4.31d). Three cores (Cores 16, 18 and 19) were selected based on the X-ray analysis. These three cores show density variations in x-rays suggesting an increase in grain size. Core 16 is sampled on top of the slope north of the main scarp and Core 18 is sampled south of the scarp to the downslope (Figure 4.31c). Core 19 in profile 2 (Figure 4.31d), is located below the moletrack scarp. They are relatively in a favorable location for receiving disturbed sediments from down slope sediment transportation.

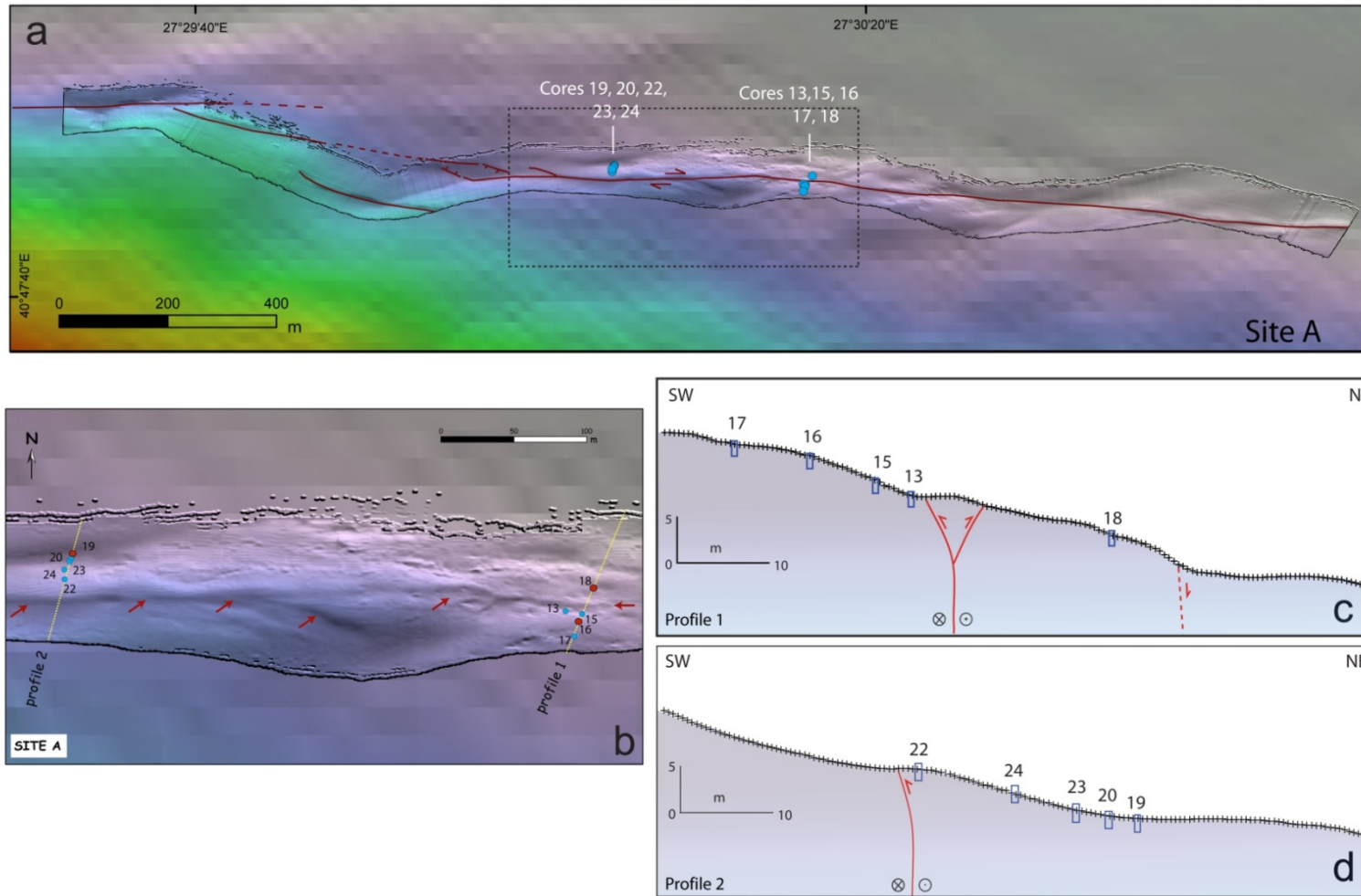


Figure 4.31 : (a) Microbathymetry map (background Le Suroit bathymetry) of Site A. Two coring transects are 200 m apart. (b) Close up of the dashed box in Figure 7a. Yellow lines indicate microbathymetry profiles; cores are given in blue circles. Analyzed cores are blue circles. Red arrows highlight the fault rupture (c) Profile 1 shows the location of the collected cores with respect to the scarp. Scarp forms in a moletrack zone (d) Profile 2 with core locations.

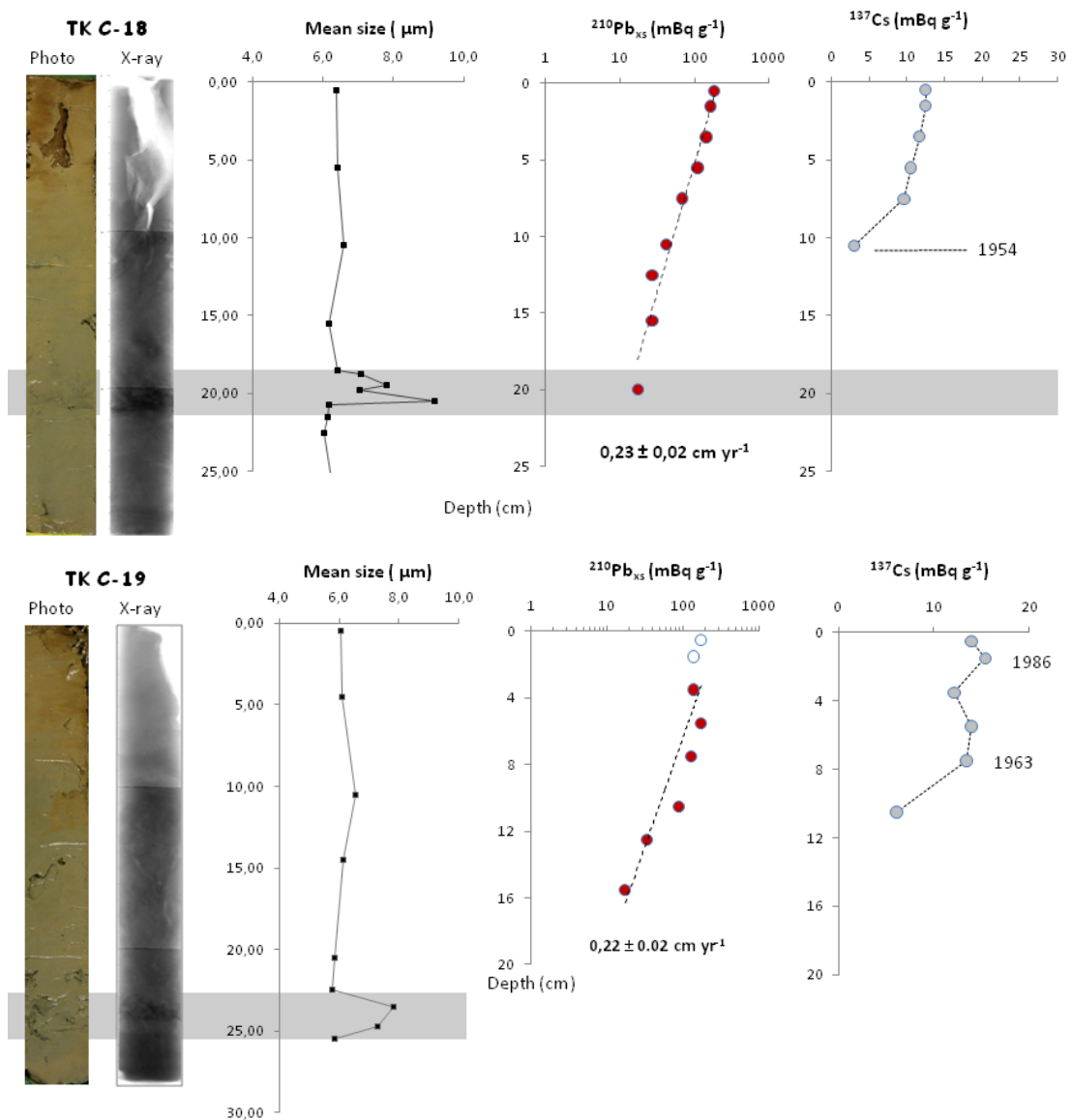


Figure 4.32 : X-ray, profiles of mean grain size, $^{210}\text{Pb}_{\text{xs}}$ and ^{137}Cs for site C4. Sedimentation rates were calculated using selected points of $^{210}\text{Pb}_{\text{xs}}$ profiles.

Core 18 presents a rather homogeneous silty clay fraction between 0-19 cm. Sedimentologic texture changes with a clayey silt between 20-22cm. This layer was observed as a density anomaly in the x-ray imagery on both three cores. Core 19 and 16 show mostly a homogeneous silty clay fraction as in Core 18. Between 22-24 cm of Core 19 a clayey silt layer reflects a significant density variation which is also observed in Core 16 between 14-15 cm. These cores are in a favorable location for receiving external sediments from down slope sediment transportation during an earthquake. Hence, we can imply that this 2-cm clayey silt fraction which was found in all three cores may have deposited during a fault rupture.

^{210}Pb profile of Core 18 presents an exponential decrease of activities to reach supported activity levels at about 20 cm depth. Such a feature is appropriate to the determination of sedimentation rates. The rather homogeneity of the first 20 cm of the sedimentary column, revealed by X-ray, explains the good fit of the decrease of ^{210}Pb activities in excess. The layer in between 20-22 cm, which may correspond to a disturbance, was not sampled for radionuclide determination. This same layer is between 14-15 cm in core PL197-16 and at about 20 cm in core PL197-18. The later one is about twice in thickness probably due to a favorable location of core PL197-18 for receiving more sediment from top. ^{210}Pb profile of Core 19 which was sampled ~200 m west of the cores 16 and 18, presents an upper mixed layer, followed by an exponential decrease. The mixed layer is restricted to the uppermost 3 cm of sediment.

In order to derive sediment accumulation rates from ^{210}Pb profiles, we applied constant flux and constant sediment accumulation rate (CF:CS method) (Krishnaswamy et al., 1971; Robbins and Edgington, 1975) method to the profiles obtained at Site A. ^{210}Pb profiles, measured on three different cores, are consistent with each other. Sedimentation rates determined on these three cores collected in October 2002 present a range: 0.23-0.22 cm/yr (Figure 4.26). Calculation of depth versus sedimentation rate gives an age range for the disturbed level. Accordingly, the disturbed layer was accumulated 87 ± 2 yrs BP (1915 ± 2) overlapping with the 1912 Ganos earthquake.

4.5.3.2 Western High cores

The 20-km-long strike-slip fault segment cuts the entire Western high EW (Figure 4.33). Microbathymetry extracts reveal continuous fault breaks are traced up to the entrance of the Central basin. The fault trace is still very linear with slight sinuosity apparently associated with the smaller-scale segmentation. Pressure ridges and sag ponds alternate at segment ends or at slight fault bends. The dimensions of such features (10–150 m in length; 10– 50 m in width, respectively along and across strike, associated with several meters of vertical relief) indicate that they may have resulted from many events. Site C is a sag pond area (Figure 4.34). Short cores are

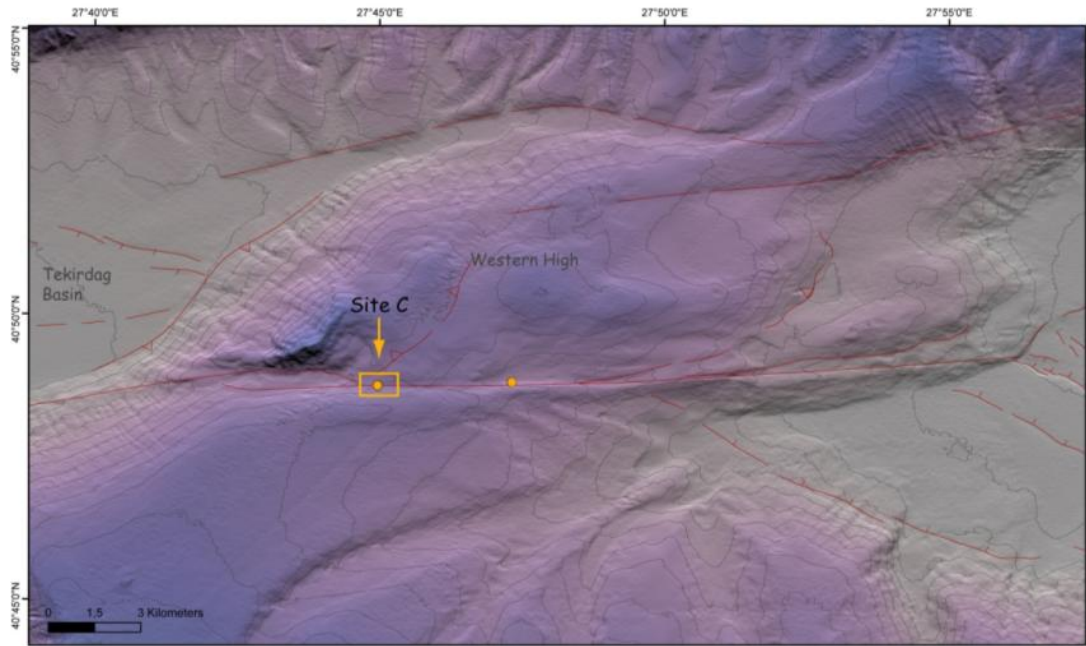


Figure 4.33 : The bathymetry map of the Western High locates the coring site C (orange box).

collected across the basin north to south. 8 cores are sampled from this site and cores 4, 5 and 6 are selected for examination based on slight variations on the x-ray images. Core 4 is on top of the northern scarp, core 5 and 6 are sampled inside the basin closer to the southern scarp. Sedimentation rate is expected to be relatively higher in the pond than on shoulders. Although x-ray imagery exposed some slight variations in density, no significant disturbed layers are detected in the core; both cores are quite homogeneous. ^{210}Pb profiles are achieved for Cores 6 and 4 in order to determine sedimentation rate. As expected, the sedimentation rate from Core 6 is 3 times higher (0.53 cm/yr) than the rate from core 4 (0.18 cm/yr) which is located on the shoulder of the scarp (Figure 4.35).

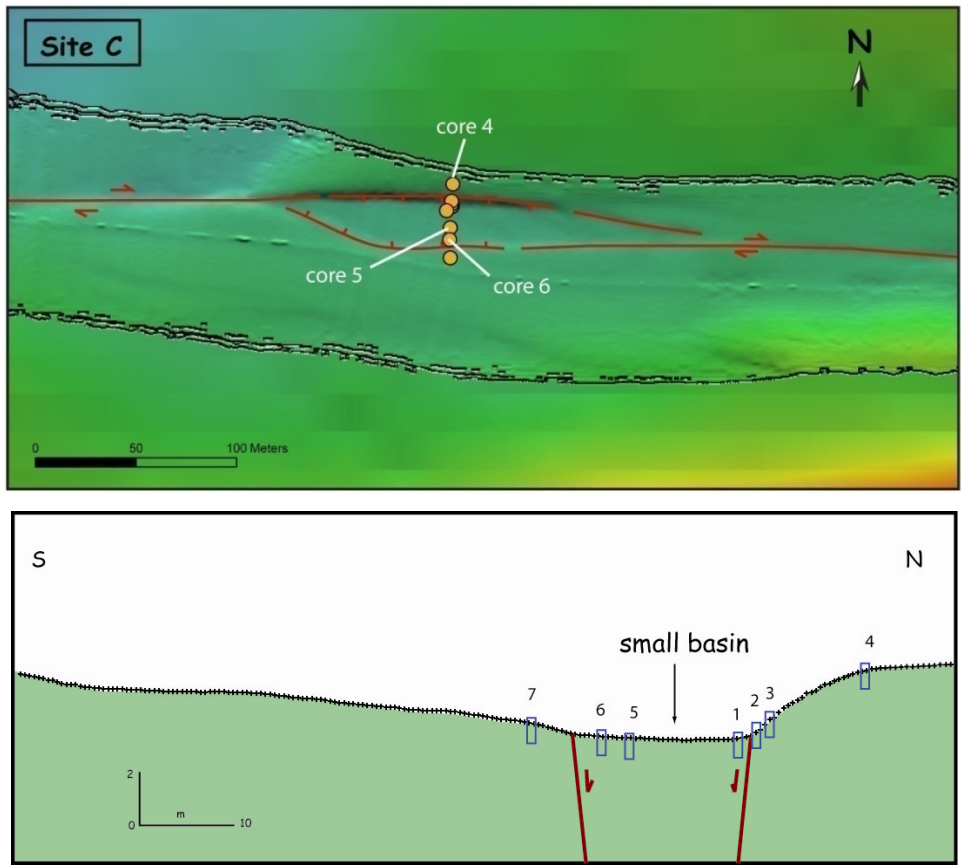


Figure 4.34 : (a) Enlargement of the Site C (orange box in Figure 33). Cores are aligned N-S across the basin. (b) Microbathymetry profile across the sag pond. Core locations are indicated with blue boxes.

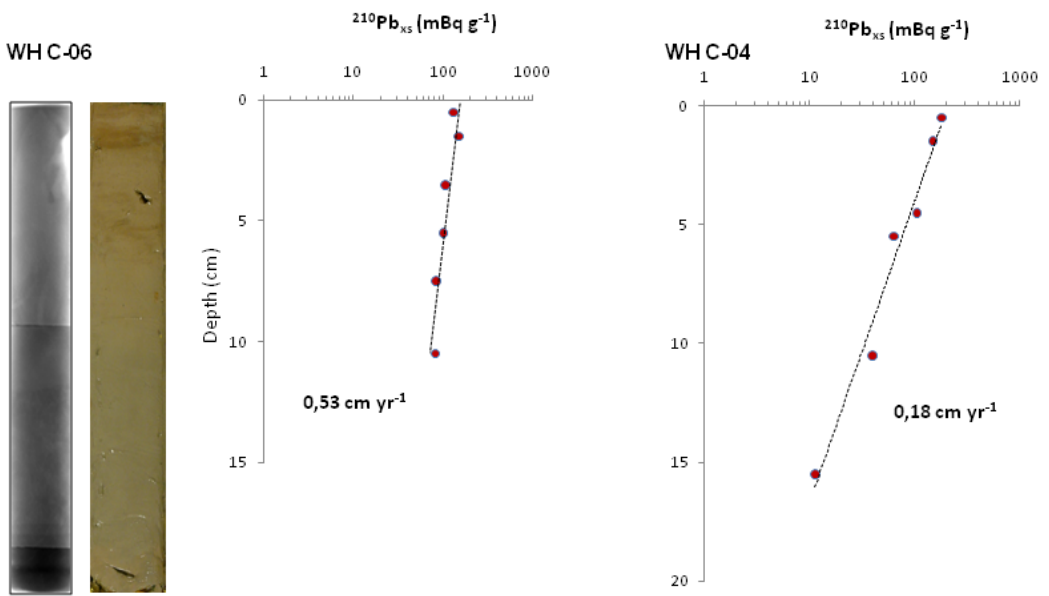


Figure 4.35 : The $^{210}\text{Pb}_{\text{xs}}$ profiles for Cores 6 and 4. Sedimentation rates were calculated using selected points of $^{210}\text{Pb}_{\text{xs}}$ profiles.

4.5.3.3 Central Basin cores

Central pull-apart basin is bounded by sharp normal fault scarps that offset the flat floor of the basin (Figure 4.36). Microbathymetry reveals cumulative scarps up to 50 m high along the SW boundary fault. This set of incremental scarps with significant normal slip is continuous all along the whole SW boundary fault of the inner pull-apart, for a total length of about 8 km. The steepness and the sharpness of the individual scarps suggest that they correspond to recent scarp-forming increments. Site E is located at the westernmost tip of the Central basin (Figure 4.36). We observe a ~20-m-high cumulative normal fault scarp with a clear free face of 5 m (Figure 4.37a).

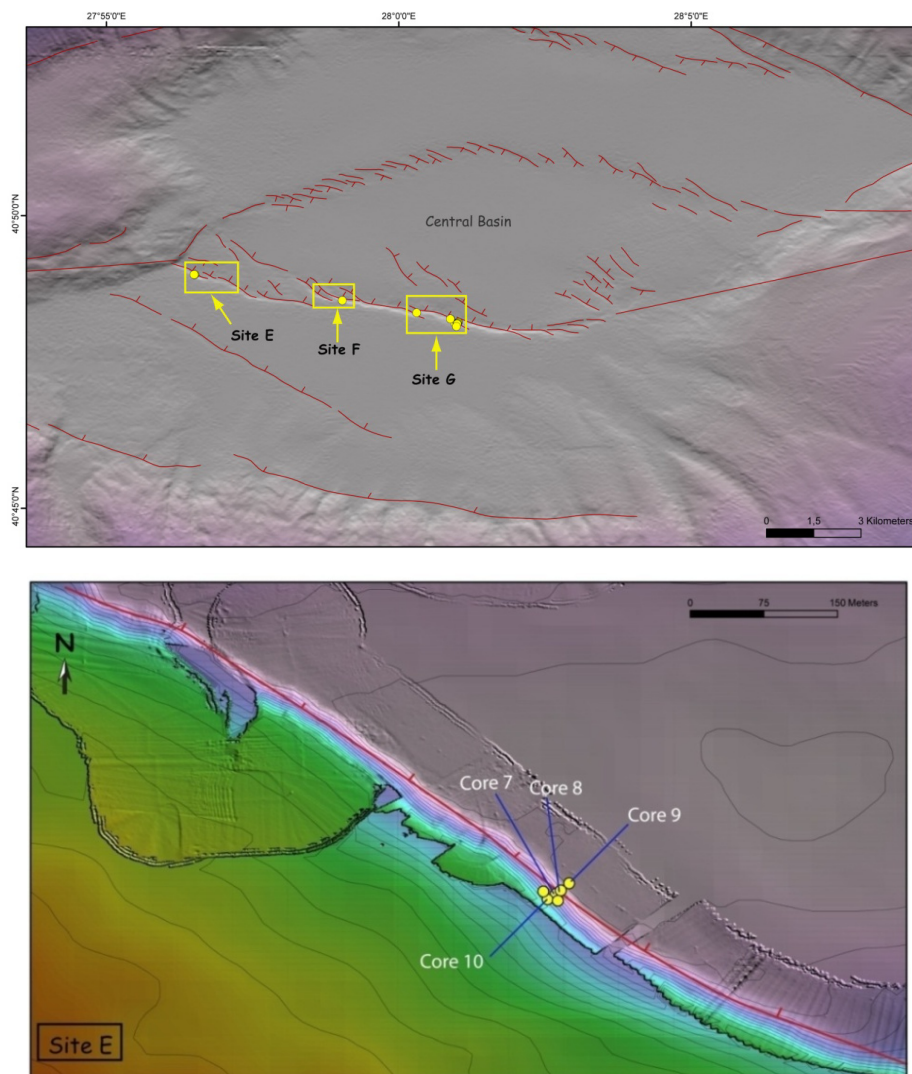


Figure 4.36 : The bathymetry map of Central basin. Yellow boxes indicate survey areas. Lower panel depicts the location of the cores (yellow circles) from Site E.

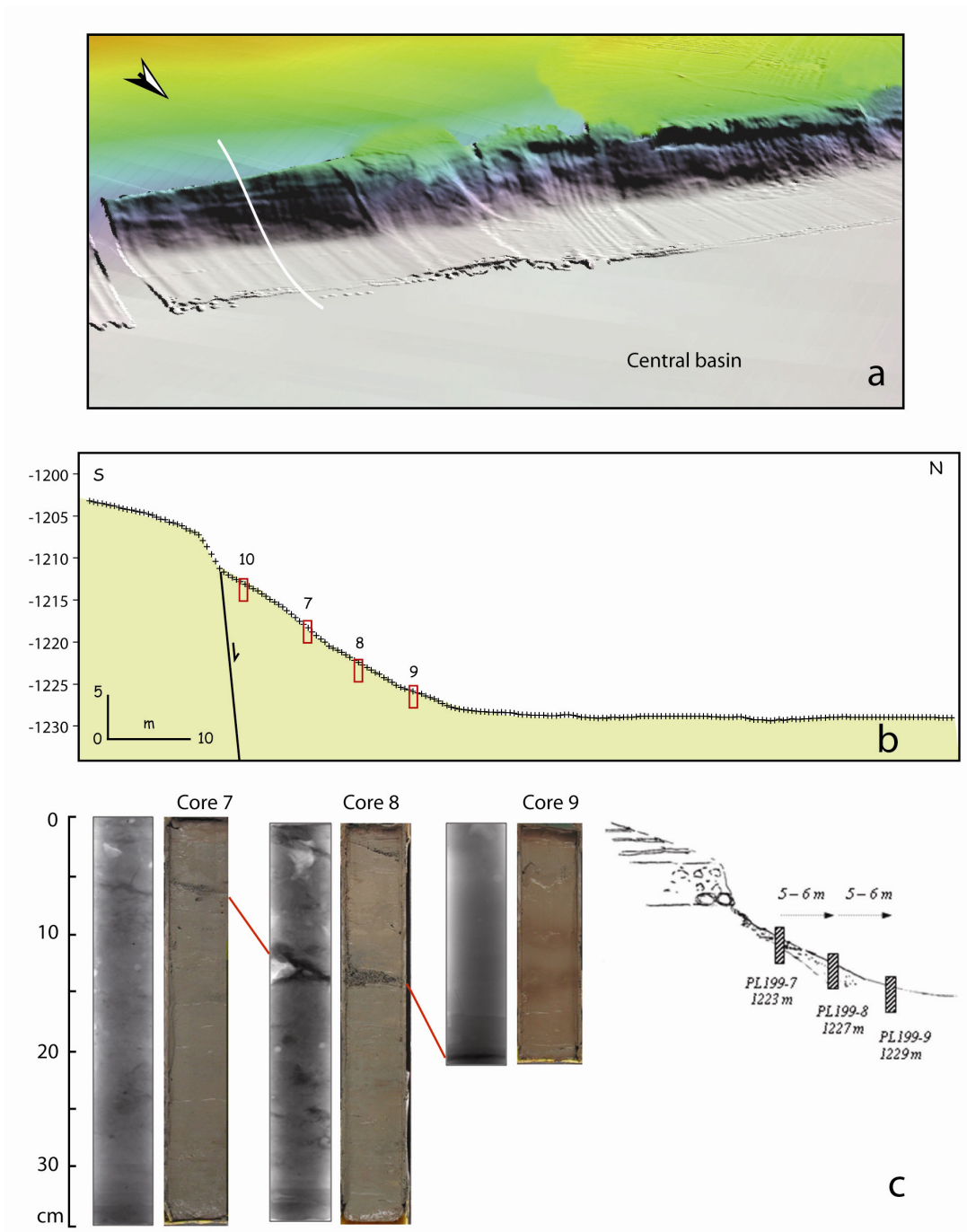


Figure 4.37 : (a) 3D view of the normal fault scarp at the southern boundary of the Central basin. Microbathymetry merged with Le Suroit bathymetry (background). (b) Profile depicts the normal fault morphology of an individual scarp (20 m). Cores are shown by red boxes. (c) X-ray images and logs of the Cores 7, 8 and 9. Note the sharp lithological contact that can be traced in all three cores. Sketch on the right illustrates the logic of coring at this site.

Cores 10, 7, 8, and 9 are aligned at the talus of the normal fault scarp (Figure 4.37b). In a dip-slip fault movement scarp-derived material are expected to be deposited in front of the scarp. In the x-ray images of 7, 8, and 9, a sharp density variation can be readily seen (Figure 4.37c). Analysis of the cores clearly confirms such a sharp disturbance in the homogeneous silt clay lithology. The abrupt sandy layer can be followed progressively in cores 7, 8 and 9, similarly to fault wedge deposits on land. However, Core 8 is disturbed with another sandy layer at 3. cm which is thinner than the layer at the middle of the core. This clearly shows that Core 8 present two separate events.

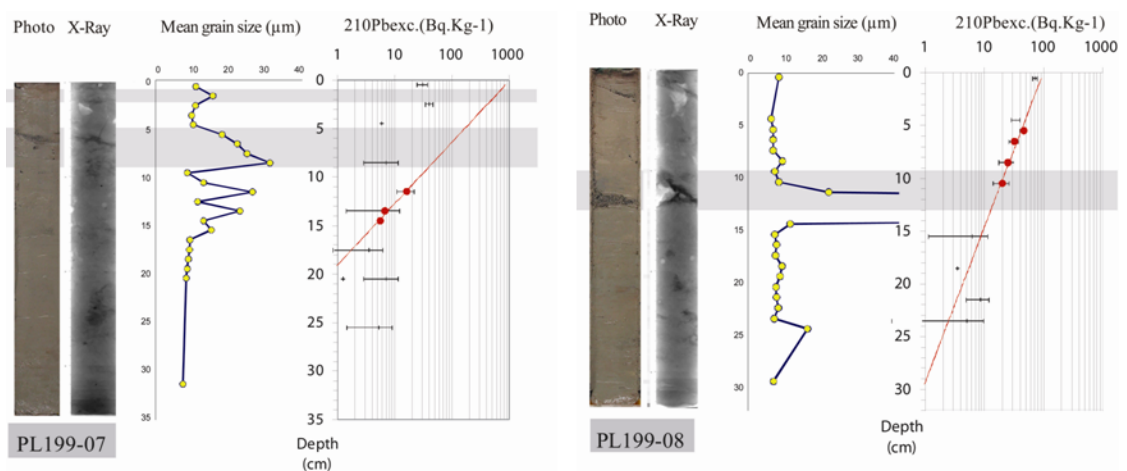


Figure 4.38 : X-ray, profiles of mean grain size, ^{210}Pb for site E, cores 7 and 8. Sedimentation rates were calculated using selected points of ^{210}Pb profiles. Top of both cores contain mixed layers.

Calculation of depth versus sedimentation rate for these 3 cores is thus relatively problematic. Sedimentation rates acquired from cores 07 and 08 are 0,11 cm/yr and 0,25 cm/yr, respectively. For core 8, depth versus sedimentation rate gives a range back to 80 ± 4 yrs BP. Accordingly, the sharp layer may have deposited associated with the 1912 Ganos earthquake. However, we get 48 ± 2 yrs BP with the same rate in Core 7, which doesn't match with any earthquake rupture around that period. Sediment removal processes should also be taken into account when trying set a geochronology for the disturbed layers. Hence, the sharp layer on Core 08 can be attributed to the 1912 earthquake.

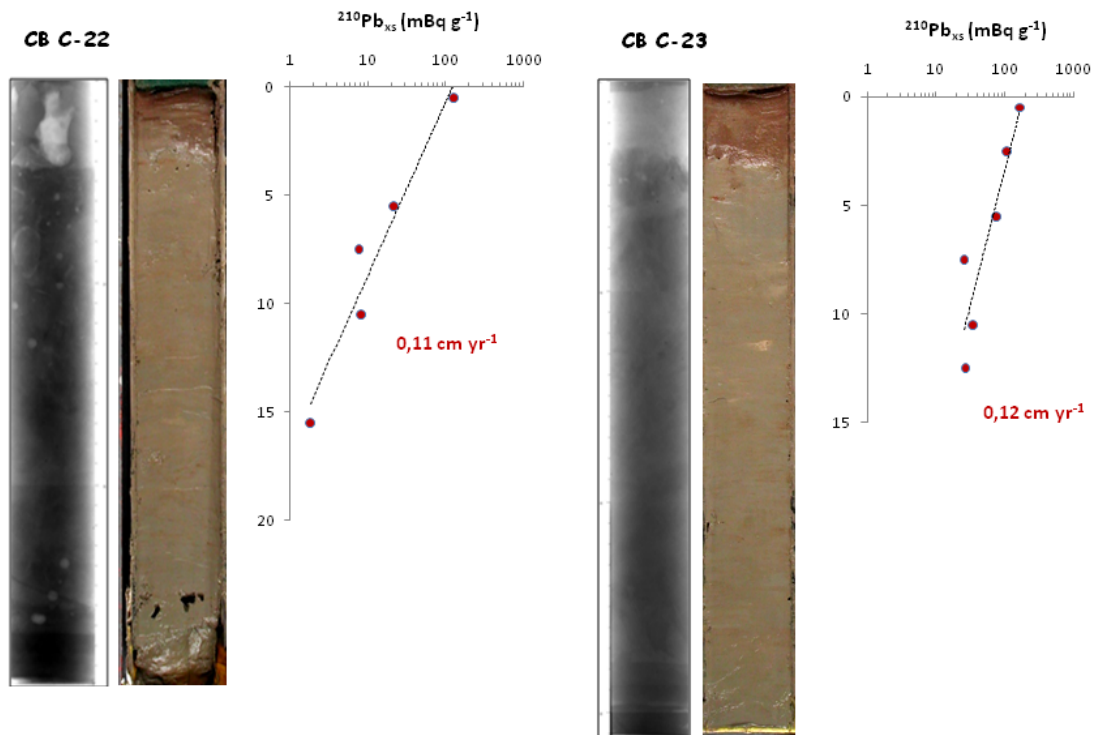


Figure 4.39 : X-ray, profiles of $^{210}\text{Pb}_{\text{XS}}$ for site E, cores 7 and 8. Note that both cores are quite homogeneous.

In order to take a rather constant sedimentation rate, two cores, C22 and C23, that are far away from the fault scarp are selected for ^{210}Pb counting. They present rather constant granulometry with depth and an exponential decrease of ^{210}Pb in excess within the upper 20 cm of cores as usually observed in marine environment. Analysis of cores 22 and 23 reveal a sedimentation rate of 0,11-0,12 cm/yr.

4.5.3.4 Çınarcık Basin cores

The northeastern Çınarcık margin is characterized by a N120°-E-trending, steep escarpment, here the seafloor abruptly deepens from 100 to 1250 m depth. At the base of this escarpment lie clear en echelon active normal fault scarps, a pattern suggestive of combined extensional and strike-slip motion (Figure 4.40).

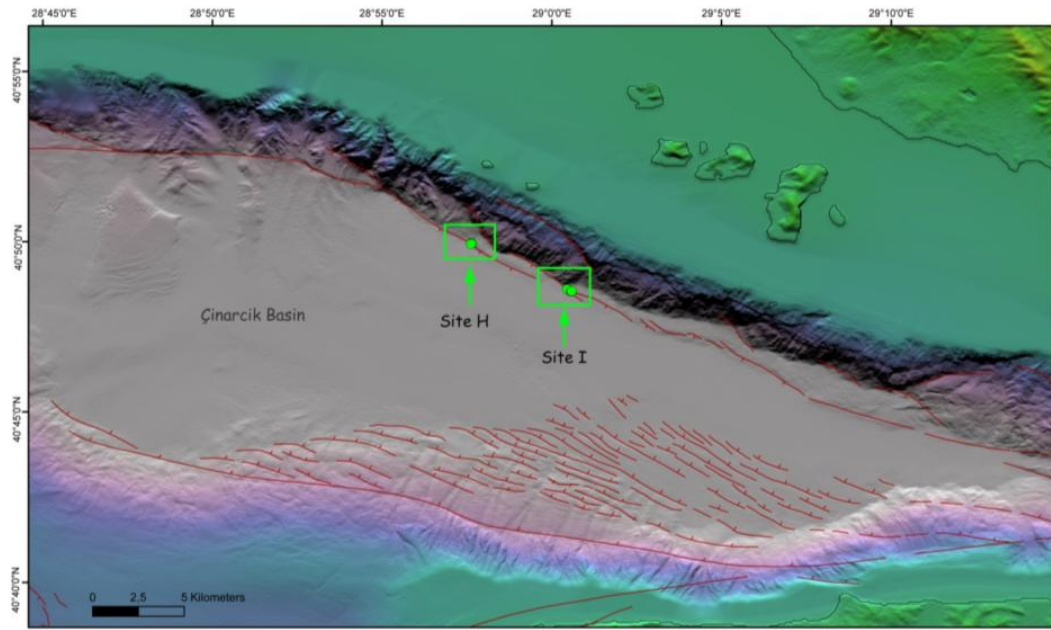


Figure 4.40 : The bathymetry map of Çınarcık basin. Green boxes exhibit the microbathymetry enlargements with core locations.

At site H, we observe a NW-SE trending 15-m-high fault scarp with vertical component of slip (Figure 4.41). In 3D view of the site, normal fault morphology is readily seen. Due to the vertical movement slope deposits shifted downward along the slope. Two sets of coring transects are taken along this fault scarp but three cores are selected for detailed analysis (Cores 17, 19, 20).

Core 20 is located at the foot of this cumulative scarp and exposes a very sharp density variation in the x-ray. This is indeed an erosional contact with small pebbles at 5cm (Figure 4.42) indicative of a significant disturbance. General sediment composition is composed of a silty clay fraction. In $^{210}\text{Pb}_{\text{xs}}$ profile, the upper mixed layer is followed by an exponential decrease. The profile depicts a sedimentation rate of 0.13 cm/yr below the sharp layer. Depth versus sedimentation rate calculation suggests an age bracket back to 38 yrs BP, which coincides with the 1963 Çınarcık earthquake.

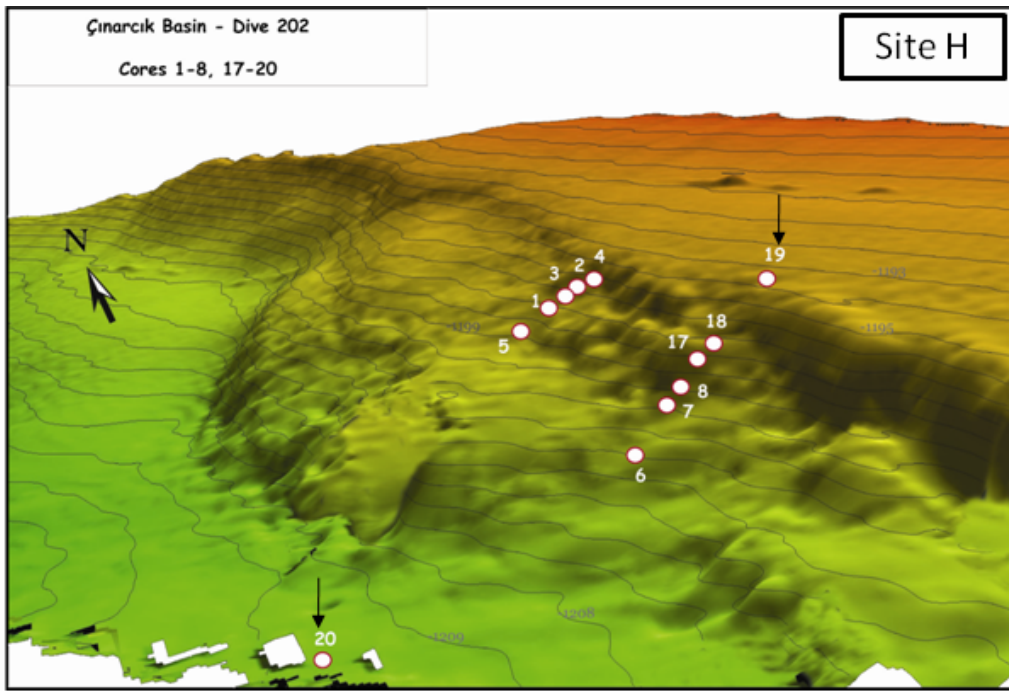


Figure 4.41 : 3D microbathymetry of site H; cores are indicated by white circles. Cores 19 and 20 are highlighted.

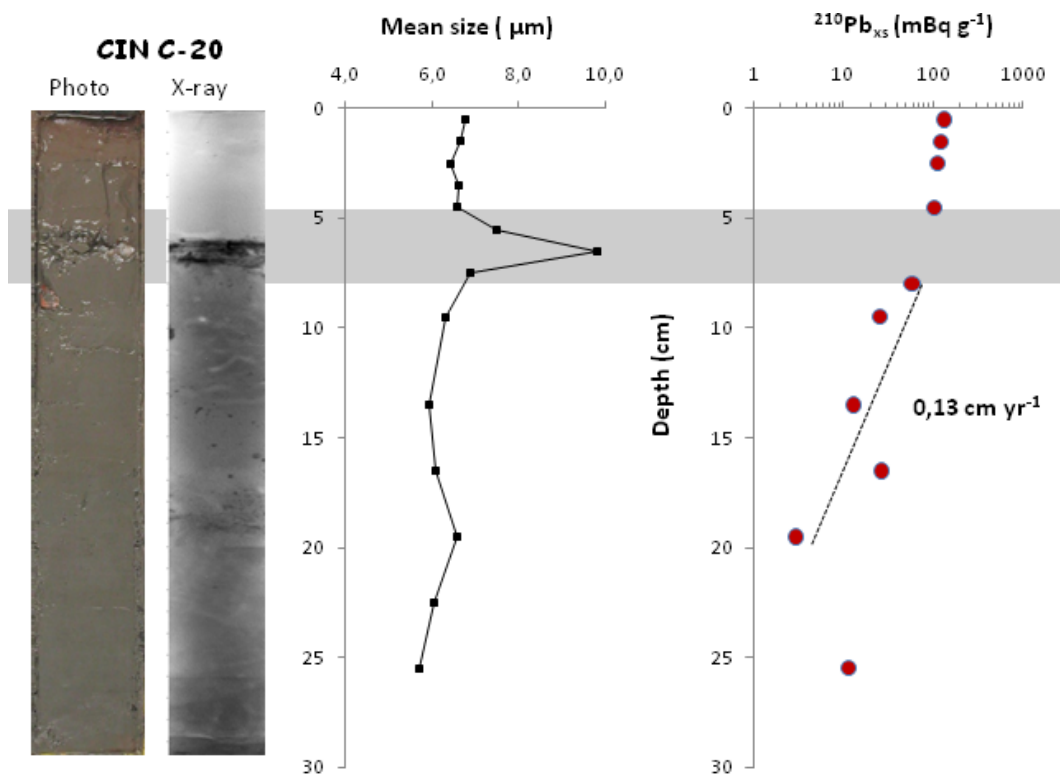


Figure 4.42 : X-ray, granulometry and $^{210}\text{Pb}_{\text{xs}}$ profiles for Core 20. Note the sharp layer in Core 20.

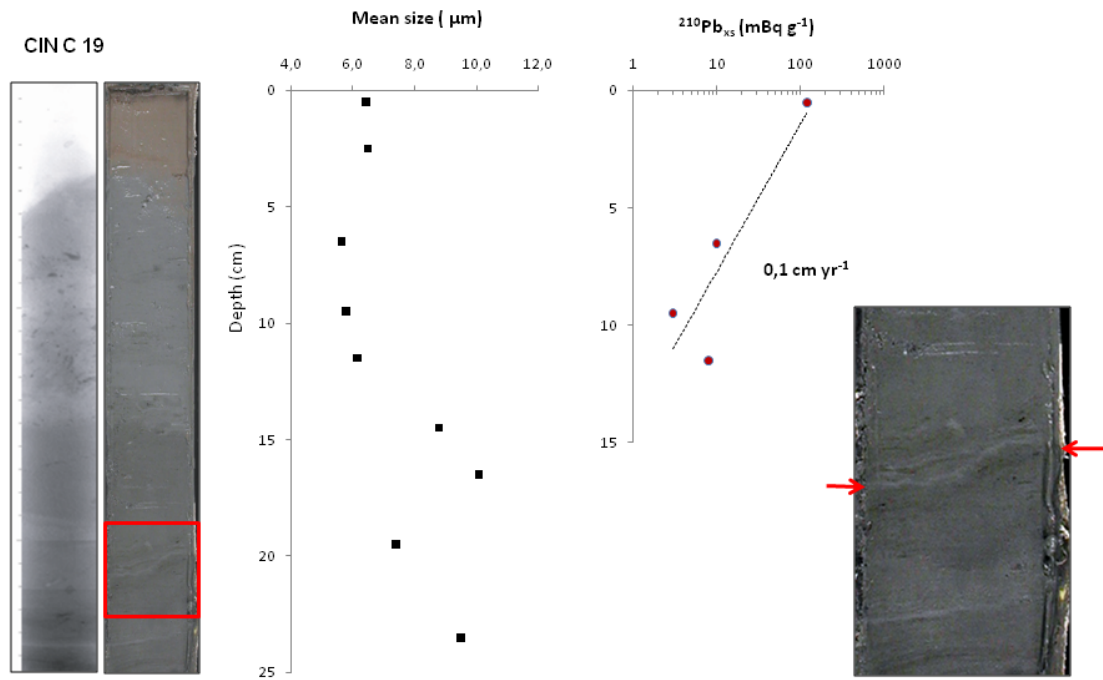


Figure 4.43 : X-ray, granulometry and $^{210}\text{Pb}_{\text{xs}}$ profiles for Core 19. Red box highlights an erosional contact at the bottom of the core (right panel). Erosional contact is marked by red arrows.

Core 19 is sampled from the shoulder of the scarp. Below the oxidized top part of core 19, two different clay packages are immediately recognizable (Figure 4.43). A light green clay deposit with some tiny dark spots is observed between 4-15 cm. Below this deposit, a dark green silty clay package is seen. Inside this darker section an erosional contact is recognized (Figure 4.43). This contact might have deposited by a slump which is normally expected due to the abundance of the landslide and slump structures at the edge of the Çınarcık escarpment. $^{210}\text{Pb}_{\text{xs}}$ profiles suggest a sedimentation rate of 0.1 cm/yr for Core 19.

A 20-m-high cumulative scarp is located at the Northern Cınarcık basin (Site I). Smaller scale, sharp scarps lacerate the cumulative scarp (Figure 4.44a). A set of cores are collected as a transect.

Core 21 is taken below the initial scarp from the top. Core 15 is taken from the slope and core 12 from the shoulder of the same scarp. A sharp intrusion of a sandy layer is seen in Core 21, as well as in the x-ray (Figure 4.45). That sharp layer is seen at 5 cm as in Core 20. That may represent the disturbance of a similar event in two sites that are 3 km apart. $^{210}\text{Pb}_{\text{xs}}$ profiles are only obtained from core 15 and 12.

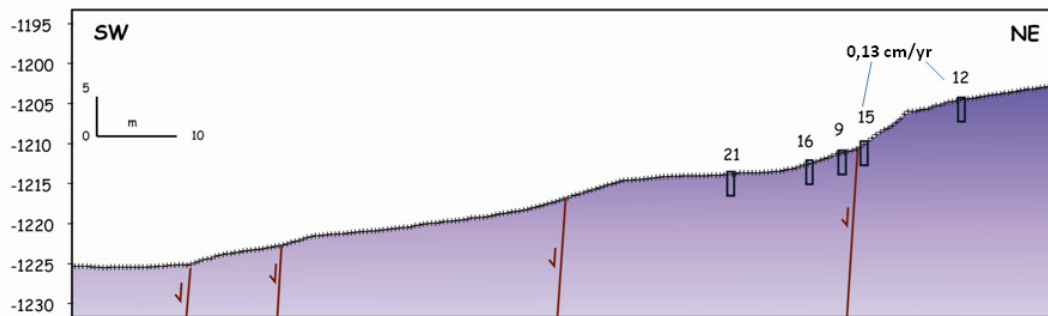
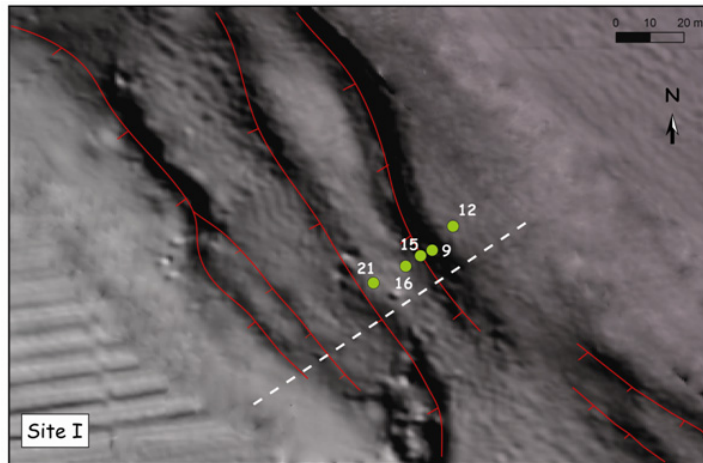


Figure 4.44 : (a) Microbathymetry map of site I. Three steps of individual scarps are observed. Cores are labeled with green dots. (b) Profile across three step-fault scarp with cores located.

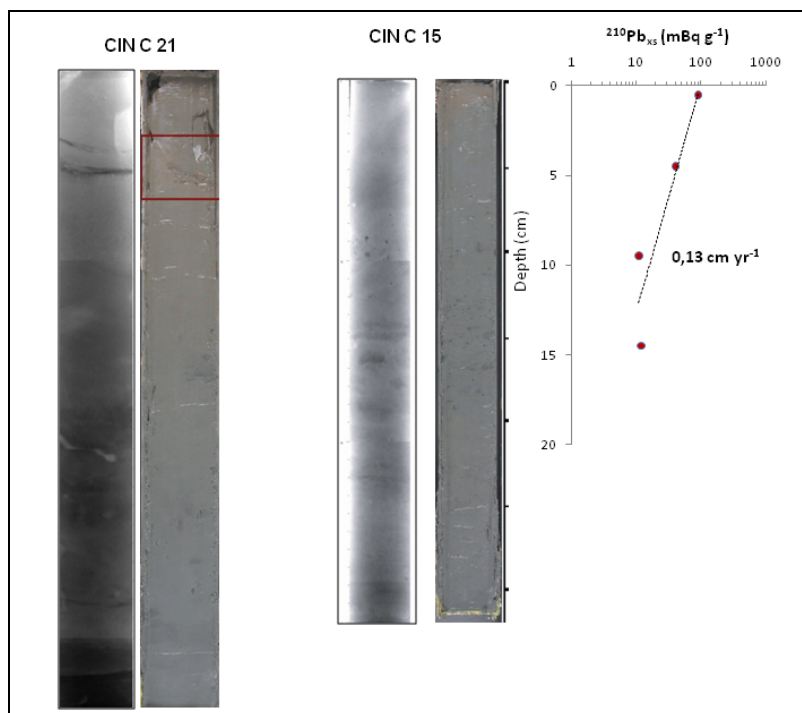


Figure 4.45 : X-rays and ^{210}Pb profiles of Cores 15 and 21.

Both cores 15 and 12 are composed of homogenous silty clay. ^{210}Pb profiles give a sedimentation rate of 0,13 cm/yr. As sedimentation rates seem to be rather homogeneous for a given site, we can extrapolate dating of layers on cores presenting a disturbed layer like in Core 21. Accordingly, 0.13 cm/yr suggest an accumulation date of 38 yrs BP similarly matching with 1963 Çınarcık earthquake.

Table 1 : All the sedimentation rates determined from the $^{210}\text{Pb}_{\text{xs}}$ profiles of selected MARMARASCARPS short cores in the Sea of Marmara

Core Number	Location	Sediment accumulation rate cm/yr
TK C16	Tekirdag basin (South)	0,22
TK C18	Tekirdag basin (South)	0,23
TK C19	Tekirdag basin (South)	0,22
Wh C06	Western high	0,53
Wh C05	Western high	0,61
Wh C04	Western high	0,18
CB C07	Central basin (South)	0,13
CB C22	Central basin (South)	0,11
CB C23	Central basin (South)	0,12
CB C14	Central basin (South)	0,17
CIN C 20	Çınarcık basin (North)	0,13
CIN C19	Çınarcık basin (North)	0,1
CIN C15	Çınarcık basin (North)	0,13

Sedimentation rates determined from ^{210}Pb profiles (excluding disturbed layers) on cores from all 4 sites show a narrow range of 0,1-0.23 cm y^{-1} (See Table 1) except the cores C06 and C05 from Western high which were collected from a sag pond (expected higher sedimentation rate). These unconflicting and consistent rates suggest the convenience of the ^{10}Pb geochronology for dating disturbed sediments.

4.6 Discussion: earthquake ruptures in the Sea of Marmara and implications for the seismic hazard for the region

The submarine observations of the fault scarps and recent studies incorporating the coseismic slip distribution on land (Altunel et al., 2004) and sea floor (Armijo et al., 2005) together with the analysis of historical seismograms (Aksoy et al., 2009)

suggest that the 1912 rupture extends most likely from Saros bay in the west all the way to the Central basin in the east (Figure 4.3). As shown above, the submarine observations concerning the western termination of the 1999 İzmit earthquake also suggest that the rupture reached the entrance of the Çınarcık basin.

Consequently, the unbroken section of the NAF under the Sea of Marmara consists of two segments, i.e., the Central Marmara and the Princes Island faults. The total size of the seismic gap is therefore about 100 km, which implies an earthquake size of M 7.3 if they both break simultaneously. However, these two fault segments may rupture alone or together, which appears to depend where the earthquake initiates (Oglesby et al., 2008). If the earthquake initiates on the Princes Islands fault, the simulations suggest that rupture, probably, will not propagate in to the neighboring faults. However, if the earthquake nucleates around the western tip of the Central Marmara segment and propagates towards east, it seems very likely that the Prince's Island segment will fail as well.

Microbathymetry and ^{210}Pb analyses suggest that the Ms 6.4 1963 Çınarcık earthquake may have occurred on the Prince's Islands fault that bounds the northeast margin of the Çınarcık basin.

5. THE AGE AND THE OFFSET OF THE NORTH ANATOLIAN FAULT IN MARMARA REGION

5.1 Introduction

Segmentation, deformation type, kinematics, slip rates, morphology, seismicity of a fault depends mainly on its age and hence its total offset. However, the age and offset of the north Anatolian fault is still a matter of debate. Below is a summary of previous studies on the age and offset of the NAF and new observations near the Marmara region.

5.2 The age of the NAF

Several age constraints have been proposed by different authors based on geological and geomorphologic observations (Ketin, 1957; Pavoni, 1961; Ketin, 1969; Erinç, 1973; Tatar, 1975; Seymen, 1975; Ketin, 1976; Şengör, 1979; Barka, 1981; Barka and Hancock, 1984; Şengör (1985), Şengör et al., 2005). Ketin (1957) proposed that the fault initiated during Neogene (15-20 Ma ago). In his 1976 paper, he suggested more specifically that the oldest sedimentary rocks along the NAF were medial Miocene in age and therefore, the fault had to be of that age at oldest. Another proposal by Erinç (1973) was taking into account the drainage network around the fault to be established by the late Miocene and modified largely by the activity of the NAF. Tatar (1975) mapped inactive branches of the NAF in the west of Erzincan, which are now covered by Pliocene sediments, and thus, was proposing that the fault must have originated in pre-Pliocene time (Figure 5.1). Seymen's (1975) detailed geological mapping around Reşadiye provided one of the most valuable contributions to the discussion. He presented that the boundary between the Pontide and Anatolide domains was cut and offset by the North Anatolian transform. In his detailed map, the fault displaces the post-Burdigalian suture between Amasya and Erzincan and it must have been at least of this age. By combining the observations of Tatar (1973) and Seymen (1975) at the same region, the age of the NAF can be bracketed between Burdigalian and Pliocene. Şengör (1985) and Şengör et al. (1985)

have concluded that the NAF initiated in early to late Miocene (~13 Ma), soon after continental collision between the Arabian and Eurasian plates. Whereas, Hancock and Barka (1984) had pointed out that during the late Miocene a broad shear zone developed earlier in the place of the future NAF. The syn-sedimentary and post-depositional meso faults of this NAF-related shear zone are confined to the late Serravallian- early Pliocene Pontus formation (Şengör et al., 1983; Hancock and Barka, 1984). On the basis of the analysis of mesoscopic and macroscopic structures, Barka and Hancock (1984) and Barka (1985) suggested that the fault zone might have initiated as a wide shear zone towards the end of Tortonian, and the main trace of the NAF may have developed in the early Pliocene.

Study of the basins along the NAF showed that only the late Miocene-Pliocene basins within the NAF are related to motion on the fault zone (Barka, 1992). They formed mainly where there are either or both releasing step-overs and releasing bends along the fault zone.

5.3 The offset of the NAF

The long term geological slip rate of the NAF is not well constrained because of difficulties in finding datable young geological markers offset by the fault. Offsets of rivers and geological markers such as suture zones and lithological units along the NAF show that the total displacement can be as much as 80 km (Figure 5.1b). Depending on the ages of the rivers and geological markers smaller offsets are also observed at many places. In their recent paper, Şengör et al. (2005) suggest that the NAF formed by progressive strain localization in a westward widening right-lateral shear zone propagating from eastern Turkey (where it started about 11 to 13 Ma ago) towards the west. The NAF is claimed to have reached the Sea of Marmara no earlier than 200 ka ago, although shear related deformation in a broad zone there had already commenced in late Miocene. Apparently, this has resulted in increase in localized offset from west to east. However, the total offset measured by various workers along the fault doesn't support this inference. On the contrary, the offset appears to be rather uniform along the fault (Figure 5.1).

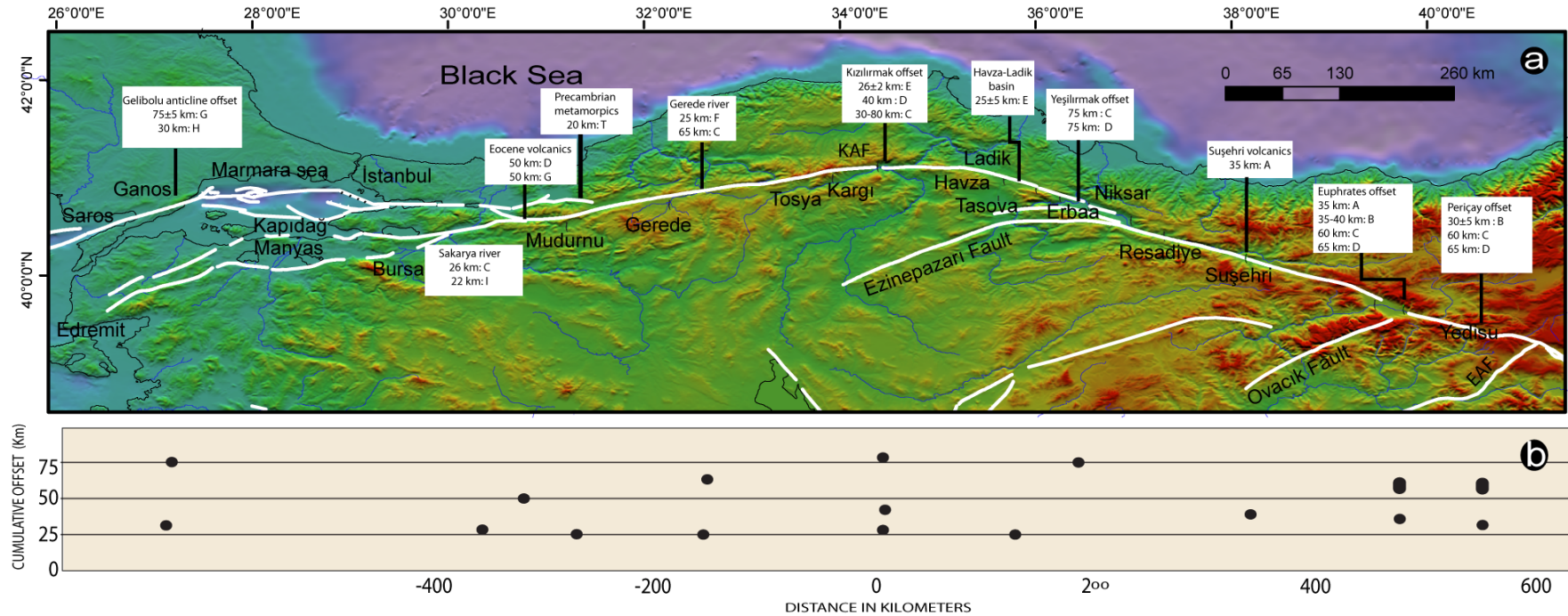


Figure 5.1 : (a) Map of the North Anatolian fault map plotted on shaded elevation image (SRTM-90 m) with location of offset measurements reported various researchers (A to I) along the fault (A: Koçyiğit et al., 1989; B: Barka, 1992; C: Şengör et al., 2005; D: Hubert-Ferrari et al., 2002; E: Barka and Hancock, 1984; F: Şaroğlu, 1998; G: Armijo et al., 1999; H: Koop, 1969; I: Koçyiğit, 1988). (b) Plot of cumulative offsets along the fault showing that the maximum offset appears to be 70-80 km and uniform between Karlıova and Tekirdağ.

Furthermore, a clear 55 ± 3 -km offset of metamorphic and Eocene volcanic rocks across the Intra-Pontite suture along the NAF in Mudurnu valley (Figure 5.2) conflicts with the theory of Şengör et al. (2005) which suggests that the total offset on a single branch such as the one running through the Sea of Marmara should not exceed several km because the localized shear and thus the NAF is only 200 ka. Figure 5.2 is a geology map of Turkey of 1:500.000 scale recently compiled by MTA showing Paleozoic and Mesozoic metamorphic and Eocene volcanic rocks displaced along the NAF bounding the southern side of the Almacık block. Several contacts between these rocks on either side of the Mudurnu valley can be matched very precisely and thus the offset can be measured with high confidence (Figure 5.2). An offset of 55 ± 3 km along this segment suggests that shearing has long been localized here, since at least several million years. Another, but a weakly constrained offset of 25 ± 5 km (Figure 5.2) is spotted along the Düzce fault that bounds the northern boundary of the Almacık block. Summing these two offsets gives a total offset of 80 km, similar to those measured across the Yeşilirmak River in the east (Hubert-Ferrari et al., 2002) and the Ganos fault in the west (Armijo et al., 1999) (Figures 5.1 and 5.3).

Armijo et al. 1999 suggest a 70 ± 5 km offset due to the truncation of the Ganos anticline by the NAF. Not all authors agree with this estimate (Yaltrak et al., 1999 ; Okay et al. 2003). However, the structural pattern given in the geology map and the range of the right lateral offset is consistent with the above mentioned geological offsets in the eastern part of the Sea of Marmara.

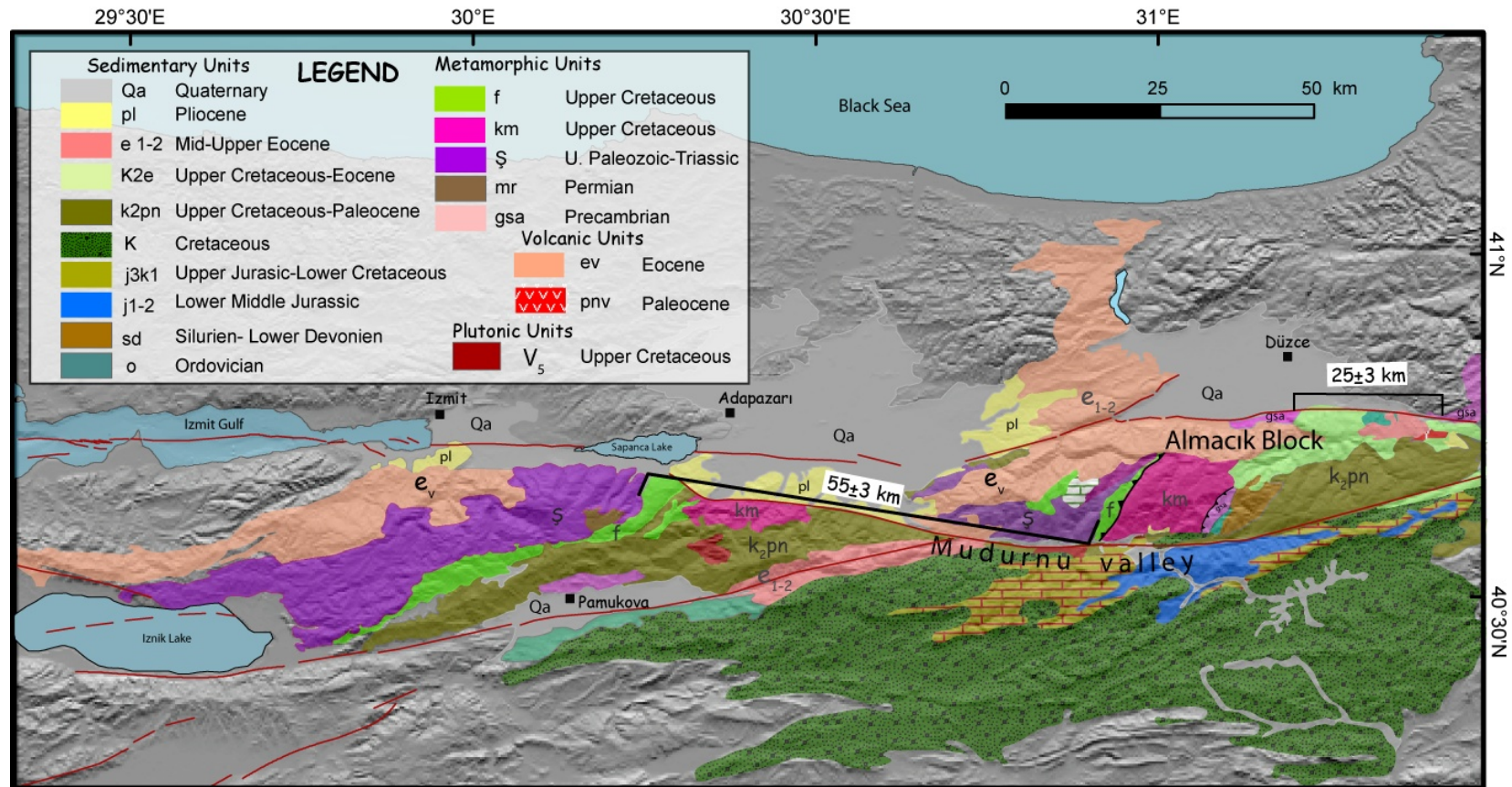


Figure 5.2 : Geological map of Mudurnu valley and its surroundings (from MTA). Note the offset of volcanic and metamorphic rocks across the southern branch of the NAF along the Mudurnu valley and south of Düzce plain.

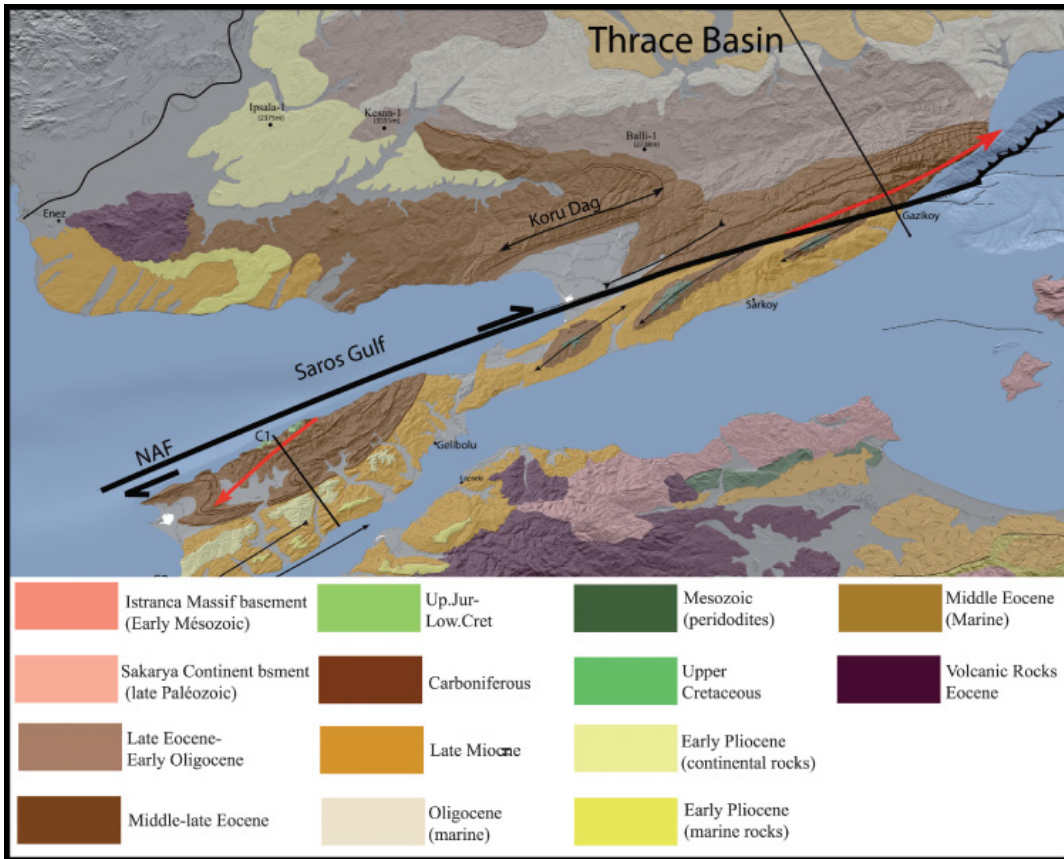


Figure 5.3 : Geological map of the Dardanelles and Ganos region. Note the offset of Middle-late Eocene rocks on either side of the NAF (geology map modified from Armijo et al. 1999).

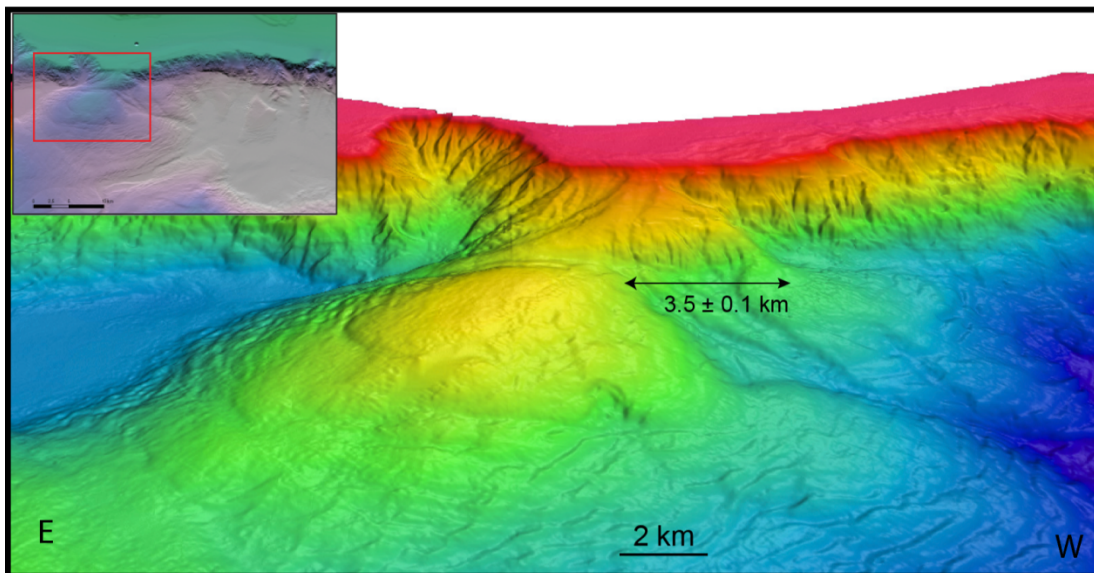


Figure 5.4 : Offsets of morphological features on the sea floor. The ridge is offset by $\sim 3.5 \pm 0.1$ km across the Eastern High.

While NAF reveals such large geological offsets of up to 80-85 km, it is rather difficult to deduce a right-lateral offsets in the Sea of Marmara compared to onland offset markers. However, submarine canyons and ridges can provide good markers. Such a ridge intersecting the Central fault segment is offset $\sim 3.5 \pm 0.1$ km right-laterally along the Central segment. This right-lateral offset was suggested by both Armijo et al. (2002) and Le Pichon et al. (2003) as 3.5 km and 4 km respectively. It has been determined as the largest offset along the submerged section of the NAF in the Sea of Marmara. However, the outer basin of the Central basin is also offset right-laterally. Reconstruction of the basin suggests a 9 ± 1 km right-lateral displacement. The reconstruction is applied based on the strike of the two strike-slip segments that embrace the inner pull-apart basin. Hence, after the reconstruction inner basin appears as a narrow basin at a different stage of its opening (Figure 5.5). A comparable offset has been proposed by Aksoy (2009) along the Ganos fault onland. Reconstruction of a large scale drainage system suggests a 9 km offset as similarly in the Central basin.

Other right lateral offsets ranging in smaller scales are also determined. East of the offset ridge in Eastern High, another ridge is offset right-laterally. The reconstruction depicts an oblique offset that requires 280 m right-lateral and 85 m vertical offset (Figure 5.5)

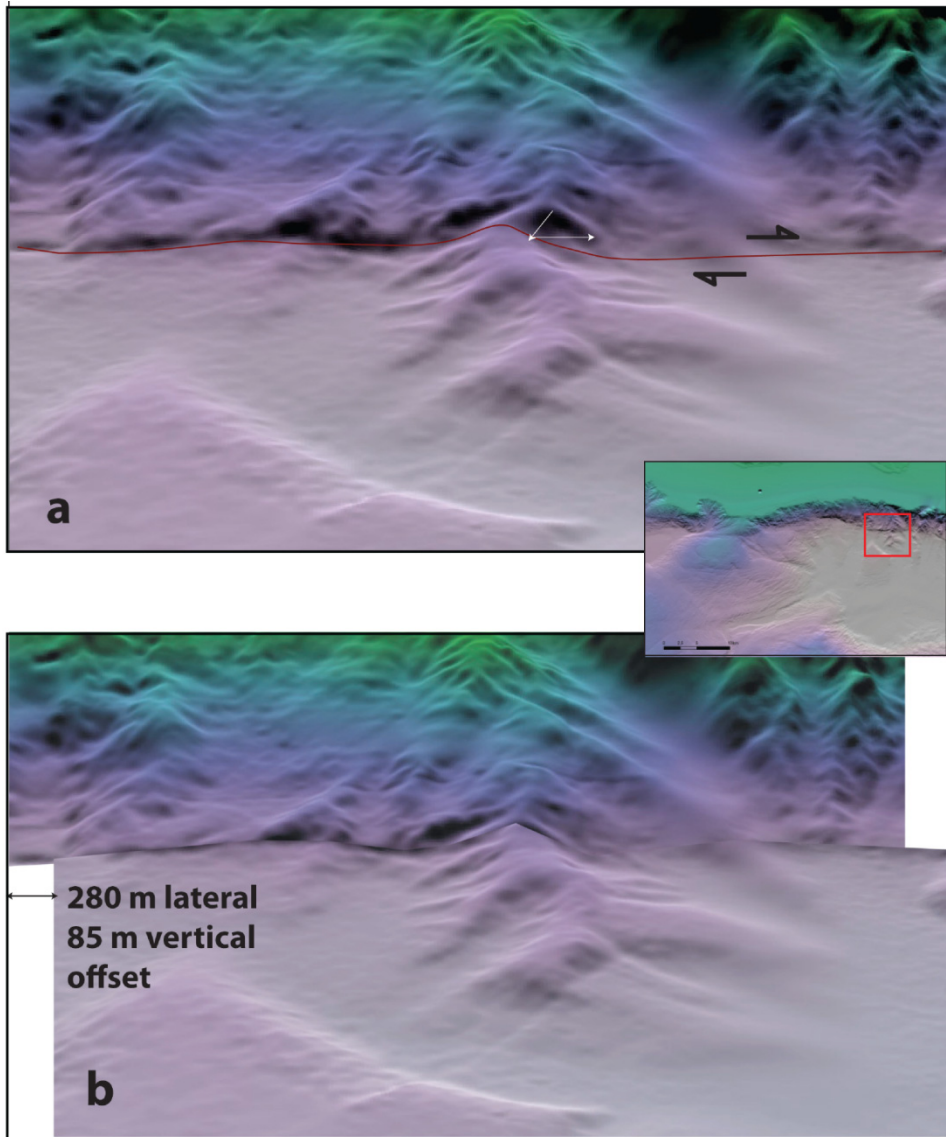


Figure 5.5 : The ridge is offset 280 m right laterally with a vertical offset of 85 m. Note the white arrows in the upper panel which indicate motion vectors for an oblique displacement.

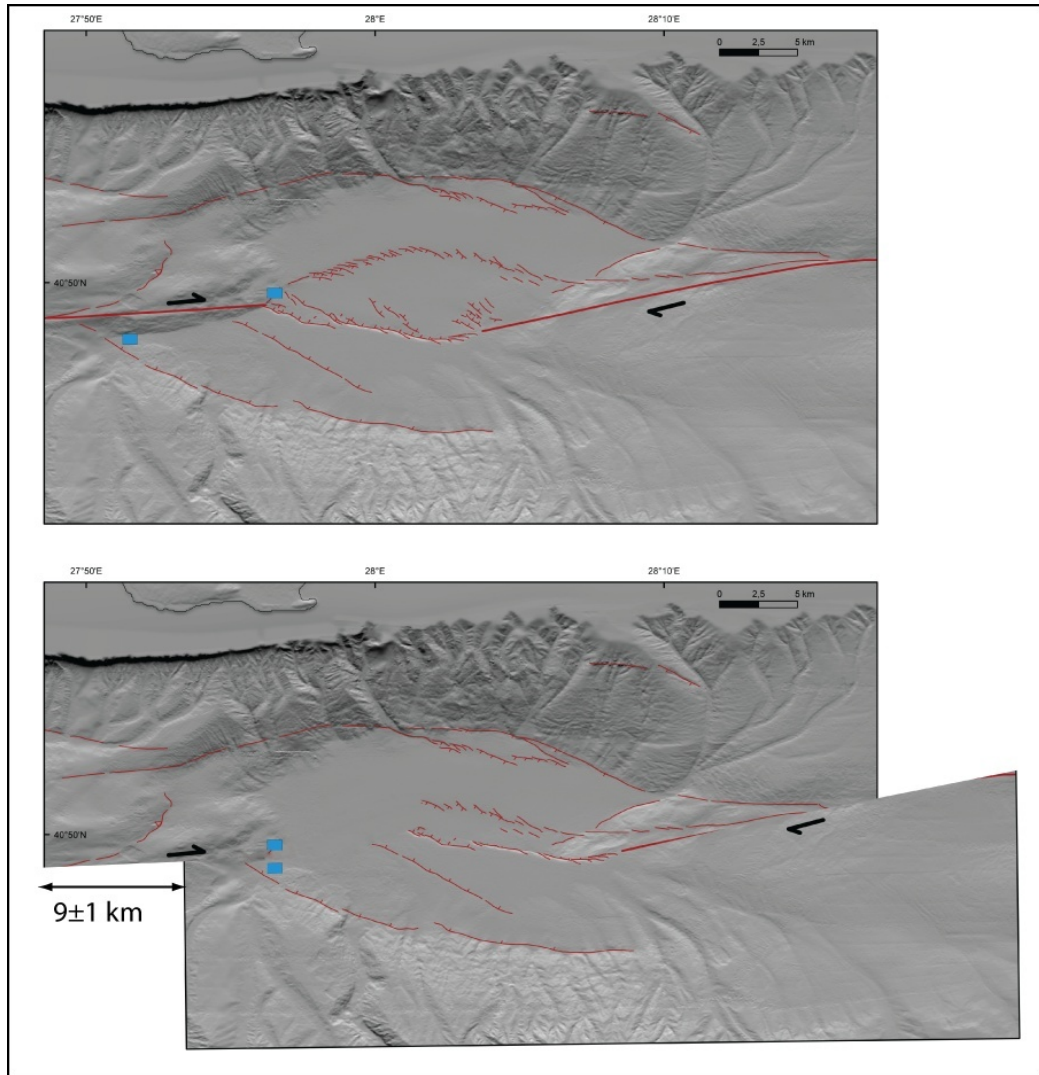


Figure 5.6 : Reconstruction of of the Central basin reveals a 9 ± 1 km of right lateral offset.

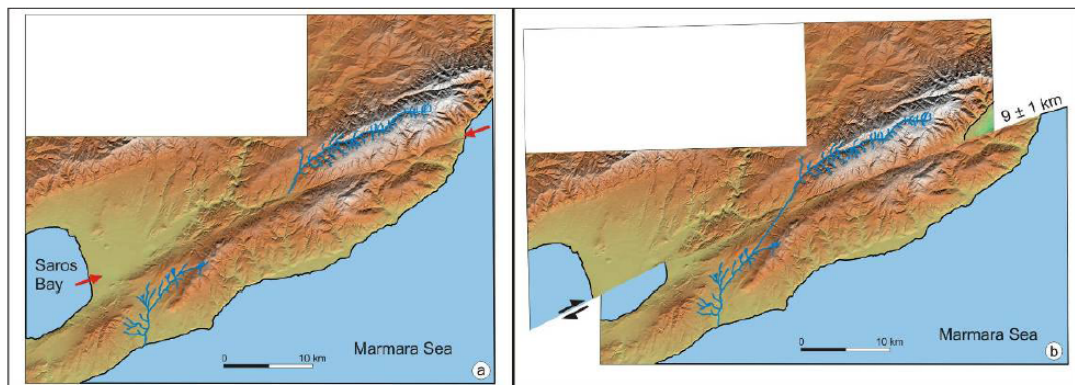


Figure 5.7 : Aksoy (2009) suggest that a large and deep incised valley which terminates abruptly at Gölcük, is offset 9 ± 1 km along the Ganos fault.

5.4 Discussion

The total offset on either side of the Sea of Marmara is over 70 km. This implies that the offset along the submarine fault segments should be comparable. Numerous offsets ranging between tens of meters to several km can also be observed along the submarine sections of the NAF in the Sea of Marmara, some of which are shown in Figure 5.4. However, the maximum offset observed on the sea floor is about 9 km and located on the Central basin (Figure 5.5). Obviously, as in the case of offsets on drainage systems on land, the amount of offset is directly related to the age of the structure sheared by the fault; the older the structure the longer the offset. Taking into account the maximum offset proposed by different researchers along the NAF, the average total offset seems to be around 75 km. Assuming that the NAF formed in late Miocene – early Pliocene (~5 m.a.) the geologic slip rate is around 15 mm/yr, 5-10 mm less than the present day plate velocity determined by GPS (Reilinger et al., 2006).

6. CONCLUSIONS

Geomorphologic and geologic evidence allows an accurate description of active submarine faults in the Sea of Marmara, next to Istanbul. Those faults exhibit earthquake scarps associated with recent historic events. The quality and dense coverage of observations using complementary high-resolution sensors (bathymetry and shallow penetration profiling), sediment cores and ^{14}C ages are comparable to the best standards in studies of active faults on land. Some major conclusions are:

- High resolution bathymetry and shallow and deep seismic reflections reveal that the Marmara contains 3 large deep (with sediment infill > 5 km) basins (i.e., Çınarcık, Central and Tekirdağ) that appear to be opening under transtension, which is confirmed by analyses and modeling of GPS velocity field.
- Taking into account the observations concerning the kinematics, geometry, morphology of the submarine faults and sedimentation rates, the northern branch of the NAF under the Sea of Marmara can be divided into 5 major segments (longer than 35 km). These are the Tekirdağ (45 km), Central (70 km), Prince's Island (35 km), Southern Çınarcık (55 km) and Izmit segments that accommodate a large portion of plate motion, hence have high slip rates, and able to generate large earthquakes.
- Analyses of high resolution bathymetry and multi-channel seismics reveals the fine detailed geometry of submarine fault scarps in the Sea of Marmara that requires a combination of strike-slip and normal faulting consistent with the transtensional tectonics.
- The submarine scarps in the northern Sea of Marmara floor have formed by accumulation of earthquake slip under competing tectonic, erosion and sedimentation processes subject to climatic change. The visible fault scarps in the sea floor have emerged progressively after the occurrence of catastrophic sedimentary events associated with Late Pleistocene deglaciation.

- Sedimentation rates in the deep pull-apart basins are fast (1-3 mm/yr), but they do not keep up with even faster fault rates and associated subsidence that create the deep bathymetric sinks. The normal faulting throw rates are up to 6 mm/yr at basin margins. Throw and right-lateral slip rates deduced from the scarp evidence are consistent with rates deduced at larger scale from geology and GPS.
- The analysis of microbathymetry suggests that the 1999 İzmit earthquake rupture reached at least to 29.38°E longitudes about 10 km west of Hersek delta in the Gulf of İzmit. We infer that the seismic break continues to the west reaching a total length of ~145 km at around 29.24°E longitudes consistent with the 1999 rupture deduced from SAR interferometry. It appears to stop at the entrance of Çınarcık basin where normal faulting component prevails. We suggest that fault complexity at the junction between dominant strike-slip faulting along the İzmit fault and significant normal faulting in the Çınarcık basin may acts as a barrier to rupture propagation of large earthquakes.
- The submarine observation of fault scarps with microbathymetry and video imaging and ²¹⁰Pb dating suggest strongly that the August 9, 1912 Ganos earthquake reached that at least to the middle of the Tekirdağ basin (27.37.69"E 40.48.17"N) and most probably all the way to the Central basin, suggesting a total rupture of 120-150 km, similar to that of the 1999 İzmit earthquake. Consequently, the unbroken section of the NAF under the Sea of Marmara and thus the size of the Marmara seismic gap is therefore about 100 km, which implies an earthquake size of M 7.3.
- A small fresh break 20-30 km long is identified in the NE Cınarcık Basin fault, which may be correlated with the 18 October 1963 (Ms 6.4) earthquake or 1894 earthquake. ²¹⁰Pb dating present evidence of disturbance in the sediments which match with the 1963 earthquake.
- Sedimentation rates determined from ²¹⁰Pb profiles show a narrow range 0.1-0.2 cm y⁻¹. Independently of the position of the cores sedimentation rates are rather constant.
- Eocene volcanic and Cambrian metamorphic rocks across the North Anatolian fault along the Mudurnu valley depicts an geologic offset of 55±3 km suggesting that shearing has long been localized in the Eastern Marmara

and thus the localization of the NAF in the Sea of Marmara must be much older than previously suggested 200 kyrs.

- In the Sea of Marmara region, block motion describes the kinematics with one block boundary (Northern Marmara Fault system) carrying a greater ratio of strike-slip to normal motion than others. The same asymmetric slip separation seems to have persisted since the inception of the NAF in the region.
- The Central and Prince's Island segments constitute the Marmara seismic gap of ~100 km. Considering their length and kinematics, it can be said that each of these segments is capable of producing earthquakes larger than magnitude 7. However, each one may be reactivated alone during an earthquake of $M > 7$ or together with the neighboring 2-3 segments generating a much larger earthquake. In addition to these major segments, there are other minor segments, such as those bounding the outer Central basin and İmralı basin. They have overwhelmingly normal slip component with lower slip rates and thus are mainly accommodation structures. They may also produce earthquakes but, of smaller size.

REFERENCES

- Abdüsselamoğlu, M. S.**, 1977. The Palaeozoic and Mesozoic in the Gebze region- Explanatory text and excursion guidebook.
- Adamia, S. A., Chkhotua, T., Kekelia, M., Lordkipanidze, M., Shavishvili, I. and Zakariadze, G.**, 1981. Tectonics of the Caucasus and adjoining regions: implications for the evolution of the Tethys ocean, *Journal of Structural Geology*, **3**, pp.437-447.
- Aksoy, E. M., Meghraoui, M., Vallée, M. and Cakir, Z.**, 2009. Rupture Characteristics of the 1912 Mürefte (Ganos) Earthquake Segment of the North Anatolian Fault (Western Turkey), *Eos Trans. AGU* San Francisco, T13C-1884.
- Aksoy, M. E.**, 2009. Active Tectonics and Paleoseismology of the Ganos Fault Segment and Seismic Characteristics of The 9 August 1912 Mürefte Earthquake of the North Anatolian Fault (Western Turkey), *PhD Thesis*, Eurasia Institute of Earth Sciences, Istanbul
- Aksoy, M. E., Meghraoui, M., Ferry, M., Çakır, Z., Akyüz, S. and Altunel, E.**, 2009. Slip distribution and rupture characteristics of the 9 August 1912 Mürefte earthquake (Ms=7.3) along the Ganos segment of the North Anatolian Fault (Turkey). , *SSA Annual Meeting* Monterey, USA.
- Aksu, A. E., Calon, T. J., Hiscott, R. N. and Yaşar, D.**, 2000. Anatomy of the North Anatolian Fault Zone in the Marmara Sea, Western Turkey: Extensional Basins Above a Continental Transform, *GSA Today*, Vol. **10**, no. 6, pp. 5.
- Aksu, A. E., Hiscott, R. N. and Yasar, D.**, 1999. Oscillating Quaternary water levels of the Marmara Sea and vigorous outflow into the Aegean Sea from the Marmara Sea-Black Sea drainage corridor, *Marine Geology*, **153**, pp. 275-302.
- Aksu, A. E., Hiscott, R. N., Kaminski, M. A., Mudie, P. J., Gillespie, H., Abrajano, T. and Yasar, D.**, 2002. Last glacial-Holocene paleoceanography of the Black Sea and Marmara Sea: stable isotopic, foraminiferal and coccolith evidence, *Marine Geology*, **190**, pp. 119-149.
- Aksu, A. E., Hiscott, R. N., Yasar, D., Isler, F. I. and Marsh, S.**, 2002. Seismic stratigraphy of Late Quaternary deposits from the southwestern Black Sea shelf: evidence for non-catastrophic variations in sea-level during the last ~10.000 yr, *Marine Geology*, **190**, pp. 61-94.

- Aksu, A. E., Yaltirak, C. and Hiscott, R. N.,** 2002. Quaternary paleoclimatic-paleoceanographic and tectonic evolution of the Marmara Sea and environs, *Marine Geology*, **190**, pp. 9-18.
- Akyüz, H.S., Hartleb, R., Barka, A., Altunel, E., Sunal, G., Meyer, B., and Armijo, R.,** 2002, Surface rupture and slip distribution of the 12 November 1999 Düzce earthquake (M 7.1) North Anatolian Fault, Bolu, Turkey, *Bull. Seism. Soc. Am*, v. **92**, p. 61-66.
- Altınok, Y., Alpar, B. and Yaltirak, C.,** 2003. Şarköy - Mürefte 1912 Earthquake's Tsunami, extension of the associated faulting in the Marmara Sea, Turkey, *Journal of Seismology*, **7**, pp. 329-346.
- Altunel, E., Barka, A. A. and Akyüz, H. S.,** 2000. Slip distribution along the 1912 Mürefte-Şarköy earthquake, the North Anatolian Fault, Western Marmara, The 1999 Izmit and Düzce Earthquakes: Preliminary Results, pp. 341-349.
- Altunel, E., Meghraoui, M., Akyüz, H. S. and Dikbaş, A.,** 2004. Characteristics of the 1912 co-seismic rupture along the North Anatolian Fault Zone (Turkey): implications for the expected Marmara earthquake, *Terra Nova*, **16**, pp. 198-204.
- Ambraseys, N. and Finkel, C.,** 1987. Seismicity of Turkey and Neighbouring Region 1899-1915, *Annales Geophys.*, 5B, pp. 701-726.
- Ambraseys, N. and Finkel, C.,** 1987. The Saros – Marmara earthquake of 9 August 1912, *Earthquake Engineering Structural Dynamics*, **15**, pp. 189–211.
- Ambraseys, N.N., and Finkel, C.,** 1991. Long-term seismicity of Istanbul and of the Marmara Sea region, *Terra Nova*, v. **3**, pp. 527-539.
- Ambraseys, N. N. and Finkel, C. F.,** 1995. The Seismicity of Turkey and adjacent areas: A Historical Review, 1500-1800, Eren Yayıncılık, İstanbul.
- Ambraseys, N. N. and Jackson, J. A.,** 2000. Seismicity of the Sea of Marmara (Turkey) since 1500, *Geophysical Journal International*, Vol. **141**, no. 3, pp. F1-F6.
- Ambraseys, N. N.,** 2000. The seismicity of the Marmara Sea area 1800 - 1899, *Journal of Earthquake Engineering*, Vol. 4, no. **3**, pp. 377-401.
- Ambraseys, N. N.,** 2001. Reassessment of earthquakes, 1900-1999, in the Eastern Mediterranean and the Middle East, *Geophysical Journal International*, Vol. **145**, no. 2, pp. 471-485.
- Ambraseys, N. N.,** 2001. The earthquake of 10 July 1894 in the Gulf of Izmit (Turkey) and its relation to the earthquake of 17 August 1999, *Journal of Seismology*, Vol. **5**, no. 1, pp. 117-128.
- Ambraseys, N. N.,** 2001. The Earthquake of 1509 in the Sea of Marmara, Turkey, Revisited, *Bulletin of the Seismological Society of America*, Vol. **91**, no. 6, pp. 1397-1416.
- Ambraseys, N. N.,** 2002. Seismic sea-waves in the Marmara Sea region during the last 20 centuries, *Journal of Seismology*, Vol. **6**, no. 4, pp. 571-578.

- Ambraseys, N. N.**, 2002. The Seismic Activity of the Marmara Sea Region over the Last 2000 Years, *Bulletin of the Seismological Society of America*, Vol. **92**, no. 1, pp. 1-18.
- Appleby, P.G., Oldfield, F.**, 1992. *Application of lead-210 to sedimentation studies*. In: Uranium-series disequilibrium: Application to Earth, Marine, and Environmental Sciences, Ivanovich, M., & Harmon, R.S. (Editors), Second Edition, Clarendon Press, Oxford, 731-778.
- Armijo, R., Meyer, B., Hubert, A. and Barka, A.**, 1999. Westward propagation of the North Anatolian fault into the northern Aegean: Timing and kinematics, *Geology*, Vol. **27**, no. pp. 267-270.
- Armijo, R., Meyer, B., Navarro, S., King, G. and Barka, A.**, 2002. Asymmetric slip partitioning in the Sea of Marmara pull-apart: a clue to propagation processes of the North Anatolian Fault, *Terra Nova*, Vol. **14**, no. 2, pp. 80-86.
- Armijo, R., Pondard, N., Meyer, B., Uçarkus, G., Lépinay, B.M.d., Malavieille, J., Dominguez, S., Gustcher, M.-A., Schmidt, S., Beck, C., Çagatay, N., Çakir, Z., Imren, C., Eris, K., Natalin, B., Özalaybey, S., Tolun, L., Lefèvre, I., Seeber, L., Gasperini, L., Rangin, C., Emre, O., and Sarikavak, K.**, 2005. Submarine fault scarps in the Sea of Marmara pull-apart (North Anatolian Fault): Implications for seismic hazard in Istanbul, *Geochem. Geophys. Geosyst.*, v. **6**, pp. Q06009.
- Aydın, Y.**, 1974. Etude pétrographique et géochimique de la partie centrale du Massif d'Istranca (Turquie)
- Bailer, A.J., Reed, L.D., Stayner, L.T., Brotzu, P., Gomes, C.B., Melluso, L., Morbidelli, L., Morra, V., Ruberti, E., Ryan, W.B.F., Pitman, W.C., Major, C.O., Shimkus, K., Moskalenko, V., Jones, G.A., Dimitrov, P., Gorur, N., Sakinc, M., and Yuce, H.**, 1997, An abrupt drowning of the Black Sea shelf, *Marine Geology*, v. **138**, pp. 119-126.
- Barka, A.A.**, 1981. Seismo-tectonic aspects of the North Anatolian Fault. *PhD thesis*. Univ. Bristol. [XX]+335 pp.
- Barka, A. A. and Hancock, P. L.**, 1984. Neotectonic deformation patterns in the convex-northwards arc of the North Anatolian fault zone, Geological Society, London, *Special Publications*, Vol. **17**, no. 1, pp. 763-774.
- Barka, A. A. and Kadinsky-Cade, K.**, 1988. Strike-slip fault geometry in Turkey and its influence on earthquake activity, *Tectonics*, Vol. **7**, no. pp. 663-684.
- Barka, A. A.**, 1992. The North Anatolian fault zone, *Annales Tectonicae*, pp. 164-195.
- Barka, A.**, 1985. Geology and tectonic evolution of some Neogene-Quaternary basins in the North Anatolian fault zone. *In Katin Symposium Spec. Publ. Geol. Soc.*, pp. 209-227.

- Barka, A., Akyuz, H. S., Altunel, E., Sunal, G., Cakir, Z., Dikbas, A., Yerli, B., Armijo, R., Meyer, B., de Chabaliér, J. B., Rockwell, T., Dolan, J. R., Hartleb, R., Dawson, T., Christofferson, S., Tucker, A., Fumal, T., Langridge, R., Stenner, H., Lettis, W., Bachhuber, J. and Page, W., 2002.** The Surface Rupture and Slip Distribution of the 17 August 1999 Izmit Earthquake (M 7.4), North Anatolian Fault, *Bulletin of the Seismological Society of America*, **92**, pp. 43-60.
- Bécel, A., Laigle, M., de Voogd, B., Hirn, A., Taymaz, T., Galvé, A., Shimamura, H., Murai, Y., Lépine, J. C., Sapin, M. and others 2009.** Moho, crustal architecture and deep deformation under the North Marmara Trough, from the SEISMARMARA Leg 1 offshore-onshore reflection-refraction survey, *Tectonophysics*, **467**, pp. 1-21.
- Beck, C., Mercier de Lépinay, B., Schneider, J.-L., Cremer, M., Çağatay, N., Wendenbaum, E., Boutareaud, S., Ménot, G., Schmidt, S., Weber, O., Eris, K., Armijo, R., Meyer, B., Pondard, N., Gutscher, M.-A., Turon, J. L., Labeyrie, L., Cortijo, E., Gallet, Y., Bouquerel, H., Gorur, N., Gervais, A., Castera, M. H., Londeix, L., de Ressaúquier, A. and Jaouen, A., 2007.** Late Quaternary co-seismic sedimentation in the Sea of Marmara's deep basins, *Sedimentary Geology*, **199**, pp. 65-89.
- Biddle, K. T., and Christie-Blick, N., 1985.** *Strike-slip deformation, basin formation, and sedimentation: based on a symposium / sponsored by the Society of Economic Paleontologists and Mineralogists ; edited by Kevin T. Biddle and Nicholas Christie-Blick.* The Society, Tulsa, Okla., U.S.A., pp. 1-34.
- Bilham, R. and King, G., 1989.** The morphology of strike-slip faults - Examples from the San Andreas Fault, California, *Journal of Geophysical Research*, Vol. **94**, no. pp. 10204-10216.
- Bozkurt, E., 2001.** Neotectonics of Turkey – a synthesis, *Geodinamica Acta*, Vol. **14**, no. pp. 18.
- Çağatay, M. N., Görür, N., Algan, O., Eastoe, C., Tchapylyga, A., Ongan, D., Kuhn, T. and Kuşçu, I., 2000.** Late Glacial-Holocene palaeoceanography of the Sea of Marmara: timing of connections with the Mediterranean and the Black Seas, *Marine Geology*, **167**, pp. 191-206.
- Çağatay, M. N., Gorur, N., Polonia, A., Demirbag, E., Sakinc, M., Cormier, M. H., Capotondi, L., McHugh, C., Emre, O. and Eris, K., 2003.** Sea-level changes and depositional environments in the Izmit Gulf, eastern Marmara Sea, during the late glacial-Holocene period, *Marine Geology*, **202**, pp. 159-173.
- Çağatay, N., M., Algan, O., Sakinç, M., Eastoe, C. J., Egesel, L., Balkis, N., Ongan, D. and Caner, H., 1999.** A mid-late Holocene sapropelic sediment unit from the southern Marmara sea shelf and its palaeoceanographic significance, *Quaternary Science Reviews*, **18**, pp. 531-540.

- Çakır, Z., Chabalier, J.-B. d., Armijo, R., Meyer, B., Barka, A. and Peltzer, G.,** 2003. Coseismic and early post-seismic slip associated with the 1999 Izmit earthquake (Turkey), from SAR interferometry and tectonic field observations, *Geophysical Journal International*, **155**, pp. 93-110.
- Carton, H.,** 2003. Structure of the Cinarcik Basin (eastern Marmara Sea) from densely-spaced multi-channel reflection profiles, *Lithos Science Report*, Bullard Laboratories, University of Cambridge, Vol. **5**, no. pp. 69-76.
- Carton, H., Singh, S. C., Hirn, A., Bazin, S., Voogd, B., Vigner, A., Ricolleau, A., Cetin, S., Oçakoğlu, N., Karakoç, F., Sevilgen, V. and Carton, H.,** 2007. Seismic imaging of the three-dimensional architecture of the Cinarcik Basin along the North Anatolian Fault, *J. Geophys. Res.*, Vol. **112**, pp. B06101.
- Chappell, J. and Shackleton, N. J.,** 1986. Oxygen isotopes and sea level, *Nature*, **324**, pp. 137-140.
- Chen, F., Siebel, W., Satir, M., Terzioğlu, M. and Saka, K.,** 2002. Geochronology of the Karadere basement (NW Turkey) and implications for the geological evolution of the Istanbul zone, *International Journal of Earth Sciences*, **91**, pp. 469-481.
- Cochran, J. K,** 1992. The Oceanic Chemistry of the Uranium and Thorium-Series Nuclides. Ivanovich, M., and Harmon, R., eds, Uranium Series Disequilibrium-Application to Environmental Problems: *Applications to Earth, Marine and Environmental Sciences*, 2nd Edition, Oxford Press, London, pp. 334-395.
- Cormier, M. H., Seeber, L., McHugh, C. M. G., Polonia, A., Çagatay, M. N., Emre, Ö., Gasperini, L., Görür, N., Bortoluzzi, G., Bonatti, E. and others,** 2006. North Anatolian Fault in the Gulf of Izmit (Turkey): Rapid vertical motion in response to minor bends of a nonvertical continental transform, *J. Geophys. Res.*, **111**, pp. B04102.
- Crampin, S. and Evans, R.,** 1986. Neotectonics of the Marmara Sea region of Turkey, *Journal of the Geological Society*, Vol. 143, no. 2, pp. 343-348.
- Dean, O. Monod, R.B. Rickards, O. Demir and P. Bultynck,** 2000. Lower Palaeozoic stratigraphy and palaeontology, Karadere–Zirze area, Pontus Mountains, northern Turkey, *Geological Magazine* **137** (2000), pp. 555–582.
- Delouis, B., Giardini, D., Lundgren, P. and Salichon, J.,** 2002. Joint Inversion of InSAR, GPS, Teleseismic, and Strong-Motion Data for the Spatial and Temporal Distribution of Earthquake Slip: Application to the 1999 Izmit Mainshock, *Bulletin of the Seismological Society of America*, **92**, pp. 278-299.
- Demirbag, E., Rangin, C., Le Pichon, X. and Celal Sengor, A. M.,** 2003. Investigation of the tectonics of the Main Marmara Fault by means of deep-towed seismic data, *Tectonophysics*, Vol. **361**, no. 1-2, pp. 1-19.

- Dewey, J. F., Hempton, M. R., Kidd, W. S. F., Saroglu, F. and Sengor, A. M. C.,** 1986. Shortening of continental lithosphere: the neotectonics of Eastern Anatolia -- a young collision zone, Geological Society, London, *Special Publications*, Vol. **19**, no. 1, pp. 1-36.
- Dorbath, C., D. Oppenheimer, F. Amelung, and G. King,** 1996. Seismic tomography and deformation modeling of the junction of the San Andreas and Calaveras faults, *J. Geophys. Res.*, **101**, pp. 27917–27941.
- Doust, H. and Arıkan, Y.,** 1974. The geology of the Thrace Basin, *Proceedings of the Second Petroleum Congress of Turkey*, pp. 119–136.
- Elliott, A.J., Dolan, J.F., and Oglesby, D.D.,** 2009. Evidence from coseismic slip gradients for dynamic control on rupture propagation and arrest through stepovers: *Journal of Geophysical Research*, v. **114**, pp. B02313.
- Emre, Ö., Awata, Y. and Duman, T. Y.,** 2003. *17 Ağustos 1999 İzmit Depremi Yüzey Kırığı*, MTA yayınları, 280 pp.
- Ergin, M., Bodur, M. N. and Ediger, V.,** 1991. Distribution of surficial shelf sediments in the northeastern and southwestern parts of the Sea of Marmara: Strait and canyon regimes of the Dardanelles and Bosphorus, *Marine Geology*, **96**, pp. 313-340.
- Ergin, M., Kapur, S., Karakaş, Z., Akca, E., Kangal, Ö. and Keskin, Ş.,** 1999. Grain size and clay mineralogy of Late Quaternary sediments on a tectonically active shelf, the southern Sea of Marmara: clues to hydrographic, tectonic and climatic evolution, *Geol. J.*, **34**, pp. 199-210.
- Ergün, M. and Özel, E.,** 1995. Structural relationship between the Sea of Marmara Basin and the North Anatolian Fault Zone, *Terra Nova*, Vol. **7**, no. 2, pp. 278-288.
- Erinç, S.,** 1973. Türkiyenin şekillenmesinde Neotektoniğin rolü ve jeomorfoloji-jeodimanik ilişkiler. *Cumhuriyetin 50. yılı Yerbilimleri Kongresi*, pp. 1-12.
- Ferry, M., Meghraoui, M., Karaki, N. A., Al-Taj, M., Amoush, H., Al-Dhaisat, S. and Barjous, M.,** 2007. A 48-kyr-long slip rate history for the Jordan Valley segment of the Dead Sea Fault, *Earth and Planetary Science Letters*, **260**, pp. 394-406.
- Flerit, F., Armijo, R., King, G. and Meyer, B.,** 2004. The mechanical interaction between the propagating North Anatolian Fault and the back-arc extension in the Aegean, *Earth and Planetary Science Letters*, Vol. **224**, no. 3-4, pp. 347-362.
- Flerit, F., Armijo, R., King, G. C. P., Meyer, B. and Barka, A.,** 2003. Slip partitioning in the Sea of Marmara pull-apart determined from GPS velocity vectors, *Geophysical Journal International*, Vol. **154**, no. 1, pp. 1-7.
- Görür, N. and Okay, A.,** 1996. A fore-arc origin for the Thrace Basin, NW Turkey, *International Journal of Earth Sciences*, Vol. **85**, no. 4, pp. 662-668.

- Görür, N., Cagatay, M., Sakinc, M., Sümengen, M., Sentürk, K., Yaltirak, C. and Tchapylyga, A.,** 1997. Origin of the Sea of Marmara as Deduced from Neogene to Quaternary Paleogeographic Evolution of its Frame, *International Geology Review*, Vol. **39**, no. 4, pp. 342-342.
- Gülen, L., Pınar, A., Kalafat, D., Özel, N., Horasan, G., Yılmaz, M. and Işıkkara, A. M.,** 2002. Surface Fault Breaks, Aftershock Distribution, and Rupture Process of the 17 August 1999 Izmit, Turkey, Earthquake, *Bulletin of the Seismological Society of America*, **92**, pp. 230-244.
- Hancock, P. L. and Barka, A. A.,** 1981. Opposed shear senses inferred from neotectonic mesofracture systems in the North Anatolian fault zone, *Journal of Structural Geology*, Vol. 3, no. 4, pp. 383-392.
- Harris, R. and Day, S.,** 1993. Dynamics of fault interaction- Parallel strike-slip faults, *Journal of Geophysical Research*, **98**, pp. 4461-4472.
- Hirn, A., Singh, S., Saatçılar, R., Laigle, M., de Voogd, B., Taymaz, T., Ozalaybey, S., Cetin, S., Bécel, A., Vigner, A., Carton, H., Shimamura, H., Lépine, J.-C., Sapin, M., Charvis, P., Karabulut, H., and Géli, L.,** 2003. Elements of structure at crustal scale under the Sea of Marmara from multichannel seismics of the SEISMARMARA survey: *Geophysical Research Abstracts*, v. 5, pp. 13126.
- Hubert-Ferrari, A. I., Armijo, R., King, G., Meyer, B. and Barka, A.,** 2002. Morphology, displacement, and slip rates along the North Anatolian Fault, Turkey, *J. Geophys. Res.*, Vol. **107**, no. B10, pp. 2235.
- Hubert-Ferrari, A., Barka, A., Jacques, E., Nalbant, S. S., Meyer, B., Armijo, R., Tapponnier, P. and King, G. C. P.,** 2000. Seismic hazard in the Marmara Sea region following the 17 August 1999 Izmit earthquake, *Nature*, Vol. **404**, no. 6775, pp. 269-273.
- Imren, C., Le Pichon, X., Rangin, C., Demirbag, E., Ecevitoglu, B. and Gorur, N.,** 2001. The North Anatolian Fault within the Sea of Marmara: a new interpretation based on multi-channel seismic and multi-beam bathymetry data, *Earth and Planetary Science Letters*, Vol. **186**, no. 2, pp. 143-158.
- Inan, S., Ergintav, S., Saatçılar, R., Tüzel, B., and İravul, Y.,** 2007. Turkey Makes Major Investment in Earthquake Research: *Eos*, v. **88**, p. P. 333-P. 333.
- Ketin, I.,** 1948. Über die tektonisch-mechanischen Folgerungen aus den großen anatolischen Erdbeben des letzten Dezenniums, *International Journal of Earth Sciences*, Vol. **36**, no. 1, pp. 77-83.
- Ketin, İ.,** 1957. Kuzey Anadolu Deprem Fayı, *İTÜ Dergisi*, Vol. **15**, no. pp. 49-52.
- Ketin, I.,** 1969. Über die nordanatolische Horizontalverschiebung, *Bull. Min. Res. Explor. Inst. Turkey*, Vol. **72**, no. pp. 1-28.
- Ketin, İ.,** 1976. San Andreas ve Kuzey Anadolu Faylari arasında bir karşılaştırma, *Türkiye Jeoloji Kurumu Bülteni*, Vol. **19**, no. pp. 149-154.

- Koçyiğit, A.**, 1989. Suşehri basin: an active fault-wedge basin on the North Anatolian Fault Zone, Turkey, *Tectonophysics*, Vol. **167**, no. 1, pp. 13-29.
- Kopp, K. O., Pavoni, N. and Schindler, C.**, 1969. Geologie Thrakiens 4: Das Ergene-Becken, *Geologisches Jahrb.*, Beiheft.
- Kozacı, Ö., Dolan, J. F. and Finkel, R. C.**, 2009. A late Holocene slip rate for the central North Anatolian fault, at Tahtaköprü, Turkey, from cosmogenic ¹⁰Be geochronology: Implications for fault loading and strain release rates, *J. Geophys. Res.*, **114**, pp. B01405.
- Kozacı, Ö., Dolan, J., Finkel, R. and Hartleb, R.**, 2007. Late Holocene slip rate for the North Anatolian fault, Turkey, from cosmogenic ³⁶Cl geochronology: Implications for the constancy of fault loading and strain release rates, *Geology*, **35**, 10, pp. 867-870.
- Krishnaswamy, S., Lal, D., Martin, J.-M. & Meybeck M.**, 1971. Geochronology of lake sediments. *Earth and Planetary Science Letters*, **11**, pp. 407-414.
- Kuscu, I., Okamura, M., Matsuoka, H., Gokasan, E., Awata, Y., Tur, H., Simsek, M. and Kecer, M.**, 2005. Seafloor gas seeps and sediment failures triggered by the August 17, 1999 earthquake in the Eastern part of the Gulf of Izmit, Sea of Marmara, NW Turkey, *Marine Geology*, **215**, pp. 193-214.
- Laigle, M., Becel, A., de Voogd, B. a., Hirn, A., Taymaz, T. and Ozalaybey, S.**, 2008. A first deep seismic survey in the Sea of Marmara: Deep basins and whole crust architecture and evolution, *Earth and Planetary Science Letters*, Vol. **270**, no. 3-4, pp. 168-179.
- Le Pichon, X., Rangin, N., Chamot-Rooke, C. and Sengör, A. M. C.**, 2003. The North Anatolian fault in the Sea of Marmara, *Journal of Geophysical Research*, Vol. 108, no. B4, pp. 2179-2179.
- Le Pichon, X., Sengor, A. M. C., Demirbag, E., Rangin, C., Imren, C., Armijo, R., Gorur, N., Cagatay, N., Mercier de Lepinay, B. and Meyer, B.**, 2001. The active Main Marmara Fault, *Earth and Planetary Science Letters*, Vol. **192**, no. 4, pp. 595-616.
- Le Pichon, X., Taymaz, T. and Sengor, A. M. C.**, 1999. The Marmara Fault and the future Istanbul earthquake. *In International Conference on the Kocaeli Earthquake*, 17 August 1999, pp. 41-54.
- Lettis, W., Bachhuber, J., Witter, R., Brankman, C., Randolph, C. E., Barka, A., Page, W. D. and Kaya, A.**, 2002. Influence of Releasing Step-Overs on Surface Fault Rupture and Fault Segmentation: Examples from the 17 August 1999 Izmit Earthquake on the North Anatolian Fault, Turkey, *Bulletin of the Seismological Society of America*, **92**, pp. 19-42.
- Macovei, G.**, 1912. Sur La Tremblement De Terre De La Mer De Marmara Le 9 Aout 1912, *Bull. sect. sci. acad. Rumanie*, **1**, pp. 9-18.
- McCaffrey, R.**, 2002. Crustal block rotations and plate coupling, Plate Boundary Zones, *Geodyn. Ser.*, **30**, pp. 101-122.

- McCalpin, J. P.**, 1994. Quaternary deformation along the East Cache fault zone, Cache County, *Utah. Spec. Stud. Utah Geol. Miner.Surv.* 83, pp. 1–37.
- McCalpin, J.**, 1996. *Paleoseismology*, Academic Press, San Diego.
- McClusky, S., Balassanian, S., Barka, A., Demir, C., Ergintav, S., Georgiev, I., Gurkan, O., Hamburger, M., Hurst, K., Kahle, H., Kastens, K., Kekelidze, G., King, R., Kotzev, V., Lenk, O., Mahmoud, S., Mishin, A., Nadariya, M., Ouzounis, A., Paradissis, D., Peter, Y., Prilepin, M., Reilinger, R., Sanli, I., Seeger, H., Tealeb, A., Toksöz, M. N. and Veis, G.**, 2000. Global Positioning System constraints on plate kinematics and dynamics in the eastern Mediterranean and Caucasus, *Journal of Geophysical Research*, Vol. **105**, no. B3, pp. 5695–5719.
- McKenzie, D.**, 1972. Active Tectonics of the Mediterranean Region, *Geophysical Journal of the Royal Astronomical Society*, Vol. **30**, no. 2, pp. 109-185.
- Meade, B. J., Hager, B. H., McClusky, S. C., Reilinger, R. E., Ergintav, S., Lenk, O., Barka, A. and Ozener, H.**, 2002. Estimates of Seismic Potential in the Marmara Sea Region from Block Models of Secular Deformation Constrained by Global Positioning System Measurements, *Bulletin of the Seismological Society of America*, Vol. **92**, no. 1, pp. 208-215.
- Meghraoui, M., H. Philip, F. Albarede, and A. Cisternas**, 1988. Trench investigations through the trace of the 1980 El Asnam thrust fault: evidence for paleoseismicity, *Bull. Seism. Soc. Amer.*, vol.**78**, 2, pp.979-999.
- Mercier de Lépinay, B., Labeyrie, L., Çagatay, N., Schneider, J.-L., Cremer, M., Turon, J.-L., Londeix, L., Meyer, B., Gallet, Y., Pondard, N., Ménot-Combes, G., Hadjas, I. and Cortijo, E.**, 2003. Interplay between recent sedimentation and active tectonics in Marmara Sea, *Geophysical Research Abstracts*, **5**, pp. 13126.
- Migeon, S., Weber, O., Fauge`res, J.C., Saint Paul, J.**, 1998. A new X-ray imaging system for core analysis. *Geomarine Letters*, **18**, pp. 251-255.
- Mihailovic, J.**, 1927. Trusne katastrofe na Mramornome moru. *In Posebno izdan.srpse akad nauka 16*, pp. 1-303.
- Muller, J., and Aydin, A.**, 2005. Using geomechanical modeling to constrain the fault geometry within the Marmara Sea, Turkey. *Journal of Geophysical Research*, v.**110**, B03407, pp. 1-13.
- Nakajima, T., Kanai, Y.**, 2000. sedimentary features of seismoturbidites triggered by the 1983 and older historical earthquakes in the eastern margin of the Japan Sea. *Sediment Geol*, **135**, pp. 1–19
- Nalbant, S. S., Hubert, A. and King, G. C. P.**, 1998. Stress coupling between earthquakes in northwest Turkey and the north Aegean Sea, *J. Geophys. Res.*, Vol. **103**, no. B10, pp. 24469-24486.

- Noller J.S., Noller, J., Sowers, S., Colman and K. Pierce**, 2000. Introduction to Quaternary geochronology. In: J.S. Noller, J.M. Sowers and W.R. Lettis, Editors, *Quaternary Geochronology; Methods and Applications* vol. 4, AGU Reference Shelf, Washington DC, USA (2000), pp. 1–10.
- Oglesby, D. D., Mai, P. M., Atakan, K. and Pucci, S.**, 2008. Dynamic models of earthquakes on the North Anatolian fault zone under the Sea of Marmara: Effect of hypocenter location, *Geophysical Research Letters*, Vol. 35, no. pp. L18302-L18302.
- Okay, A. I. and Naci, G.**, 1995. Time and space relations in the formation of the West Black Sea and Thrace Basins, *Symp. on the Geology of the Thrace Basin*, pp. 9-10.
- Okay, A. I. and Tansel, I.**, 1992. New data on the upper age of the Intra-Pontide Ocean from north of Şarköy (Thrace), *Min. Res. Expl. Bull. Turkeu*, Vol. 114, no. pp. 23–26.
- Okay, A. I. and Tuysuz, O.**, 1999. Tethyan sutures of northern Turkey, *Geological Society, London, Special Publications*, Vol. 156, no. 1, pp. 475-515.
- Okay, A. I.**, 1989. Tectonic units and sutures in the Pontides, northern Turkey, NATO ASI series. Series C, *Mathematical and physical sciences*, Vol. 259, no. pp. 109-116.
- Okay, A. I.**, 2008. Geology of Turkey: A Synopsis, *Der ANSCHNITT*, Vol. 21, no. pp. 19-42.
- Okay, A. İ., Demirbağ, E., Kurt, H., Okay, N. and Kuşcu, İ.**, 1999. An active, deep marine strike-slip basin along the North Anatolian fault in Turkey, *Tectonics*, 18, pp. 129-147.
- Okay, A. İ., Kaşlılar-Özcan, A., İmren, C., Boztepe-Guney, A., Demirbag, E. and Kuşcu, İ.**, 2000. Active faults and evolving strike-slip basins in the Marmara term Sea, northwest Turkey: a multichannel seismic reflection survey, *Tectonophysics*, 321, pp. 189-218.
- Okay, A. I., Satir, M., Maluski, H., Siyako, M., Monie, P., Metzger, R. and Akyüz, S.**, 1996. Paleo-and Neo-Tethyan events in northwest Turkey: geological and geochronological constraints, *Tectonics of Asia*, pp. 420-441.
- Okay, A.**, 1996. Granulite facies gneisses from the Pular region, Eastern Pontides, *Turkish Journal of Earth Sciences*, 5, pp. 55-61.
- Özalaybey, S., Ergin, M., Aktar, M., Tapirdamaz, C., Biçmen, F., and Yörük, A.**, 2002. The 1999 Izmit Earthquake Sequence in Turkey: Seismological and Tectonic Aspects: *Bulletin of the Seismological Society of America*, v. 92, pp. 376-386.
- Pamir, H. N. and Baykal, F.**, 1947. Istranca Masifi'nin jeolojik yapısı, *Turk Geol Soc Bull*, 1, pp. 7-26.
- Pantosti, D., Schwartz, D. P., and Valensise, G.**, 1993. Paleoseismology along the 1980 surface rupture of the Irpina fault: Implications for earthquake recurrence in the southern Apennines, Italy. *J. Geophys. Res.*, 98, pp. 6561–6577.

- Parke, J. R., White, R. S., McKenzie, D., Minshull, T. A., Bull, J., Kuşçu, I., Görür, N. and Şengör, A. M. C.,** 2003. The Sea of Marmara: A two-dimensional seismic reflection profile data archive, *Geochem. Geophys. Geosyst.*, **4**(10), pp.1084.
- Parke, J. R., White, R. S., McKenzie, D., Minshull, T. A., Bull, J. M., Kuşçu, I., Görür, N. and A.M.C., Şengör,** 2002. Interaction between faulting and sedimentation in the Sea of Marmara, western Turkey, *J. Geophys. Res.*, Vol. **107**, no. B11, pp. 2286.
- Parke, Minshull, Anderson, White, McKenzie, Kuscu, Bull, Gorur and Sengor,** 1999. Active faults in the Sea of Marmara, western Turkey, imaged by seismic reflection profiles, *Terra Nova*, Vol. **11**, no. 5, pp. 223-227.
- Parsons, T.,** 2004. Recalculated probability of $M \geq 7$ earthquakes beneath the Sea of Marmara, Turkey, *J. Geophys. Res.*, Vol. **109**, no. B05304, pp. 10.1029/2003JB002667.
- Parsons, T., Stein, R. S., Dieterich, J. H., Barka, A. and Toda, S.,** 2000. Influence of the 17 August 1999 Izmit earthquake on seismic hazards in Istanbul. *In The 1999 Izmit and Düzce Earthquakes: Preliminary Results*, pp. 295-310.
- Pavoni, N.,** 1961. Die Nordanatolische Horizontalverschiebung, *Geologische Rundschau*, Vol. **51**, no. pp. 122–139.
- Perincek, D.,** 1991. Possible strand of the North Anatolian Fault in the Thrace Basin, Turkey; an interpretation, *AAPG Bulletin*, Vol. **75**, no. 2, pp. 241-257.
- Piper, D.J.W, Shor, A.N., Hughes Clarke JE,** 1988. The 1929 ‘Grand Banks’ earthquake, slump and turbidity current. In: Clifton HE (ed) Sedimentologic consequences of convulsive geologic events. *Geol Soc Am Spec Publ*, **229**, pp. 77–92.
- Pınar, N.,** 1943. Marmara denizi Havzasının Sismik Jeoloji ve Meteorolojisi / Geologie et Meteorologie Sismique du Bassin de Mer Marmara, *Doktora tezi*, Fen Fakültesi, İstanbul
- Polonia, A., Cormier, M. H., Cagatay, N., Bortoluzzi, G., Bonatti, E., Gasperini, L., Seeber, L., Gorur, N., Capotondi, L., McHugh, C., Ryan, W. B. F., Emre, O., Okay, N., Ligi, M., Tok, B., Blasi, A., Buseti, M., Eris, K., Fabretti, P., Fielding, E. J., Imren, C., Kurt, H., Magagnoli, A., Marozzi, G., Ozer, N., Penitenti, D., Serpi, G. and Sarikavak, K.,** 2002. Exploring submarine earthquake geology in the Marmara Sea, *EOS - Transactions American Geophysical Union*, **83**, no. 21, p. 229.
- Polonia, A., Gasperini, L., Amorosi, A., Bonatti, E., Bortoluzzi, G., Cagatay, N., Capotondi, L., Cormier, M. H., Gorur, N., McHugh, C. and Seeber, L.,** 2004. Holocene slip rate of the North Anatolian Fault beneath the Sea of Marmara, *Earth and Planetary Science Letters*, **227**, pp. 411-426.

- Pondard, N., Armijo, R., King, G. C. P., Meyer, B. and Flerit, F.,** 2007. Fault interactions in the Sea of Marmara pull-apart (North Anatolian Fault): earthquake clustering and propagating earthquake sequences, *Geophysical Journal International*, v. **171**, pp. 1185-1197.
- Rangin, C., Pichon, X. L., Demirbag, E. and Imren, C.,** 2004. Strain localization in the Sea of Marmara: Propagation of the North Anatolian Fault in a now inactive pull-apart, *Tectonics*, v. **23**, pp. TC2014.
- Reilinger, R. E., Ergintav, S., Burgmann, R., McClusky, S., Lenk, O., Barka, A., Gurkan, O., Hearn, L., Feigl, K. L., Cakmak, R., Aktug, B., Ozener, H. and Toksoz, M. N.,** 2000. Coseismic and Postseismic Fault Slip for the 17 August 1999, M = 7.5, Izmit, Turkey Earthquake, *Science*, **289**, pp. 1519-1524.
- Reilinger, R. E., McClusky, S. C., Oral, M. B., King, R. W., Toksöz, M. N., Barka, A. A., Kınık, I., Lenk, O. and Şanlı, I.,** 1997. Global Positioning System measurements of present-day crustal movements in the Arabia-Africa-Eurasia plate collision zone, *J. Geophys. Res.*, Vol. **102**, no. B5, pp. 9983–9999.
- Reilinger, R. E., McClusky, S., Vernant, P., Lawrence, S., Ergintav, S., Cakmak, R., Ozener, H., Kadirov, F., Guliev, I., Stepanyan, R., Nadariya, M., Hahubia, G., Mahmoud, S., Sakr, K., ArRajehi, A., Paradissis, D., Al-Aydrus, A., Prilepin, M., Guseva, T., Evren, E., Dmitrotsa, A., Filikov, S. V., Gomez, F., Al-Ghazzi, R. and Karam, G.,** 2006. GPS constraints on continental deformation in the Africa-Arabia-Eurasia continental collision zone and implications for the dynamics of plate interactions, *J. Geophys. Res.*, Vol. **111**, pp. B05411.
- Ryan, W.B.F., Pitman, W.C., Major, C.O., Shimkus, K., Moskalenko, V., Jones, G.A. Dimitrov, P., Gorür, N., Sakinc, M. and Yüce, H.,** 1997. An abrupt drowning of the Black Sea shelf, *Marine Geology*, **138**, pp. 119-126.
- Robertson, A. H. F. and Grasso, M.,** 1995. Overview of the Late Tertiary;Recent tectonic and palaeo-environmental development of the Mediterranean region, *Terra Nova*, Vol. **7**, no. 2, pp. 114-127.
- Robbins, J., Edgington, D.N.,** 1975. Determination of recent sedimentation rates in Lake Michigan using 210Pb and 137Cs. *Geochimica Cosmochimica Acta*, **39**, pp. 285-304.
- Rockwell, T. K.,** 1987. Recognition of individual paleoseismic events in strike-slip environments. In *Directions in Paleoseismology* (A. J. Crone, and E. M. Omdahl, Eds.), *U.S. Geol. Surv. Open File Rep.* 87–673, pp. 129–135.
- Sadi, D. Y.,** 1912. Marmara Havzasının 26-27 Temmuz Hareket-i Arzı 15 Eylül 1328, *Resimli Kitap Matbaası, İstanbul*, 45.
- Sarı, E. and Çağatay, N.,** 2006. Turbidites and their association with past earthquakes in the deep Çınarcık Basin of the Marmara Sea. *Geo-Marine Letters*, **26**, pp. 69-76.

- Sarıbudak, M., Sanver, M. and Ponat, E.,** 1989. Location of western Pontides, NW Turkey, during Triassic time: preliminary palaeomagnetic results, *Geophys. J.*, Vol. **96**, no. pp. 43-50.
- Schmidt, S., Jouanneau, J-M., Weber, O., Lecroart, P., Radakovitch, O., Gilbert, F. and Jezequel, D.,** 2007. Sedimentary processes in the Thau Lagoon (South France): from seasonal to century time scales. *Estuarine Coastal Shelf Science*, **72**, pp. 534-542.
- Schmidt S., Howa H., Mouret A., Lombard F., Anschutz P. and Labeyrie L.,** 2009. Particle fluxes and recent sediment accumulation on the Aquitanian margin of Bay of Biscay. *Continental Shelf Research*, **29**, pp. 1044-1052.
- Schwartz, D.P., and Coppersmith, K.J.,** 1984. Fault behavior and characteristic earthquakes: Examples from the Wasatch and San Andreas fault zones: *J. Geophys. Res.*, v. **89**, pp. 5681-5698.
- Seeber, L., Emre, O., Cormier, M. H., Sorlien, C. C., McHugh, C. M. G., Polonia, A., Ozer, N. and Cagatay, N.,** 2004. Uplift and subsidence from oblique slip: the Ganos-Marmara bend of the North Anatolian Transform, western Turkey, *Tectonophysics*, **391**, pp. 239-258.
- Shiki T, Kumon F, Inouchi Y, Kontani Y, Sakamoto T, Tateishi M, Matsubara H and Fukuyama K,** 2000. Sedimentary features of the seismo-turbidites, Lake Biwa, Japan. *Sediment Geol*, **135**, pp. 37–50
- Sieh, K., and Jahns, R.H.,** 1984. Holocene activity of the San Andreas Fault at Wallace Creek, California: *Geol. Soc. America Bull.* **95**, pp. 883-896.
- Seymen, İ.,** 1975. Kelkit vadisi kesiminde Kuzey Anadolu Fay Zonunun tektonik özelliği, İTÜ Maden Fak. Yay., İstanbul.
- Smith, A. D., Taymaz, T., Oktay, F., Yuce, H., Alpar, B., Basaran, H., Jackson, J. A., Kara, S. and Simsek, M.,** 1995. High-resolution seismic profiling in the Sea of Marmara (Northwest Turkey); late Quaternary sedimentation and sea-level changes, *GSA Bulletin*, Vol. **107**, no. 8, pp. 923-936.
- Sorlien, C. C., Seeber, L., Diebold, J., Shillington, D., Steckler, M. S., Gurcay, S., Kucuk, H. M., Akhun, S. D., Timur, D. and Dondurur, D.,** 2008. The seismic stratigraphic record of Quaternary deformation across the North Anatolian fault system in southern Marmara Sea, Turkey, *Eos Trans. AGU*, v.89, pp. T21A-1915
- Steckler, M. S., Çifçi, G., Demirbağ, E., Akhun, S. D., Büyükaşık, E., Cevatoglu, M., Coşkun, S., Diebold, J., Dondurur, D., Gürçay, S., Imren, C., Küçük, H. M., Kurt, H., Özer, P. G., Perinçek, E., Seeber, L., Shillington, D., Sorlien, C. and Timur, D.,** 2008. High Resolution Multichannel Imaging of Basin Growth Along a Continental Transform: The Marmara Sea Along the North Anatolian Fault in NW Turkey, *Eos Trans. AGU*, v.89, pp.T21A-1921.
- Stein, R. S., Barka, A. A. and Dieterich, J. H.,** 1997. Progressive failure on the North Anatolian fault since 1939 by earthquake stress triggering, *Geophysical Journal International*, Vol. **128**, no. pp. 594-604.

- Straub, C.**, 1996. Recent crustal deformation and strain accumulation in the Marmara Sea Region, NW Anatolia, inferred from GPS measurements *Ph. D. thesis*, Zürich Swiss Federal Institute of Technology, 123.
- Sungurlu, O.**, 1971. Geology of the Black Sea coast between the Bosphorus and the Bulgarian border, *TPAO Reports*, TPAO, Ankara.
- Şaroğlu F., Emre, Ö. ve Kuşçu İ.**, 1992. *Active Fault Map of Turkey*, General Directorate of Mineral Research and Exploration (MTA), Ankara, Turkey.
- Şengör, A. M. C. and Kidd, W. S. F.**, 1979. Post-collisional tectonics of the Turkish-Iranian plateau and a comparison with Tibet, *Tectonophysics*, Vol. **55**, no. 3-4, pp. 361-376.
- Şengör, A. M. C. and Yılmaz, Y.**, 1981. Tethyan evolution of Turkey: A plate tectonic approach, *Tectonophysics*, Vol. **75**, no. 3-4, pp. 181-241.
- Şengör, A. M. C.**, 1987. Cross-faults and differential stretching of hanging walls in regions of low-angle normal faulting: examples from western Turkey, *Geological Society London Special Publications*, **28**, pp. 575-575.
- Şengör, A. M. C., Görür, N. and Şaroğlu, F.**, 1985. Strike-slip deformation basin formation and sedimentation: strike-slip faulting and related basin formation in zones of tectonic escape: Turkey as a case study, *Soc. Econ. Paleontol. Mineral. Spec. Publ.*, Vol. **37**, pp. 227-264.
- Şengör, A. M. C., Okan, T., Caner, İ., Mehmet, S., Haluk, E., Naci, G., Xavier Le, P. and Claude, R.**, 2005. The North Anatolian Fault: A New Look, *Annual Review of Earth and Planetary Sciences*, Vol. **33**, pp. 37-112.
- Şengör, A. M. C., Tüysüz, O., Imren, C., Sakiñç, M., Eyidogan, H., Görür, N., Le Pichon, X. and Rangin, C.**, 2004. The North Anatolian Fault: A new look, *Annu. Rev. Earth Planet. Sci.*, Vol. **33**, pp. 1-75.
- Şengör, A. M. C., Yılmaz, Y. and Sungurlu, O.**, 1984. Tectonics of the Mediterranean Cimmerides: nature and evolution of the western termination of Palaeo-Tethys, *Geological Society, London, Special Publications*, Vol. **17**, no. 1, pp. 77-112.
- Şengör, A. M., Büyükaşikoğlu, S. and Canitez, N.**, 1983. Neotectonics of the Pontides: implications for incompatible structures along the North Anatolian fault, *Journal of Structural Geology*, **5**, pp. 211-216.
- Tan, O., Tapırdamaz, M. C. and Yörük, A.**, 2008. The Earthquake Catalogues for Turkey, *Turkish J. Earth Sci.*, Vol. **17**, no. 2, pp. 405-418.
- Tatar, Y.**, 1975. Tectonic structures along the North Anatolian fault zone, northeast of Refahiye (Erzincan), *Tectonophysics*, Vol. **29**, no. 1-4, pp. 401-409.
- Toda, S., Stein, R. S., Richards-Dinger, K. and Bozkurt, S. B.**, 2005. Forecasting the evolution of seismicity in southern California: Animations built on earthquake stress transfer, *J. Geophys. Res.*, **110**, pp. B05S16.
- Toksöz, M. N., Shakal, A. F. and Michael, A. J.**, 1979. Space-time migration of earthquakes along the North Anatolian fault zone and seismicity gaps, *Pure and Applied Geophysics*, **117**, pp. 1258-1270.

- Tolun, L., Çagatay, M. N. and Carrigan, W. J.,** 2002. Organic geochemistry and origin of Late Glacial-Holocene sapropelic layers and associated sediments in Marmara Sea, *Marine Geology*, 190, 1-2, pp. 47-60.
- Turgut, S., Türkaslan, M. and Perinçek, D.,** 1991. Evolution of the Thrace sedimentary basin and its hydrocarbon prospectivity, Generation, accumulation, and production of Europe's hydrocarbons. *Spec Publ Eur Assoc Petrol Geosci*, 1, pp. 415-437.
- Uçarkuş, G., Çakır, Z., Armijo, R.** (in press). Western Termination of the Mw 7.4, 1999 Izmit Earthquake Rupture: Implications for the Expected Large Earthquake in the Sea of Marmara. *Turkish Journal of Earth Sciences*. doi:10.3906/yer-0911-72.
- Ustaömer, P. A., Mundil, R. and Renne, P. R.,** 2005. U/Pb and Pb/Pb zircon ages for arc-related intrusions of the Bolu Massif (W Pontides, NW Turkey): evidence for late Precambrian (Cadomian) age, *Terra Nova*, 17, pp. 215-223.
- Wells, D. L. and Coppersmith, K. J.,** 1994, Updated empirical relationships among magnitude, rupture length, rupture area, and surface displacement, *BSSA* 70(4), pp. 1337–1346.
- Wesnousky, S. G.,** 2006. Predicting the endpoints of earthquake ruptures, *Nature*, 444, 7117, pp. 358-360.
- Wong, H. K., Ludmann, T., Ulug, A. and Gorur, N.,** 1995. The Sea of Marmara: a plate boundary sea in an escape tectonic regime, *Tectonophysics*, Vol. 244, no. 4, pp. 231-250.
- Wood, R. A., Pettinga, J. R., Bannister, S., Lamarche, G. and McMorran, T. J.,** 1994. Structure of the Hanmer strike-slip basin, Hope fault, New Zealand, *Geological Society of America Bulletin*, Vol. 106, no. 11, pp. 1459-1473.
- Woodcock, N. H. and Schubert, C.,** 1994. *Continental strike-slip tectonics*, Pergamon Press, Oxford, pp. 251–263.
- Wright, T., Fielding, E. and Parsons, B.,** 2001. Triggered Slip: Observations of the 17 August 1999 Izmit (Turkey) Earthquake Using Radar Interferometry, *Geophysical Research Letters*, 28, pp. 1079-1082.
- Wald, D.J., and Heaton, T.H.,** 1994. Spatial and temporal distribution of slip for the 1992 Landers, California, earthquake: **Bulletin of the Seismological Society of America**, v. 84, pp. 668-691.
- Wu, J. E., McClay, K., Whitehouse, P. and Dooley, T.,** 2009. 4D analogue modelling of transtensional pull-apart basins, *Marine and Petroleum Geology*, 26, pp. 1608-1623.
- Yaltrak, C., Sakıncı, M., Aksu, A. E., Hiscott, R. N., Galleb, B. and Ulgen, U. B.,** 2002. Late Pleistocene uplift history along the southwestern Marmara Sea determined from raised coastal deposits and global sea-level variations, *Marine Geology*, Vol. 190, no. 1-2, pp. 283-305.

- Yigitbas, E., Kerrich, R., Yilmaz, Y., Elmas, A. and Xie, Q.,** 2004. Characteristics and geochemistry of Precambrian ophiolites and related volcanics from the Istanbul-Zonguldak Unit, Northwestern Anatolia, Turkey: following the missing chain of the Precambrian South European suture zone to the east, *Precambrian Research*, **132**, pp. 179-206.
- Yilmaz Y, Tuysuz, O, Yiğitbaş, E, Genç, Ş. C. and Şengör, A.M.C.,** 1997. Geology and tectonic evolution of the Pontides. In *Regional and Petroleum Geology of the Black Sea and Surrounding Region*, *Am. Assoc. Pet. Geol. Mem.* 68, ed. AG Robinson, pp. 183–266.

CURRICULUM VITAE



Candidate's Full Name: Gülsen UÇARKUŞ

Place and date of birth: Istanbul – 18.10.1976

Permanent Address: ITU Eurasia Institute of Earth Sciences
34469 Maslak, Istanbul TURKEY

Universities and

Colleges attended: Istanbul Technical University, Eurasia Institute of Earth Sciences

Publications:

- **Uçarkuş, G.**, Çakır, Z., Armijo, R. (in press). Western Termination of the Mw 7.4, 1999 Izmit Earthquake Rupture: Implications for the Expected Large Earthquake in the Sea of Marmara. *Turkish Journal of Earth Sciences*. doi:10.3906/yer-0911-72.
- Melinte-Dobrinescu, M.C., Suc, J.-P., Clauzon, G., Popescu, S.-M., Armijo, R., Meyer, B., Biltekin, D., Çagatay, M.N., **Uçarkuş, G.**, Jouannic, G., Fauquette, S., and Çakır, Z., 2009, The Messinian Salinity Crisis in the Dardanelles region: Chronostratigraphic constraints. *Palaeogeography, Palaeoclimatology, Palaeoecology*, v. 278, p. 24-39.
- Géli, L., Henry, P., Zitter, T., Dupré, S., Tryon, M., Çagatay, M. N., de Lépinay, B., Mercier, Le Pichon, X., Sengör, A. M. C., Görür, N., Natalin, B., **Uçarkuş, G.**, Özeren, S., Volker, D., Gasperini, L., Burnard, P., Bourlange, S., the Marnaut Scientific, Party, 2008. Gas emissions and active tectonics within the submerged section of the North Anatolian Fault zone in the Sea of Marmara. *Earth and Planetary Science Letters*, 274(1-2): 34-39.
- Armijo, R., Pondard, N., Meyer, B., **Uçarkuş, G.**, Mercier de Lépinay, B., and the MARMARASCARPS cruise party, 2005. Submarine fault scarps in the Sea of Marmara pull-apart (North Anatolian Fault): Implications for seismic hazard in Istanbul, *Geochem. Geophys. Geosyst.*, 6, Q06009, doi:10.1029/2004GC000896
- Rockwell, T.K., Ragona, D., Seitz, G., Langridge, R., Aksoy, M.E., **Uçarkuş, G.**, Ferry, M., Meltzner, A., Klinger, Y., Megharoui, M., Satir, D., Barka, A., Akbalik, B., 2009. Palaeoseismology of the North Anatolian Fault near the Marmara Sea: implications for fault segmentation and seismic hazard.

Geological Society of London, Speacial Publication. v. 316; p. 31-54.

- **Uçarkuş, G.,** Taymaz, T., Obituary: Prof. Dr. Aykut Barka, *Turkish Journal of Earth Sciences*, v.11 no.1 p.83, TÜBİTAK, Ankara, 2002
- **Ucarkus, G.,** Armijo, R., Cakir, Z., Pondard,N., Meyer, B., Late Pleistocene-Holocene Evolution Of Faulting In The Sea Of Marmara Pull-Apart (North Anatolian Fault), 2009. Eos Trans. AGU, 89(53), Fall Meet. Suppl., T24A-07. San Francisco. 15-19 December.
- **Ucarkus, G.,** Armijo, R., Cakir, Z., Schmidt, S., Meyer, B., Recent Earthquake Breaks at the Sea of Marmara Pull-apart (North Anatolian Fault), 2008. Eos Trans. AGU, 89(53), Fall Meet. Suppl., T24A-07. San Francisco. 15-19 December.
- **Uçarkus, G.,** Armijo, R.; Pondard, N.; Meyer, B.; Çakir, Z, 2006. The Eastern Marmara pull-apart junction (North Anatolian Fault) and its relation to the submarine end of the 1999 Izmit earthquake rupture. European Geosciences Union, General Assembly, EGU06-A-08807, Viyana, 2-7 Nisan.